Unfolding the Excited States Dynamics of Tm^{2+}-doped Halides
In Prospect of Novel Luminescence Solar Concentrators

Plokker, M.P.

DOI
10.4233/uuid:cf9005a0-20bf-436e-abb9-19112f23274d

Publication date
2021

Document Version
Final published version

Citation (APA)
Plokker, M. P. (2021). *Unfolding the Excited States Dynamics of Tm^{2+}-doped Halides: In Prospect of Novel Luminescence Solar Concentrators*. [Dissertation (TU Delft), Delft University of Technology]. https://doi.org/10.4233/uuid:cf9005a0-20bf-436e-abb9-19112f23274d

Important note
To cite this publication, please use the final published version (if applicable).
Please check the document version above.

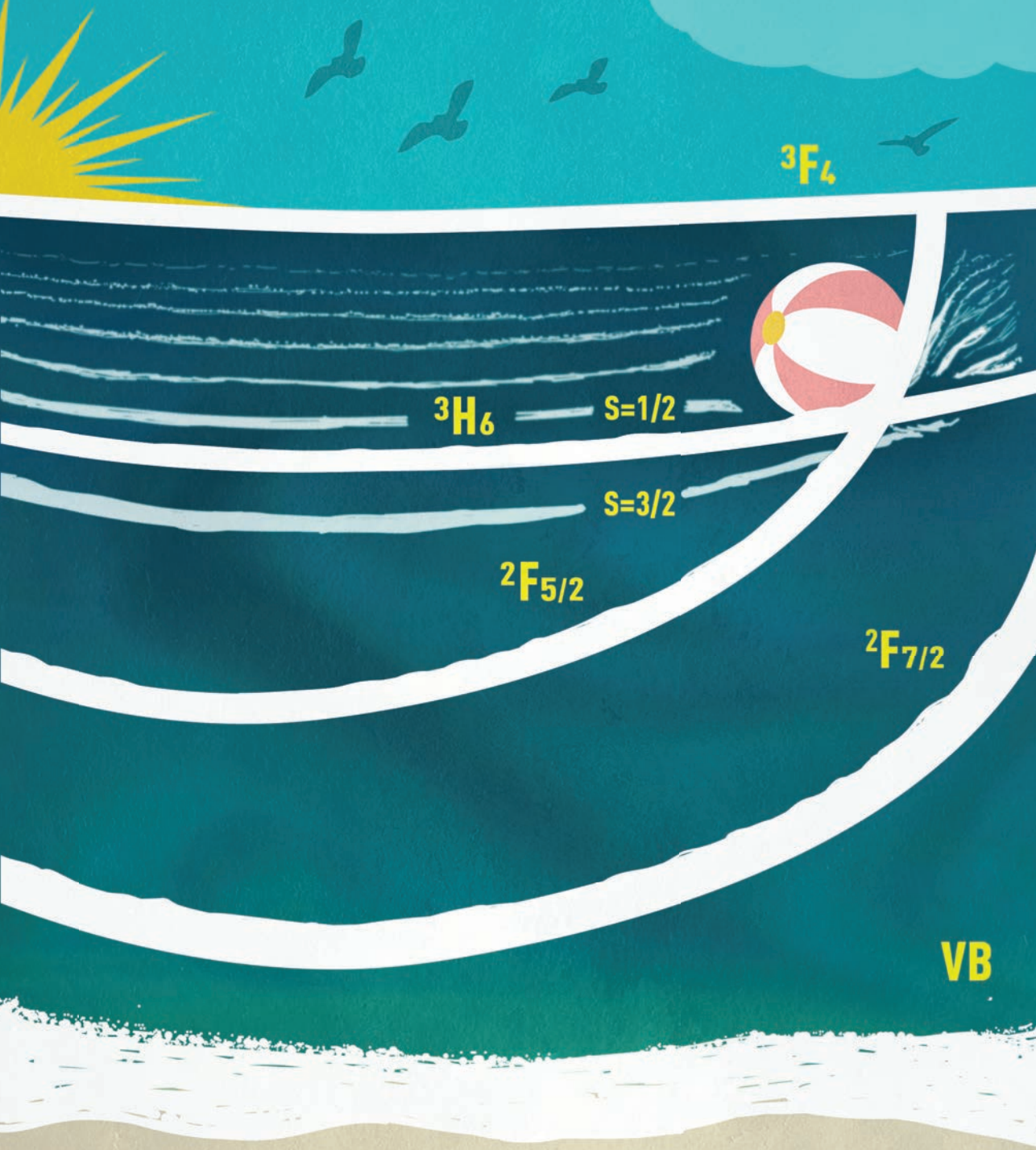

Unfolding the Excited States Dynamics of Tm^{2+}-doped Halides

In Prospect of Novel Luminescence Solar Concentrators

Maarten Plokker

Unfolding the Excited States Dynamics of Tm^{2+}-doped Halides

In Prospect of Novel Luminescence Solar Concentrators

M.P. Plokker

Unfolding the Excited States Dynamics of Tm^{2+}-doped Halides

In Prospect of Novel Luminescence Solar Concentrators

Proefschrift

ter verkrijging van de graad van doctor
aan de Technische Universiteit Delft,
op gezag van de Rector Magnificus Prof.dr.ir. T.H.J.J. van der Hagen,
voorzitter van het College voor Promoties,
in het openbaar te verdedigen op woensdag 1 december 2021 om 15:00 uur

door

Maarten Pieter PLOKKER

Natuurkundig Ingenieur, Technische Universiteit Delft, Nederland
geboren te Hellevoetsluis, Nederland

Dit proefschrift is goedgekeurd door de promotoren:
Prof.dr. P. Dorenbos
Dr. E. van der Kolk

Samenstelling promotiecommissie:

Rector Magnificus,	voorzitter
Prof.dr. P. Dorenbos,	Technische Universiteit Delft, promotor
Dr. E. van der Kolk	Technische Universiteit Delft, promotor

Onafhankelijke leden:

Prof.dr. E.H. Brück	Technische Universiteit Delft
Prof.dr. L.D.A. Siebbeles	Technische Universiteit Delft
Prof.dr. C. Wickleder	Universität Siegen, Germany
Prof.dr. K.W. Krämer	Universität Bern, Switzerland
Prof.dr. P. Smet	Universiteit Gent, Belgium

TU Delft Delft University of Technology

NWO Nederlandse Organisatie voor Wetenschappelijk Onderzoek

This research is supported by The Netherlands Organisation for Scientific Research (NOW/OCW) as part of the LumiCon project (15024).

Keywords: Tm^{2+}-doped halides, luminescence, quenching, excited states dynamics, internal quantum efficiency, luminescence solar concentrator materials.

Printed by: ProefschriftMaken || www.proefschriftmaken.nl

Cover design: Maikel Awater

Front: Simplified momentary expression of the Tm^{2+} excited states dynamics. The wavefronts portray the Tm^{2+} energy levels, while the beach ball dancing on top represents an excited electron that will traverse from one wavefront/level to another via (photoluminescence) quenching.

ISBN 978-94-6423-417-6

An electronic version of this dissertation is available at: http://repository.tudelft.nl/.

"If I abandon this project I would be a man without dreams and I don't want to live like that: I live my life or I end my life with this project!"

Werner Herzog on the fateful set of Fitzcarraldo

To Wilma, Hugo,
Matthijs and Michiel

If you truly want to accomplish something great you must meet the impossible odds with relentless determination!

Table of Contents

1.

Research Topic Introduction

1.1 Sustainability

As fossil fuel reserves are vastly diminishing and the global energy consumption is ever increasing [1-3], world governments have turned their attentions to renewable energy technologies to maintain balance between energy demand and supply; and to drastically reduce Greenhouse gas emissions. Such technologies largely comprise of: photovoltaics, wind power, hydropower and geothermal. Over the last two decades, extensive progress was made into the feasibility, commercialisation and efficiency enhancement of these technologies. This research has led to a framework that allows for a mutual comparison between their strengths and weaknesses based on: overall cost of device production and maintenance, Greenhouse gas emission and costs per generated kWh, longevity and recyclability and overall ecological footprint. [3]

Concerning the global demand for energy, various studies reveal that around 40.3% of all energy is consumed by households and services. An enormous sum! For industry, transportation and agriculture this figure respectively amounts to 25.6%, 31.8% and 2.3%. [4,5,6] In fulfilling the energy demand of households and services, the assemblage of large solar fields and windfarms requires the excessive allocation of scarce free space and introduces overstretched supply lines. A solution is found in the strategy to implement sustainable technologies in buildings. [3] This was appended in the climate and energy framework as designed by the European Commission. The initial Energy Performance of Buildings Directive (EPBD), launched in 2002, [7] strongly emphasised on the energy performances of buildings. This for instance resulted in: the development of an uniform method to calculate the energy performance of buildings, the implementation of basic energy performance standards in newly constructed buildings, energy certification for buildings and mandatory annual inspections of central heating and cooling systems. In 2010, this directive was reformed into EPBD II [8] with additional requirements for buildings. From 2021 onwards, all new buildings within the European Union would have to comply with a nearly zero-energy consumption policy and should be self-sustaining. However, in 2018 the directive was recalled and transformed into EPBD III [9] where by 2050 all buildings should be decarbonised and hence independent of fossil fuels.

With regard to buildings, three main components can be identified: the roof, façade and glazing. These components can all be adapted to include sustainable technologies that generate electricity and/or reduce the external power supply based on fossil fuel combustion. Moreover, this would allow buildings to become self-sustaining and energy independent commodities. Photovoltaic devices, that utilise the enormous energy potential of the sun, can be applied to all three components and are dominating the field. These

devices are united in a collective term coined Building-Integrated Photovoltaics (BIPV) [10] and range from rooftile shaped crystalline silicon solar cells [11,12] to for instance coloured solar cell façades [13,14] and glazing based on luminescence solar concentrators. [15]

1.2 Sustainable Window Technologies

In view of BIPV, various sustainable window technologies can be applied. These mainly include: chromogenic smart windows, transparent Cadmium Telluride thin film solar cells and luminescence solar concentrators. This last technology is of central interest in this dissertation and will be addressed exclusively in the next section.

1.2.1 Chromogenic Smart Windows

Chromogenic materials consist of a wide variety of different compounds. In view of sustainable window technologies three main subclasses of chromogenic materials can be distinguished: photochromic (AgCl, $ZnBr_2$, YH_xO_y), thermochromic (VO_2, Cu_2HgI_4, Cr_2O_3) and electrochromic compounds (WO_3, WCl_6, TiO_2). [16,17,19,20,21] For each such compounds, the optical properties change under exposure to certain specific conditions. In case of photochromic compounds this involves exposure to UV-light, while for thermochromic compounds the change occurs after significant temperature fluctuations such as for instance the seasonal transition from a cold winter to a warm summer. Electrochromic materials form a special instance where the shift in optical properties is induced by applying a voltage over the material. [18,19,20,21]

Figure 1.1 shows an example of a photochromic smart window, and its change in optical properties, covering the time spawn of a full day. As the amount of UV-rich sunlight imminent on the photochromic coating increases, a special photodarkening reaction is triggered that obscures the colour of the coating. In optical terms, its transmittance undergoes a profound decrease, while its reflectance or absorbance increase significantly. The reduced amount of light, that enters the building through the smart window, will result in less heat being generated. Therefore, less energy is required for the internal cooling of the building. When the sun is setting, the photochromic reaction reverses and the coating bleaches back to its original colour. It will then once more exhibit a high optical transmittance combined with a low absorbance and reflectance. Consequently, a large fraction of the incident sunlight will be admitted into the building, resulting in less energy to be consumed for lighting and heating. [18]

Thermochromic smart windows operate in a very similar manner, but are more regionally bounded by the required large temperature fluctuations. Nevertheless, these windows are highly popular for application in vehicles. In contrast to photochromic and thermochromic

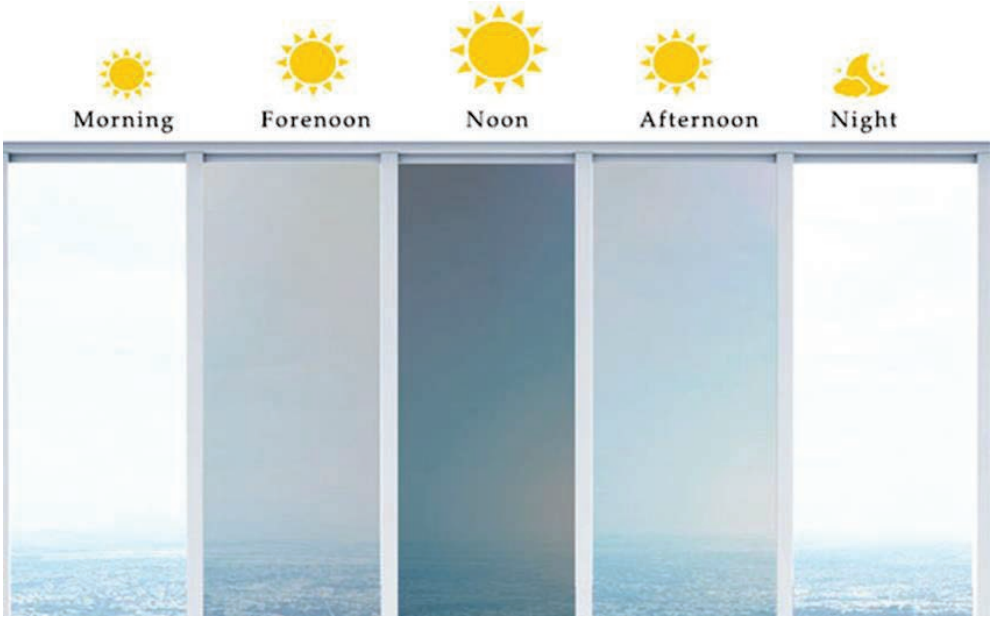

Figure 1.1: A photochromic smart window whose coating undergoes photodarkening as the exposure to UV-rich sunlight intensifies. When the sun sets, the photochromic coating bleaches back to its original colour. [22]

smart windows, a window based on electrochromism allows the consumer to darken it on desire by pressing a simple electronic switch. [20] In the past few years, several pilot projects with chromogenic smart windows have been applied to buildings. Figures show that such devices are able to provide: up to 60% energy savings on lighting, a reduction of the cooling load of up to 20% and a reduction in peak power of 26%. [23]

1.2.2 CdTe Thin Film Solar Cells

As an alternative to chromogenic smart windows, thin film solar cells based on Cadmium Telluride (CdTe) are also highly suited for sustainable window applications. These solar cells are highly transparent and their efficiency ranges from 16-21%. [24,25] The overall power output of a module, based on CdTe solar cells, amounts to 180-320 W_p for an optical transparency of 10-40%. [26] A rough calculation reveals, that such a module would in best case be able to generate 5% of the annual energy consumption of a standard household. Furthermore, CdTe solar cells hold the record of exhibiting the lowest carbon footprint of all solar cells and have the shortest energy payback time, which is less than a year. [24,25] However, the toxicity of Cadmium makes the end-use recycling of CdTe modules a

significant environmental concern. Besides, Tellurium, as required raw material for the fabrication of such solar cells, is a rare element whose natural abundancy is very limited. This compellingly adds to a higher module cost and limits the industrial scalability. [24,25] An example of how CdTe solar cells can be applied as sustainable window technology is shown in figure 1.2.

Figure 1.2: A glass patio cover based on highly transparent Cadmium Telluride thin film solar cells. [27]

1.3 Luminescent Solar Concentrators

1.3.1 Operational Principles

Figure 1.3 provides a basic overview of a Luminescence Solar Concentrator (LSC) system with its main components indicated. In its most basic design, an LSC consist of an inexpensive plastic or glass waveguide with small solar cells attached to its edges. Furthermore, the waveguide contains 'special' luminescent molecules that are represented by organics dyes, inorganic phosphor or quantum dots. Organic dyes are generally embedded inside the waveguide, as shown for example in figure 1.3, whereas inorganic phosphors are imposed in a separate layer or coating on the bottom or top of the waveguide. Quantum dots, on the other hand are incorporated into a liquid solution in between two glass plates. When sunlight falls onto the LSC, it will propagate into the waveguide where part of it is absorbed by the luminescent molecules. The molecules spectrally transform the absorbed light into light of lower energy, which is diffusely re-emitted. Some of this re-emitted light will escape from the waveguide. Nevertheless, a large fraction of it remains trapped inside and undergoes total internal reflection. Such concentrated light is guided towards the solar cells in the edges, where it is photovoltaically converted into an electronic current. [28]

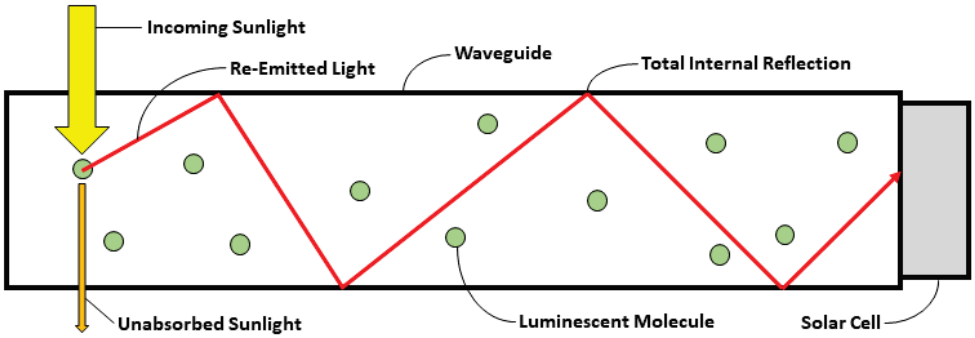

Figure 1.3 Concept of an LSC system explained: incoming sunlight enters the waveguide and is for a large fraction absorbed by the luminescent molecules present in the organic dye. These molecules diffusely re-emit light of lower energy. The re-emitted light undergoes total internal reflection at the sides of the waveguide and propagates towards the edges. Solar cells mounted on the edges transform the re-emitted light into a current via photovoltaic energy conversion.

1.3.2 Efficiency

The overall efficiency of an LSC system is governed by a combination of different factors. It can generally be described by relation (1). In this equation, the highlighted factors are determined by the properties of the selected luminescent molecules, while the others are related to the optical properties of the waveguide.

$$\eta_{Opt} = (1-R)P_{TIR} \cdot \boldsymbol{\eta_{Abs}} \cdot \boldsymbol{\eta_{PLQY}} \cdot \boldsymbol{\eta_{Stokes}} \cdot \eta_{Host} \cdot \eta_{TIR} \cdot \boldsymbol{\eta_{Self}} \quad (1)$$

As *R* resembles the reflection on top of the waveguide, the factor (1-R) represents the amount of light that enters it. P_{TIR} is the total internal reflection efficiency, a factor determined by the critical angle of incidence. Snell's law shows that for light propagating towards a material-air interface, total internal reflection occurs when the angle of incidence is higher than the critical angle. As the critical angle is defined as: $Arcsin(\theta_c) = \left(\frac{1}{n}\right)$, it is the refractive index *n* of the waveguide that determines the total internal reflection efficiency P_{TIR}. For a glass waveguide with $1.5 < n < 1.6$, around 75% of the re-emitted photons will undergo total internal reflection. Furthermore, η_{Host} is the transport efficiency of the re-emitted photons through the waveguide and η_{TIR} represents the reflection efficiency of the waveguide in terms of waveguide surface smoothness. [28]

The factors determined by the choice of luminescent molecules involve: η_{Abs} which represents the fraction of sunlight absorbed by the molecules, η_{PLQY} that corresponds to the photoluminescent quantum yield or internal quantum efficiency, η_{Stokes} which indicates the energy lost due to heat generation in the process of sunlight absorption-light re-emission, and η_{Self} that expresses self-absorption losses due to re-absorption of the re-emitted light by the luminescent molecules. [28]

1.3.3 Typology

As mentioned earlier, there are three common types of materials that can carry the luminescence molecules: organics dyes, quantum dots and inorganic phosphors. Several examples of these materials are displayed in figure 1.4. Organic dyes such as Coumarin CRS040 and Lumogen F-Red305, demonstrate high internal quantum efficiencies η_{PLQY} of around 98%. [29] However, the materials suffer from significant self-absorption losses η_{Self} and their absorption range η_{Abs} is limited, which gives rise to bright colours. [28] Quantum dots, especially core-shell QDs, have lower quantum efficiencies than organic dyes. Nevertheless, the absorption and emission properties can be spectrally tuned to circumvent self-absorption losses. [28] Despite this most LSC quantum dots, like for instance PbS, PbS/CdS, CdSe/CdS, still suffer from these effects. [30] Inorganic phosphors, also referred to as rare-earth based LSC materials, such as Nd^{3+}/Yb^{3+}-, and Cr^{3+}-doped glasses have a clear spectral separation between the absorption bands and emission and hence self-absorption losses are absent. However, the sunlight absorption ranges and internal quantum efficiencies are low. Besides, the emission and the silicon solar cell band gap share a non-perfect spectral match. [28]

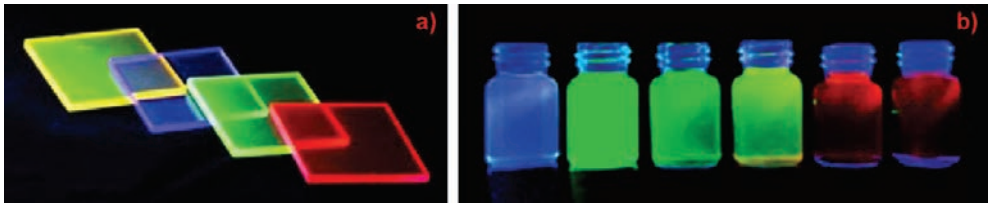

Figure 1.4 Visualisation of two common LSC materials: a) organic LSC dyes where the different colours emerge from particular electron transitions and b) CdSe quantum dots with different spectrally tuned emission wavelengths. [28]

1.3.4 LSC Applications

Up to now, several LSC systems have been practiced in sustainable applications. Two such examples are displayed in figure 1.5. The Italian company Eni, together with the Massachusetts Institute of Technology, developed a special LSC bus shelter that is able to charge electronic bikes. The yellow organic dyes generate a total power output of 500 W_p. [31,32] Another noteworthy LSC application involves a so called Solar Noise Barrier (SONOB). It was developed in 2017 by the Dutch company Heijmans N.V.. in collaboration with the Technical University of Eindhoven and blocks highway noise while at the same time it generates electricity for close surroundings The SONOB was used in a test setup along the Dutch A50 highway, but was dismantled due to too low power yields. [33] Both LSC applications display a profound colouring which is not troublesome. Yet, for sustainable window applications where the focus lies on households and office buildings a transparent non-coloured LSC is wishful.

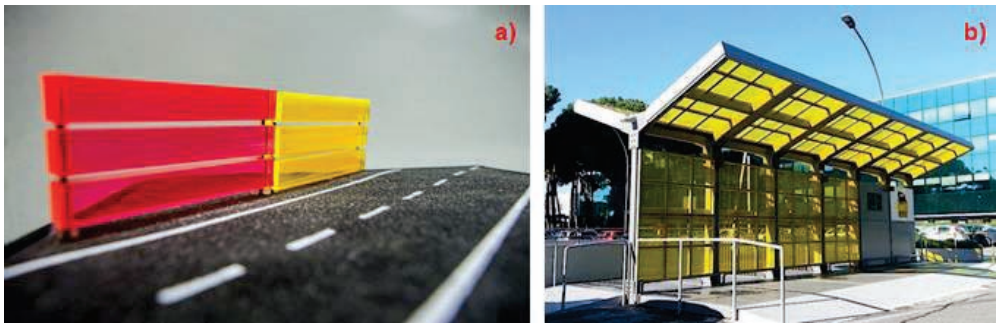

Figure 1.5 Two examples of LSC systems applied in sustainable applications. a) scale model of the Heijmans N.V.. solar noise barrier [33] and b) the Eni bus shelter in Rome that serves as a charging station for electronic bikes. [31]

1.4 Tm^{2+}-doped Halide LSCs

In 2015 a new inorganic rare-earth based composition was introduced within the field of LSCs. With great enthusiasm, Ten Kate et al. [34] announced that some of the major drawbacks of rare-earth based LSCs were de facto neutralised in Tm^{2+}-doped halides. In such compounds, the divalent state of rare-earth metal Thulium (Tm) is used as dopant, whereas metal halides as wide abundant class of materials represent the host lattice. A graphical representation of an LSC based on Tm^{2+}-doped halides is provided in the left panel of figure 1.6.

Intermezzo I: Halides

In almost all cases, metal halides form binary MX_z phases where a metallic element M is bonded to a halogen X such as: F, Cl, Br or I. In the final compound, M will be ionised to z and X will have oxidation state -1. In this context, the binary phase includes: monohalides with z=1, dihalides where z=2, and trihalides by z=3. Monohalides typically involve alkali-metals, such as: Na, K, Rb and Cs, and include by far the most famous halide NaCl, which is also known as 'kitchen salt'. Notable dihalides include: MgF_2, $CaBr_2$, SrI_2, $BaCl_2$ and $CuCl_2$; while $LaBr_3$ is a well-known trihalide. Halides that form ternary AMX_3 phases are a special case. These compounds consist of metallic elements A and M that respectively exhibit oxidation states +1 and +2, and a halogen X with oxidation state -1. The classification follows that of trihalides. In addition to that, the compounds exhibit the crystallographic structure of a Perovskite. Special ternary halides involve BMX_4 compounds, where both B and M have a +2 oxidation state. An example involves $SrZnCl_4$. Such compounds are registered as tetrahalide. [35]

Intermezzo II: Thulium

The rare-earth element Thulium was first discovered in 1879 by Per Theodor Cleve at Ytterby (Sweden). Its name refers to Thule, which in Greek and Roman mythology was regarded as the most northern place on Earth. The collective name rare-earth refers to the fact that these elements are found and extracted as oxides. This can be attributed to the extremely large free enthalpy of formation that amounts to around -1890 kJ/mol for Tm_2O_3. [36] By using various chemical methods, it is possible to separate Tm^{3+} and bind it to a halogen, or even reduce its oxidation state to Tm^{2+} or Tm. Nevertheless, the separated material remains prone to oxidation. Like most other rare-earths, Thulium was initially thought of as 'rare' with limited availability. However, figures show that there is more than $3.6 \cdot 10^5$ kg of Tm_2O_3 present in the deposits: Misery Lake, Mountain Pass and Steenkampskraal. When taking into account the vast rare-earth deposits located in China, such as: Batou and Bayan Obo, this number will even be higher. Moreover, Tm_2O_3 is stockpiled in large reserves, but its low demand warrants a high price. [37]

As a subgroup within the rare-earths, the lanthanides are often used in studying luminescence phenomena. Their 4f-shells are gradually filled from Lanthanum to Lutetium. As such, Thulium with electronic configuration $[Xe]4f^{13}6s^2$ has 13 electrons in the 4f-shell. Tm^{2+} also has 13 electrons in the 4f-shell while in case of Tm^{3+} this number is 12. In a broad range of insulator hosts, the 4f-levels fall inside the relatively wide forbidden zone, between the valence band and conduction band. Therefore, by selective excitation into these levels it is possible to trigger luminescence. Particularly for Tm^{2+}, two 4f-levels can be distinguished: the $^2F_{5/2}$ excited state and $^2F_{7/2}$ ground state. Tm^{3+} has many 4f-levels. [37]

1.4.1 Sunlight Absorption Fraction η_{abs}

The absorption spectrum in the right panel of figure 1.6 reveals that Tm^{2+}, as doped in CaI_2, shares a 63% overlap with the AM 1.5 solar spectrum. It indicates that this coating material, as dependent upon the layer thickness and doping concentration, exhibits the potency to absorb a large proportion of the incident sunlight. For organic dyes as Red 305 and L170, such values are much lower and respectively amount to 36 and 28%. The broad absorption range of CaI_2:Tm^{2+} is caused by the favourable positioning of the Tm^{2+} $4f^{12}5d^1$-bands. This depends on the $4f^{12}5d^1$-crystal field splitting and inherently the choice of halide. [34]

1.4.2 Colour and Transparency

Figure 1.6 also shows that for CaI_2:Tm^{2+} the absorption bands are positioned well over the entire visible range of the electromagnetic spectrum (380-750 nm). With little capricious abnormalities in absorption strength, all wavelengths in this domain are about equally absorbed; resulting in an almost colourless appearance of the material as coating. Besides,

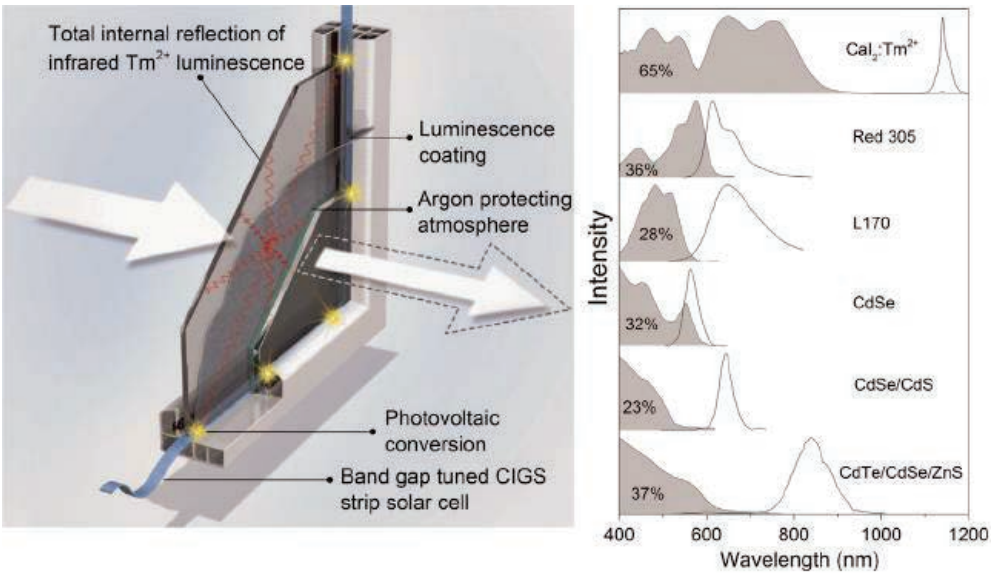

Figure 1.6: Left) concept of a colourless semi-transparent LSC based on Tm^{2+}-doped halides. The luminescence coating positioned between the two glass plates, and protected by an inert Argon atmosphere, absorbs part of the incident sunlight and subsequently re-emits diffusive light with energy 1.09 eV. Via total internal reflection the re-emitted light enters the window edges where CIGS/CIS strip solar cells photovoltaically convert it into a current. Right) comparison between the absorption (grey shaded) and photoluminescence (white shaded) spectra of various LCS materials. An overlap between the two spectra results in self-absorption losses. Sunlight absorption fraction are indicated for each material. Upon comparing, the properties of the Tm^{2+}-doped halide CaI_2:Tm^{2+} appear to be by far superior to other LSC materials. [34]

the absorption is less than 100% at each wavelength. A coating based on Tm^{2+}-doped halides will then be slightly tinted and as such semi-transparent. This is what makes them ideally suited for households and office buildings where non-coloured glass and some degree of transparency is required. [34]

1.4.3 Self-Absorption Losses η_{self}

The Tm^{2+} $^2F_{5/2}\rightarrow{}^2F_{7/2}$ luminescence, used for photovoltaic energy conversion, is positioned remotely from the $4f^{12}5d^1$ absorption bands and hence virtually no self-absorption can occur. As illustrated in figure 1.6, the other LSC materials do suffer from such an effect. However, since the Tm^{2+} luminescence involves a $4f^{13}\rightarrow4f^{13}$ transition, and with a very weak $4f^{13}$-crystal field splitting, there will always be a slight overlap between $^2F_{5/2}$ absorption and $^2F_{5/2}\rightarrow{}^2F_{7/2}$ emission. Nevertheless, this sharp $4f^{13}$ line absorption is typically 100x less intense than the broad $4f^{12}5d^1$ absorption bands and in practical considerations can be neglected. In this sense, one of the main LSC efficiency limitations is removed from the equation. [34]

1.4.4 Photovoltaic Energy Conversion

The Tm^{2+} $^2F_{5/2}\rightarrow{}^2F_{7/2}$ luminescence has a wavelength of around 1140 nm and energy of 1.09 eV. Unfortunately, this energy value is slightly below the electronic bandgap of much used crystalline silicon (~1.14 eV). [38] Therefore a different semiconductor should be used for the photovoltaic energy conversion. A suitable replacement is found among bandgap-tuned Copper-Indium-Gallium-Selenide (CIGS) thin-film semiconductors. For CIGS the electronic bandgap energy amounts to 1.7 eV and too large. However, when the Gallium content is gradually decreased, the bandgap energy also decreases. For Copper-Indium-Selenide (CIS) the bandgap is close to 1.0 eV. [34,39,40] The lower Gallium content also results in a relatively lower environmental impact during the deposition of these kind of solar cells. [41]

1.4.5 Internal Quantum Efficiency η_{PLQY}

Another important LSC parameter is the internal Quantum Efficiency (QE) of the luminescence coating. This value reveals how much of the absorbed sunlight, by the $4f^{12}5d^1$ absorption bands, is effectively transformed into the $^2F_{5/2}\rightarrow{}^2F_{7/2}$ luminescence of energy 1.09 eV. For Tm^{2+}-doped halides, no QE values are available from previous research.

Intermezzo III: Halide Hygroscopicity

Halides are hygroscopic and thereby react with water to form halide hydrates. This rigorous degradation also occurs in open air under the influence of water vapour. It is generally monitored by the weight gain of the compound after one hour of exposure to ambient atmosphere. The hygroscopicity allows it to distinguish three main groups of halides. Least hygroscopic compounds have almost no weight gain after one hour of exposure and involve: LiCl, KCl, KBr, KI, CsCl and CsI. In contrast, CaI_2 and YCl_3 form highly hygroscopic compounds whose weight rapidly increases upon exposure. A third group shows various water absorption rates. Considering the different species, chlorides and bromides display an almost linear dependence between weight gain and exposure time. Iodides show the largest fluctuations in hygroscopic behaviour. Weakly hygroscopic iodides have a similar behaviour as the chlorides and bromides, while strongly hygroscopic iodides show a sub-linear or polynomial dependence between weight gain and exposure time. The rate at which these latter compounds gain weight increases rapidly at the beginning and after a certain exposure time it slows down. [42]

1.4.6 Protection Measures

Due to the oxidation sensitivity of Tm^{2+} and the hygroscopicity of halides, a coating based on Tm^{2+}-doped halides needs to be protected from open-air. [42] This can be envisioned by various means. One option would be the use of inert conditions such as a small protective

atmosphere of Argon or Nitrogen gas, or preserving it under vacuum. Another option involves the encapsulation of the coating into Polyvinyl Butyral (PVB) or Ethylene-Vinyl Acetate (EVA) foils and using glass-to-glass lamination techniques. [43] Crystalline silicon solar cells processed in such a way are able to withstand 30 years of outdoor active service. [44]

1.4.7 Overall Efficiency

Based on the aforementioned properties of Tm^{2+}-doped halides, the LSC efficiency relation, optical loss factors and the photovoltaic efficiency of the CIGS solar cells, Ten Kate et al. made an estimate of the power efficiency of a CaI_2:Tm^{2+} LSC device. This figure amounts to 14.9% and is much higher compared to that of the organic dye Red 305, which is estimated at 3.7%. The difference can be attributed to a two times larger sunlight absorption range for CaI_2:Tm^{2+} and the absence of self-absorption losses. In this comparative analysis, however, the QE value related to the $^2F_{5/2} \rightarrow {}^2F_{7/2}$ emission in CaI_2:Tm^{2+} was not known and considered to be 100%. The QE value for the luminescence signal related to the organic dye Red 305 was also chosen to be 100%. This is actually close to its actual value. The estimation also does not involve surface scattering losses and no accurate value for refractive index of a CaI_2:Tm^{2+} coating was available. [34]

1.5 Historical Overview of Tm^{2+} Research

The research on divalent Thulium can in essence be characterised as a traffic light situation, where intense periods of interest were followed by silent lolls. As a whole it can be divided into four main periods. *(1) The Prehistoric Age* of the 1960s, where a lot of trickery still had to be invented. *(2) The Middle Ages* of the 1970s and 1980s, where there were many realms without a central Tm^{2+} research aim. *(3) The Renaissance* of the 1990s and 2000s that symbolises a complete rebirth of the topic where one discovery was quickly followed by another. *(4) The Re-Defining Age* of present day, where previous enterprises that did not took-off became the feeding ground for new applications.

Intermezzo IV: Masers & Lasers

In his famous article ''Zur Quantentheorie der Strahlung" [45], Albert Einstein predicted the process of spontaneous emission in which an excited atom in isolation can return to a lower energy state by emitting photons. This concept was however not exploited at the time as no application could be thought of. With the rapid advancements of (RADAR) technology in the 1940s, it suddenly became of central interest to various researchers. In 1952, J. Weber first described the theoretical principles of a Microwave Amplification by Stimulated Emission of Radiation (Maser) device. [46,47] Within the same year Nikolay Basov and Alexander

Prokhorov came with a similar, independent, description of a Maser. [46,48] Embroidering on this information, Townes et al. [46,48,49] built the first operational Maser in 1953 at Columbia University. This prototype can be classified as an atomic beam Maser and is based on Ammonia. Soon after, additional maser materials were discovered. Their broad application, ranging from atomic clocks to spacecraft communication technology, led to a vibrant research interest. In 1960, T. Maiman discovered the phenomena of Light Amplification by Stimulated Emission of Radiation (Laser) in $Al_2O_3:Cr^{3+}$ (ruby). [46] It involves the same principles as a Maser only that it uses higher frequency coherent radiation. With the amount of Maser and Laser applications rapidly growing, an all-out research was conducted at the time to find new materials able to mimic such phenomena. One investigated class of such materials involved solid state compositions based on rare-earth ions, such as Tm^{2+}.

Intermezzo V: Lanthanide Spectroscopy

In 1906, J. Becquerel studied the optical properties of Xenotime minerals, an YPO_4 compound containing traces of rare-earths Erbium and Cerium combined with the actinide Thorium. [50-52] The results showed three unusually sharp absorption lines. Subsequent low temperature measurements at the laboratory of Kamerlingh Onnes revealed that the narrowness of the lines resembled that of free atoms or molecules. [53,54] Furthermore, in an applied magnetic field the crystal absorption lines were demonstrated to undergo a considerable Zeeman splitting. [55] The origin of the absorption lines remained a mystery that long puzzled the scientific community. It was only in 1930 that H. Bethe, H. Kramers and J. Becquerel suggested a possible link to transitions within the $4f^n$ configuration, presently known as $4f^n \rightarrow 4f^n$ transitions. [56] As the electrons in the 4f-shell are located in the [Xe] core and shielded from their surrounding by the more outward 5s- and 5p-shells, the 4f-electrons are not (further) involved in the chemical bonding between lanthanide and host. Therefore, the influence of the host on the optical transitions within the 4f-shell is relatively weak. The $4f^n \rightarrow 4f^n$ transitions then result in sharp line absorptions. However, the parity selection rule of Laporte did not allow for such transitions to occur. [57] In 1937, J. van Vleck revealed that such transitions become partly allowed as electric dipole transitions in a combination of configurations of opposite parity. [58] In the 1930s and early 1940s spectroscopic studies on lanthanides commenced with solutions containing trivalent Europium. However, electronic energy levels schemes were incomplete and only qualitatively understood. In the 1950s and 1960s various research groups committed themselves to lab-based experiments and the assigning of lanthanide energy levels. Theoretical methods developed by G. Racah in the 1940s provided quantitative fits of the energy level positioning throughout the lanthanide series. [51] The first overview of trivalent lanthanide $4f^n$ energy levels in UV, VIS and IR was provided by G. Dieke. Since the energy of the 4f-levels do not change significantly for

different hosts, the experiments were all conducted in $LaCl_3$. The established diagram was posthumously called Dieke diagram. [59,60] To extend the Dieke diagram further into UV and VUV, spectroscopic data for LaF_3 was used from Bill Carnall, resulting in the final Dieke-Carnall diagram. [60] In 2000, R.T. Wegh et al. [61] extended the range of the Dieke-Carnall diagram from 40 000-70 000 cm^{-1}, into the Vacuum Ultra-Violet (VUV), using $LiYF_4$ single crystals doped with various lanthanides and VUV synchrotron radiation.

1.5.1 The Prehistoric Age (1960s)

As the development of Lasers and Masers was met with full interest across the globe and with lanthanide spectroscopy rapidly evolving, a group of researchers within Radio Corporation of America (RCA) started to look into solid-state masers based on lanthanides. [62-65] Due to the relatively small ionic radius of Al^{3+}, the initial Al_2O_3 (sapphire) host used in lasers proved to be unsuited for lanthanide dopants. A solution for this was found in the use of cubic fluoride hosts: CaF_2, SrF_2 and BaF_2. These crystals were known to be exhibit excellent optical quality and proved to be stable and non-hygroscopic. However, as Laser action proved to be more difficult to realise in BaF_2 and SrF_2 hosts, the researchers at RCA decided instead to fully focus on CaF_2. Via Bridgman-Stockbarger techniques [66], small amounts of lanthanide oxides could be incorporated into the CaF_2 lattice. However, problems arose in form of the charge compensation required for substituting a trivalent lanthanide on a divalent Calcium position in the lattice. Charge compensation mechanisms of fluoride interstitials and oxygen substitution on the site of a neighbouring fluoride resulted in a destruction of the cubic symmetry. The CaF_2 host was therefore deemed only suited for divalent lanthanide doping. The method of Hayes et al [67] to reduce trivalent Thulium to divalent Thulium in CaF_2 crystals via ionising radiation and electron trapping proved fruitful. Within RCA, researchers were able to repeat this trick on a broader range of lanthanides. [68] In 1962, an RCA researcher by the name of Kiss managed to chart the $4f^{13}$ energy levels of Tm^{2+} in CaF_2. This study [62] contained the first official sighting of the Tm^{2+} $4f^{13}\rightarrow4f^{13}$ emission at 4.2 K and room temperature. Excitation spectra as acquired on this emission revealed the clear presence the $4f^{12}5d^1$-levels. Barely a year later a design was published for a CaF_2:Tm^{2+} continuous operating Maser. [64] However, it proved to be difficult to grow a pure one-valence CaF_2:Tm^{2+} crystal and hence the reported spectra also display traces of CaF_2:Tm^{3+}. Subsequently, more designs of divalent lanthanide doped CaF_2 Masers followed. Later on, in 1968, a researcher named Loh from McDonnel/Douglas Corporation, measured the room temperature absorption spectra of Tm^{2+} in the hosts CaF_2, SrF_2 and BaF_2. [69] In the early 1970s, however, RCA Laboratories suffered from financial losses and had to cut in research projects. In 1986 the company was reacquired by General

Electric and research funds were again drastically cut. Due to the valency problem, the CaF_2:Tm^{2+} Maser application never took off. There was also no general consensus on how to continue the research on Tm^{2+} and the focus was shifted to other easier to understand divalent lanthanides such as: Eu^{2+}, Yb^{2+}, Sm^{2+}, Nd^{2+} and Dy^{2+}. [70]

1.5.2 The Middle Ages (1970-1980s)

During the 1970-1980s only a few articles on Tm^{2+} were published. [71-80] These covered exotic topics such as: electron paramagnetic resonance measurements on the interaction between Tm^{2+} ions in CaF_2, SrF_2 and BaF_2 [76]; distortions of Tm^{2+} trigonal centres in CaF_2, SrF_2 and BaF_2 [73,74]; and reduced 4f-5d electrostatic interaction of Tm^{2+} in $SrCl_2$ [75]. At the time, important progress was made in the field of molten salt chemistry and the metallothermic reduction of halides. Already in 1939, W. Klemm had shown a way to transform trivalent lanthanides, bound to halogens, into lanthanide metals. [79,80] With an increased availability of lanthanides, in the 1960s, synproportionation reactions were developed that slowly became the standard method for valence reduction of lanthanides. Such reactions can be classified as a redox reaction and in case of Thulium can be written as: $Tm + 2\,TmX_3 \rightarrow 3\,TmI_2$ with (X = F, Cl, Br, I). Since the reduction takes place during crystal growth, the main advantage of this technique over the post-synthesis use of ionising radiation is the fact that no charge compensation is required. Other research topics at the time included: valency stability studies and the crystal phase formation in halides. [80,81] For CaF_2:Tm^{2+} a thermodynamic instability was discovered that caused Tm^{2+} to slowly degrade to Tm^{3+}. [80]

1.5.3 The Renaissance (1990-2000s)

From the 1990s to the early 2000s, a series of dared creative enterprises led to stunning discoveries. A thorough investigation into the suitability of strontium tetraborate hosts for divalent lanthanides resulted in the discovery of the first Tm^{2+} $4f^{12}5d^1 \rightarrow 4f^{13}$ emission by Schipper et al. [82]. It was found at room temperature and upon cooling down of the SrB_4O_7:Tm^{2+} sample both its decay time and intensity started to increase. At 4.2 K the decay time of the emission was determined to be 232±10 µs. The strontium tetra borates form a special class of hosts in which it was discovered that several divalent lanthanides were found to remain stable over time. Furthermore the charge reduction from trivalent to divalent lanthanides can effectively take place in open air. In 1995, a year later, Peterson et al. [83] showed that for SrB_4O_7:Tm^{2+} the optimum production of Tm^{2+} occurs when the starting materials are heated in air at 650 °C.

Up to now, the luminescence properties of Tm^{2+} had only been investigated in CaF_2, SrF_2, BaF_2 and SrB_4O_7 hosts. In comparison, divalent Europium had been studied in a much wider variety of halides and into much more detail. Possible reasons lie in the difficulties related

to the relatively higher charge reduction potential and the extreme oxygen and moisture sensitivity of Tm^{2+}-doped halides. However, in 2000, C. Wickleder [84] investigated the $4f^{n-1}5d^1 \rightarrow 4f^n$ luminescence in $SrZnCl_4:M^{2+}$ and $BaZnCl_4:M^{2+}$ (M = Eu, Sm, Tm) compounds. As the ionic radius of these dopants is much larger compared to Zn^{2+} and smaller than Sr^{2+} and Ba^{2+}, the dopants will only occupy the latter sites and exhibit an 8-fold coordination geometry. The compounds were synthesised in a special manner with most care for the oxygen and moisture sensitivity. $TmCl_3$ was synthesised via the so called ammonium chloride route. Subsequently, its charge was reduced via the synproportionation reaction with Tm metal in a 2:1 ratio at 750 °C and in sealed Tantalum containers. Next, synthesised hosts and $TmCl_2$ were mixed in a 1:0.05 ratio and fired using Bridgman techniques. This many step preparation resulted in a good quality sample without the presence of Tm^{3+}. At room temperature a deep red $4f^{12}5d^1 \rightarrow 4f^{13}$ luminescence was observed, whose position was found to undergo a blue shift with increasing temperature. In case of $BaZnCl_4:Tm^{2+}$, it was perceived at a slightly shorter wavelength compared to $SrZnCl_4:Tm^{2+}$ and appeared much wider due to the relatively larger difference in ionic radii between Ba^{2+} and Tm^{2+}. In the wake of this study, C. Wickleder and researchers from Bern University investigated the very first Tm^{2+} upconvertor: $SrCl_2:Tm^{2+}$. [85] This compound was synthesised in like manner. During upconversion, irradiation at long wavelengths triggers short wavelength emission. It is based on multiple metastable luminescent excited states and is commonly encountered in trivalent lanthanides. The case of $SrCl_2:Tm^{2+}$ proved to be the very first divalent lanthanide displaying this phenomena, where upon excitation into the $4f^{13}\ ^2F_{5/2}$ excited state, an emission was observed from both the $^2F_{5/2}$ state and the lowest energy $4f^{13}5d^1$ state. This discovery led to an extensive conquest at Bern University in search for more Tm^{2+}-doped halides that exhibited upconversion. [86-92] The studied compounds were all synthesised in aforementioned way and included: $RbCaI_3:Tm^{2+}$, $CsCaX_3:Tm^{2+}$ (X = Cl, Br, I), $CaY_2:Tm^{2+}$ (Y = F, Cl) and $MCl_2:Tm^{2+}$ (Sr, Ba). The research, most notably conducted by J. Grimm, provided a clear classification of the $4f^{12}5d^1$-levels and thorough analysis of the $4f^{13}$ Stark splitting in these compounds. Apart from the lowest energy $4f^{12}5d^1 \rightarrow 4f^{13}$ emission, that occasionally survives at room temperature, many more $4f^{12}5d^1 \rightarrow 4f^{13}$ emissions were discovered at lower temperatures. The emissions were all carefully labelled in according to their transition and even include very rare cases of luminescence from higher energy $4f^{12}5d^1$-levels. The temperature-dependent behaviour of these emission was intensively studied and possible quenching mechanisms were unravelled to allow for an efficient tuning of the upconversion process. Although this process was encountered in each of the studied compounds, no patent or application followed. The research on Tm^{2+} was again abandoned. Nevertheless, the works of Grimm et al. would come to serve as a valuable beacon for follow-up studies.

1.5.4 The Re-Defining Age (Present Day)

In 2015 a new application for Tm^{2+}-doped halides was discovered. At TU Delft, Ten Kate et al [34] proved the suitability of these materials for LSCs. This discovery led to the establishing of a patent by TU Delft and forms the starting point for this dissertation and current research. The Tm^{2+}-doped trihalide Perovskites studied by Grimm et al. caused for some follow-up studies by De Jong et al. [93,94] at Utrecht University (2016-2017), Koster et al. [95] at the University of Canterbury (2014) and Karbowiak et al. [96] from Wroclaw University (2018). The latter group [97] also reinvestigated $CaCl_2:Tm^{2+}$. Solarz et al. [98] from Wroclaw University (2017) reexplored $SrB_4O_7:Tm^{2+}$ for the use in luminescence thermometers. Therefore, the temperature-dependent luminescence lifetime behaviour of the $4f^{12}5d^1 \rightarrow 4f^{13}$ emission was used in a special temperature parameter that allows for efficient ambient temperature readings. The technique of charge reduction by ionising radiation and electron trapping, as first introduced by Hayes et al. [67], was reinvestigated by J. Zhang et al [99] at the University of New South Wales (2017) for synthesising $BaFCl:Tm^{2+}$ compounds. Such compounds are almost non-hygroscopic and stable in open-air. Similar compounds of $CaFCl:Tm^{2+}$ were also investigated by C. Wickleder in 2018. [100]

1.6 Research Objective and Dissertation Outline

Tm^{2+}-doped halides form a highly potential class of materials for use in LSCs. Furthermore, their colourless and semi-transparent appearance renders them ideal for application in sustainable window technologies. Although many Tm^{2+}-doped halides remain unexplored, several such compounds have been studied for upconversion applications. Yet, these studies leave many important LSC parameters unaddressed and not investigated. For instance, virtually nothing is known on the internal quantum efficiency of the Tm^{2+} $4f^{13} \rightarrow 4f^{13}$ emission. This parameter directly determines the overall LSC efficiency and its value is governed by the Tm^{2+} temperature-dependent excited states dynamics, which will be different for various halide host materials. Previously, Grimm et al. intensely researched the excited states dynamics in $CsCaX_3:Tm^{2+}$ (X = Cl, Br, I) and $MCl_2:Tm^{2+}$ (M = Ca, Sr, Ba) compounds. A qualitative analysis was provided on the non-radiative quenching processes related to the different $4f^{12}5d^1 \rightarrow 4f^{13}$ emissions. However, an attempt to quantify the quenching processes and predict the quantum efficiency was not partaken. Such an analysis would eventually allow it to tune the various quenching processes and maximise the quantum efficiency of the $4f^{13} \rightarrow 4f^{13}$ emission. This will in turn increase the overall efficiency of the LSC. This important notion lies at the heart of this dissertation and will form the main research goal.

A quantitative study of the Tm^{2+} temperature-dependent relaxation dynamics requires the use of equipment that allows for a broad wavelength detection of photoluminescence

signals. Additionally, this equipment should be corrected for the sensitivity of the wavelength-dependent light detection and the output of the different detectors should be scaled relative to each other. Highly sensitive luminescence lifetime measurements should be conducted parallel to the luminescence measurements to obtain complementary data. Above all, the hygroscopicity of the halides and oxidation sensitivity of Tm^{2+} demands the design and use of appropriate sampleholders for hygroscopic materials. Any unexplored material that is studied along the way will also immediately provide information on, for instance, its sunlight absorption range and hence also its suitability for LSCs.

An initial choice for such a study involves the NaX (X = Cl, Br, I) series and includes regular 'kitchen salt'. These materials have previously only been examined in modest extend. Their synthesis is fairly simple and the materials are known to survive for up to an hour in open air. The results of this study are presented in chapter 2. Unfortunately, the required charge compensation of Tm^{2+} on a Na^{+}-site does not allow for a straightforward interpretation of gathered results. Such effects are avoided when considering dihalides. Chapter 3 therefore presents a similar analysis performed on CaX_2:Tm^{2+} (X = Cl, Br, I). Alongside the experiments, a numerical rate equation model was established based on the observed trends. This model was tested on two independent sets of data and despite some small discrepancies was able to provide a fit. It provided the necessary information on which quenching processes play a role in the Tm^{2+} excited states dynamics. A follow-up study was conducted on $CsCaX_3$:Tm^{2+} (X = Cl, Br, I), where the concept of solid solutions enabled it to study shifts in the quenching temperatures and onset of the various quenching processes. This allows for a selective tuning of the internal quantum efficiency of the Tm^{2+} $4f^{13}\rightarrow4f^{13}$ emission. The results are shown in chapter 4. The final quantum efficiency of the $4f^{13}\rightarrow4f^{13}$ emission is influenced by the choice of nominal Tm^{2+} doping percentage. Therefore, a first ever study on the phenomena of Tm^{2+} concentration quenching is performed. The results for SrI_2:Tm^{2+} are disclosed in chapter 5.

1.7 References

[1] International Energy Agency, World energy balances overview: complete energy balances for over 180 countries and regions, statistics report (2020).

[2] British Petrol, Statistical review of world energy, 69th edition (2020).

[3] D.J.C. Mackay, Sustainable energy -without the hot air, UIT Cambridge, ISBN: 978-0-9544529-3-3 (2008)

[4] P. Nejat, F. Jomehzadeh, M.M. Taheri, M. Gohari, M.Z.A. Majid, A global review of energy consumption, CO_2 emissions and policy in the residential sector (with an

overview of the top ten CO_2 emitting countries), Renew. Sust. Energ. Rev. 843-862 (2015) 42.

[5] M.C. Felgueiras, R. Santos, L.M. Fonseca, N.S. Caetano, Buildings sustainability: the HVAC contribution, J. Clean Energy Technol. 4 (2016) 5.

[6] X. Cao, X. Dai, J. Liu, Building energy-consumption status worldwide and the state-of-the-art technologies for zero-energy buildings during the past decade, Energy Build. 198-213 (2016) 128.

[7] Publications Office of the European Union, Directive 2002/91/EC of the European Parliament and Council (2002).

[8] Publications Office of the European Union, Directive 2010/31/EU of the European Parliament and Council (2010).

[9] Publications Office of the European Union, Directive 2012/27/EU of the European Parliament and Council (2012).

[10] International Energy Agency, International definitions of BIPV, Photovoltaic power systems programme report IEA-PVPS T15-04 (2018).

[11] L. Clasing, C.P. Dick, U. Blieske, J. Münzberg, M. Nennewitz, K. Birkholz, P. Hakenberg, S. Leyer, J.R. Hadji-Minaglou, Analysis of a novel improved BIPV/T roof tile design, 15th Conference on sustainable development of energy, water and environment systems (SDEWES), Cologne (2020).

[12] Exasun bv., Den Hague (The Netherlands), X-Roof system' and 'X-Tile module. Specifications available at: https://exasun.com/bestellen/zonnepanelen/, retrieved on: 7th of June 2021.

[13] Exasun bv., Den Hague (The Netherlands), X-Colour technology. Specifications available at: https://exasun.com/bestellen/zonnepanelen/x-colour/, retrieved on: 7th of June 2021.

[14] Soluxa bv., Nijmegen (The Netherlands), Gekleurde zonnepanelen gevel toepassingen. Specifications available at: https://www.soluxa.solar/nl/, retrieved on: 7th of June 2021.

[15] Signify, Eindhoven (The Netherlands), Harvest the sunlight; reap the opportunities. Specifications available at: https://www.signify.com/global/our-company/intellectual-property/licensing/luminescent-solar-concentrator, retrieved on: 8th of June 2021.

[16] A.V. Dotsenko, L.B. Glebov, V.A. Tsechomsky, Physics and chemistry of photochromic glasses, CRD Press, ISBN-9780849337802 (1997).

[18] T.T. Mongstad, Thin film metal hydrides for solar energy applications, PhD Thesis, University of Oslo - Faculty of Mathematics and Natural Sciences - Department of Physics, ISSN-1501-7710, (2012).

[19] P. Bamfield, M. Hutchings, Chromic phenomena: technological applications of colour chemistry, RSC Publishing, ISBN-978-1-84755-868-8 (2010).

[20] C.M. Lampert, Chromogenic smart materials, Mater. Today Commun. 28-35 3 (2004) 7.

[21] C.G. Granqvist, Handbook of inorganic electrochromic materials, Elsevier Science, ISBN-9780080532905 (1996).

[22] Smart Glass VIP, Privacy PDLC film manufacturer, Shenzhen (China), Photochromic light-control smart film. Image available at: https://smartglassvip.com/photochromic-smart-light-control-film/, retrieved on: 8th of June 2021.

[23] M. Casini, Smart windows for energy efficiency of buildings, Conference on Advances in Civil, Structural and Environmental Engineering (ACSEE) Zurich (2014).

[24] Sinovoltaics Group, Sai Kung (Hong Kong), CdTe cells efficiency. Information available at: https://sinovoltaics.com/learning-center/solar-cells/cdte-cells-efficiency/ retrieved on: 9th of June 2021.

[25] A. Smets, K. Jäger, O. Isabella, R. van Swaaij, M. Zeman, Solar energy: the physics and engineering of photovoltaic conversion, technologies and systems, ISBN-10-1906860327 (2016).

[26] Sanko Solar, Schoonebeek (The Netherlands), Datasheets and technical info NL/BRD/GB/FR. Available at: https://www.sanko-solar.nl/nl/downloads, retrieved on: 9th of June 2021.

[27] Sanko Solar, Schoonebeek (The Netherlands), Transparente Solarzellen geliefert nach Graz in Österreich. Image available at: https://www.sanko-solar.de/fotogalerie, retrieved on: 9th of June 2021.

[28] M.G. Debye, P.P.C. Verbunt, Thirty years of luminescent solar concentrator research: solar energy for the built environment, Adv. Energy Mater. 12-35 (2012) 2.

[29] W.G.J.H.M. van Sark, K.W.J. Barnham, LH. Slooff, A.J. Chatten, A. Büchtemann, A. Meyer, S.J. McCormack, R. Koole, D.J. Farrell, R. Bose, E.E. Bende, A.R. Burgers, T. Budel, J. Quilitz, M. Kennedy, T. Meyer, C. De Mello Donegá, A. Meijerink, D. Van maekelbergh, Luminescent solar concentrators: a review of recent results, Opt. Express 16 26 21773 (2008).

[30] F. Meinardi, F. Bruni, S. Brovelli, Luminescent solar concentrators for building-integrated photovoltaics, Nature Reviews Materials (2017) 2 17072.

[31] Eni, Rome (Italy), LSC: transparent sheets for capturing solar energy Luminescent solar concentrators transform diffused light into electricity, information and image

Available at: https://www.eni.com/en-IT/operations/concentrators-solar-luminescent.html, retrieved on: 10th of June 2021.

[32] N. Conenna, Luminescent Solar Concentrator LSC, Energy CuE (2017), Available at: https://energycue.it/luminescent-solar-concentrator-lsc/9655/, retrieved on: 10th of June 2021.

[33] Heijmans N.V. and Solar Energy Application Community, Eindrapportage Solar Noise Barriers (SONOB), (2017).

[34] O.M. ten Kate, K.W. Krämer, E. Van der Kolk, Efficient luminescent solar concentrators based on self-absorption free Tm^{2+} doped halides, Sol. Energy Mater. Sol. Cells 115-120 (2015) 140.

[35] V. Gutmann, Halogen Chemistry, Academic Press, ISBN-9780323148474 (1967).

[36] M. Binneweis, E. Milke, Thermochemical Data of Elements and Compounds, WILEY-VCH Verlag GmbH, ISBN-9783527305247 (2002).

[37] J.H.L. Voncken, The Rare Earth Elements, Springer Verlag, ISBN-978-3-319-26807-1 (2016).

[38] B.G. Streetman, S. Banerjee, Solid State Electronic Devices, Prentice Hall, ISBN-9780130261014 (2000).

[39] T. Tinoco, C. Rincón, M. Quintero, G. Sánchez Pérez, Phase Diagram and Optical Energy Gaps for CuInyGa1−ySe2 Alloys, Phys. Status Solidi (a) 427-434 2 (1991) 14.

[40] R. Kamada, W.N. Shafarman, R.W. Birkmire, Cu(In,Ga)Se2 film formation from selenization of mixed metal/metal–selenide precursors, Sol. Energy Mater. Sol. Cells 451-456 (2010) 94.

[41] Zonnepanelen-Info, CIGS zonnepanelen, (2008-2021). Available via: https://www.zonnepanelen-info.nl/cigs-zonnepanelen/, retrieved on: 14th of June 2021.

[42] M. Zhuravleva, L. Stand, H. Wei, C. Hobbs, L. A. Boatner, J.O. Ramey, K. Shah, A. Burger, E. Rowe, P. Bhattacharya, E. Tupitsyn, C.L. Melcher, Hygroscopicity Evaluation of Halide Scintillators, Conference: Nuclear Science Symposium and Medical Imaging Conference (NSS/MIC), Seoul, South Korea, IEEE (2013).

[43] R. Färm, PVB and EVA foils in glass lamination – what's the difference and which should you choose?, (2020). Available at: https://www.glastory.net/pvb-and-eva-foils-in-glass-lamination-whats-the-difference/ retrieved on: 14th of June 2021.

[44] Exasun bv., Den Hague (The Netherlands). Available at: https://exasun.com/, retrieved on: 14th of June 2021.

[45] A. Einstein, Zur Quantentheorie der Strahlung, Physikalische Zeitschrift Band 18, p.121-128 (1917).

[46] J. Hecht, Laser Guidebook, McGraw-Hill Inc, ISBN-9780071359672 (1999).

[47] American Institute of Physics, Oral history interviews: Interviews that offer unique insights into the lives, works, and personalities of modern scientists, Joseph Weber, April 8th (1983). Available at: https://www.aip.org/history-programs/niels-bohr-library/oral-histories/4941 retrieved on: 16th of June 2021.

[48] The Nobel Prize in Physics (1964): Charles H. Townes, Nicolay G. Basov and Aleksandr M. Prokhorov.

[49] C. H. Townes, Production of coherent radiation by atoms and molecules, Nobel lecture, December 11th (1964).

[50] J. McCarthy, Rare earths in modern science and technology, ISBN-10-0306409194 (1982).

[51] M.H.V. Werts, Making sense of lanthanide Luminescence, Sci. Prog. 101-131 2 (2005) 88.

[52] J. Becquerel, Sur les variations des bandes d'absorption d'un crystal dans un champ magnetique, Comptes rendus hebdomadaires des séances de l'Académie des sciences 775-779 (1906) 142.

[53] J. Bequerel, Influence des variations de température sur l'absorption dans les corps solides, Le Radium 328-339 (1907) 4.

[54] J. Becquerel, H. Kamerlingh Onnes, The absorption spectra of the compounds of the rare earths at the temperatures obtainable with liquid hydrogen, and their change by the magnetic field, Le Radium (1908) 5.

[55] J. Becquerel, Einleitung in eine Theorie der magneto-optischen Erscheinungen in Kristallen, Z. Phys 205-216 (1929) 58.

[56] H. Bethe, Zur Theorie des Zeemaneffektes an den Salzen der seltenen Erden, Z. Phys (1930) 60.

[57] O. Laporte, W.F. Meggers, Some rules of spectral structure, J. Opt. Soc. Am. 5 (1925) 11.

[58] J.H. van Vleck, The puzzle of rare-earth spectra in solids, J. Chem. Phys 67-80 (1937) 41.

[59] G.H. Dieke, H.M. Crosswhite, The spectra of the doubly and triply ionized rare earths, Appl. Opt. 675-686 7 (1963) 2.

[60] P.S. Peijzel, A. Meijerink, R.T. Wegh, M.F. Reid, G.W. Burdick, A complete $4f^n$ energy level diagram for all trivalent lanthanide ions, J. Solid State Chem. 448-453 (2005) 178.

[61] R.T. Wegh, A. Meijerink, R.J. Lamminmäki, J. Hölsä, Extending Dieke's diagram, J. Lumin. 1002-1004 (2000) 87-89.

[62] Z.J. Kiss, Energy levels of divalent thulium in CaF_2, Phys. Rev. 3 (1962) 127.

[63] D.S. McClure, Z. Kiss, Survey of the spectra of the divalent rare-earth ions in cubic crystals, J. Chem. Phys (1963) 39.

[64] R.C. Duncan Jr. Z.J. Kiss, Continuously operating CaF_2:Tm^{2+} optical Maser, Appl. Phys (1963) 3.

[65] Z.J. Kiss, R.J. Pressley, Crystalline solid lasers, Appl. Opt. 10 (1966) 5.

[66] D.C. Stockbarger, The production of large single crystals of lithium fluoride, Rev. Sci. Instrum. 133-136 (1936) 7.

[67] W Hayes, G.D. Jones, J.W. Twidell, Paramagnetic resonance and optical absorption of irradiated CaF_2:Ho, Proceedings of the Physical Society 81 371 (1963).

[68] RCA Laboratories quarterly status reports No. 4, Wright-Patterson Ohio (USA) April (1962).

[69] E. Loh, '$4f^n \rightarrow 4f^{n-1}5d^1$ Spectra of rare-earth ions in crystals', Phys. Rev. 2(1968) 175.

[70] Engineering and Technology History (ETHW), Radio Corporation of America (RCA), RCA Engineers Oral History Collection (2015). Available at: https://ethw.org/RCA_(Radio_Corporation_of_America) retrieved on: 18th of June 2021.

[71] H.A. Weakliem, C.H. Anderson, E.S. Sabisky, Magnetic circular dichroism spectra of divalent lanthanide ions in calcium fluoride, Phys. Rev. 8 11 (1970) 2.

[72] J. Sugar, Spectrum of doubly ionized thulium (Tm III)*, J. Opt. Soc. Am. 4 (1970) 60.

[73] F. Anisimov, R. Dagys, Electronic structure and spectrum of the (TmF8)6− cluster, Chemistry Physica Status Solidi B (1972).

[74] D. Marsh, Distortions of Tm^{2+} trigonal centres in alkaline earth fluorides, J. Phys. C: Solid State Physics 8 (1972) 5.

[75] R.C. Alig, R.C. Duncan Jr., B.J. Mokross, Reduced 4f-5d electrostatic interaction of Tm^{2+} in $SrCl_2$, J. Chem. Phys 11 (1973) 59.

[76] J. Baker, D. Marsh, EPR measurements of interactions between pairs of Tm^{2+} ions in alkaline-earth fluorides, J. Phys. C: Solid State Physics 14 (1979) 12.

[77] C. Pedrini, D.S. McClure, C.H. Anderson, Photoionization thresholds of divalent rare earth ions in alkaline earth fluorides, J. Chem. Phys. 11 (1979) 70.

[78] A. Penzkofer, Solid state lasers, Prog. Quantum. Electron. 291-427 (1988) 12.

[79] S.P. Sinha, Systematics and the properties of the lanthanides, p. 3-16 author W. Klemm, NATO ASI Series C, Reidel Publishing, ISBN-978-94-009-7175-2 (1982).

[80] G. Meyer, Reduced halides of the rare-earth elements, Chem. Rev. Vol. 88, p. 93-107 (1988).

[81] J.O. Rubio, Doubly-valent rare-earth ions in halide crystals, J. Phys. Chem. Vol. 52, No. 1, p. 101-174 (1991).

[82] W.J. Schipper, A. Meijerink, G. Blasse, The luminescence of Tm^{2+} in strontium tetraborate, J. Lumin. 55-59 (1994) 62.

[83] J.R. Peterson, W. Xu, S. Dai, Optical properties of divalent thulium in crystalline strontium tetraborate, Chem. Mater. 1686-1689 (1995) 7.

[84] C. Wickleder, Spectroscopic properties of $SrZnCl_4:M^{2+}$ and $BaZnCl_4:M^{2+}$ (M = Eu, Sm, Tm), J. Alloys Compd, 193-198 (2000) 300–301.

[85] O.S. Wenger, C. Wickleder, K.W. Krämer, H.U. Güdel, Upconversion in a divalent rare earth ion: optical absorption and luminescence spectroscopy of Tm^{2+} doped $SrCl_2$, J. Lumin. 101-105 (2001) 94–95.

[86] J. Grimm, E. Beurer, H.U. Güdel, Crystal absorption spectra in the region of 4f-4f and 4f-5d excitations in Tm^{2+}-doped $CsCaCl_3$, $CsCaBr_3$, and $CsCaI_3$, Inorg. 10905-10908 (2006) 45.

[87] J. Grimm, H.U. Güdel, Five different types of spontaneous emission simultaneously observed in Tm^{2+} doped $CsCaBr_3$, Chem. p. 40-43 (2005) 404.

[88] E. Beurer, J. Grimm, P. Gerner, H.U. Güdel, New type of near-infrared to visible photon upconversion in Tm^{2+}-doped $CsCaI_3$, J. Am. Chem. Soc. 3110-3111 (2006) 128.

[89] E. Beurer, J. Grimm, P. Gerner, H.U. Güdel, Absorption, light emission, and upconversion properties of Tm^{2+}-doped $CsCaI_3$ and $RbCaI_3$, Inorg. 9901-9906 (2006) 45.

[90] J. Grimm, J.F. Suyver, E. Beurer, G. Carver, H.U. Güdel, Light-emission and excited-state dynamics in Tm^{2+} doped $CsCaCl_3$, $CsCaBr_3$, and $CsCaI_3$, J. Phys. Chem. B 2093-2101 (2006) 110.

[91] J. Grimm, O.S. Wenger, K.W. Krämer, H.U. Güdel, 4f–4f and 4f–5d excited states and luminescence properties of Tm^{2+}-doped CaF_2, $CaCl_2$, $SrCl_2$ and $BaCl_2$, J. Lumin. 590-596 (2007) 126.

[92] J. Grimm, E. Beurer, P. Gerner, H.U. Güdel, Upconversion between 4f–5d excited states in Tm^{2+}-doped $CsCaCl_3$, $CsCaBr_3$, and $CsCaI_3$, Eur. J. Chem. 1152-1157 (2007) 13.

[93] M. de Jong, D. Biner, K.W. Krämer, Z. Barandiarán, L. Seijo, A. Meijerink, *New* insights in $4f^{12}5d^1$ excited states of Tm^{2+} through excited state excitation spectroscopy, J. Phys. Chem. Lett. 2730-2734 (2016) 7.

[94] M. de Jong, A. Meijerink, L. Seijo, Z. Barandiaran, Energy level structure and multiple $4f^{12}5d^1$ emission bands for Tm^{2+} in halide perovskites: theory and experiment, J. Phys. Chem. C 10095-10101 18 (2017) 121.

[95] S. Koster, M. Reid, J.P. Wells, R. Reeves, Energy levels and dynamics of Tm^{2+} doped into AMX_3 salts, Msc Thesis S. Koster, University of Canterbury (2014).

[96] M. Karbowiak, R. Lisiecki, P. Solarz, J. Komar, W. Ryba-Romanowski, Spectroscopic peculiarities of $CsCaI_3:Tm^{2+}$ single crystals examined through one-photon and excited state excitation spectroscopy, J. Alloys Compd 1165-1171 (2018) 740.

[97] M. Karbowiak, C. Rudowicz, Trends in Hamiltonian parameters determined by systematic analysis of f-d absorption spectra of divalent lanthanides in alkali-halides hosts: II. $CaCl_2:Ln^{2+}$ (Ln = Sm, Eu, Tm, and Yb), J. Lumin. 66-75 (2018) 197.

[98] P. Solarz, J. Komar, M. Głowacki, M. Berkowski, W. Ryba-Romanowski, Spectroscopic characterization of $SrB_4O_7:Tm^{2+}$, a potential laser material and optical temperature sensor, RSC Adv. 21085-21092 (2017) 7.

[99] J. Zhang, H. Riesen, Controlled generation of Tm^{2+} ions in nanocrystalline $BaFCl:Tm^{3+}$ by X-ray irradiation, J. Phys. Chem. A 803-809 (2017) 121.

[100] M. Adlung, C. Wickleder, Photoluminescence of Tm^{2+} ions in several chloride host lattices, 7th International Conference on f Elements, Cologne (Germany) August 23-27th (2009).

2.

Temperature-Dependent Relaxation Dynamics of Luminescent NaX:Tm^{2+} (X = Cl, Br, I)

This chapter is based on the publication: M.P. Plokker, E. van der Kolk, Temperature dependent relaxation dynamics of luminescent NaX:Tm^{2+} (X = Cl, Br, I), Journal of Luminescence 216 (2019).

Thanks to: P. Dorenbos, J.T.M. de Haas, B.E. Terpstra, R.D. Abellon, M. Kerklaan, O.M. ten Kate and M. Hendriks.

Abstract

In recent years, Thulium in its 2+ oxidation state has been identified as candidate dopant in halide hosts for luminescent solar concentrators. Yet, some of its luminescent properties with regard to these applications remain unexplored. In this study we report on the temperature-dependent photoluminescent behaviour of NaCl:Tm^{2+}, NaBr:Tm^{2+}, and NaI:Tm^{2+}. These monohalide materials demonstrate up to five distinct emission peaks which can be attributed to the $4f^{13}\rightarrow4f^{13}$ and $4f^{12}5d^{1}\rightarrow4f^{13}$ transitions of Tm^{2+}. Their time- and temperature-dependent luminescence intensity behaviours are explained by a qualitative model describing the thermally stimulated radiative- and non-radiative relaxation dynamics. The behaviour of Tm^{2+} in these monohalides proves to be largely similar to earlier reported findings on Tm^{2+}-doped trihalide Perovskites of the form $CsCaX_3$ (X = Cl, Br, I). A major exception is found in the strength of the $4f^{13}\rightarrow4f^{13}$ emission, which remains by far the most dominant emission between 10-300 K.

2.1. Introduction

The luminescent properties of Tm^{2+}-doped trihalide Perovskites have been charted quite intensively over the past years. Most notably by Grimm et al. [1-6], and more recently by the theoretical work of De Jong et al. [7,8] and experimental study by Karbowiak et al. [9]. This all mainly involved the $CsCaX_3$:Tm^{2+} (X = Cl, Br, I) series where the upconversion characteristics, quenching mechanisms and temperature-dependent relaxation dynamics were investigated. Beside the earlier reported $4f^{13}\rightarrow4f^{13}$ emission of Tm^{2+} [10], surprisingly enough, also emissions from higher lying $4f^{12}5d^{1}$-states were observed at low temperatures. Furthermore, it was brought to light that the anion variation along the series leads to a remarkable change in the radiative and non-radiative relaxation properties and their related temperature regimes of pre-eminence. For non-Perovskite Tm^{2+}-doped halides these attributes have been investigated to much less extent. Besides a few low temperature studies [10-13], only a single study exists on the temperature-dependent relaxation dynamics of some Tm^{2+}-doped dihalides. [14] It indisputably reveals that the temperature-dependent luminescence behaviour of Tm^{2+} varies drastically over the different halide hosts. For Tm^{2+}-doped monohalides no such study exists at all.

However, the room temperature luminescent properties of NaX:Tm^{2+} (X = Cl, Br, I) have recently been investigated by Ten Kate et al. with the aim of exploring their potential for Luminescent Solar Concentrators (LSCs). [15] Overall, it was found that Tm^{2+}-doped halides are typically able to absorb up to 63% of the AM 1.5 solar spectrum. In addition to that, the large energy difference between the $4f^{13}\rightarrow4f^{13}$ emission and the $4f^{13}\rightarrow4f^{12}5d^{1}$

absorption bands of the materials entails that at room temperature there are virtually no self-absorption losses, neutralising a well-known problem for LSCs. Since the light emerging from the $4f^{13} \rightarrow 4f^{13}$ emission falls within the spectral absorption range of Copper Indium Selenium (CIS) thin film solar cells, it can be used for photovoltaic energy conversion. Besides, alkali metal halides, with NaX (X = Cl, Br, I) in particular, are prominent materials among the broader class of halides and on average their hygroscopicity is slightly less intense than that of common dihalides and trihalides. [16]

The prospect of Tm^{2+}-doped halides as LSC material and the absence of a detailed analysis into the temperature-dependent luminescence behaviour of the Tm^{2+}-doped alkali metal halides, has therefore incited us to investigate the relaxation dynamics of $NaX:Tm^{2+}$ (X = Cl, Br, I). First, the different luminescent emissions of the materials are classified in accordance to their energy level-transitions, as based on the luminescence excitation spectra. Subsequently, the luminescence relaxation dynamics is investigated over a broad temperature range, using both temperature-dependent luminescence and time-resolved spectroscopic measurements. The findings are used to constitute a qualitative model that is able to describe the relaxation dynamics of the materials in a correct fashion only when non-radiative processes via conduction band states are included.

2.2. Experimental Section

2.2.1 Powder Synthesis and Preparation

The $NaCl:Tm^{2+}$, $NaBr:Tm^{2+}$ and $NaI:Tm^{2+}$ powder samples were prepared by respectively mixing NaCl, NaBr and NaI (Alfa Aeser, 99.99%) with 1 mol % TmI_2 powder (Sigma Aldrich, 99.9%) under inert conditions. The mixtures were stored in quartz ampoules. The ampoules were then individually sealed off by a vacuum valve and connected to a KF-vacuum system that evacuated them towards a pressure of 10^{-2} mbar. Subsequently, a conventional Tecla burner was used to heat the ampoules until the powder liquefied. The burner was switched off typically after 3 minutes as the mixture started to boil momentarily. After that, the ampoules were cooled back to room temperature and the resulting samples were crushed to powder in a N_2-filled glovebox (MBraun, Garching, Germany). For all powder characterisation measurements, specially designed sampleholders, similar to those described by Rogers et al. [17], were employed to protect the samples against hygroscopicity and unwanted oxidation reactions.

2.2.2 Powder Characterisation

The crystal structures of the powder samples were monitored using a Philips X'pert-Pro diffractometer (Philips, Eindhoven, The Netherlands) in Bragg-Brentano geometry with CuK_α radiation (1.5419 nm). All three samples were found to exhibit the NaCl rock-salt

structure type ($Fm\bar{3}m$), as elucidated in figure 2.1. For NaCl:Tm^{2+} the presence of a very weak NaI phase was observed, which is most likely related to iodine originating from the TmI_2 starting powder. The corresponding NaCl:NaI peak intensity ratio was estimated to be 100:3 at most. In addition, the Tm concentrations of the samples were determined via ICP-OES measurements with a Perkin Elmer Optima 4300DV spectrometer (Perkin Elmer, Waltham Massachusetts, USA). These were found to be: 0.69, 0.75 and 1.0 mol % for NaCl:Tm^{2+}, NaBr:Tm^{2+} and NaI:Tm^{2+} respectively. Furthermore, diffuse reflectance measurements were done with a Bruker Vertex V80 spectrometer (Bruker, Karlsruhe, Germany), from which Kubelka-Munk absorption spectra were constructed. These spectra are displayed in figure 2.2 and reveal the presence of small quantities of Tm^{3+}. Yet, the selected wavelength of excitation of 420 nm does not overlap with any of the Tm^{3+} excitation bands, as explicated in the Dieke diagram. [18] In addition, no energy transfer

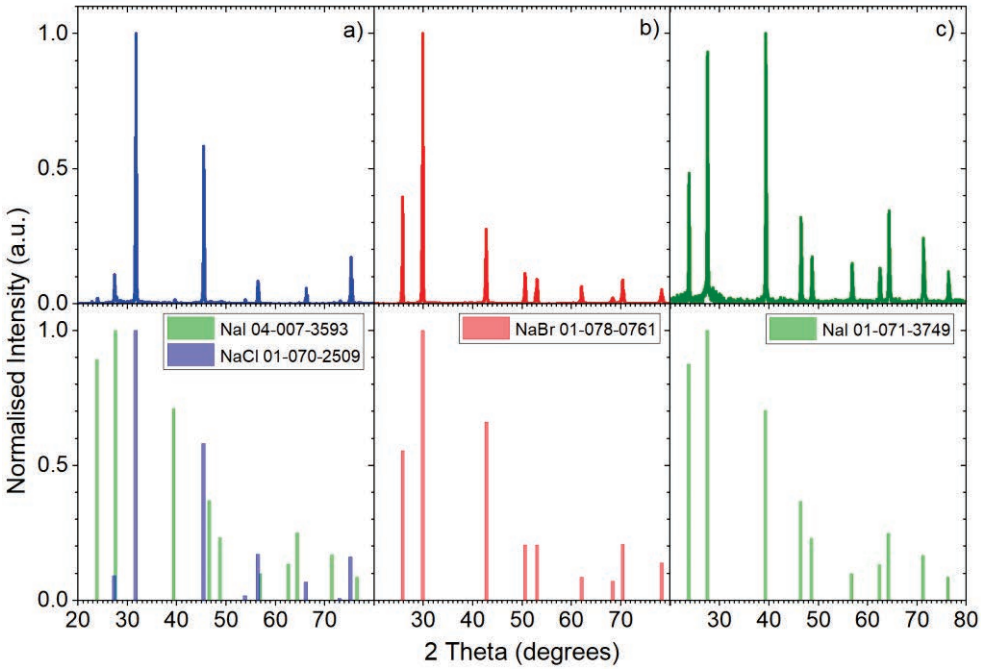

Figure 2.1: The X-ray diffraction spectra of: a) NaCl:Tm^{2+}, b) NaBr:Tm^{2+}, and c) NaI:Tm^{2+} as normalised on their main diffraction peak. The related reference patterns are plotted below the spectra and are classified in accordance to the Highscore expert Pro Database.

Pattern References

NaCl 01-070-2509	R.B. Srinivasa, S.P. Sanyal, Phys. Rev. B: Condens. Matter. Mater. Phys. 42, 1810 (1990)
NaI 04-007-3593	W.P. Davey, Phys. Rev. 21, 143(1923)
NaBr 01-078-0761	J.E. Nickels, M.A. Fineman, W.E. Wallace, J. Phys. Chem. 53, 625 (1949)
NaI 01-071-3749	G.J. Finch, S. Fordham, Proc. Phys. Soc., London, 48, 85 (1936)

between Tm^{2+} and Tm^{3+} was observed. Besides, diffuse reflectance measurements were also performed on purely Tm^{2+}- and Tm^{3+}-doped NaI samples. The integrated absorption bands of the Tm^{2+} $^2F_{7/2}\rightarrow{}^2F_{5/2}$ and the Tm^{3+} $^3H_6\rightarrow{}^3H_5$ transitions in combination with ICP-OES measurements allowed it to determine the relative Tm^{2+} and Tm^{3+} absorption strengths in NaI, which respectively amounted to 1 and 3.4. The fraction Tm^{2+} in the NaX (X = Cl, Br, I) sample series is then determined to be 0.87, 0.87 and 0.85, respectively, and renders their Tm^{2+} concentrations on 0.60, 0.65 and 0.85 mol %.

Fluorescence quantum yield measurements were done with an Edinburgh FLS980 integrating sphere (Edinburgh Instruments, Livingston, UK) with a 450W Xenon arc lamp and Hamamatsu C9940-02 near infrared (NIR) photomultiplier tube (PMT) (Hamamatsu Photonics, Hamamatsu, Japan). After exciting into the $(^3H_6,t_{2g})_{S=1/2}$ $4f^{12}5d^1$ band, positioned between 560-600 nm, internal quantum efficiencies of 16±1 %, 32±2 %, and 33±2 % were respectively retrieved for $NaCl:Tm^{2+}$, $NaBr:Tm^{2+}$ and $NaI:Tm^{2+}$.

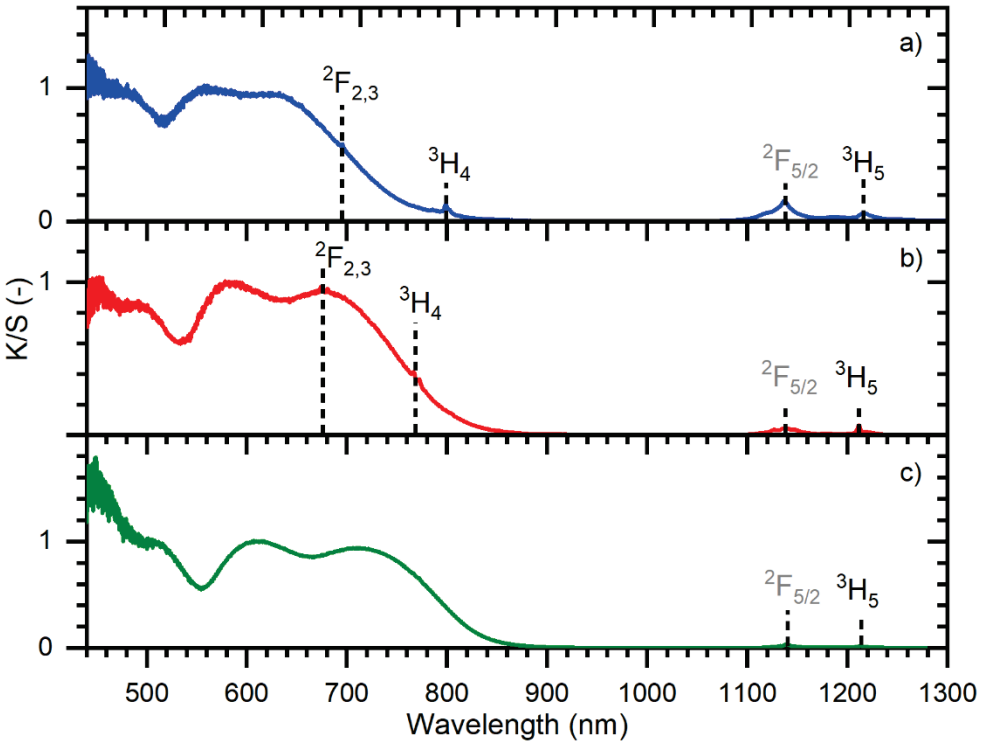

Figure 2.2: The room temperature Kubelka-Munk absorption spectra of: a) $NaCl:Tm^{2+}$, b) $NaBr:Tm^{2+}$, and c) $NaI:Tm^{2+}$. The spectra are normalised on the Tm^{2+} $(^3H_6,t_{2g})_{S=1/2}$ absorption band positioned between 560-600 nm. The absorption peaks of Tm^{2+} and Tm^{3+} are labelled and respectively indicated in grey and black.

2.2.3 Luminescence Spectroscopy

For excitation of the powder samples, either a Xenon lamp coupled to a double monochromator with three gratings or a tuneable EKSPLA laser (EKSPLA, Vilnius, Lithuania) was used. In addition, the samples were cooled or heated using a APD Cryogenic Helium cooler (APD Cryogenics, Allentown Pennsylvania, USA) with Lakeshore temperature controller (Lakeshore Cryotronics, Westerville Ohio, USA). Furthermore, the luminescence emerging from the samples was measured using a Hamamatsu C9100-13 EM-CCD or H1033A-75 NIR-PMT (Hamamatsu Photonics, Hamamatsu, Japan) that are respectively sensitive between 400-1150 nm and 950-1600 nm and that are attached to a single monochromator with three gratings. The wavelength-dependent detection efficiency of the detectors was established using a calibrated EPLAB NBS 1000W Quartz Iodine lamp. In addition, the overlap in detection of the 1140nm $4f^{13} \rightarrow 4f^{13}$ emission peak of Tm^{2+} allowed us to scale the relative output of both detectors. Time resolved measurements were performed by connecting a DT5724F (0-2 ms) or DT5730 (0-40 ms) CAEN digitiser (CAEN, Viareggio, Italy) to the same NIR-PMT or a Hamamatsu R7600U-20HV-800V PMT. The related decay curves were acquired by averaging 1000 individual laser excited spectra.

2.3. Results and Discussion

2.3.1 Classification of Excitation Bands and Emissions

The well-known NaCl ($Fm\bar{3}m$) crystal structure type of the three samples implies that the Tm^{2+} dopant ions that occupy the Na^{+}-lattice sites are octahedrally coordinated, leading to a 5d-crystal field splitting where the t_{2g} levels are situated below the e_g levels. However, it should be noted that the incorporation of the Tm^{2+} dopants must result in the formation of charge compensating defects, that will distort the perfect octahedron and by consequence the related crystal field splitting. Charge compensating mechanisms in monohalides have been described extensively by Rubio et al. [19] for dopant ions such as Eu^{2+}. Nevertheless, a description of the $4f^{12}5d^{1}$-states assuming an octahedral symmetry still remains a useful first order approximation that will be adopted here.

Figure 2.3 shows the excitation spectra of the three Tm^{2+}-doped powders at 20 K. The overall shape of the spectra is quite similar, especially at the longer wavelengths, and proves to be largely identical to the room temperature absorption spectra found previously by Ten Kate et al. [15] for NaX:3%Tm^{2+} (X = Cl, Br, I). The described method by Ten Kate et al. [15] allows it to estimate the AM 1.5 solar absorption fractions of the materials on 55-61%. [15,20,21] The Tm^{2+} 5d-levels are split several times and most prominently by: 1) the crystal field interaction, 2) the Coulomb repulsion and spin orbit coupling within the

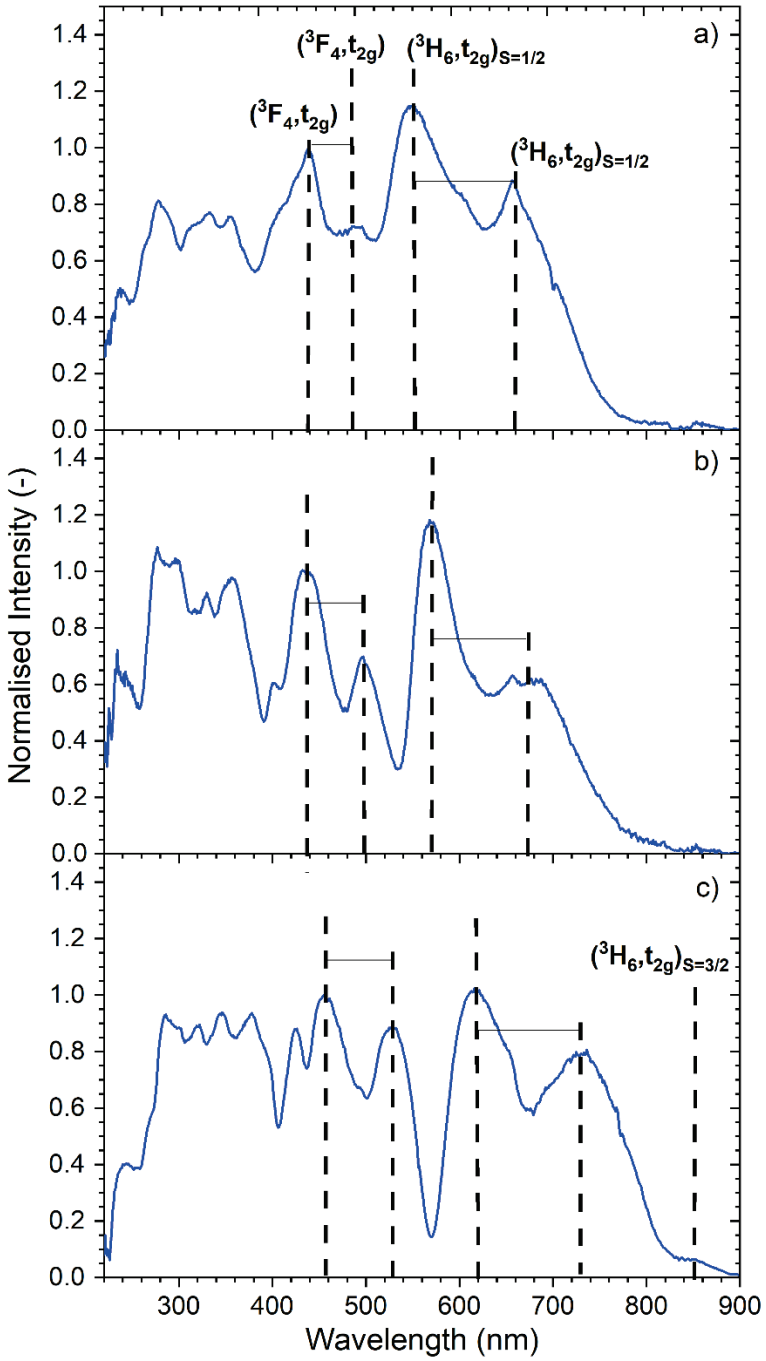

Figure 2.3: The excitation spectra of: a) NaCl:Tm^{2+}, b) NaBr:Tm^{2+} and c) NaI:Tm^{2+} as acquired monitoring the Tm^{2+} $4f^{13}\rightarrow4f^{13}$ emission at 20 K. For each of the materials, the excitation bands at long wavelengths are classified. The normalisation was done on the left ($^3F_4$,t_{2g}) band.

$4f^{12}$-configuration, 3) the Coulomb repulsion between the 4f- and 5d-electrons, and 4) the spin-orbit interaction of the 5d-electron. The first interaction causes for a splitting in a doublet e_g and a triplet t_{2g}, whereas the second interaction results in an additional splitting into $^{2S+1}L_J$ terms, which are analogous to the Tm^{3+} multiplets in the Dieke diagram. In addition to that, the third interaction results in a further splitting into spin S=1/2 and S=3/2 states and the fourth interaction splits the levels even further. A more detailed discussion about the structure of the $4f^{12}5d^1$ configuration of Tm^{2+} can be found in the works of Grimm et al. [2] and De Jong et al.. [7,8]

Based on our acquired spectra, two main sets of excitation bands can be distinguished; as indicated by the dashed lines in figure 2.3. For NaBr:Tm^{2+} the bands of the first set are located at around 433 nm and 497 nm; and those of the second set are positioned close to 568 nm and 656 nm. A brief calculation reveals that the difference between the highest energy band of each set amounts to 5490 cm^{-1}. Similarly, the mutual difference between the lowest energy bands amounts to 4880 cm^{-1}. This corresponds fairly well to the difference of 5700 cm^{-1} between the $^3F_4$ and $^3H_6$ levels of Tm^{3+} in the Dieke diagram. The set of excitation bands located at longer wavelength can thus most likely be related to the ($^3H_6$,t_{2g}) levels of Tm^{2+}, while the two excitation bands located at shorter wavelength correspond to the ($^3F_4$,t_{2g}) levels. A quick verification of all this is offered via work of Rubio et al. on NaCl:Eu^{2+} [19], where the lowest energy spin-allowed $4f^7 \rightarrow 4f^6 5d^1$ absorption band is observed at around 400 nm. Subtracting the material independent energy difference of 1.27 eV, as explicated by Dorenbos et al. [22], the lowest energy $4f^{12}5d^1$ band for NaCl:Tm^{2+} should be located at 676 nm. This falls almost exactly on the assigned position of the ($^3H_6$,t_{2g}) band. In addition, a weak excitation band is observed for NaI:Tm^{2+} at around 850 nm. It can be classified as the ($^3H_6$,t_{2g})$_{S=3/2}$ band and in contrast to the previous spin-allowed bands it is spin-forbidden. [2]

Upon varying the anion species from Cl→Br→I, it can be observed that the assigned excitation bands gradually shift towards longer wavelengths. This can be related to nephelauxetic effects and a change in crystal field strength as caused by slight changes in the distance between the Tm^{2+} ion and its immediate surrounding anions.

The emission spectra in figure 2.4 reveal up to five distinct Tm^{2+} emissions that are present at 20 K for all three materials. The emissions are labelled A to E in analogy to the work of Grimm et al. [6] Their wavelengths and luminescence decay time are provided in table 2.1. Furthermore, a schematic representation of the different $4f^{12}5d^1 \rightarrow 4f^{13}$ and $4f^{13} \rightarrow 4f^{13}$ emissions is added for convenience in figure 2.5.

The previously assigned excitation bands together with Stokes shift energy values, provide a means to classify the emissions in accordance to their transitions. The Stokes shift energy values for NaCl, NaBr, and NaI as based on the Eu^{2+} $4f^6 5d^1 \rightarrow 4f^7$ emission respectively

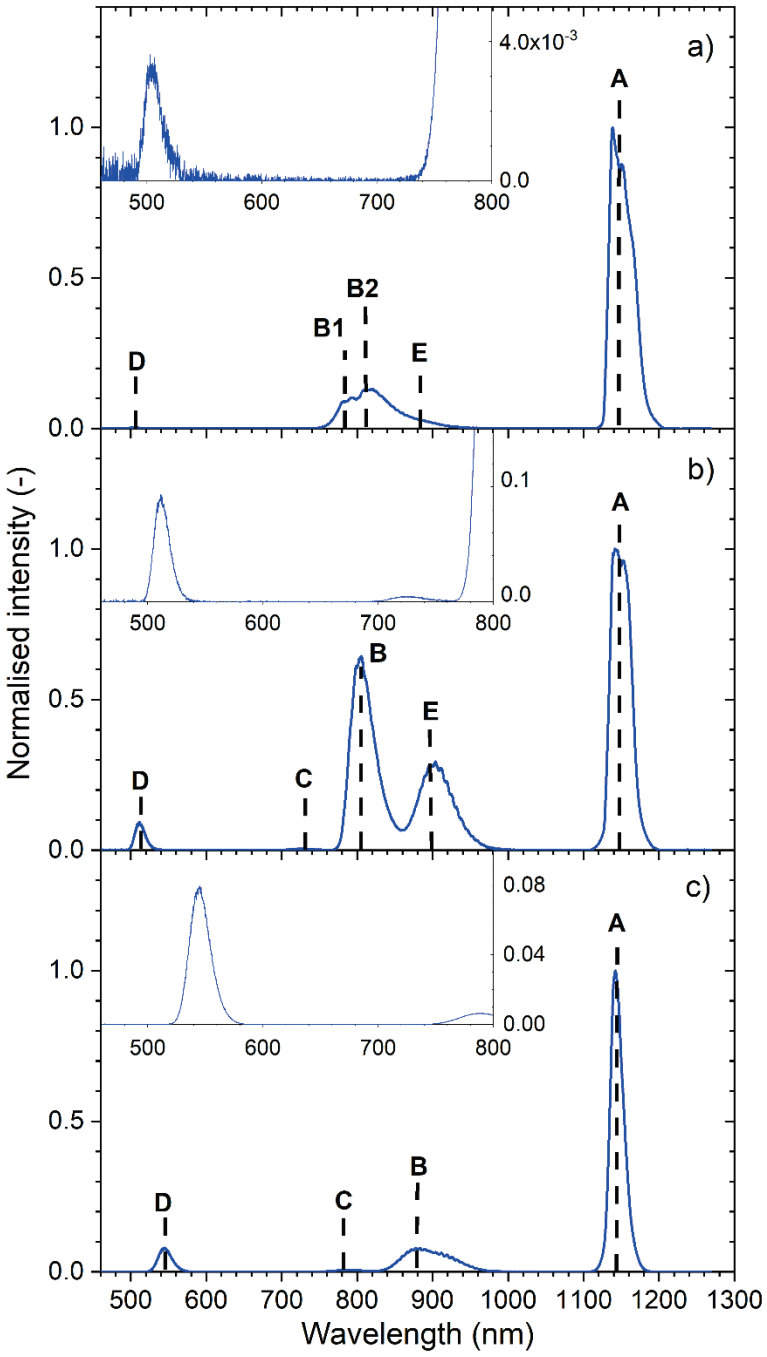

Figure 2.4: The emission spectra of: a) NaCl:Tm^{2+}, b) NaBr:Tm^{2+} and c) NaI:Tm^{2+} as photo-excited at 420 nm and recorded at 20 K. As described in section 2.2.3, the emissions are corrected for the sensitivity of detection to allow for a relative comparison in intensity. The emission peak intensities are normalised on that of emission A.

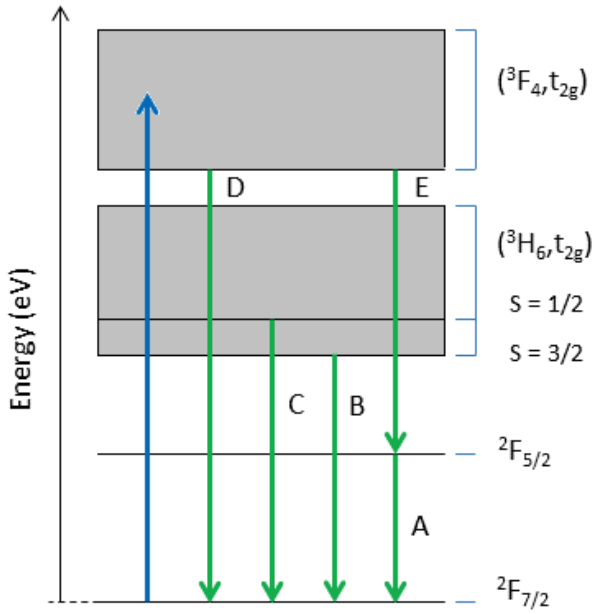

Figure 2.5: Schematic overview of the five observed Tm^{2+} emissions, taking into account the Stokes shifts. The photoexcitation wavelength of 420 nm falls within the $(^3F_4,t_{2g})$ $4f^{12}5d^1$ band.

Table 2.1: Classification and properties of the observed Tm^{2+} emissions in NaX:Tm^{2+} (X = Cl, Br, I).

Sample [-]	Emission [-]	Transition [-]	Wavelength [nm] (20K)	Energy [eV] (20K)	Decay Time (20K)	Rel.Intgr.Int. [-] (20K)
NaCl:Tm^{2+}	D	$(^3F_4,t_{2g})\rightarrow{}^2F_{7/2}$	503	2.47	120 ns	1
	B1	$(^3H_6,t_{2g})_{S=3/2}\rightarrow{}^2F_{7/2}$	779	1.60	380 µs	24
	B2	$(^3H_6,t_{2g})_{S=3/2}\rightarrow{}^2F_{7/2}$	811	1.53	400 µs	4
	E	$(^3F_4,t_{2g})\rightarrow{}^2F_{5/2}$	883	1.41	-	2
	A	$^2F_{5/2}\rightarrow{}^2F_{7/2}$	1139	1.09	2.7 ms	52
NaBr:Tm^{2+}	D	$(^3F_4,t_{2g})\rightarrow{}^2F_{7/2}$	511	2.43	1.0 µs	7
	C	$(^3H_6,t_{2g})_{S=1/2}\rightarrow{}^2F_{7/2}$	728	1.71	5.0 µs, 59 µs	1
	B	$(^3H_6,t_{2g})_{S=3/2}\rightarrow{}^2F_{7/2}$	804	1.55	430 µs	28
	E	$(^3F_4,t_{2g})\rightarrow{}^2F_{5/2}$	898	1.38	710 ns	9
	A	$^2F_{5/2}\rightarrow{}^2F_{7/2}$	1142	1.09	4.2 ms	33
NaI:Tm^{2+}	D	$(^3F_4,t_{2g})\rightarrow{}^2F_{7/2}$	545	2.28	810 ns	6
	C	$(^3H_6,t_{2g})_{S=1/2}\rightarrow{}^2F_{7/2}$	789	1.58	12 µs, 51 µs	1
	B	$(^3H_6,t_{2g})_{S=3/2}\rightarrow{}^2F_{7/2}$	877	1.42	440 µs	22
	A	$^2F_{5/2}\rightarrow{}^2F_{7/2}$	1142	1.09	3.7 ms	54

amount to 0.12 eV, 0.13 eV, and 0.19 eV. [19] Upon adding these values to the perceived Tm^{2+} $4f^{12}5d^1\rightarrow4f^{13}$ emissions, a good resemblance is obtained with the bands observed in the excitation spectra presented earlier in figure 2.3. Emission D in NaBr:Tm^{2+} is detected at 511 nm, as can be seen in figure 2.4b. If we add the Stokes shift energy for NaBr of 0.13 eV we should denote an excitation band at 486 nm. Figure 2.3b indeed shows an excitation band, which is very close to 500 nm. Therefore, we assign emission D to a transition from

the ($^3F_4$,t_{2g}) levels to the $^2F_{7/2}$ ground state. It has been observed several times before in Tm^{2+}-doped di- and trihalides. [2,4,6,9] Its parity-allowed nature, belonging to a $4f^{12}5d^1 \rightarrow 4f^{13}$ transition, is reflected into its relatively short decay time of 1015 ns at 20 K.

In a similar manner, the wavelength of emission C can be coupled to an excitation band located at 676 nm, which represents the spin-allowed ($^3H_6$,t_{2g})$_{S=1/2}$ band. Hence, emission C can be associated with ($^3H_6$,t_{2g})$_{S=1/2} \rightarrow {}^2F_{7/2}$ transition. Furthermore, emission B located at 804 nm should correspond to an excitation band at 740nm. For NaBr:Tm^{2+} this band is not noticed clearly, but it most likely represents the spin-forbidden ($^3H_6$,t_{2g})$_{S=3/2}$ band that is only observed for NaI:Tm^{2+} at around 850 nm. Therefore, emission B can be linked to the spin-forbidden ($^3H_6$,t_{2g})$_{S=3/2} \rightarrow {}^2F_{7/2}$ transition. The dissimilarity in decay time between emissions C and B, 5-59 µs versus 432 µs, respectively reflects their spin-allowed and spin-forbidden nature. In case of our NaCl:Tm^{2+} sample two distinct B emissions are observed. This is most likely associated with the presence of two different luminescence centres as a result of the charge compensating mechanisms. The luminescence seems too strong to be related to the weak NaI phase present in the sample. Moreover, emission C was not observed for this material. Its absence is echoed by previous studies performed on Tm^{2+}-doped halides that involve chloride as anion species. [4,5,14] The energy of emission E corresponds well to the energy gap between the ($^3F_4$,t_{2g}) and $^2F_{5/2}$ levels. Moreover, the energy difference of emission D and E is exactly equal to the energy difference between the $^2F_{5/2}$ and $^2F_{7/2}$ $4f^{13}$-levels. Emission E can therefore be attributed to the ($^3F_4$,t_{2g})$\rightarrow {}^2F_{5/2}$ transition. Previously, it has only been reported for Tm^{2+}-doped trihalide perovskites and we are therefore the first to report its presence in Tm^{2+}-doped monohalides. [1,4-6,14] Emission E is clearly observed in NaBr:Tm^{2+}, whereas for NaCl:Tm^{2+} it is present as a weak shoulder of emission B.

Lastly, the wavelength of emission A perfectly matches the wavelength difference between the $^2F_{5/2}$ and $^2F_{7/2}$ $4f^{13}$-levels. It can hence be related to the $^2F_{5/2} \rightarrow {}^2F_{7/2}$ transition and has been observed many times before. [1,4-6,8,9,14] Since its transition is non-parity allowed, emission A has a relatively long decay time of 4.2 ms at 20 K.

As an overall observation, all $4f^{12}5d^1 \rightarrow 4f^{13}$ emissions gradually shift towards longer wavelength when the anion is varied from Cl→Br→I. For NaBr:Tm^{2+} the average shift, with respect to NaCl:Tm^{2+}, is around 16 nm. For NaI:Tm^{2+} it is close to 58 nm.

2.3.2 Temperature- and Time-Dependence of Emissions

With the emissions now classified in accordance to their transitions, the temperature-dependence of the luminescence intensity and luminescence lifetime were investigated between 20 and 300 K. In the following, emission A through E will be separately presented and discussed. The acquired intensity and time resolved results are summarised in Arrhenius plots that are respectively exhibited in figures 2.6 and 2.7.

Emission D

Emission D emerges from a higher energy $4f^{12}5d^{1}$-state, which in regard to all lanthanide ions has so far only been observed for Tm^{2+}. Its presence has been reported before in $CsCaX_3:Tm^{2+}$ (X = Cl, Br, I) and $ACl_2:Tm^{2+}$ (A = Ca, Sr) [1,3-6,14]. In this study both its temperature- and time-dependence are reported for the very first time, as respectively portrayed by the green curves in figures 2.6 and 2.7. In addition to that, temperature-dependent emission spectra of emission D in $NaBr:Tm^{2+}$ are provided in figure 2.9a. The spectra show that the luminescence intensity starts to decrease rapidly at a temperature close to 80 K and that emission D has quenched completely at 170 K. This is also perceived in the Arrhenius plot in figure 2.6b, from which a thermal deactivation energy of 11 meV or 88 cm^{-1} was retrieved. For $NaCl:Tm^{2+}$ and $NaI:Tm^{2+}$ the related emission spectra are presented in figures 2.8a and 2.10a, revealing a very similar temperature behaviour. In case of $NaCl:Tm^{2+}$, emission D already starts to quench at a temperature of 20 K. At 100 K it is no longer observed. The related thermal deactivation energy amounts to 23 meV or 185 cm^{-1}. For $NaI:Tm^{2+}$, emission D starts to quench at 90 K and at 190 K it has vanished from the spectra. A thermal deactivation energy of 37 meV or 298 cm^{-1} could be retrieved. The trends in thermally stimulated quenching behaviour are confirmed by the luminescence decay spectra shown for $NaBr:Tm^{2+}$ in figure 2.9b. For increasing temperature the luminescence lifetime decreases. The lifetime-temperature Arrhenius plots in figure 2.7 reveal that for $NaBr:Tm^{2+}$, the luminescence lifetime has decreased from 1.0 μs at 20 K to 360 ns at 170 K. Similarly, the lifetime of emission D in $NaCl:Tm^{2+}$ and $NaI:Tm^{2+}$ respectively decreases from 120 ns at 20 K to 28 ns at 70 K, and from 810 ns at 20 K to 150 ns at 190 K. Upon a closer inspection, the energy difference between $(^3F_4,t_{2g})$ and the $(^3H_6,t_{2g})_{S=1/2}$ levels of $NaX:Tm^{2+}$ (X = Cl, Br, I) respectively amounts to around 283, 320 and 330 meV. These differences correspond to energy gaps of 2283, 2581 and 2662 cm^{-1}; which are close to those found previously for other Tm^{2+}-doped halides [1,4,6,8,13], resembling about 13, 18 and 21 vibrational quanta. [23,24,25,26] The ascending order of the quanta reflects the respective higher temperatures of quenching: emission D quenches first for $NaCl:Tm^{2+}$, followed by $NaBr:Tm^{2+}$ and finally $NaI:Tm^{2+}$. Since the relative Stokes shift difference between emission D and B is very small, 506-649 cm^{-1}, the related quenching mechanism can most likely be attributed to multi-phonon relaxation, as was for instance also concluded by Grimm et al. [1,4,6] The peculiar evolution in shape of the decay curves in figure 2.9b is also seen for emission D in $NaCl:Tm^{2+}$ and $NaI:Tm^{2+}$. Below 100 K a single exponential decay is observed consisting of a slow component. Toward higher temperatures a fast component develops. Moreover both slow and fast components start to quench as the temperature increases. At the moment we have no clear explanation for this unusual behaviour.

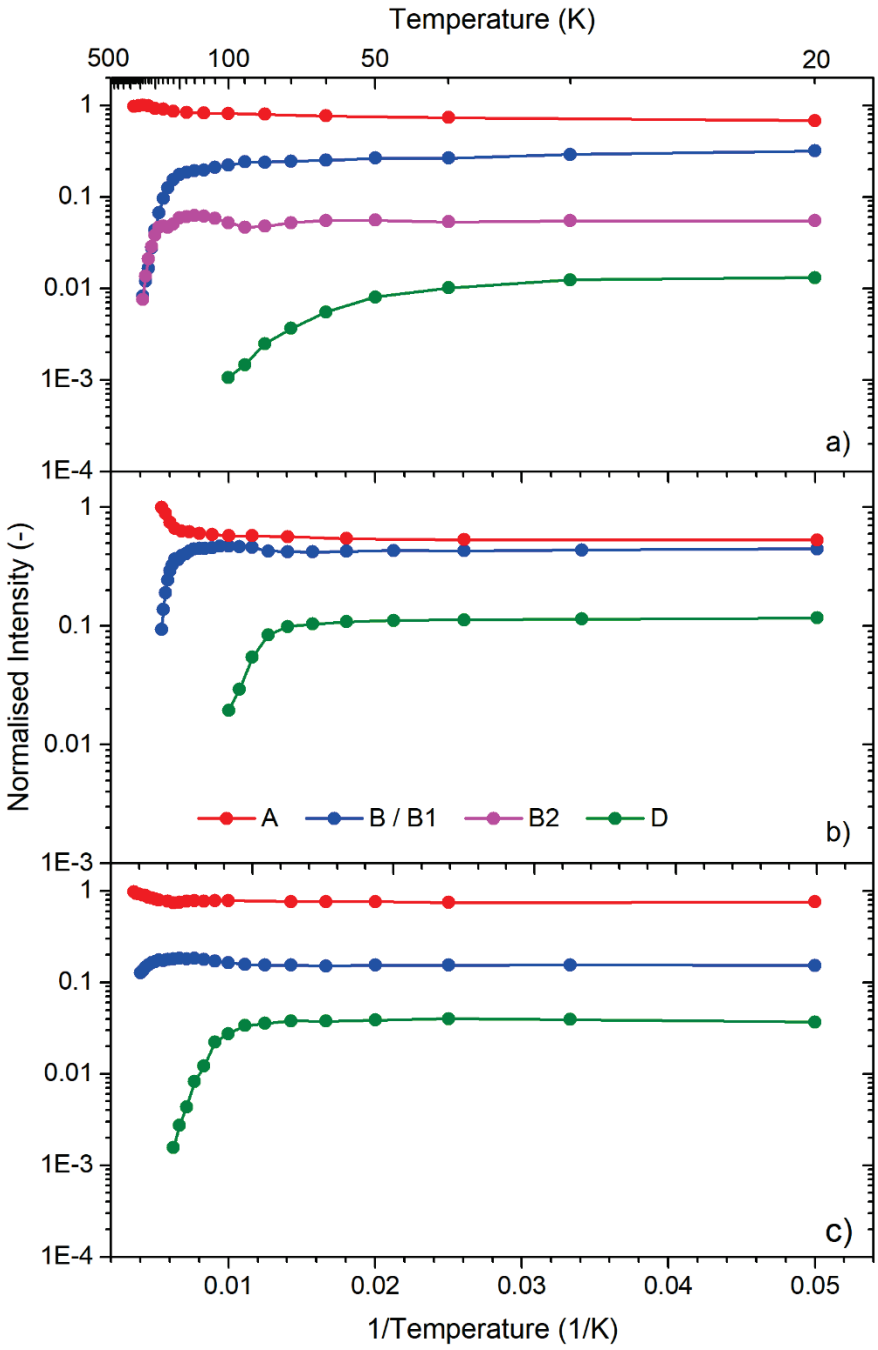

Figure 2.6: Arrhenius plots as based on the integrated emission intensity of the various Tm^{2+} emissions. In this figure a) corresponds to NaCl:Tm^{2+}, b) to NaBr:Tm^{2+} and c) to NaI:Tm^{2+}. Photoexcitation occurred at 420 nm, whereas normalisation was performed on emission A at 300 K.

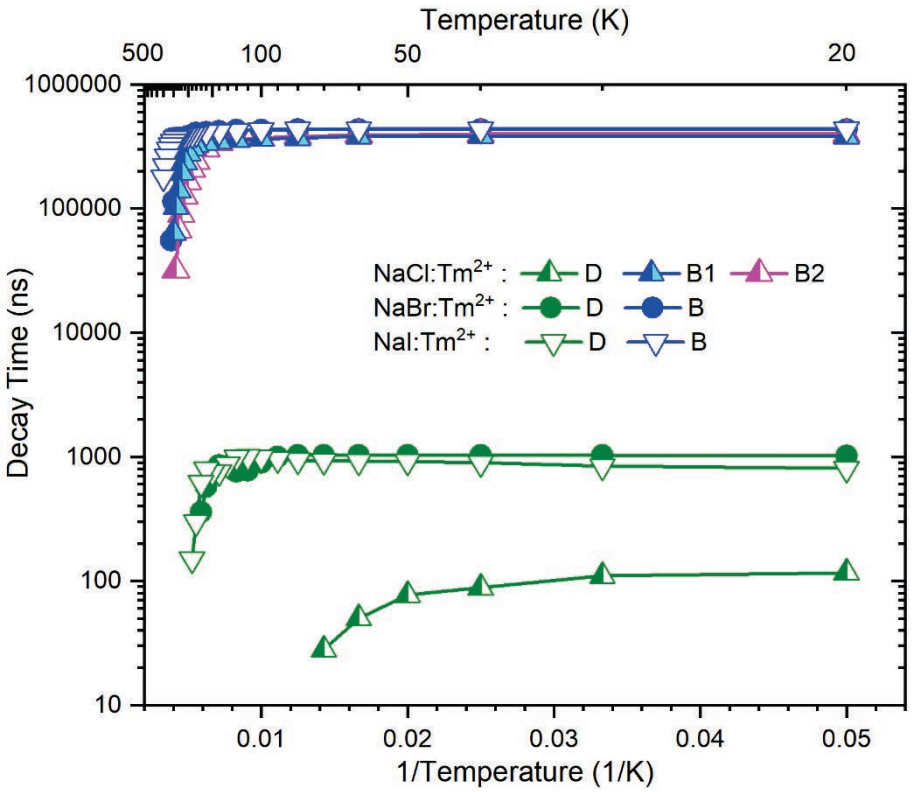

Figure 2.7: Arrhenius plot as based on the luminescence lifetimes of emissions B and D for all three materials. Laser excitation took place at 420nm.

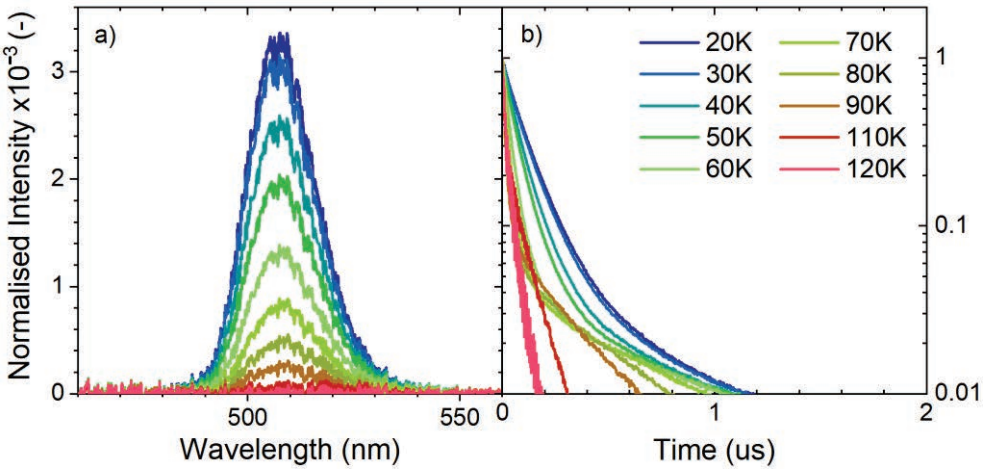

Figure 2.8: The temperature-dependent emission spectra (a) and decay spectra (b) of emission D in NaCl:Tm^{2+} as respectively photo- or laser excited at 420 nm. The emission spectra are normalised on emission A at 20 K.

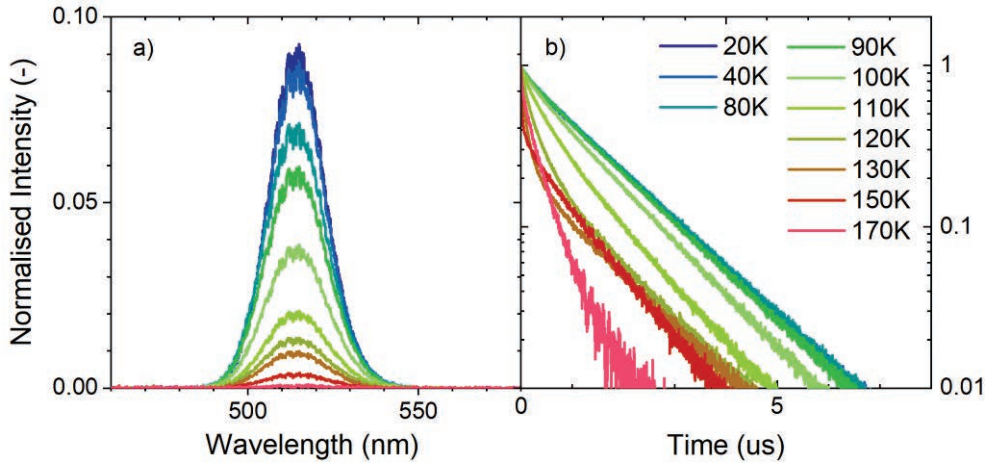

Figure 2.9: The temperature-dependent emission spectra (a) and decay spectra (b) of emission D in NaBr:Tm^{2+} as respectively photo- or laser excited at 420 nm. The emission spectra are normalised on emission A at 20 K.

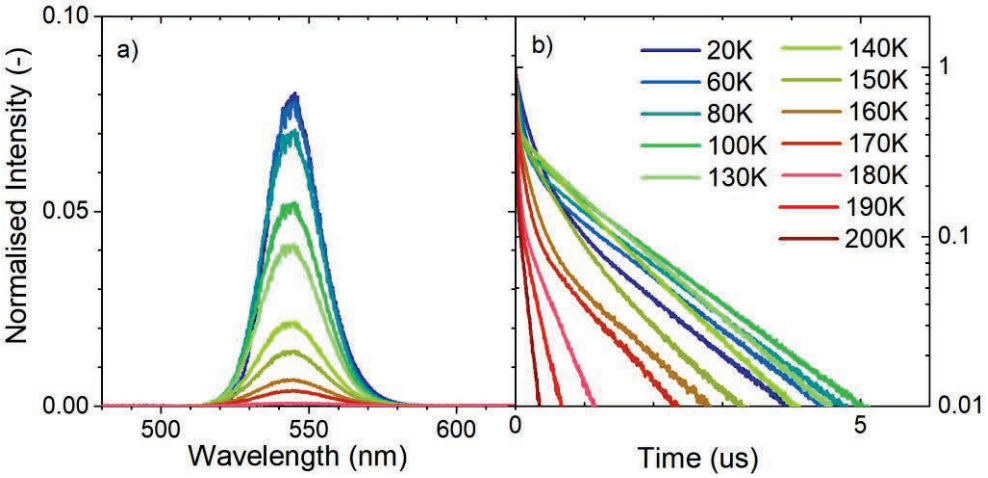

Figure 2.10: The temperature-dependent emission spectra (a) and decay spectra (b) of emission D in NaI:Tm^{2+} as respectively photo- or laser excited at 420 nm. The emission spectra are normalised on emission A at 20 K.

Emission E

As emission E originates from the same energy level as emission D, the temperature-dependence of the emission intensity and luminescence lifetime should be equivalent. This is true to a large extent. Figure 2.11 displays the temperature-dependent emission spectra of emission E in NaBr:Tm^{2+}. Much like emission D, the intensity of emission E decreases within the temperature range of 20 K to 200 K. The decline is about 50% from 20 K to 80 K, indicating that the temperature-dependence of emission E lies indeed in the very same

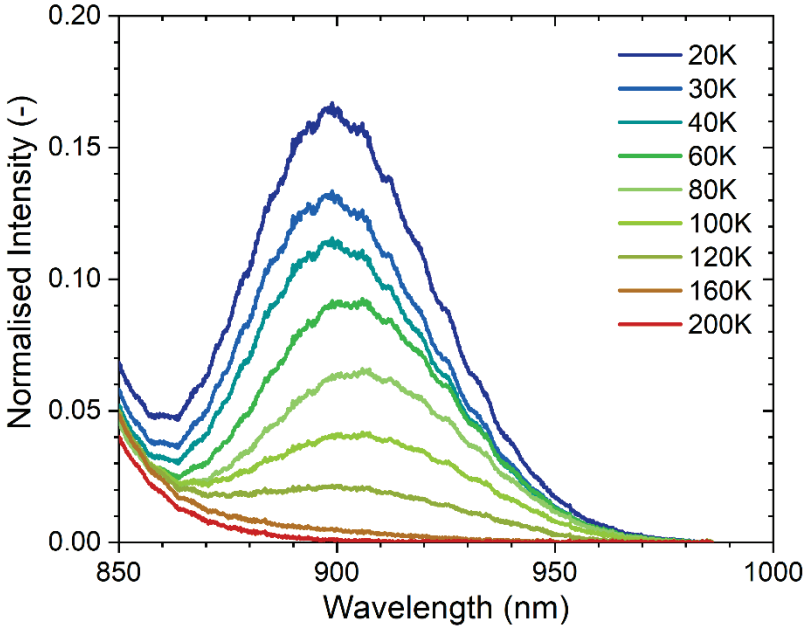

Figure 2.11: Temperature-dependent emission spectra of emission E in NaBr:Tm^{2+} as photoexcited at 420 nm. The spectra are normalised on the peak of emission A at 20 K.

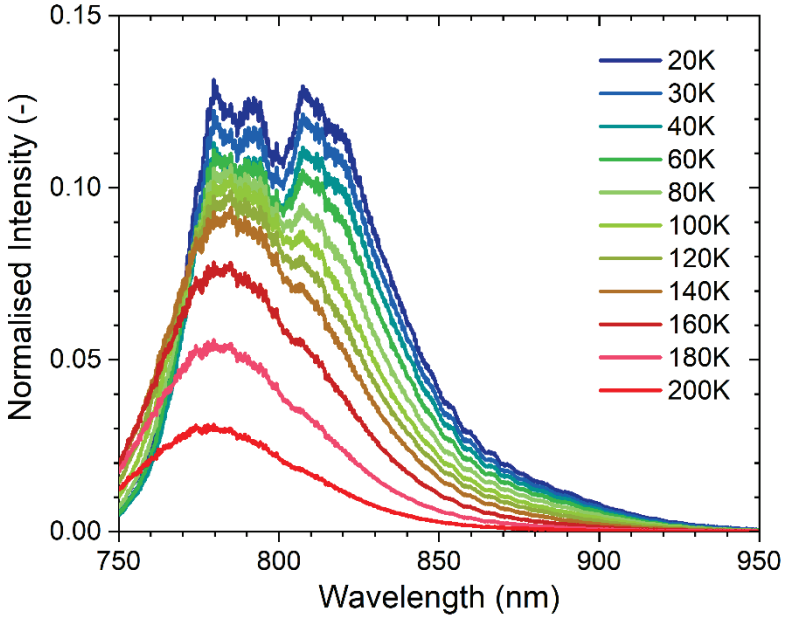

Figure 2.12: Temperature-dependent emission spectra of emissions B and E in NaCl:Tm^{2+}, where emission E is hidden in the tail of emission B. Photoexcitation occurred at 420 nm and the spectra are normalised on the peak of emission A at 20 K.

range of that of emission D. Furthermore, the related luminescence lifetimes of emission D and E are 1.0 μs and 710 ns at 20 K, respectively, and 900 ns and 450 ns at 100 K. Since the wavelength of emission E lies in a range where the Hamamatsu R7600U-20HV-800V PMT has a very low efficiency, we had to increase the laser power by more than a factor 10. This may have caused the decay spectra of emission E to become slightly non-exponential and develop a fast component, which makes a more detailed quantitative comparison speculative. In NaCl:Tm^{2+} emission E was also observed, but only as a weak shoulder of emission B. The related temperature-dependent emission spectra are plotted in figure 2.12, with deconvoluted spectra provided in Appendix A. No reliable temperature-dependent intensity values or luminescence lifetimes could be obtained. For NaI:Tm^{2+}, emission E should be expected at a wavelength of around 1040 nm, but it was not observed.

Emission B

From the temperature-dependent emission spectra of NaBr:Tm^{2+} in figure 2.14a, it can be deduced that the luminescence intensity of emission B gradually decreases over temperature. The blue curve in figure 2.6b provides a more detailed insight, where two downward slopes can be distinguished. This indicates that emission B is likely to undergo quenching in two different stages. The first stage is already active at 20 K and could possibly be attributed to $4f^{12}5d^{1}$-$4f^{13}$ multi-phonon relaxation [1,4,14] with a weak temperature dependence, while the second stage setting in at around 170 K is likely to be related to thermal stimulated quenching with a much higher thermal deactivation energy. [15] This latter process is also known under the name of interband crossing and typically involves relaxation via the crossing point between the $(^3H_6,t_{2g})_{S=3/2}$ and $^2F_{5/2}$ parabolas in the configuration diagram, for which a certain amount of thermal energy is required. By comparison, the thermal deactivation energy of the first process amounts to around 0.13 meV or 1.1 cm^{-1}, whereas that of the second process comes close to 136 meV or 1097 cm^{-1}. For NaCl:Tm^{2+} and NaI:Tm^{2+} the first quenching process also commences at 20 K with respective thermal deactivation energies of 0.17 meV or 1.4 cm^{-1} and 0.13 meV or 1.1 cm^{-1}, whereas the second process respectively sets in at around 190 K and 150 K with deactivation energies of 189 meV or 1524 cm^{-1} and 27 meV or 217 cm^{-1}.

The quenching of emission B predicts a shortening of its luminescence lifetime. Figure 2.14b shows that for NaBr:Tm^{2+} this is indeed true. Furthermore, the blue curve in the lifetime-temperature Arrhenius plot in figure 2.7 reveals that the luminescence lifetime decreases from 430 μs at 20 K to 55 μs at 260 K. The decay spectra of NaCl:Tm^{2+} and NaI:Tm^{2+} in figures 2.13 and 2.15 display a similar behaviour. For the former material, the luminescence lifetime respectively decreases from 380 μs and 400 μs at 20 K to 100 μs and 32 μs at 240 K; and for the latter it changes from 440 μs at 20 K to 180 μs at 300 K. The close resemblance in the behaviour of the luminescence intensity and lifetime is expected since both are

essentially caused by the same quenching process. The quenching of emissions D and E over temperature, as triggered by $4f^{12}5d^1$-$4f^{12}5d^1$ multi-phonon relaxation, should cause for a feeding of the lowest $4f^{12}5d^1$-state from which emission B originates. An observed decrease in the intensity of emissions D and E should then essentially result in an increase in the intensity of emission B. The respective decrease and increase would be equal only if the quantum efficiency of emission B is 100%, which is not the case as $4f^{13}\rightarrow4f^{13}$ emission A dominates. Yet, a slight intensity increase for emission B can be seen in figure 2.6b and c, exactly within the same temperature range where emission D starts to quench.

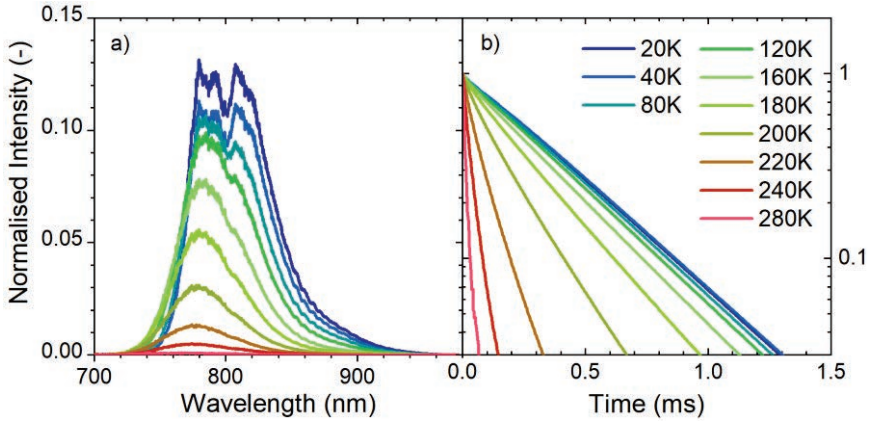

Figure 2.13: The temperature-dependent emission spectra (a) and decay spectra (b) of emission B in NaCl:Tm^{2+} as respectively photo- or laser excited at 420 nm. The emission spectra are normalised on emission A at 20 K, while the decay spectra are normalised on their origin.

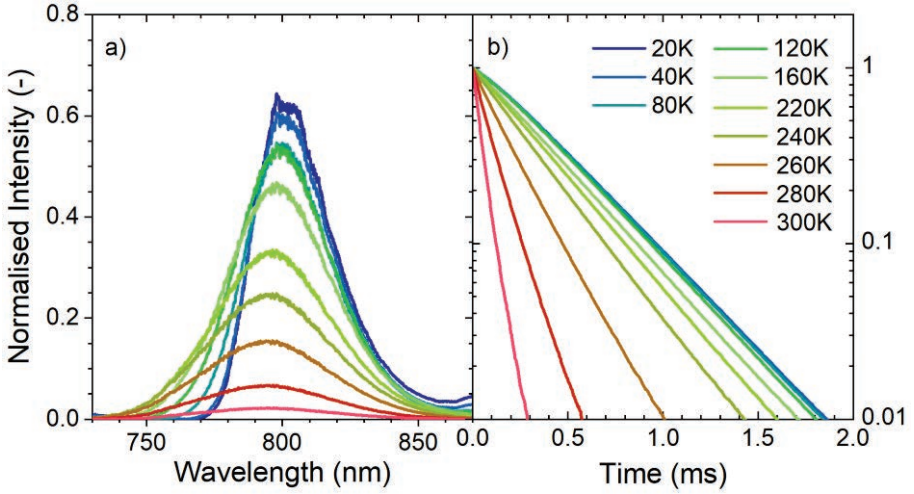

Figure 2.14: The temperature-dependent emission spectra (a) and decay spectra (b) of emission B in NaBr:Tm^{2+} as respectively photo- or laser excited at 420 nm. The emission spectra are normalised on emission A at 20 K, while the decay spectra are normalised on their origin.

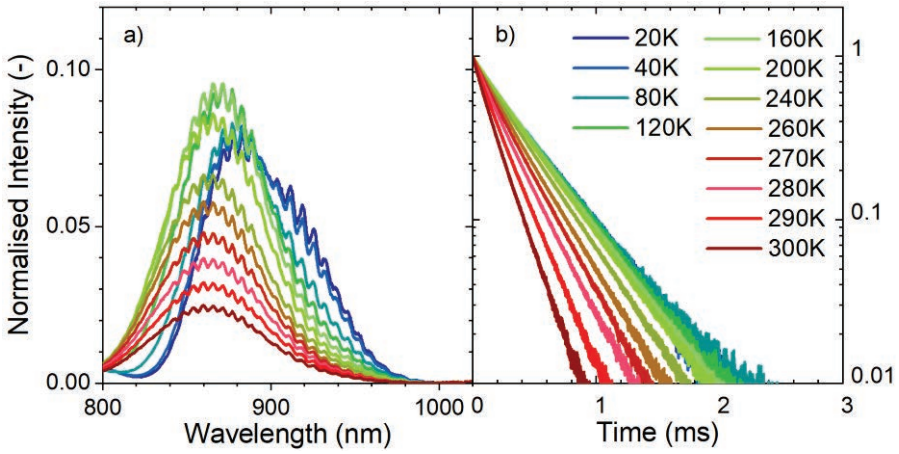

Figure 2.15: The temperature-dependent emission spectra (a) and decay spectra (b) of emission B in NaI:Tm^{2+} as respectively photo- or laser excited at 420 nm. The emission spectra are normalised on emission A at 20 K, while the decay spectra are normalised on their origin.

Emission C

Previously, emission C has been observed in $CsCaY_3$:Tm^{2+} (Y = Br, I). [1,4-6] The temperature-dependent emission spectra in figure 2.16 reveal that it is only present for NaBr:Tm^{2+} and NaI:Tm^{2+} and that it is most intense at 20 K. For NaBr:Tm^{2+} it already starts to undergo quenching at this temperature and has quenched completely at 140 K. For NaI:Tm^{2+}, the quenching of emission C also commences at 20 K. Yet, it remains present all the way up to room temperature. The energy difference between the $(^3H_6,t_{2g})_{S=1/2}$ and $(^3H_6,t_{2g})_{S=3/2}$ levels is respectively around 1298 and 1271 cm^{-1} for NaBr:Tm^{2+} and NaI:Tm^{2+}.This represents about 9 and 10 vibrational quanta and hence the related quenching mechanism can most likely be attributed to multi-phonon relaxation. For NaCl:Tm^{2+} the absence of this emission was earlier described for $CsCaCl_3$:Tm^{2+} [4] by a highly efficient quenching. The relatively low

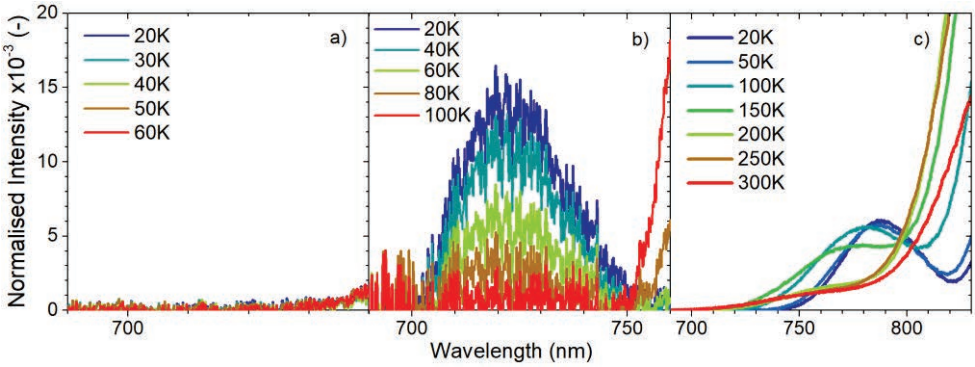

Figure 2.16: The temperature-dependent emission spectra of emission C in: a) NaCl:Tm^{2+} (absent), b) NaBr:Tm^{2+} and c) NaI:Tm^{2+} as photo-excited at 420 nm. The spectra are normalised on emission A at 20 K.

intensity of the emission and the overlap with emission B has prevented a further temperature analysis of its intensity and its luminescence lifetime.

Emission A

As perceived in the previous section, emission A is already present at 20 K for all three studied materials. Figure 2.17 shows that its intensity gradually increases over temperature. Moreover, the related integrated emission intensity curve in figure 2.6 reveals that, for NaBr:Tm^{2+}, this increase happens in two different stages; as witnessed by the two upward slopes. The first stage is observed up to a temperature of 200 K, after which the second stage clearly starts to manifests itself. At around the very same temperature, emission B displays an anti-correlated behaviour that can also be noticed for NaCl:Tm^{2+} and NaI:Tm^{2+}, although somewhat less clear.

The decay curves in figure 2.18 reveal that the luminescence lifetime of emission A remains constant with temperature. This indicates that as soon as the ($^2F_{5/2}$) $4f^{13}$-level is populated by the higher energy $4f^{12}5d^1$-levels, there is no quenching of the $4f^{13}\rightarrow4f^{13}$ emission itself. For NaCl:Tm^{2+} and NaI:Tm^{2+}, the decay curves of emission A are single exponential with respective lifetimes 2.7 ms and 3.7 ms and without any temperature-dependence.

The thermally stimulated quenching of emission B and the directly related thermally stimulated feeding of emission A, predicts a risetime in the decay spectrum of emission A

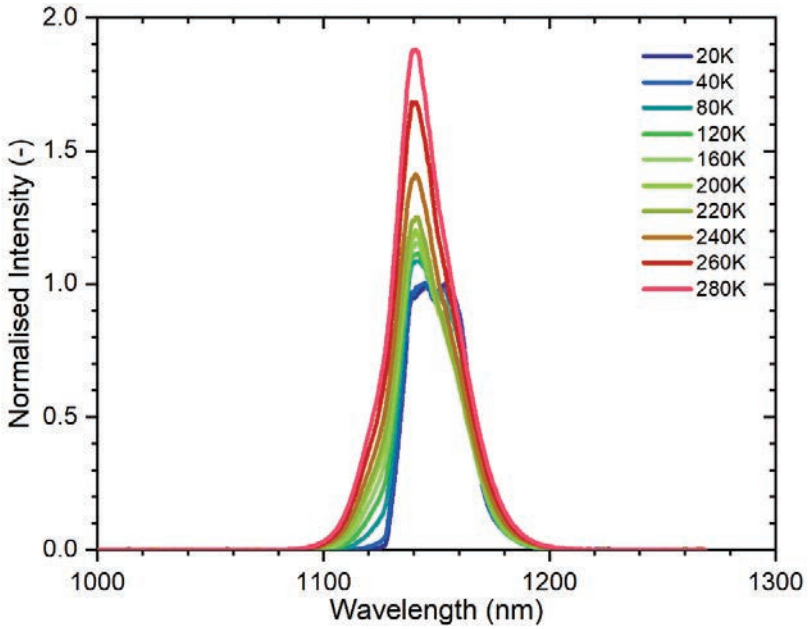

Figure 2.17: The temperature-dependent emission spectra of emission A in NaBr:Tm^{2+} as photo-excited at 420 nm. The spectra are normalised on the emission peak at 20 K.

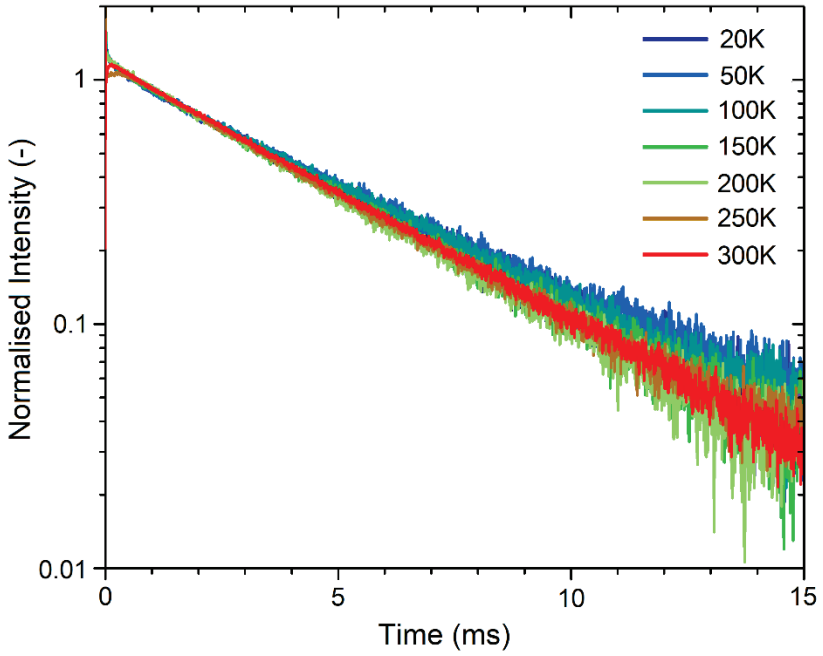

Figure 2.18: The decay spectra of emission A in NaBr:Tm^{2+} for different temperatures as laser excited at 420 nm.

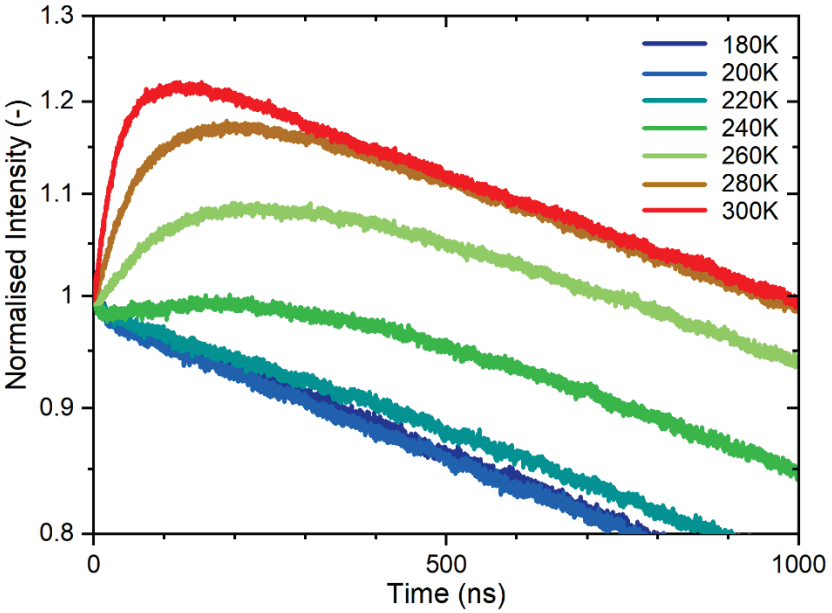

Figure 2.19: The decay spectra of emission A in NaBr:Tm^{2+} plotted at a short time scale between 180 and 300 K. The decay curves were acquired using pulsed laser excitation at 420 nm and clearly exhibit a risetime phenomenon for temperatures above 200 K.

with a timescale that corresponds to the lifetime of emission B. Figure 2.19 shows that such a risetime actually exists. At temperatures below 220 K, where there is no significant thermally stimulated population of the $^2F_{5/2}$ level, there is no risetime. Below this temperature, the presence of $4f^{13}\rightarrow4f^{13}$ emission A is likely to be caused by $4f^{12}5d^1$-$4f^{13}$ multi-phonon relaxation, as mentioned previously by Grimm et al. [1,4,14]

Above 200 K, the thermally stimulated population of the ($^2F_{5/2}$) $4f^{13}$-level becomes active and a corresponding risetime evidently develops, which enhances the total $4f^{13}\rightarrow4f^{13}$ emission intensity. The risetime becomes shorter as the temperature increases further, indicating that the feeding of the ($^2F_{5/2}$) $4f^{13}$-level starts to happen at a faster rate. No clear risetime phenomena were witnessed for NaCl:Tm^{2+} and NaI:Tm^{2+}, possibly due to the smaller amplitude related to the intensity increase of emission A.

2.4. Overall Discussion

Our findings can be summarised with a qualitative model that we exemplify for NaBr:Tm^{2+} in figure 2.20. The most elementary situation is encountered at room temperature. All non-radiative $4f^{12}5d^1$-$4f^{12}5d^1$ and $4f^{12}5d^1$-$4f^{13}$ relaxation processes dominate over the radiative transitions so that excitation in the high energy $4f^{12}5d^1$-states results almost exclusively in emission A, as indicated by the red arrows. At low temperature (20 K) the situation is far more complex. Excitation in the high energy $4f^{12}5d^1$-states results in emissions: A, B, C, D, and E with a relative intensity of 33, 28, 1, 7, and 9.

When it is assumed that there are no non-radiative $4f^{12}5d^1$-$4f^{12}5d^1$ relaxation processes active, the intensity of emission E should be equal to that of emission A and in addition emissions C and B should be absent. This is clearly not what is observed in figure 2.4. If we allow for non-radiative 5d-5d multi-phonon relaxation as indicated by the red curly arrows in figure 2.20, the presence of emission C and B can be explained but emissions E and A should still have the same intensity which is not the case. Grimm et al. opted for a very efficient non-radiative process from the higher energy $4f^{12}5d^1$-state to the emitting $4f^{13}$-level. [4] If such a non-radiative channel is assumed directly, as indicated by Y, emission E can be of lower intensity than emission A, which is what we observe. The introduction of a further non-radiative channel Z from the excited ($^3F_4$,t_{2g}) levels towards the $4f^{13}$ ground state would allow for a lower than unity quantum efficiency for emission A.

The higher energy $4f^{12}5d^1$ ($^3F_4$,t_{2g}) levels might be positioned close or in to the conduction band. For excited electrons in these levels it then becomes possible to ionise from the Tm^{2+}-luminescence centre towards the conduction band and form an impurity bound or unbound exciton state. In the latter case, the electrons become simply delocalised from the Tm^{3+} impurity ions and constitute a photocurrent that eventually recombines non-radiatively

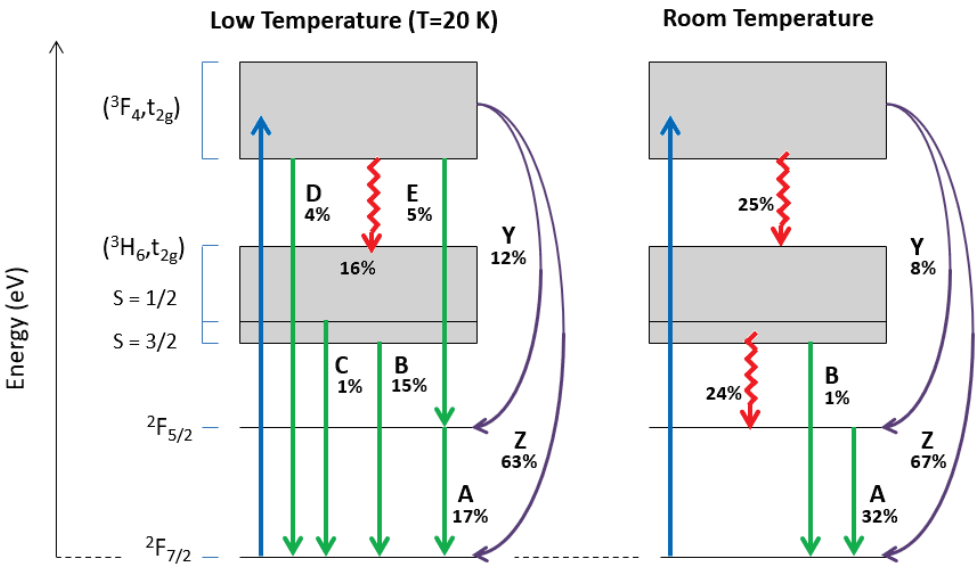

Figure 2.20: Schematic overview of the two proposed non-radiative channels Y and Z together with the observed emissions and quenching processes as present at low temperatures of 20 K and room temperature. Percentage labels are provided to account for the dominance of the different pathways.

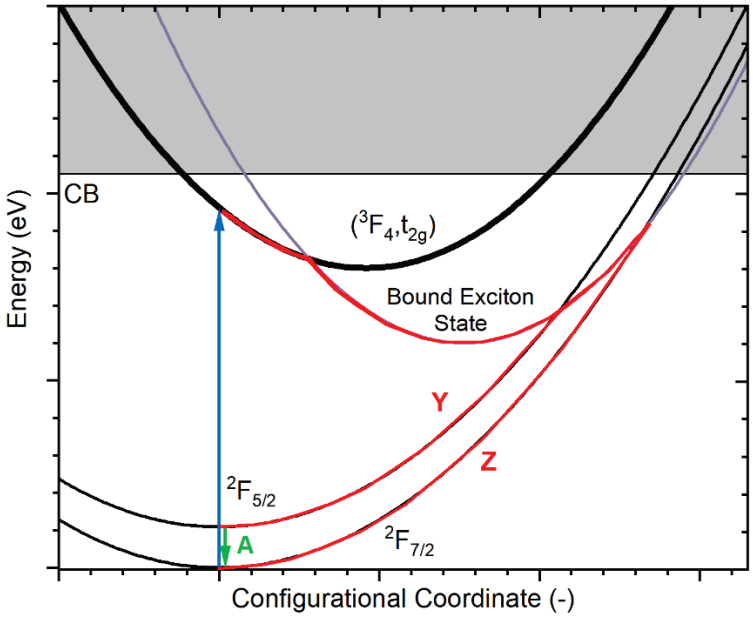

Figure 2.21: Configurational coordinate diagram showing the $4f^{12}5d^1$ ($^3F_4$,t_{2g}) levels as closely positioned to the Conduction Band (CB). Excitation into these levels results in a photo-excited ionisation to the conduction band and, in this case, the formation of a bound exciton state (purple) that leads to a strong non-radiative relaxation towards the excited $^2F_{5/2}$ $4f^{13}$-level and the $4f^{13}$ $^2F_{7/2}$ ground state. From the $^2F_{5/2}$ level, emission A takes place.

with a hole in the valence band. [27,28] For bound exciton states, the electron remains localised on Tm^{3+} and undergoes either a radiative transition, often referred to as anomalous emission, or non-radiative transition towards the ($^2F_{5/2}$) or ($^2F_{7/2}$) $4f^{13}$-levels; after which it recombines with the hole localised on the ($^2F_{7/2}$) $4f^{13}$ ground state. [28] The proposed non-radiative channels Y and Z thus stem from a photo-excited ionisation to the conduction band, where the electrons form a bound exciton state and eventually undergo a strong relaxation towards, respectively, the emitting ($^2F_{5/2}$) $4f^{13}$-level and $4f^{13}$ ($^2F_{7/2}$) ground state. Such a strong relaxation process has been observed many times before in various compounds. [27,29,30] Figure 2.21 illustrates the proposed situation via a configurational coordinate diagram.

With help of an integrating sphere, the internal quantum efficiency of the Tm^{2+} $4f^{13}\rightarrow4f^{13}$ emission at room temperature was measured to be 32% at room temperature and estimated on 17% at 20 K using figure 2.6b and table 2.1. So in summary, upon excitation into the higher energy ($^3F_4$,t_{2g}) $4f^{12}5d^1$-state of Tm^{2+}, 63% of the excitations return non-radiatively towards the $^2F_{7/2}$ ground state via channel Z and 12% relaxes to the emitting $^2F_{5/2}$ $4f^{13}$-level through channel Y. In addition, 16% of the excitations relax to the lowest energy ($^3H_6$,t_{2g})$_{s=1/2}$ $4f^{12}5d^1$-state via multi-phonon relaxation, resulting in an identical 15% of emission B plus 1% emission C. Furthermore, 5% of the excitations result in emission E, followed by an equal amount of emission A. In combination with the earlier mentioned 12% this adds up to 17%, which is the QE at 20K that we estimated. Besides, 4% of the excitations result in emission D.

The processes related to channel Y and Z are known to be only weekly dependent on temperature and should therefore have similar efficiency at room temperature. [27] So now we may assume that at room temperature, after excitation into the ($^3F_4$,t_{2g}) $4f^{12}5d^1$-state of Tm^{2+}, 67% of the excitations return to the $^2F_{7/2}$ ground state non-radiatively by channel Z and 8% to the emitting $^2F_{5/2}$ $4f^{12}5d^1$-level through channel Y. In addition, 25% of the excitations will relax to the lowest energy ($^3H_6$,t_{2g})$_{S=1/2}$ $4f^{12}5d^1$-state, followed by either 1% in emission B or a thermally stimulated relaxation to the emitting $^2F_{5/2}$ $4f^{13}$-level causing 24% of emission A. Together with the 8% that feeds this level through channel Y, this adds up to 32% which is the QE recorded at room temperature.

Although our temperature resolved intensity and decay data display clear trends for the NaX:Tm^{2+} (X = Cl, Br, I) series, which can qualitatively be well explained in a consistent manner, a more quantitative modelling involving all data using for instance rate equations proved unsuccessful. Our experimental data and the work of Rubio et al. [19] has given us some ideas why this might be the circumstance. First of all, as discussed in section 2.3.1, we can expect that for all materials there might be multiple Tm^{2+}-sites present because of the

necessity for charge compensation when Tm^{2+} enters the monohalides on the Na^{+}-site. Even though there is a dominant site with an octahedral coordination, there are many distorted sites reported in literature for Eu^{2+}-doped monohalides [19], that can all have slightly different relaxation dynamics properties. Since the measurements were performed over several months, the hygroscopicity of the halides and oxidation sensitivity of Tm^{2+} might also have caused for a gradual degradation of our samples. Furthermore, we have seen that in Eu^{2+}-doped NaCl and NaI, photochromic behaviour involving the photo-creations of colour centres can occur. Such behaviour has also been reported for LnAlO3:Ce^{3+}, where excited electrons become delocalised and trapped in the host lattice and display photochromic behaviour after absorption of light. [31] It may therefore be that our Tm^{2+}-doped samples suffer from the same behaviour, which goes on the expense of reproducibility. We therefore believe that a more detailed and quantitative discussion of our results would become too speculative.

2.5. Conclusion

The luminescence behaviour of Tm^{2+} in NaCl and NaBr proves to be remarkable similar to that in trihalide Perovskites, as five different types of emissions are observed. For NaI:Tm^{2+} four emissions are observed and the behaviour is therefore analogous to the Tm^{2+}-doped dihalides: $CaCl_2$:Tm^{2+} and $SrCl_2$:Tm^{2+}. Besides, the $4f^{13}\rightarrow4f^{13}$ emission in the three studied monohalides is by far the most dominant emission at all temperatures; much akin to $RbCaI_3$:Tm^{2+} and $BaCl_2$:Tm^{2+}. This is tentatively explained by a non-radiative pathway involving conduction band states. In view of the LSC application, the (almost) complete absence of the $4f^{12}5d^{1}\rightarrow4f^{13}$ emissions at room temperature ensures that self-absorption losses are non-imminent and the relative intenseness of the $4f^{13}\rightarrow4f^{13}$ emission is highly beneficial. In addition, the sunlight absorption fraction and QE are reasonably high. However, the latter seems to be restricted due to the presence of a non-radiative pathway. It is therefore recommended to perform a similar study on Tm^{2+}-doped dihalides to investigate if the observed radiative and non-radiative processes, with related QE values, follow the same temperature dependence.

2.6. Appendix A

Table 2.2: Additional information on the deconvolved emission peaks from emission B of NaCl:Tm^{2+}.

Peak [-]	Transition [-]	Center [eV]	Wavelength [nm]	FWHM [eV]
1	$(^3H_6,t_{2g})_{S=3/2} \rightarrow F_{7/2}$	1.60	779	4.3×10^{-2}
2	$(^3H_6,t_{2g})_{S=3/2} \rightarrow F_{7/2}$	1.53	811	1.2×10^{-1}
3	$(^3F_4,t_{2g}) \rightarrow {}^2F_{5/2}$	1.41	883	8.7×10^{-2}

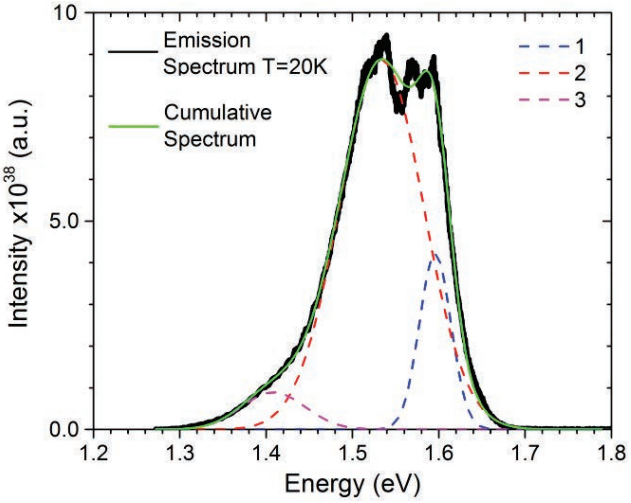

Figure 2.22: The deconvolution of emission peak B, centred at around 800 nm, in NaCl:Tm^{2+} into three different luminescence components. Observed are two luminescence centres corresponding to emission B1 and B2, and emission E as hidden in the tail of the peak.

2.7. References

[1] E. Beurer, J. Grimm, P. Gerner, H.U. Güdel, Absorption, Light Emission, and Upconversion Properties of Tm^{2+}-doped $CsCaI_3$ and $RbCaI_3$, Inorg. Chem. 9901-9906 (2006) 45.

[2] J. Grimm, E. Beurer, H.U. Güdel, Crystal Absorption Spectra in the region of 4f-4f and 4f-5d Excitations in Tm^{2+}-doped $CsCaCl_3$, $CsCaBr_3$, and $CsCaI_3$, Inorg. Chem. 10905-10908 (2006) 45.

[3] E. Beurer, J. Grimm, P. Gerner, H.U. Güdel, New Type of Near-Infrared to Visible Photon Upconversion in Tm^{2+}-doped $CsCaI_3$, J. AM. CHEM. SOC. 3110-3111 (2006) 128.

[4] J. Grimm, J.F. Suyver, G. Carver, H. U. Güdel, Light-Emission and Excited-State Dynamics in Tm^{2+} Doped $CsCaI_3$, $CsCaBr_3$, and $CsCaI_3$, J. Phys. Chem. B 2093-2101 (2006) 110.

[5] J. Grimm, E. Beurer, P. Gerner, H.U. Güdel, Upconversion Between 4f-5d Excited States in Tm^{2+}-Doped $CsCaCl_3$, $CsCaBr_3$, and $CsCaI_3$, Chem. Eur. J. 1152–1157 (2007) 13.

[6] J. Grimm, H.U. Güdel, Five different types of spontaneous emission simultaneously observed in Tm^{2+} doped $CsCaBr_3$, Chemical Physics Letters 40–43 (2005) 404

[7] M. de Jong, D. Biner, K.W. Krämer, Z. Barandiarán, L. Seijo, A. Meijerink, New Insights in $4f^{12}5d^1$ Excited States of Tm^{2+} through Excited State Excitation Spectroscopy, J. Phys. Chem. Lett. 2730-2734 (2016) 7.

[8] M. de Jong, A. Meijerink, L. Seijo, Z. Barandiarán, Energy Level Structure and Multiple $4f^{12}5d^1$ Emission Bands for Tm^{2+} in Halide Perovskites: Theory and Experiment, J. Phys. Chem. C 10095−10101 (2017) 121.

[9] M. Karbowiak, R. Lisiecki, P. Solarz, J. Komar, and W. Ryba-Romanowski, Spectroscopic peculiarities of $CsCaI_3$:Tm^{2+} single crystals examined through one-photon and excited state excitation spectroscopy, J. Alloy. Comp. 1165-1171 (2018) 740.

[10] Z.J. Kiss, Energy levels of divalent Thulium in CaF_2, Phys. Rev. 718-724 (1962) 127.

[11] H.A. Weakliem, C.H. Anderson, and E.S. Sabisky, Magnetic Circular Dichroism Spectra of Divalent Lanthanide Ions in Calcium Fluoride, Phys. Rev. B 4354-4365 (1970) 11.

[12] R.C. Alig, R.C. Ducan Jr., and B.J. Mokross, Reduced 4f-5d electrostatic interaction of Tm^{2+} in $SrCl_2$, J. Chem. Phys. 5837-5841 (1973) 59.

[13] M. Karbowiak, C. Rudowicz, Trends in Hamiltonian parameters determined by systematic analysis of f-d absorption spectra of divalent lanthanides in alkali-halides hosts: II. $CaCl_2$:Ln^{2+} (Ln = Sm, Eu, Tm, and Yb), J. Lumin. 66-75 (2018) 197.

[14] J. Grimm, O.S. Wenger, K.W. Krämer, H.U. Güdel, 4f-4f and 4f-5d excited states and luminescence properties of Tm^{2+}-doped CaF_2, $CaCl_2$, $SrCl_2$, $BaCl_2$, J. Phys. Chem. B 101-105 (2006) 110.

[15] O.M. ten Kate, K.W. Krämer, E. Van der Kolk, Efficient luminescent solar concentrators based on self-absorption free, Tm^{2+} doped halides, Sol. Energy Mater Sol. Cells 115-120 (2015) 140.

[16] M. Zhuravleva, L. Stand, H. Wei, Hygroscopicity Evaluation of Halide Scintillators, Conference Paper, Nuclear Science Symposium and Medical Imaging Conference (NSS/MIC) IEEE, Seoul, South Korea (2013).

[17] E. Rogers, P. Dorenbos, J.T.M. de Haas, E. van der Kolk, Experimental study of the $4f^n \rightarrow 4f^n$ and $4f^n \rightarrow 4f^{n-1}5d^1$ transitions of the lanthanide diiodides LnI_2 (Ln = Nd, Sm, Eu, Dy, Tm, Yb), J. Phys.: Condens. Matter (2012) 24.

[18] G.H. Dieke, H.M. Crosswhite, The Spectra of the Doubly and Triply Ionized Rare Earths, Appl. Opt. 675-686 (1963) 2.

[19] J.O. Rubio, Doubly-Valent Rare-Earth Ions in Halide Crystals, J. Phys. Chem. Solids 101-174 (1991) 52.

[20] T. Dienel, C. Bauer, I. Dolamic, D. Brühwiler, Spectral-based analysis of thin film luminescent solar concentrators, Solar Energy 1366-1369 (2010) 84(4).

[21] American Society for Testing and Materials (ASTM), G-173 (Air Mass 1.5g) spectra.

[22] P. Dorenbos, Energy of the first $4f^7 \rightarrow 4f^6 5d$ transition of Eu^{2+} in inorganic compounds, J. Lumin. 239-260 (2003) 104.

[23] G. Raunio, S. Rolandson, Lattice dynamics of NaCl, KCl, RbCl & RbF, Phys. Rev. B2 (1970) 2098.

[24] J.S. Reid, T. Smith, Phonon frequencies in NaBr, Phys. Rev. B1 (1970) 1833.

[25] A.D.B Woods, W. Cochran, B.N. Brockhouse, Lattice dynamics of alkali halide crystals, Phys. Rev. 119 (1960) 980.

[26] A.D.B. Woods, B.N. Brockhouse, R.A. Cowley, Lattice dynamics of alkali halide crystals. II: Studies of KBr & NaI, Phys. Rev. 131 (1963) 1025.

[27] E. van der Kolk, P. Dorenbos, J.T.M. de Haas, and C.W.E. van Eijk, Thermally stimulated electron delocalization and luminescence quenching of Ce impurities in $GdAlO_3$, Phys. Rev. B (2005) 71.

[28] G. Blasse and B.C. Grabmeier, Luminescent Materials, Springer Verlag ISBN-13: 978-3-540-58019-5 (1994).

[29] P. Dorenbos, Anomalous luminescence of Eu^{2+} and Yb^{2+} in inorganic compounds, J. Phys.: Condens. Matter 2645-2665 (2003) 15.

[30] E. van der Kolk, O.M. ten Kate, J.W. Wiegman, D. Biner, K.W. Krämer, Enhanced $^1G_4$ emission in $NaLaF_4$: Pr^{3+}, Yb^{3+} and charge transfer in $NaLaF_4$: $Ce3^+$, Yb3+ studied by fourier transform luminescence spectroscopy, Opt. Mater. 1024-1027 (2011) 33.

[31] P. Dorenbos, Anomalous luminescence of Eu^{2+} and Yb^{2+} in inorganic compounds, J. Phys.: Condens. Matter 2645-2665 (2003) 15.

[32] E. van der Kolk, J.T.M. de Haas, A.J.J. Bos, C.W.E. van Eijk, P. Dorenbos, Luminescence quenching by photoionization and electron transport in a $LaAlO_3$:Ce^{3+} crystal, Int. J. Appl. Phys.(2007) 101, 083703.

3.

Experimental and Numerical Analysis of Tm^{2+} Excited-States Dynamics and Luminescence in $CaX_2:Tm^{2+}$ (X = Cl, Br, I)

This chapter is based on the publication: M.P. Plokker, I.C. van der Knijff, A.V. de Wit, B. Voet, T. Woudstra, V. Khanin, P. Dorenbos and E. van der Kolk, Experimental and Numerical Analysis of Tm^{2+}Excited States Dynamics and Luminescence in CaX_2 (X = Cl, Br, I), Journal of Physics: Condensed Matter 33 (2021).

Thanks to: J.T.M. de Haas, B.E. Terpstra, R.D. Abellon and F. van Dam

Abstract

The prospect of using Tm^{2+}-doped halides for luminescence solar concentrators requires a thorough understanding of the temperature dependent Tm^{2+} excited states dynamics that determines the internal quantum efficiency and thereby the efficiency of the LSC. In this study we investigated the dynamics in $CaX_2:Tm^{2+}$ (X = Cl, Br, I) by temperature- and time-resolved measurements. At 20 K up to four distinct Tm^{2+} emissions can be observed. Most of these emissions undergo quenching via multi-phonon relaxation below 100 K. At higher temperatures, only the lowest energy $4f^{12}5d^1 \rightarrow 4f^{13}$ emission and the $4f^{13} \rightarrow 4f^{13}$ emission remain. Fitting a numerical rate equation model to the data shows that the subsequent quenching of the $4f^{12}5d^1 \rightarrow 4f^{13}$ emission is likely to occur initially via multi-phonon relaxation, whereas at higher temperatures additional quenching via interband crossing becomes thermally activated. At room temperature only the $4f^{13} \rightarrow 4f^{13}$ emission remains and the related QE becomes close to 30%. Possible reasons for the quantum efficiency not reaching 100% are provided.

3.1. Introduction

Luminescence Solar Concentrators (LSCs) can become one of many Building-Integrated PhotoVoltaic (BIPV) solutions that contribute to more sustainable buildings. LSCs make use of a special luminescent coating that absorbs sunlight and emits light of different energy towards solar cells mounted in the edges of a window. The window glass serves as a waveguide for the emitted light. Key material challenges for the LSC coating involve: a large sunlight absorption fraction that includes ultraviolet and visible light, a high internal luminescence Quantum Efficiency (QE) and the absence of self-absorption losses caused by a direct re-absorption of the emitted light by the coating. [1,2] Tm^{2+}-doped halides have been identified as potential LSC coating material. The broad $4f^{12}5d^1$ absorption bands, of for instance $CaI_2:Tm^{2+}$, exhibit a 63% overlap with the solar spectrum (AM 1.5), while no self-absorption losses can occur due to the energy difference between the $4f^{13} \rightarrow 4f^{12}5d^1$ absorption and the $4f^{13} \rightarrow 4f^{13}$ emission. Besides, the energy of this emission corresponds well with the bandgap of Copper Indium Selenide (CIS) solar cells. Furthermore, an optimised coating based on Tm^{2+}-doped halides can appear colourless due to the broad absorption range over the entire visible light region. [3] However, not much is known about the QE of the $4f^{13} \rightarrow 4f^{13}$ emission after $4f^{13} \rightarrow 4f^{12}5d^1$ excitation. This parameter is directly proportional to the overall LSC efficiency and is mainly determined by the Tm^{2+} excited-states dynamics. [1,2] Such dynamics has been studied intensely for $CsCaX_3:Tm^{2+}$ (X = Cl, Br,

I) ternary systems [4,5,6], but only once for some calcium dihalides [7]. No QE values were reported in these works. In our previous study on NaX:Tm^{2+} (X = Cl, Br, I) monohalides [8] we investigated the excited-states dynamics and measured the QE, but we were unable to provide a full quantitative description of important processes such as: the quenching mechanism related to the lowest energy $4f^{12}5d^1 \rightarrow 4f^{13}$ emission, the presence of the $4f^{13} \rightarrow 4f^{13}$ emission at 20 K, and the efficient non-radiative $4f^{12}5d^1 \rightarrow 4f^{13}$ ground state route. We have therefore decided to extend our Tm^{2+} excited-states dynamics study to CaX_2:Tm^{2+} (X = Cl, Br, I), where the substitution of Tm^{2+} on Ca^{2+}-sites required no charge compensation. Albeit, CaI_2 appears to be strongly hygroscopic. [9] We will make use of temperature- and time-resolved experiments; and a more quantitative approach using a numerical rate equation analysis. First, the excitation bands and emissions are classified. Subsequently, a qualitative description of the excited-states dynamics is provided for all three materials, followed by a quantitative modelling on $CaBr_2$:Tm^{2+} of time- and temperature-dependent $4f^{12}5d^1 \rightarrow 4f^{13}$ and $4f^{13} \rightarrow 4f^{13}$ intensities and finally an overall discussion is provided focusing on the recorded QE-values.

3.2. Experimental Section

3.2.1 Powder Synthesis and Preparation

The $CaCl_2$:Tm^{2+}, $CaBr_2$:Tm^{2+} and CaI_2:Tm^{2+} powder samples were respectively prepared by mixing $CaCl_2$, $CaBr_2$ and CaI_2 (Alfa Aeser, 99.99%) with 1.0-2.0 mol % TmI_2. The mixtures were ground into a homogeneous powder and inserted into quartz ampoules, which were then attached to a vacuum/inert gas system. After evacuation to 10^{-1} mbar and three succeeding purges with dry nitrogen, the ampoules were evacuated further to 10^{-3} mbar. Subsequently, the powders were heated using four Tecla burners. After 0.5-1 minute the powders had completely molten and the heating was stopped. The solidified samples were removed from the ampoules and ground into a fine powder sample. All handlings were performed under strictly inert and dry conditions in a glovebox (MBraun, Garching, Germany).

3.2.2 Analytical Characterisations

The Tm concentration in the samples was determined by means of Inductively Coupled Plasma–Optically Enhanced Spectroscopy (ICP-OES) measurements, using a Perkin Elmer Optima 4300DV spectrometer (Perkin Elmer, Waltham Massachusetts, USA). Diluted standards of Ca and Tm were used to constitute an intensity-concentration calibration line. The obtained values are reported in table 3.1. Differences with the nominal TmI_2 doping can largely be attributed to the accuracy of the used balance.

Diffuse reflectance spectra were recorded with a Bruker Vertex V80 spectrometer (Bruker, Karlsruhe, Germany), where the determined Kubelka-Munk (K-M) absorption was used to estimate the Tm^{2+}/Tm^{3+} ratio present in the samples. This ratio is derived from the integrated absorption bands of the Tm^{2+} $^2F_{7/2}\rightarrow{}^2F_{5/2}$ and the Tm^{3+} $^3H_6\rightarrow{}^3H_5$ transitions, in combination with their relative absorption strengths in NaI, that respectively amount to 1 and 3.4. These latter values were determined from the integrated absorption band values of purely doped Tm^{2+} and Tm^{3+} NaI samples combined with their ICP-OES Tm concentrations. The K-M spectra of the samples are provided in figure 3.1 and the retrieved Tm^{2+}/Tm^{3+} ratios are listed in table 3.1.

The X-ray diffraction patterns of the powders were obtained with a Philips X'pert-Pro diffractometer (Philips, Eindhoven, The Netherlands) in Bragg-Brentano geometry using CuK_α radiation. The measurements took place at room temperature from 8° to 80° 2-theta with a 0.008° resolution. Figure 3.2 shows the diffractograms. The crystallographic structures imply that the Tm^{2+} dopant ions that occupy Ca^{2+} sites have a (distorted) octahedral coordination leading to a lower 5d-triplet t-state and upper 5d-doublet e-state that are further split due to the octahedral distortion. Throughout this work we will use the short hand notation ($^{2S+1}L_J$,t_{2g})S to assign the excited $4f^{12}5d^1$-levels, where $^{2S+1}L_J$ represents the state of $4f^{12}$, t_{2g} denotes that the 5d-electron is in a level and stemming from the

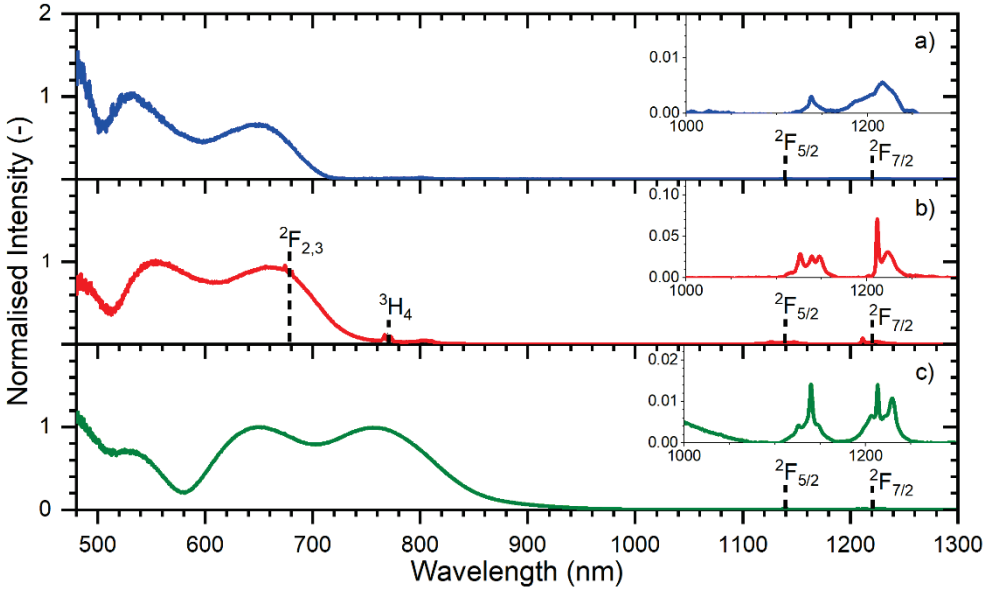

Figure 3.1: The Kubelka-Munk absorption spectra of: a) $CaCl_2$:Tm^{2+}, b) $CaBr_2$:Tm^{2+}, and c) CaI_2:Tm^{2+} as normalised on the ($^3H_6$,t_{2g}) absorption band of Tm^{2+}. The related Tm^{3+} absorption peaks and the Tm^{2+} absorption bands and peaks are indicated by their levels. The measurements were performed using a Bruker Vertex 80v with Si and InGaAs photodiode detectors and a Pike Optics EasiDiff diffuse reflectance tool.

t-triplet, and S denotes the total electron spin of the excited state.

Fluorescence quantum yield measurements were performed using an Edinburgh FLS980 spectrometer (Edinburgh Instruments, Livingston, UK) with an integrating sphere, a 450 W Xenon arc lamp and a Hamamatsu C9940-02 near infrared (NIR) PhotoMultiplier Tube (PMT) (Hamamatsu Photonics, Hamamatsu, Japan). The $CaX_2:Tm^{2+}$ (X = Cl, Br, I) samples were excited into the Tm^{2+} $({}^3H_6,t_{2g})_{S=1/2}$ level at room temperature and the reflectance was measured and compared to that of highly reflecting $BaSO_4$ and their undoped hosts. The absorption contributions of the CaX_2 (X = Cl, Br, I) hosts were respectively estimated at 4, 2 and 4%. From the amount of emitted and host-corrected absorbed photons, QE values were calculated and also added to table 3.1.

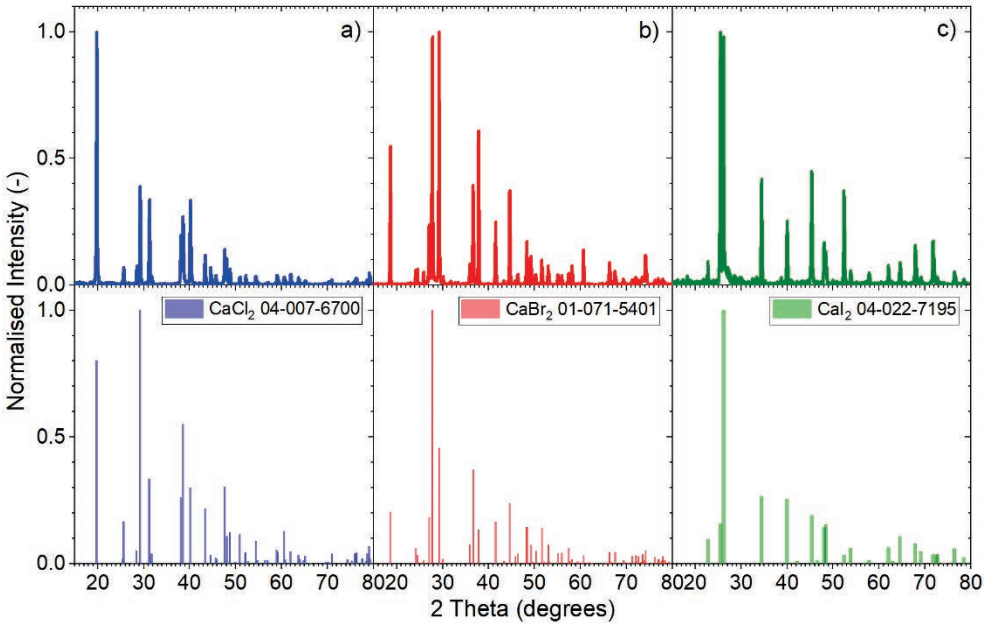

Figure 3.2: The X-ray diffraction spectra of: a) $CaCl_2:Tm^{2+}$, b) $CaBr_2:Tm^{2+}$, and c) $CaI_2:Tm^{2+}$ as normalised on the main diffraction peak. The related reference patterns are plotted below the spectra and are classified in accordance to the Highscore expert Pro Database. The measurements were performed using an X'pert-Pro X-ray diffractometer that operated at 45kV and 40mA. In addition, the generated x-rays had a wavelength of 1.5419nm and diffraction angles amounted to 15-80 degrees 2-theta.

Pattern References

$CaCl_2$	04-007-6700	Lasocha W., Lasocha A., Eick H.A., J. Solid State Chem., 87, 64, (1990)
$CaBr_2$	01-071-5401	Anselment, B., Phase Transitions, 38, 127, (1992)
CaI_2	04-022-7195	Hadenfeldt C., Z. Naturforsch., B: Anorg. Chem., Org. Chem., 30, 165, (1975)

Table 3.1: Summary of the analytical sample characterisations.

Sample	mol % TmI_2 [a]	mol % Tm ICP-OES	Tm^{2+}/Tm^{3+} ratio [b]	mol % Tm^{2+} [c]	Crystal phase	$\hbar\omega_{max}$ cm^{-1}	Host-corrected absorption % [d]	QE % [d]
$CaCl_2:Tm^{2+}$	2.0	1.6	0.5 : 0.5	0.8	*Pnnm*	270 [10]	45 ± 2 [d]	25 ± 2 [d]
$CaBr_2:Tm^{2+}$	2.0	1.5	0.8 : 0.2	1.2	*Pnnm*	160 [11]	53 ± 2 [e]	27 ± 2 [e]
$CaI_2:Tm^{2+}$	1.0	1.2	0.7 : 0.3	0.8	*P-3m1*	120 [12]	44 ± 2 [f]	28 ± 2 [f]

[a] nominal doping [b] from K-M absorption spectra [c] calculated from ICP-OES and K-M absorption spectra

[d] λ_{exc} = 645 nm $\{(^3H_6,t_{2g})_{S=1/2}\}$ [e] λ_{exc} = 665 nm $\{(^3H_6,t_{2g})_{S=1/2}\}$ [f] λ_{exc} = 760 nm $\{(^3H_6,t_{2g})_{S=1/2}\}$

3.2.3 Temperature-Dependent Measurements

The temperature dependent emission and excitation spectra were obtained by using a Xenon lamp coupled to a double monochromator with three gratings and a Hamamatsu C9100-13 EM-CCD or H1033A-75 NIR-PMT that was attached to a single monochromator with three gratings to record the luminescence emerging from the samples. A calibrated EPLAB NBS 1000W Quartz Iodine lamp was used to acquire the wavelength dependent sensitivity of the detectors. The detection ranges of 400-1150 nm and 950-1600 nm for CCD and NIR-PMT, respectively, share an overlap that allows it to couple the output of both detectors and hence accurately determine the $4f^{12}5d^1 \rightarrow 4f^{13}$ and $4f^{13} \rightarrow 4f^{13}$ emission ratios over temperature. Since the Tm^{2+} $^2F_{7/2} \rightarrow {}^2F_{5/2}$ emission lies too close to the detection limit of the CCD detector, a small spatula amount of $Ca_2Si_5N_8:Yb^{3+}$ was added to the samples. After exciting the Yb^{3+} at 360 nm, the $^2F_{5/2} \rightarrow {}^2F_{7/2}$ emission at 985 nm was observed and used for the detector coupling. With the applied Tm^{2+} excitation wavelengths ($(^3H_6,t_{2g})_{S=1/2}$-level), there is no overlap with any of the $Ca_2Si_5N_8:Yb^{3+}$ excitation levels and hence only Tm^{2+} luminescence is observed. [13] Time resolved measurements were done with a tuneable EKSPLA NT230 laser (EKSPLA, Vilnius, Lithuania) that has a 7 ns pulse duration. DT5724F (0-2 ms) or DT5730 (0-40 ms) CAEN digitisers (CAEN, Viareggio, Italy) measured the signal from a H1033A-75 NIR-PMT or a Hamamatsu R7600U-20HV-800V PMT. The related decay curves were acquired by averaging over 1000 individual spectra. The samples were heated and cooled with an APD Cryogenic Helium cooler (APD Cryogenics, Allentown Pennsylvania, USA) and Lakeshore temperature controller (Lakeshore Cryotronics, Westerville Ohio, USA).

Special sample holders protected the hygroscopic samples, during all measurements, against moisture and oxidation reactions. Similar sample holders were described by Rogers et al. [14].

3.3. Results and Discussion

3.3.1 Assignment of Excitation Bands

Figure 3.3 shows the excitation spectra of $CaX_2:Tm^{2+}$ (X = Cl, Br, I) monitoring the Tm^{2+} $^2F_{5/2}\rightarrow{}^2F_{7/2}$ $4f^{13}\rightarrow4f^{13}$ emission, at different temperatures. For $CaCl_2:Tm^{2+}$ the spectra show much resemblance in shape to the earlier reported low temperature absorption spectra by Grimm et al. [7] and Karbowiak et al. [10]. Similarly, those of $CaI_2:Tm^{2+}$ are akin to the room temperature absorption spectrum of Ten Kate et al. [3]. The therein reported $4f^{12}5d^1$-level classifications are appended to the spectra in figure 3.3. The spectra display a clear separation of around 5700 cm^{-1} between the ($^3H_6$,t_{2g}) and ($^3F_4$,t_{2g}) levels, which follows from the $4f^{12}$-level splitting into $^{2S+1}L_J$ terms that are analogous to the Tm^{3+} multiplets of the Dieke diagram. [15] In case of $CaI_2:Tm^{2+}$, an additional weak excitation band is observed close to 860 nm. Upon applying a redshift of 12480 cm^{-1}, based on the works of Dorenbos [16], it follows that it represents a Spin-Forbidden (SF) transition to the ($^3H_6$,t_{2g})$_{S=3/2}$ High-Spin (HS) levels. For $CaBr_2:Yb^{2+}$, Larsen et al. [17] observed the lowest energy Low-Spin (LS) and HS 5d-levels at respectively 25133 and 23696 cm^{-1}. Using retrieved redshifts of 10797 and 10304 cm^{-1}, respectively, these levels should then lie near 673 and 740 nm for $CaBr_2:Tm^{2+}$. The spectra in figure 3.3b indeed show a broad excitation band located at around 675 nm, thus representing the Spin-Allowed (SA) transition to the ($^3H_6$,t_{2g})$_{S=1/2}$ LS levels. No band is observed near 740 nm in the excitation spectra of the $4f^{13}\rightarrow4f^{13}$ emission. Instead the expected ($^3H_6$,t_{2g}) HS band is well observed at low temperatures in the excitation spectra monitoring the HS 5d-emission itself, see figure 3.4. As the excitation spectra of the $4f^{13}\rightarrow4f^{13}$ transition only become intense at elevated temperatures, the HS band is likely hidden due to the broadening of the LS bands. This clearly seems to happen for $CaI_2:Tm^{2+}$ and might also be the case for $CaCl_2:Tm^{2+}$.

3.3.2 Classification of Emissions

In figure 3.5 the temperature dependent emission spectra of the three samples are displayed upon exciting into their ($^3F_4$,t_{2g}) levels. Up to four different Tm^{2+} emissions can be distinguished. These emissions are labelled R_{10} to R_{40} and their decay times and relative intensities are provided at 20 K or 300 K in table 3.2. For $CaCl_2:Tm^{2+}$, Grimm et al. [7] already identified the emissions in accordance to their transition. Since the energy of the Stokes shift is in first approximation the same for all lanthanides in a specific host, reported literature values from for instance $CaBr_2:Eu^{2+}$ and $CaI_2:Eu^{2+}$ can be added to our observed emissions in $CaBr_2:Tm^{2+}$ and $CaI_2:Tm^{2+}$ to establish a direct connection with the excitation bands in figure 3.3 and hence retrieve the transitions related to the emissions. Figure 3.6 serves as a schematic overview of all excitation bands and emissions.

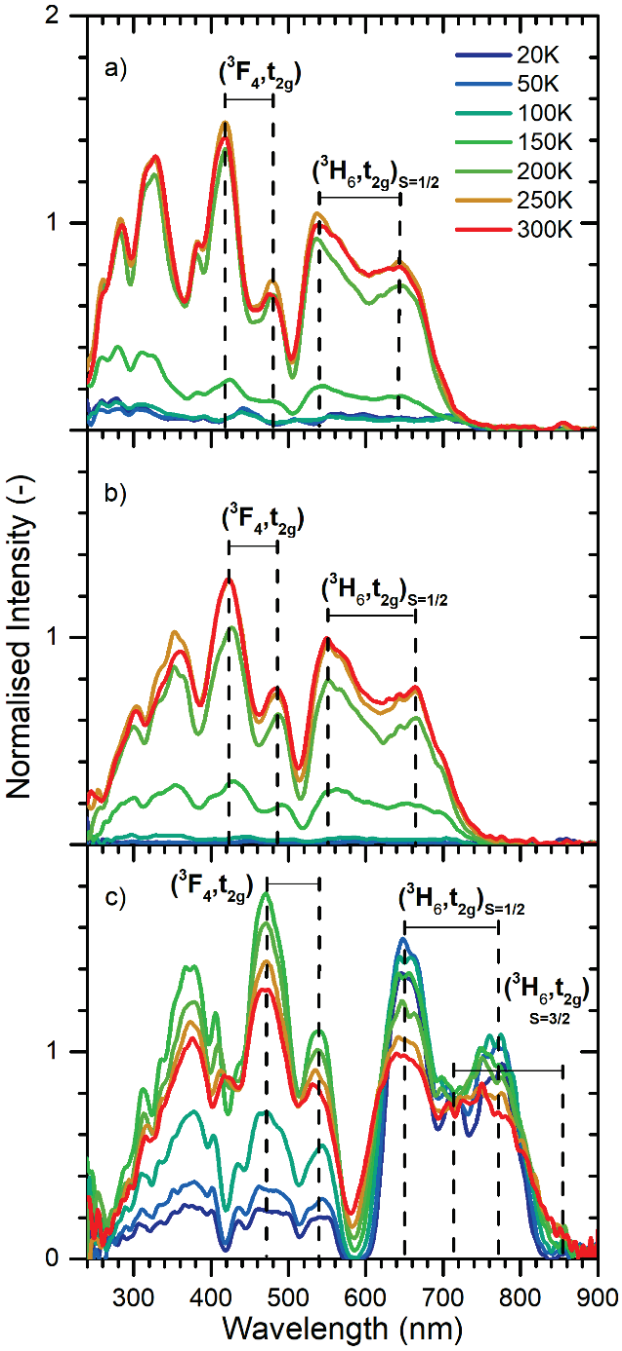

Figure 3.3: Normalised excitation spectra of: a) $CaCl_2:Tm^{2+}$, b) $CaBr_2:Tm^{2+}$ and c) $CaI_2:Tm^{2+}$ as acquired on the Tm^{2+} $^2F_{5/2}\rightarrow{}^2F_{7/2}$ $4f^{13}\rightarrow4f^{13}$ emission at 1140 nm and for different temperatures. The spectra are normalised on the LS $(^3H_6,t_{2g})_{S=1/2}$ band at 300 K.

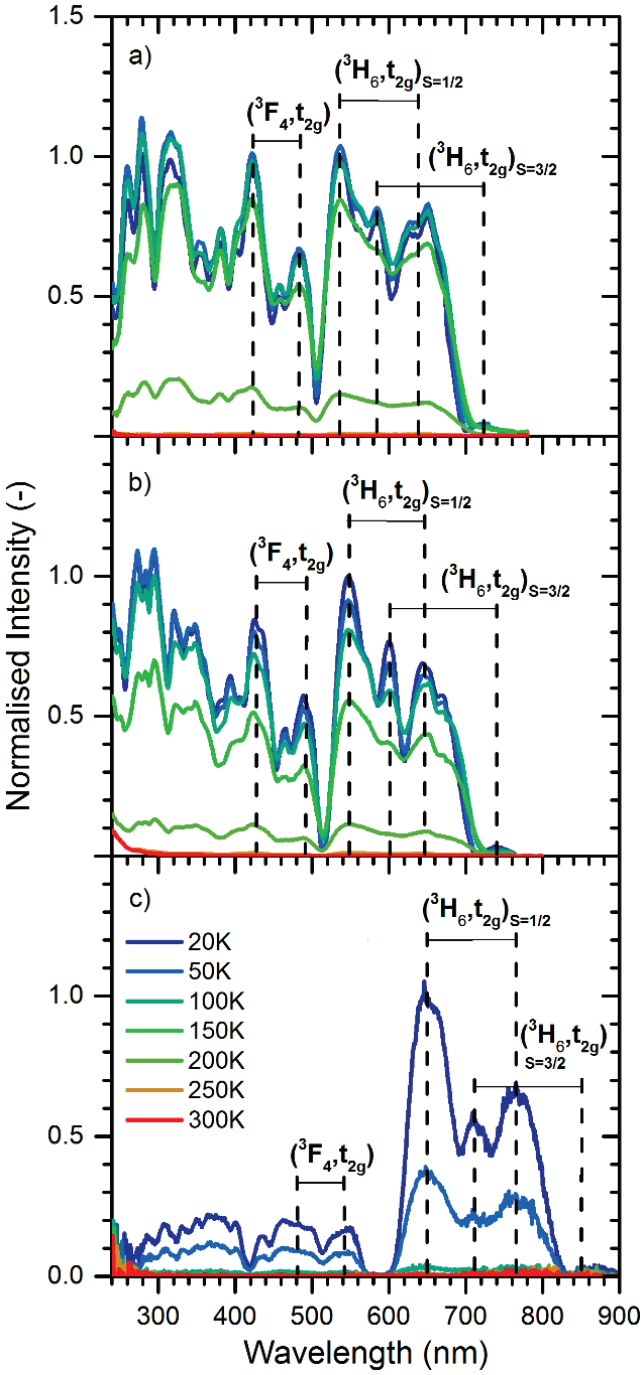

Figure 3.4: Normalised excitation spectra of: a) $CaCl_2:Tm^{2+}$, b) $CaBr_2:Tm^{2+}$ and c) $CaI_2:Tm^{2+}$ as acquired on the Tm^{2+} $(^3H_6,t_{2g})_{S=3/2} \rightarrow {}^2F_{7/2}$ $4f^{12}5d^1 \rightarrow 4f^{13}$ emission at different temperatures.

Table 3.2: Summary of observed Tm^{2+} emissions in CaX_2 (X = Cl, Br, I) after excitation into the $(^3F_4,t_{2g})$ levels.

Sample [-]	Emission [-]	Transition [-]	Wavelength (20K) [nm]	Energy (20K) [cm^{-1}]	Decay Time	Rel.Intgr.Int. (20K) [-]
$CaCl_2:Tm^{2+}$	R_{40}	$(^3F_4,t_{2g}) \rightarrow {}^2F_{7/2}$	508	19685	9 ns (20K)	1
	R_{20}	$(^3H_6,t_{2g})_{S=3/2} \rightarrow {}^2F_{7/2}$	801	12484	350 µs (20K)	3679
	R_{10}	$^2F_{5/2} \rightarrow {}^2F_{7/2}$	1138	8787	4.7 ms (300K)	82
$CaBr_2:Tm^{2+}$	R_{40}	$(^3F_4,t_{2g}) \rightarrow {}^2F_{7/2}$	526	19012	16 ns (20K)	1
	R_{20}	$(^3H_6,t_{2g})_{S=3/2} \rightarrow {}^2F_{7/2}$	815	12270	340 µs (20k)	399
	R_{10}	$^2F_{5/2} \rightarrow {}^2F_{7/2}$	1139	8780	4.3 ms (300K)	2
$CaI_2:Tm^{2+}$	R_{40}	$(^3F_4,t_{2g}) \rightarrow {}^2F_{7/2}$	596	16779	1.5 µs (20K)	933
	R_{30}	$(^3H_6,t_{2g})_{S=1/2} \rightarrow {}^2F_{7/2}$	883	11325	1.6 µs (20K)	1
	R_{20}	$(^3H_6,t_{2g})_{S=3/2} \rightarrow {}^2F_{7/2}$	978	10225	36 µs (20K)	37
	R_{10}	$^2F_{5/2} \rightarrow {}^2F_{7/2}$	1141	8764	3.6 ms (300K)	193

In case of $CaBr_2:Eu^{2+}$, the Stokes shift energy related to the SA $4f^6[^7F_0]5d^1 \rightarrow 4f^7[^8S_{7/2}]$ transition amounts to 1232 cm^{-1}. [17] When adding this value to the observed $4f^{12}5d^1 \rightarrow 4f^{13}$ emissions in $CaBr_2:Tm^{2+}$ a good match is found with the excitation bands in figure 3.3b. Emission R_{40} is found to stem from the $(^3F_4,t_{2g})$ band near 490 nm, relating it to the $(^3F_4,t_{2g}) \rightarrow {}^2F_{7/2}$ transition. It has a rather short decay time of 16 ns. Emission R_{20} corresponds to the HS $(^3H_6,t_{2g})$ level close to 740 nm, coupling it to the SF $(^3H_6,t_{2g})_{S=3/2} \rightarrow {}^2F_{7/2}$ transition. Applying the Stokes shift of 1885 cm^{-1} from $CaI_2:Eu^{2+}$ [18,19] onto $CaI_2:Tm^{2+}$, emission R_{30} can be coupled to the LS $(^3H_6,t_{2g})$ band at 770 nm and thus related to the $(^3H_6,t_{2g})_{S=1/2} \rightarrow {}^2F_{7/2}$ transition. Its SA nature is reflected in its order of magnitude shorter decay time compared to emission R_{20}. For $CaCl_2:Tm^{2+}$ and $CaBr_2:Tm^{2+}$, emission R_{30} seems absent. The energy of emission R_{10} perfectly matches the $^2F_{5/2} \rightarrow {}^2F_{7/2}$ transition. Its strongly forbidden nature is reflected in a relatively long decay time of a few milliseconds.

3.3.3 Qualitative Description of Temperature-Dependent Luminescence Behaviour

The temperature dependent emission spectra of the materials reveal that, upon exciting into the $(^3F_4,t_{2g})$ band at 20 K, all four Tm^{2+} emissions are present. For $CaCl_2:Tm^{2+}$ and $CaBr_2:Tm^{2+}$ emission R_{40} quenches at a very fast rate and is barely observed at 100 K. In case of $CaI_2:Tm^{2+}$ emission R_{40} survives longer and vanishes at 190 K. The energy gap between the lowest energy $(^3F_4,t_{2g})$ and highest energy $(^3H_6,t_{2g})$ LS levels in $CaX_2:Tm^{2+}$ (X = Cl, Br, I) respectively amounts to 2245, 2160 and 3310 cm^{-1} which comprises approximately 9, 14 and 28 vibrational quanta, see table 3.1. Assuming a small configurational offset between the two $4f^{12}5d^1(t_{2g})$-levels [20], the quenching W_{43} as illustrated in figure 3.6 most likely occurs via multi-phonon relaxation. The fast quenching of emission R_{40} leads to a feeding of the $(^3H_6,t_{2g})$ LS levels and in case of $CaI_2:Tm^{2+}$ the presence of emission R_{30}. With an energy gap of 1100 cm^{-1} (around 10 vibrational quanta) between the LS and HS levels, the emission will quench rapidly via multi-phonon relaxation W_{32}, as witnessed in the emission spectra

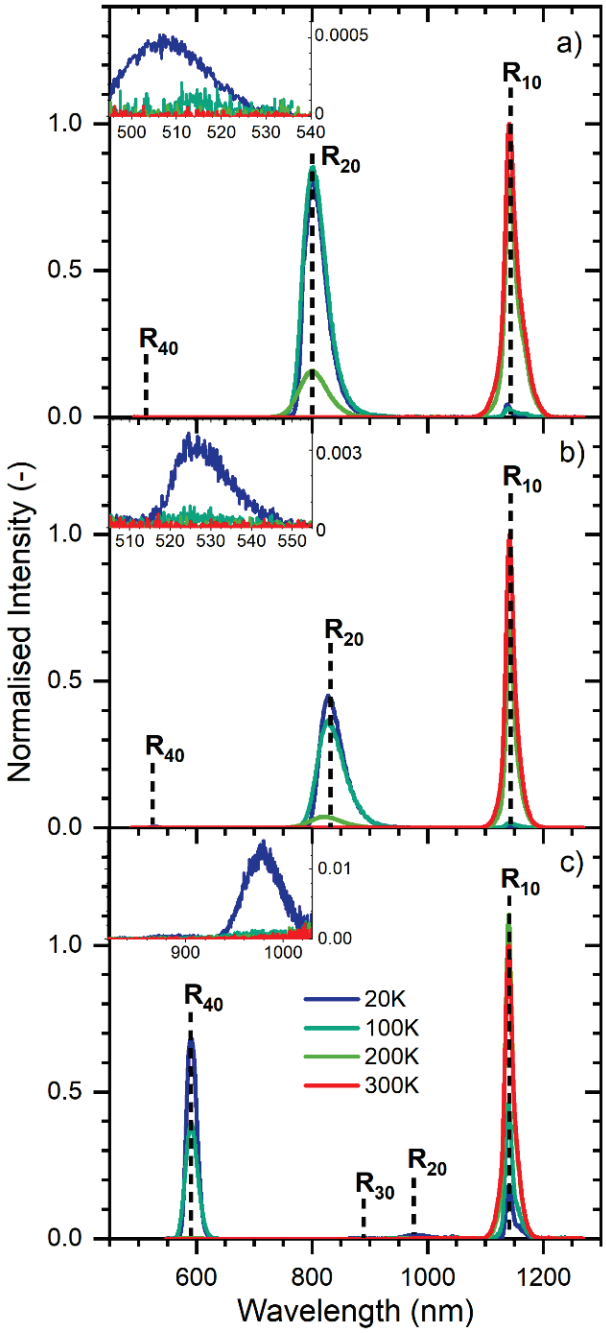

Figure 3.5: Normalised emission spectra of: a) $CaCl_2:Tm^{2+}$, b) $CaBr_2:Tm^{2+}$ and c) $CaI_2:Tm^{2+}$ at different temperatures and normalised on the Tm^{2+} $^2F_{5/2}\rightarrow{}^2F_{7/2}$ emission at 300 K. Photoexcitation occurred within the ($^3F_4$,t_{2g}) levels at respectively 480 nm, 490 nm and 535 nm.

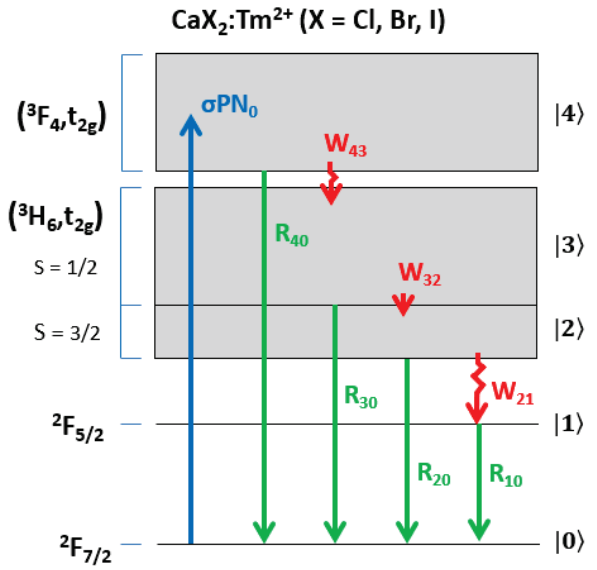

Figure 3.6: Schematic energy level diagram for $CaX_2:Tm^{2+}$ upon exciting into the ($^3F_4$,t_{2g}) levels (blue arrow). At 20 K up to four distinct Tm^{2+} emissions are be observed. These radiative transitions are indicated by the green straight arrows R_{ij}, while non-radiative quenching transitions W_{ij} are indicated by the red curly arrows. Here, index i refers to starting level and j the closing level.

at 100 K. For $CaCl_2:Tm^{2+}$ and $CaBr_2:Tm^{2+}$ no emission R_{30} is detected. This could be explained by a very rapid quenching via multi-phonon relaxation [19] or a LS→HS resonance energy transfer exciting a neighbouring Tm^{2+} ion to its ($^3H_6$,t_{2g}) HS levels [21], as described further in section 3.3.5. When subtracting the Stokes shift energies for $CaBr_2:Eu^{2+}$ from the lowest energy LS excitation bands of $CaBr_2:Tm^{2+}$ it follows that the energy of the ($^3H_6$,t_{2g}) LS emission is close to the ($^3H_6$,t_{2g}) HS absorption. The same is true for $CaCl_2:Tm^{2+}$. Both scenarios lead to a feeding of the ($^3H_6$,t_{2g}) HS levels from which emission R_{20} occurs. For $CaCl_2:Tm^{2+}$ and $CaBr_2:Tm^{2+}$ this $4f^{12}5d^1 \rightarrow 4f^{13}$ emission already has a strong presence at 20 K. It gradually becomes weaker as the temperature increases. The opposite behaviour is observed for $4f^{13} \rightarrow 4f^{13}$ emission R_{10} because of a non-radiative feeding process W_{21}. For both materials the $4f^{12}5d^1 \rightarrow 4f^{13}$ emission has fully quenched at respectively 270 K and 260 K and only $4f^{13} \rightarrow 4f^{13}$ emission R_{10} remains. For $CaI_2:Tm^{2+}$, emission R_{20} quenches at a significantly lower temperature of 110 K. It implies that within the temperature range of 110-190 K, only $4f^{12}5d^1 \rightarrow 4f^{13}$ emission R_{40} is present; the others already feeding the $^2F_{5/2}$ level and leading to $4f^{13} \rightarrow 4f^{13}$ emission R_{10}. This behaviour for $CaI_2:Tm^{2+}$ is especially noticeable upon comparing with the excitation spectra of $CaCl_2:Tm^{2+}$ and $CaBr_2:Tm^{2+}$ in figure 3.3. For these latter materials the relative intensity of the $4f^{12}5d^1$-excitation bands when monitoring the $^2F_{5/2} \rightarrow {}^2F_{7/2}$ emission, is the same for all temperatures. For $CaI_2:Tm^{2+}$ the higher energy $4f^{12}5d^1$-bands have a much lower intensity (because these result in

emission R_{40}) compared to the lower energy $4f^{12}5d^1$-bands that do result in $^2F_{5/2} \rightarrow {}^2F_{7/2}$ emission. From 190 K onwards all $4f^{12}5d^1 \rightarrow 4f^{13}$ emissions in $CaI_2:Tm^{2+}$ have quenched so that excitation into the different $4f^{12}5d^1$-bands all result in $4f^{13} \rightarrow 4f^{13}$ emission. The $4f^{12}5d^1$-bands are now dictated by the oscillator strength of the $4f^{13} \rightarrow 4f^{12}5d^1$ transitions, as is also observed in case of $CaCl_2:Tm^{2+}$ and $CaBr_2:Tm^{2+}$.

As the energy gap between the $(^3H_6,t_{2g})_{S=3/2}$ and $^2F_{5/2}$ levels for $CaCl_2:Tm^{2+}$, $CaBr_2:Tm^{2+}$ and $CaI_2:Tm^{2+}$ respectively amounts to 3700, 3500 and 1460 cm^{-1} or 14, 22 and 13 vibrational quanta, the quenching mechanism related to emission R_{20} can well be Multi-Phonon Relaxation (MPR). However, since it involves a $4f^{12}5d^1 \rightarrow 4f^{13}$ relaxation there is a large configurational offset and the optical phonon coupling strength, as defined by the Huang-Rhys factor, will be strong. The configurational offset could enable quenching via Interband Crossing (IC) or inter-configurational relaxation [3,22]. This quenching mechanism involves the configurational cross-over-point between the $(^3H_6,t_{2g})_{S=3/2}$ and $^2F_{5/2}$ levels, that can be breached at certain temperatures when enough energy becomes available. In case of a large Stokes shift, the crossing point is likely to be breached at a lower temperature. [23] In the next subsection, the two proposed quenching mechanisms of MPR and IC for emission R_{20} will be examined into more detail.

3.3.4 Quantitative Description of Temperature-Dependent Luminescence Behaviour

Since the quenching mechanism of $4f^{12}5d^1 \rightarrow 4f^{13}$ emission R_{20} remains unclear, we have decided to evaluate it by performing a luminescence rate equations analysis on $CaBr_2:Tm^{2+}$ involving all radiative and temperature-dependent non-radiative transitions after excitation into the $(^3H_6,t_{2g})$ LS band. With LS emission R_{30} not observed in $CaBr_2:Tm^{2+}$, we initially neglect its influence and assume the excitation will automatically end up in the lowest energy $(^3H_6,t_{2g})$ HS levels. The scheme portrayed in figure 3.6 then allows us to describe the excited state population N_i (i = 1,2) of the $^2F_{5/2}$ and $(^3H_6,t_{2g})_{S=3/2}$ levels, respectively, via the rate equations below.

$$\frac{dN_2(t)}{dt} = \sigma P N_o - N_2(t)\{R_{20} - W_{21}\}$$

$$\frac{dN_1(t)}{dt} = N_2(t)W_{21} - N_1(t)R_{10}$$

In this coupled set of equations, R_{20} and R_{10} represent the radiative transition rates in s^{-1}, W_{21} the non-radiative transition or quenching rate of emission R_{20} in s^{-1}, P portrays the laser power in $cm^{-1}\ s^{-1}$, σ the absorption cross section per wavelength of excitation energy in cm and N_0 the electron ground state population, which is in good approximation considered to be unaffected by the excitation.

Following the scenario that emission R_{20} quenches via multi-phonon relaxation, the non-radiative rate W_{21} can be described according to the Reisfeld model [25-27] that is provided below.

$$W_{21}(T) = W_p(0) \cdot \left\{1 - e^{\frac{-\hbar\omega_{max}}{kT}}\right\}^{-p}$$

In this relation: $\hbar\omega_{max}$ represents the maximum optical phonon energy in cm^{-1}, k the Boltzmann constant in $cm^{-1}\cdot K^{-1}$ and T the temperature in K. Furthermore, p embodies the number of phonons consumed during the relaxation: $p \cong \Delta E/\hbar\omega_{max}$ where ΔE is the energy gap in cm^{-1}. $W_p(0)$ is the multi-phonon decay rate at 0 K and is defined further via the following relation:

$$W_p(0) = W_0(0) \cdot e^{\frac{-\alpha\Delta E}{\hbar\omega max}} \quad \text{with:} \quad \alpha = \ln\left(\frac{p}{g}\right) - 1$$

Here, $W_0(0)$ is the decay rate at ΔE = 0 cm^{-1} and T = 0 K, and g the dimensionless electron-phonon coupling strength (Huang Rhys factor).

By considering the option of interband crossing, the non-radiative rate W_{21} follows the relation below [28,29], where s represents the frequency factor in s^{-1}, ε the activation energy of the quenching process in cm^{-1}, k the Boltzmann constant in $cm^{-1}\cdot K^{-1}$ and T the temperature in K.

$$W_{21}(T) = s \cdot e^{\left(\frac{-\varepsilon}{kT}\right)}$$

Especially at low temperatures the two expressions for the non-radiative rate W_{21} predict a different temperature dependence, which should allow us to draw conclusions on their contribution to the observed non-radiative relaxation.

Model Setting

The fitting of our rate equation model and related quenching mechanisms to the temperature- and time-dependent intensity data, requires a set of starting values for the different parameters. The pump rate constant σPN_0 can be chosen arbitrary and is set at 1, where upon exciting into level $|3\rangle$ we assume a rapid quenching towards level $|2\rangle$ from which we monitor emission R_{20}. The radiative rates R_{10} and R_{20} were estimated based on the luminescence lifetime of the emissions at respectively 20 and 30 K, assuming no quenching takes place at these temperatures.

For CaX_2:Tm (X = Cl, Br, I) no direct values for the phonon energies $\hbar\omega_{max}$ coupling to Tm^{2+} are reported in literature. We have therefore decided to estimate these values based on known studies that involve such hosts, see table 3.1. [10-12] The values are close to those

reported for LaY_3 (Y = Cl, Br). [25] The energy gap ΔE between levels $|2\rangle$ and $|1\rangle$ was determined on 3500 cm^{-1} and the required amount of vibrational quanta p to bridge it is around 22. A reasonable starting value for the $W_0(0)$ parameter was estimated from literature to be $1 \cdot 10^{14}$ s^{-1}. [25,26] Since not much is known on the electron-phonon coupling strength g between $4f^{12}5d^1$- and $4f^{13}$-states, the rough starting value of 2 was used from the numerical modelling work of Grimm et al. [6]. The parameters constitute an overall $W_p(0)$ parameter of 18.7 s^{-1}. As an overall fitting strategy $\hbar\omega_{max}$ and $W_p(0)$ are fitted, while ΔE was kept fixed. In the case of IC, the thermal activation energy ε was approximated at 1694 cm^{-1} and retrieved from an Arrhenius plot of the integrated luminescence intensity of R_{20}, see figure 3.14 in Appendix A. From this Arrhenius plot the pre-exponential factor A was also determined and multiplied by R_{20} to obtain the frequency factor s of $1 \cdot 10^9$ s^{-1}. Both values are fitted to the data. All used starting values are listed in table 3.3.

Table 3.3: List of inserted starting parameters and obtained values from the steady state (st.st.) and non-steady state (non.st.st.) fitting on $CaBr_2:Tm^{2+}$. Also listed are the values related to the st.st. fitting of $CaCl_2:Tm^{2+}$ along with R^2-values that signify the accuracy of the fits.

Parameter	Start. Values $CaBr_2:Tm^{2+}$	Non.St.St Values $CaBr_2:Tm^{2+}$	St.St Values $CaBr_2:Tm^{2+}$	Start. Values $CaCl_2:Tm^{2+}$	St.St Values $CaCl_2:Tm^{2+}$
σPN_0 [s^{-1}]	1	-	-	1	-
R_{10} [s^{-1}]	187	-	-	212	-
R_{20} [s^{-1}]	2952	-	-	2857	-
$\hbar\omega_{max}$ [cm^{-1}]	160	197	191	270	195
ΔE [cm^{-1}]	3500	-	-	3700	-
$W_p(0)$ [s^{-1}]	52.4	30.9	72.53	235	22.0
k [$cm^{-1} \cdot K^{-1}$]	0.695	-	-	0.695	-
s	$2 \cdot 10^9$	$1.20 \cdot 10^9$	$1.97 \cdot 10^9$	$1 \cdot 10^9$	$1 \cdot 10^{10}$
ε [cm^{-1}]	1694	1685	1785	2549	2010
R^2-value	-	0.9957	0.9991	-	0.9989

Non-Steady State Rate Equation Analysis

The derived rate-equations can be solved in a non-steady-state manner, assuming a time-dependent depopulation of the levels, with solutions provided in Appendix B. The solution for level $|2\rangle$ was fitted onto the measured luminescence lifetime curves of $4f^{12}5d^1 \rightarrow 4f^{13}$ emission R_{20}. The related fits are displayed in figure 3.7, where from 300 K onwards the now weak emission is only faintly recorded. From each of the fit a value for W_{21} was obtained, allowing us to establish a $W_{21}(T)$ point series onto which the two quenching models can be tested.

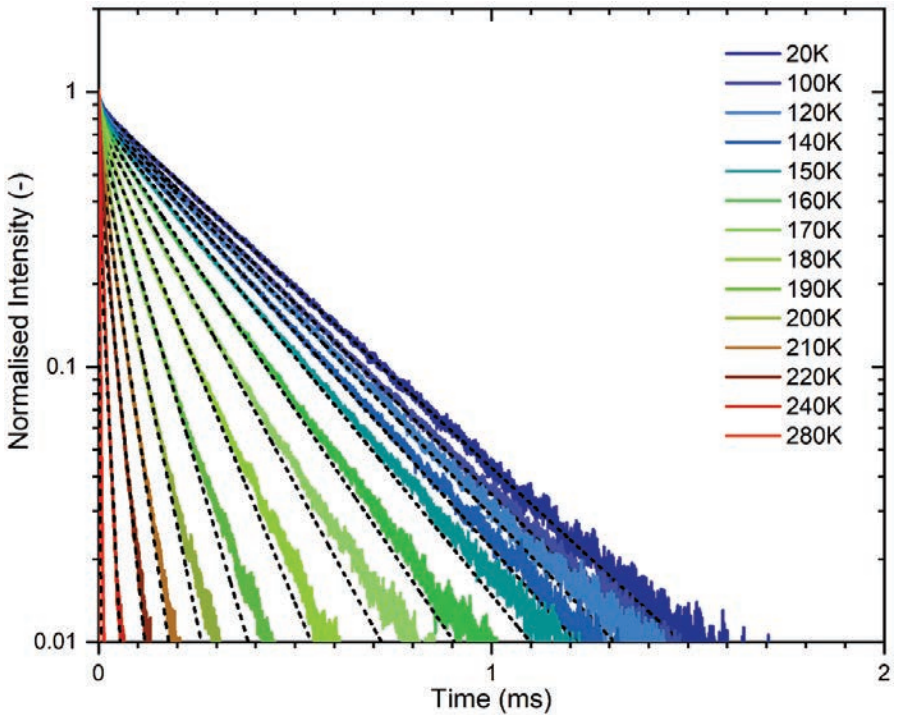

Figure 3.7: Normalised luminescence lifetime curves of $4f^{12}5d^1 \rightarrow 4f^{13}$ emission R_{20} plotted at various temperatures. The dashed lines represent the single exponential fits based on our rate equations from which $W_{21}(T)$ values were obtained.

Figure 3.8 shows this series as represented in black, where small error bars of 0.1-5%, based on the fitting, are attached. The MPR model, shown in solid dark red, is able to reproduce the low-temperature trend among the W_{21} points. Yet, at high temperatures it is unable to mimic this and overall no accurate fit could be obtained. For IC, illustrated in solid orange, it is the other way around: an inaccurate representation at low temperature and a good depiction at high temperatures. Once more, the fit proved to be inaccurate. Based on these findings, the combined quenching via both MPR and IC was investigated. This option, as portrayed in blue, was able to provide a reasonable fit for both the low and high temperature range. The herewith obtained fitting parameters are added to table 3.3 and are close to our initial starting values; all within the same order of magnitude. For the combined quenching, the overall temperature development of MPR and IC are respectively portrayed in dashed red and dashed orange. The curves reveal that the low temperature regime is governed by MPR, whereas IC is dominant within the high temperature range. Furthermore, at around 170 K the non-radiative rate W_{21} becomes stronger than the radiative rate R_{20}, shown in dotted black, indicating that the quenching takes the upper hand.

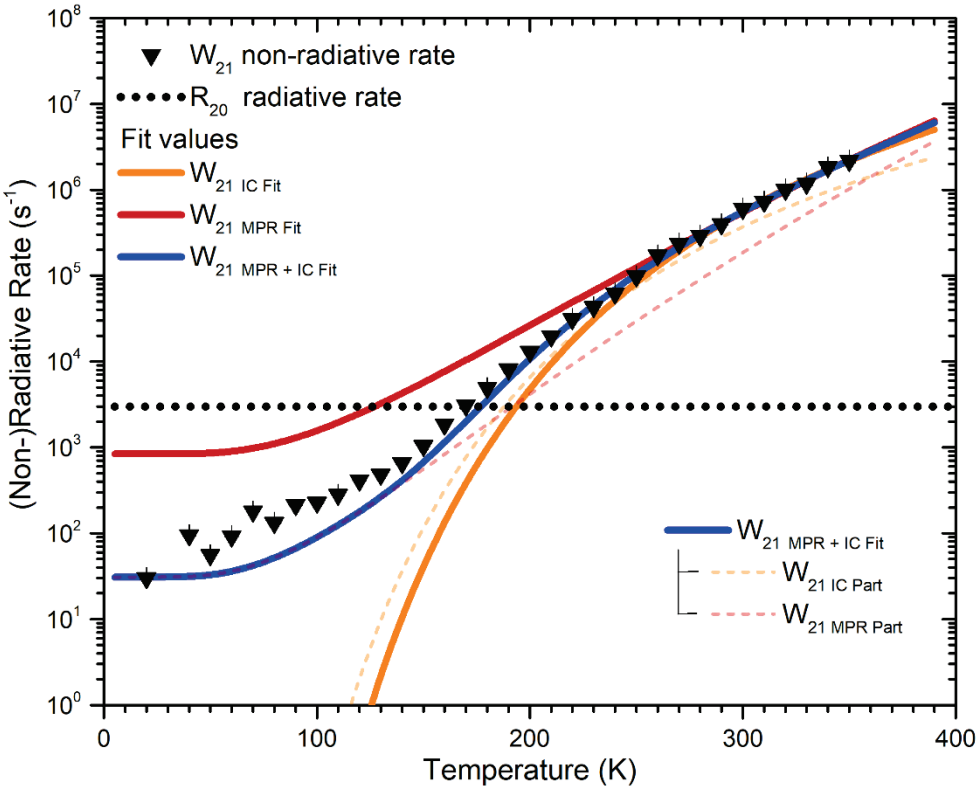

Figure 3.8: The obtained W_{21} values from figure 3.7 plotted as black triangular points versus temperature. The fit based on purely MPR is shown in solid dark red, whereas that of IC is displayed in solid orange. The fit of the combined quenching (MPR + IC) is illustrated in blue with constituents MPR and IC respectively portrayed in dashed red and orange. The dotted black line shows the R_{20} radiative rate.

Steady State Rate Equation Analysis

The previously outlined set of coupled rate equations can also be solved in a steady state fashion, where a steady depopulation of the levels is assumed. As elaborated in Appendix B, the solutions combined with the radiative rates can be used for fitting luminescence intensity curves. Figure 3.9 shows such curves for emissions R_{20} and R_{10} in $CaX_2:Tm^{2+}$ (X = Cl, Br, I) as a function of temperature, where the luminescence intensities of both emissions were corrected for the sensitivity of detection and coupled via the method described in section 3.2.3. The data was normalised on the measured QE values of emission R_{10} at room temperature, see table 3.1. For $CaBr_2:Tm^{2+}$, provided in panel b, the observed trends among the solid measured intensity data points are supported by those of the integrated luminescence lifetime curves from figure 3.7, displayed as open symbols. The light blue line shows a good fit for our combined quenching model (MPR + IC) onto the data points of emission R_{20}. The retrieved fitting parameters are appended to table 3.3 and are very close

to both our original starting values and those obtained from the non-steady state fitting. When inserting these fitted parameter values in the rate equation solution for level N_1 (note that the fits were done on level N_2), the dotted red line is acquired which follows the overall data trend, but is shifted by 10 K towards lower temperature. Our fitted model predicts a lower temperature and intensity for the intersection point between the R_{20} and R_{10} curves. Furthermore, at 250 K the fitted model reaches an intensity plateau while for the experimental data it is reached at a higher temperature.

The similarity between the luminescence intensity curves of $CaBr_2:Tm^{2+}$ and $CaCl_2:Tm^{2+}$ has incited us to extend the fitting of our model onto the latter. Starting values for this fitting are also provided in table 3.3. The light blue line in figure 3.9a again shows the fit of our model onto the data points of emission R_{20}. It clearly follows the trends among the data points and the obtained fitting parameters, appended to table 3.3, are reasonably close to their starting values. The dashed dark red line, as based on inserting the obtained fitting parameters into the rate equation solution for N_1, is not able to perfectly mirror the measured intensity trends in emission R_{10}. Especially at temperatures below 100 K, where $4f^{13} \rightarrow 4f^{13}$ emission R_{10} is measured but not simulated by our model, and above 200 K, where the measured intensity is much lower than predicted.

From figure 3.9c, it follows that for $CaI_2:Tm^{2+}$ the quenching of emission R_{20} is too strong for performing a fitting analysis with our model. Panel d shows that this is due to a large value of W_{21} compared to W_{32} as explained at the end of section 3.3.3.

The obtained steady-state fitting parameters for $CaBr_2:Tm^{2+}$ and $CaCl_2:Tm^{2+}$, allow it to plot the non-radiative rate W_{21} over temperature and inspect the development of the MPR and IC processes. Figure 3.10 shows these plots with colour coding in analogy to figure 3.8. For both materials the low temperature region is governed by MPR, while at high temperatures IC is dominant in $CaCl_2:Tm^{2+}$ (panel a). In case of $CaBr_2:Tm^{2+}$ (panel b), the MPR process stays strongest at even high temperatures; which differs from figure 3.8. Nevertheless both processes seems clearly involved in the quenching. For $CaBr_2:Tm^{2+}$, the non-radiative rate W_{21} outmatches the radiative rate R_{20} at around 160 K and the quenching prevails. For $CaCl_2:Tm^{2+}$ this seems to happen at a slightly higher temperature.

Figure 3.9 (Next Page): Plots of integrated emission intensity of $4f^{12}5d^1 \rightarrow 4f^{13}$ emission R_{20} (solid blue) and $4f^{13} \rightarrow 4f^{13}$ emission R_{10} (solid red) versus temperature for: a) $CaCl_2:Tm^{2+}$, b) $CaBr_2:Tm^{2+}$ and c) $CaI_2:Tm^{2+}$ upon excitation into $(^3H_6,t_{2g})$ LS levels. For $CaBr_2:Tm^{2+}$ the open symbols correspond to the integrated lifetime curves of emissions R_{20} and R_{10} revealing much equivalent trends. For $CaCl_2:Tm^{2+}$ and $CaBr_2:Tm^{2+}$, the light blue lines represent the steady state fits onto emission R_{20} with related plots of R_{10} displayed as dashed dark red lines. .For $CaI_2:Tm^{2+}$ the data of emission R_{30} is portrayed in orange. Panel d) shows similar data upon exciting into the $(^3F_4,t_{2g})$ levels with emission R_{40} displayed in green.

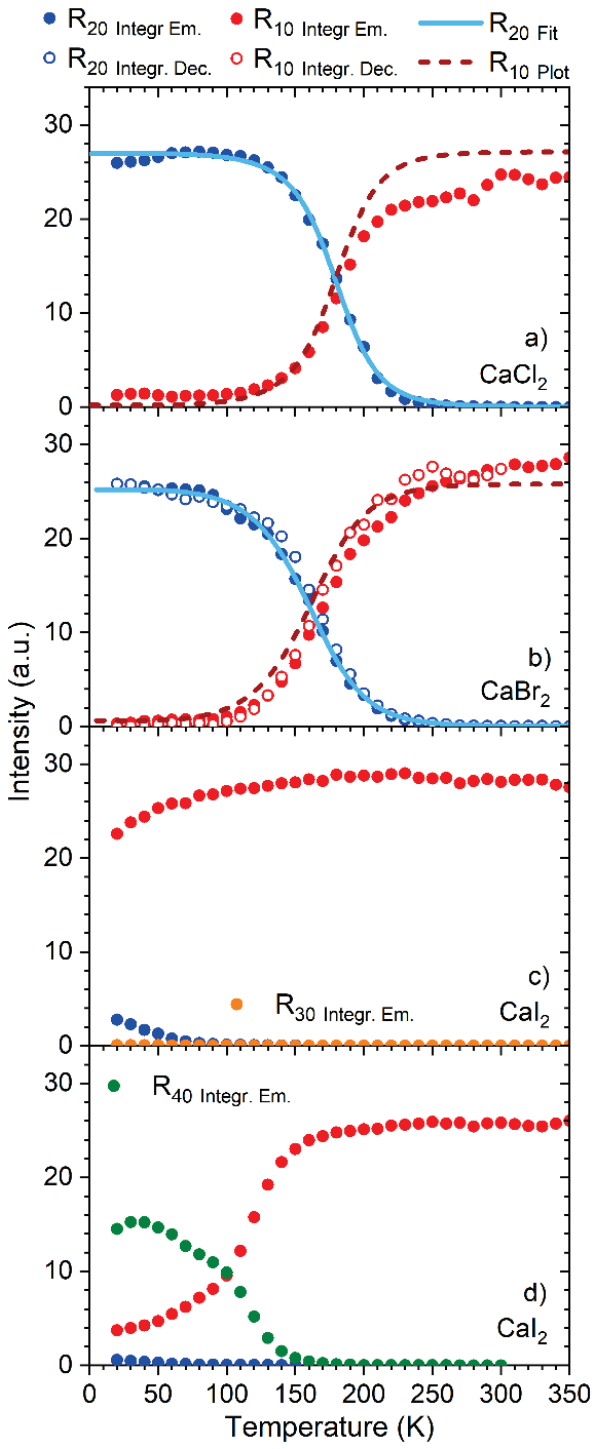
R20 Integr Em.
R10 Integr Em.
R20 Fit
R20 Integr. Dec.
R10 Integr. Dec.
R10 Plot
a)
CaCl2
b)
CaBr2
c)
CaI2
R30 Integr. Em.
d)
CaI2
R40 Integr. Em.
Intensity (a.u.)
Temperature (K)
0
10
20
30
50
100
150
200
250
300
350

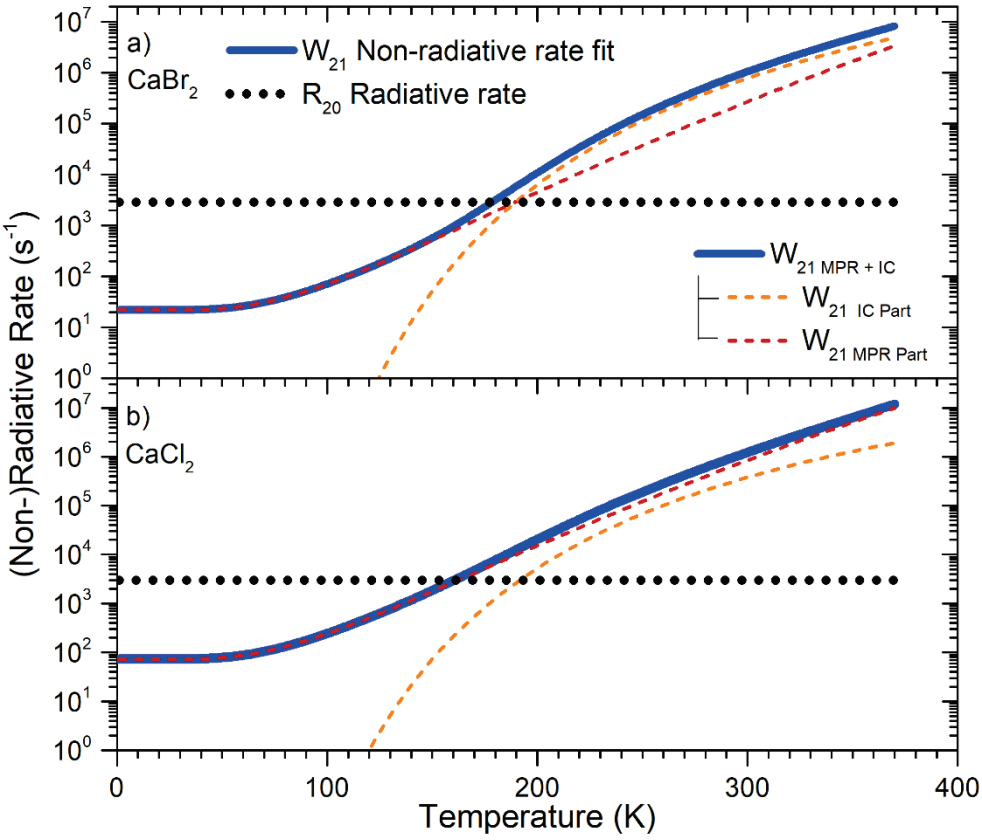

Figure 3.10: The obtained W_{21} parameters of a) $CaCl_2:Tm^{2+}$ and b) $CaBr_2:Tm^{2+}$ plotted in blue and versus temperature. The dark red and orange dashed lines respectively reveal the MPR and IC constituents, while the dotted black line shows the R_{20} radiative rate.

3.3.5 Model Limitations

The quenching of $4f^{12}5d^1 \rightarrow 4f^{13}$ emission R_{20} and intensification of $4f^{13} \rightarrow 4f^{13}$ emission R_{10} predicts the presence of a risetime phenomenon in the luminescence lifetime curves of the latter. Such a phenomena has been observed several times before in similar materials. [8,23] The solid curves in figure 3.11 reveal that also for $CaBr_2:Tm^{2+}$ a risetime is measured, even at 20 K. The curves predicted by our three-level combined quenching model (MPR + IC), using fitting parameters from table 3.3 column 3, are provided by the dashed curves. For temperatures above 200 K, the curves overlap well with the experimental data. At lower temperatures however, where the $4f^{13} \rightarrow 4f^{13}$ emission intensity is very weak, the risetime predicted by the model is longer than experimentally measured. This discrepancy arises from a limitation of our model that is discussed in the next subsection.

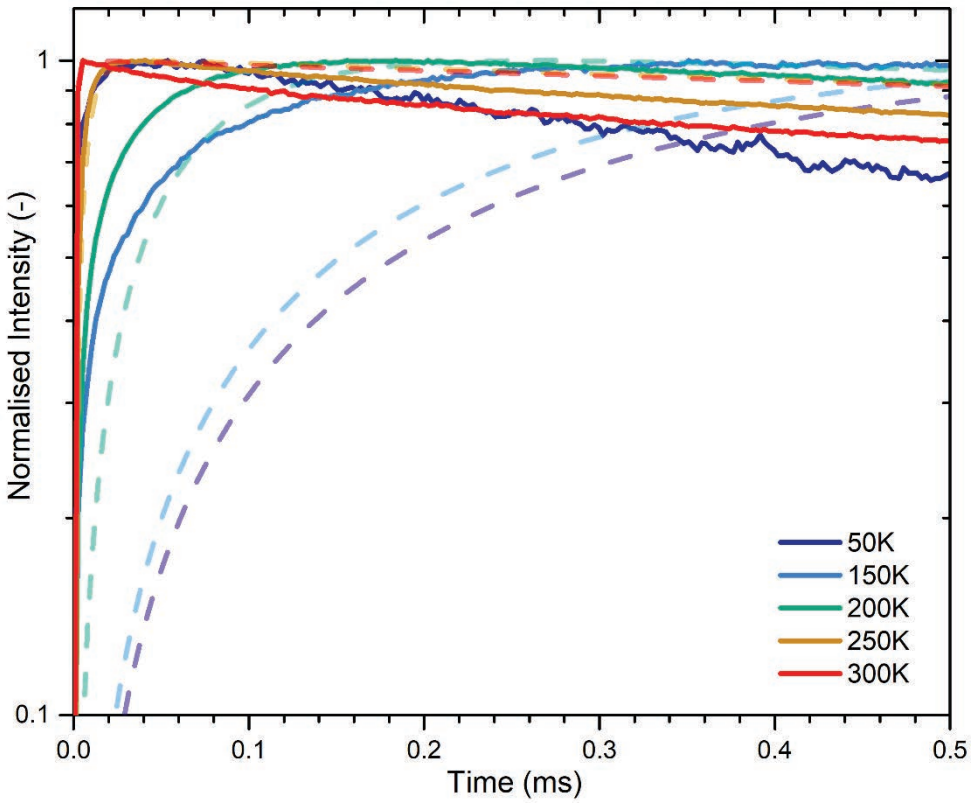

Figure 3.11: Normalised luminescence lifetime curves of $4f^{13} \rightarrow 4f^{13}$ emission R_{10} plotted at various temperatures, clearly displaying a risetime phenomenon. The solid curves represent experimental data, whereas the dashed transparent curves are plots based on our combined quenching model.

HS→LS Interaction and 4-Level Model

So far we have assumed that the population of the $4f^{12}5d^1$ ($^3H_6$,t_{2g}) LS state, immediately after excitation, is lost to the lower lying $4f^{12}5d^1$ ($^3H_6$,t_{2g}) HS state at all temperatures. It has allowed us to describe the feeding of $4f^{13} \rightarrow 4f^{13}$ luminescence by the $4f^{12}5d^1$ manifold and assign a combination of multi-phonon relaxation and interband crossing to such a temperature quenching process. However, it has been observed in various halides [5,30] that at low temperatures the LS-state population is significant and actually also the required time and/or temperature for LS→HS depopulation cannot be neglected. Here we present some evidence for LS→HS states interaction and discuss its influence on our model.

In figure 3.12 the lifetimes of the $4f^{12}5d^1 \rightarrow 4f^{13}$ ($^3H_6$,t_{2g}) HS emission (blue dots) are compared to the risetimes of the $4f^{13} \rightarrow 4f^{13}$ emission (red dots) for CaX_2:Tm^{2+} (X = Cl, Br, I). Both emissions are monitored after excitation into the $4f^{12}5d^1$ ($^3H_6$,t_{2g}) LS levels. The ($^3H_6$,t_{2g}) HS lifetimes were obtained via a single exponential fitting of the $4f^{12}5d^1 \rightarrow 4f^{13}$ decay curves,

whereas a similar fitting strategy on 0-1 ms timescale was used for retrieving the $4f^{13}\rightarrow4f^{13}$ risetimes. As is observed the lifetime of the ($^3H_6$,t_{2g}) HS emission behaves in a simple manner: at 20 K the lifetime τ_d amounts to ~300 µs (~30 µs for CaI_2:Tm^{2+}) and as the temperature increases it becomes shorter due to thermal quenching. This is well in-line with the measurements and modelling of its emission behaviour, see for instance figure 3.9. As discussed in previous sections, the quenching is due to a non-radiative feeding of the $4f^{13}$ $^2F_{5/2}$ level. As such, it is expected that the time scale related to the decay of the $4f^{12}5d^1\rightarrow4f^{13}$ HS emission is reflected in the risetime components of the $4f^{13}\rightarrow4f^{13}$ $^2F_{5/2}\rightarrow^2F_{7/2}$ emission. In case of CaI_2:Tm^{2+} this is observed at all temperatures. For $CaCl_2$:Tm^{2+} and $CaBr_2$:Tm^{2+} the risetime τ_r components of the $4f^{13}\rightarrow4f^{13}$ emission (red) are in good agreement with the $4f^{12}5d^1\rightarrow4f^{13}$ HS lifetimes τ_d (blue) only above ~150 K. Below 150 K the $4f^{13}\rightarrow4f^{13}$ risetimes deviate strongly from the $4f^{12}5d^1\rightarrow4f^{13}$ HS lifetimes. While the $4f^{12}5d^1$-$4f^{13}$ HS lifetimes are around ~300 µs, the τ_r rise-times behave in a non-monotonic manner: for example in $CaBr_2$:Tm^{2+} at 20-50 K τ_r is relatively short, in the order of a few microseconds; whereas between 50-150 K it increases up to ~100 µs. This behaviour of the $4f^{13}\rightarrow4f^{13}$ emission risetimes has been reported for $CsCaX_3$:Tm^{2+} (X = Cl, Br, I) [31] and is connected to the non-radiative relaxation from a LS to HS $4f^{12}5d^1$-state during the feeding of a $4f^{13}$ excited state. Applied to our case, the short risetimes at 10-50 K could then be due to a LS $4f^{12}5d^1\rightarrow4f^{13}$ non-radiative relaxation with strong electron-phonon coupling. The 50-150 K increase in τ_r is due to LS→HS thermally activated relaxation: partially populated HS and LS $4f^{12}5d^1$-states both feed the $^2F_{5/2}$ state.

The existence of $4f^{13}\rightarrow4f^{13}$ emission after excitation into $4f^{12}5d^1$ manifold already at 10 K points to multi-phonon channel as the only relaxation process not disabled at He-temperatures [25,29]. In various compounds, the onset of LS→HS non-radiative relaxation is related to the energy difference between LS and HS states, the optical phonon mode to which the relaxation couples and the phonon coupling strength [25,27,29]. For the former two parameters (host phonon modes, $h\omega_{LO}$, and LS-HS energy separation, $E_{HS\text{-}LS}$) the values can be obtained from literature. We have decided to check the relation between LS-HS populations with risetime behaviour for various compounds known from literature. Figure 3.13 reveals that there is a trend between the energy difference between the LS and HS states, in number of required phonons, and the T_{50} temperature quenching onset related to the $4f^{12}5d^1$ LS-depopulation. The dependence has a huge uncertainty and deviation due to unknown phonon coupling strengths, but still we can expect that in our $CaCl_2$:Tm^{2+} and $CaBr_2$:Tm^{2+} compounds the LS $4f^{12}5d^1$-state actively loses population at around 100-150 K, which is consistent with the observations in risetime kinetics in figure 3.12.

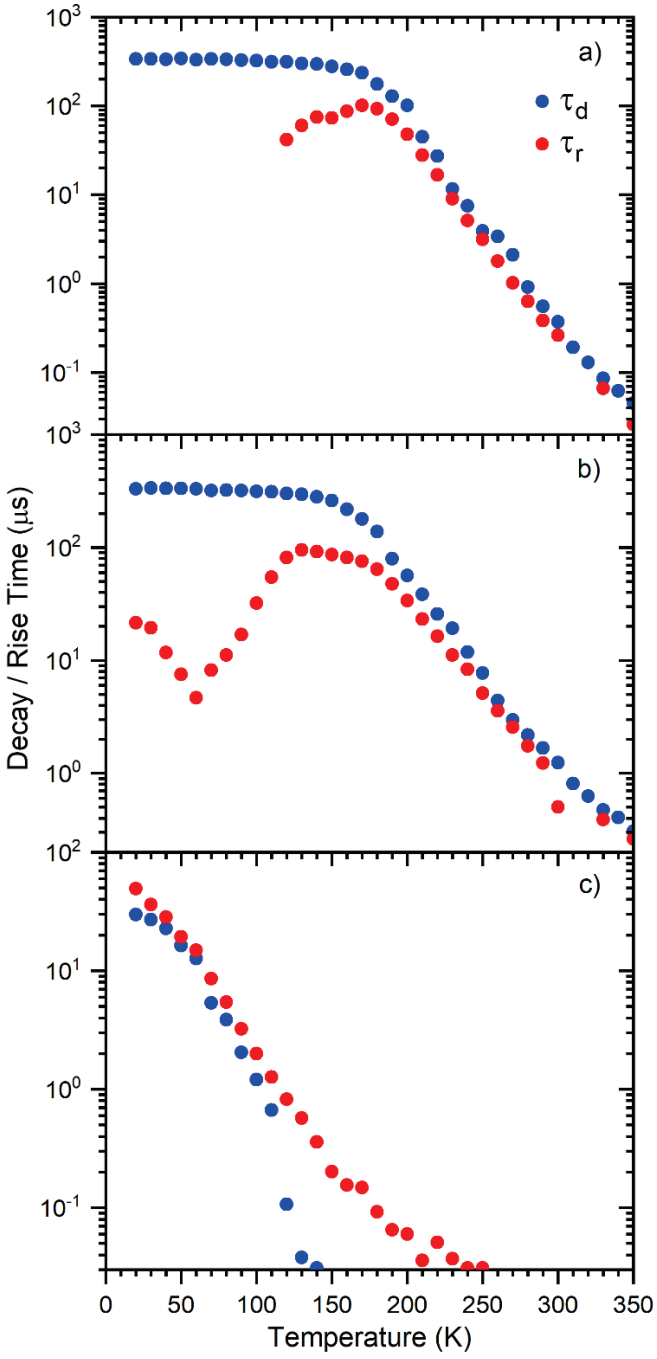

Figure 3.12: Temperature dependence of the lifetime (τ_d) related to the $4f^{12}5d^1 \rightarrow 4f^{13}$ ($^3H_6$,t_{2g}) HS emission and risetime (τ_r) of the $4f^{13} \rightarrow 4f^{13}$ emission in: a) $CaCl_2:Tm^{2+}$, b) $CaBr_2:Tm^{2+}$ and c) $CaI_2:Tm^{2+}$. The emissions were monitored after excitation into the ($^3H_6$,t_{2g}) LS levels.

In the new assumption that below 150 K the electrons in the $4f^{12}5d^1$ ($^3H_6$,t_{2g}) LS state do not immediately thermally relax to the HS state, we need to consider a 4-level system for our modelling.

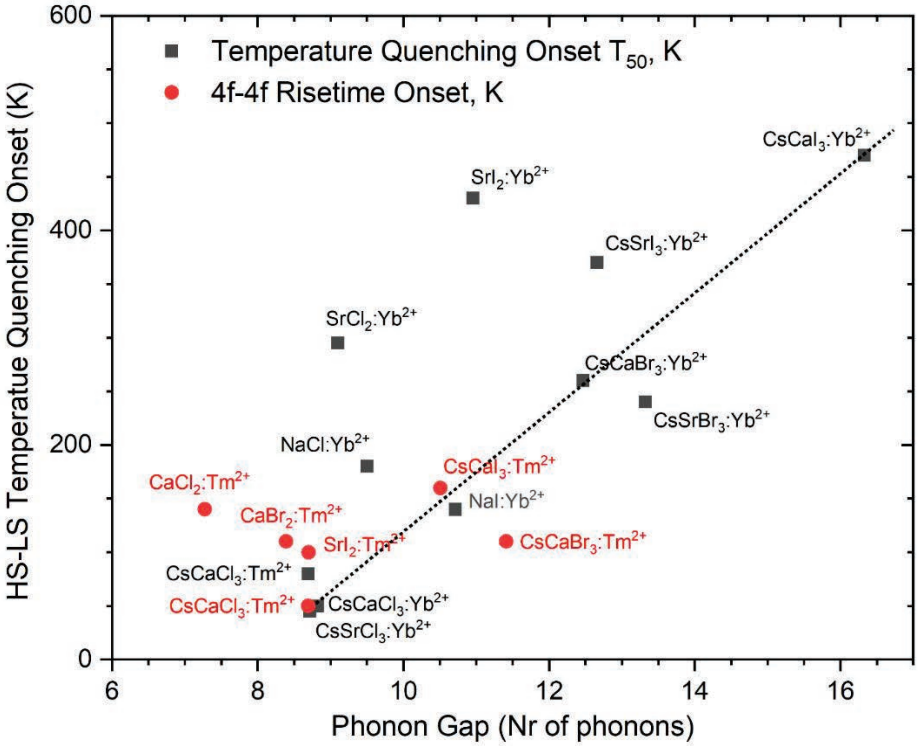

Figure 3.13: The correlation between HS-LS temperature quenching onset T_{50}, K versus the energy difference between HS and LS 5d states expression in the number of host optical phonons for various halides doped with Tm^{2+} and Yb^{2+}. The black dots represent the emission. Source data and references are provided in table 3.4.

With regard to figure 3.13, the x-axis represents the energy difference between LS and HS states derived as the number of phonons:

$$\text{phonon gap} = \frac{E_{HS-LS}}{\hbar\omega_{LO}}$$

On the y-axis the temperature scale is shown. The so-called T_{50}, K onsets are plotted for the LS-state emission quenching (black dots) and rise-time constants τ_r of $4f^{13} \rightarrow 4f^{13}$ emission (fed from $4f^{13} \rightarrow 4f^{12}5d^1$ excitation, red dots) for a variety of halide compounds doped with Tm^{2+} or Yb^{2+}. We have found only one reported compound of $CsCaI_3:Yb^{2+}$, for which both the rise-times and the LS-HS temperature-dependent emissions are present. All the dots from figure 3.13 are provided in table 3.4, with source references.

Table 3.4: Parameters obtained from literature and used in the construction of figure 3.13.

Tm^{2+}							
	HS Absorption (cm^{-1})	LS Absorption (cm^{-1})	Energy Difference (cm^{-1})	$h\omega_{LO}$ (cm^{-1})	Phonon gap (-)	T_{50} emission onset (K)	T_{50} onset for rise-time (K)
$CaCl_2$ [10,32]	13785	15300	1520	230	7		140
$CaBr_2$ [11]	13505	14800	1300	147	9		110
$CsCaCl_3$ [5,30]	13290	15030	1740	200	9	80 [31]	50
$CsCaBr_3$ [5,30]	13490	15140	1655	145	11		110
SrI_2 [24,33]	14070	15260	1200	124	9		100
$CsCaI_3$ [5,30]	12860	14180	1315	125	11		160
Yb^{2+}							
	HS Emission (cm^{-1})	LS Emission (cm^{-1})	Energy Difference (cm^{-1})	$h\omega_{LO}$ (cm^{-1})	Phonon gap (-)	T_{50} emission onset (K)	T_{50} onset for rise-time (K)
$CsCaCl_3$ [30]	22610	24375	1765	200	9	50	
$CsCaBr_3$ [30]	22510	24315	1805	145	12	260	
$CsCaI_3$ [30]	21585	23625	2040	125	16	470	
$CsSrCl_3$ [30]	22920	24315	1395	160	9	45	
$CsSrBr_3$ [30]	22820	24615	1798	135	13	240	
$CsSrI_3$ [30]	21220	22610	1390	110	13	370	
NaCl [34,38]	23080	25050	1970	207	10	180	
SrI_2 [35,33]	22460	23800	1340	107	12	430	
NaI [36,38]	21725	23515	1790	167	11		140
$SrCl_2$ [37,39]	24740	26440	1700	140	12	295	

Possible Mechanisms for Confined QE

Direct QE measurements with an integrating sphere have resulted in QE-values that are considerably lower than the 100% predicted by our model. Our data does not hint at any process explaining the lower-than-expected QE values. Below we suggest four possibilities that still need to be confirmed experimentally in future work. It may be that the QE-measurements are inaccurate. The special sample holder in the integrating sphere, that protects the powder sample from hygroscopicity and oxidation, may absorb part of the Tm^{2+}

NIR luminescence despite the fact it is made from Teflon and quartz parts. Alternatively, our samples may partly absorb excitation light by impurities or defects other than the Tm^{2+} ions, this despite our approach to measure the absorption relative to undoped samples when calculating QE-values. In terms of luminescence quenching mechanisms, the lower QE-values may be caused by a thermally stimulated electron delocalisation to the conduction band as was explained in our work on NaX:Tm^{2+} halides. [8] In addition, concentration quenching from the excited $4f^{13}$- or $4f^{12}5d^1$-states can also result in a QE lower than unity. In SrI_2:Tm^{2+} [24] concentration quenching only starts above 3 mol % Tm^{2+}-doping. In other hosts this is still unknown. With a Tm^{2+} concentration of about 1 mol % in our samples, there may be some quenching but from the observed decay times of the $4f^{13}\rightarrow4f^{13}$ emission of 3.6-5.3 ms it is likely not a strong process.

3.4. Conclusions

The excited states dynamics of Tm^{2+} as doped in CaX_2 (X = Cl, Br, I) were investigated. At 20 K up to three $4f^{12}5d^1\rightarrow4f^{13}$ emissions and the $4f^{13}\rightarrow4f^{13}$ emission were observed. As the temperature increases to 100 K most of the $4f^{12}5d^1$-$4f^{13}$ emissions undergo quenching via $4f^{12}5d^1\rightarrow4f^{12}5d^1$ multi-phonon relaxation and, in most cases, only the lowest energy $4f^{12}5d^1\rightarrow4f^{13}$ emission and the $4f^{13}\rightarrow4f^{13}$ emission remain. A rate equation model was developed to describe the subsequent non-radiative feeding from the lowest energy $4f^{12}5d^1$-state towards the excited $4f^{13}$-state. The model was successfully fitted onto the temperature- and time-dependent luminescence intensity data of $CaBr_2$:Tm^{2+} and $CaCl_2$:Tm^{2+}, where it is revealed that the non-radiative relaxation occurs via two different processes. At low temperatures multi-phonon relaxation towards the excited $4f^{13}$-level dominates, which explains the presence of the $4f^{13}\rightarrow4f^{13}$ emission at 20 K. As the temperature increases, to typically 130 K, the additional process of interband crossing is thermally activated. As a result only the $4f^{13}\rightarrow4f^{13}$ emission is observed at room temperature.

Although the quantitative fitting approach describes the overall temperature- and time-dependent well, two interesting deviations were observed and discussed. Firstly, at low temperature, we observe a risetime for the $4f^{13}\rightarrow4f^{13}$ emission, 15 times shorter as predicted by the model; which can likely be explained by a LS→HS resonance energy transfer interaction. Secondly, we observe a $4f^{13}\rightarrow4f^{13}$ quantum efficiency of 20-30% after $4f^{13}\rightarrow4f^{12}5d^1$ excitation for all three dihalides. Our model predicts a QE of 100% as it does not contain a non-radiative process to the ground state. Different explanations were provided and discussed.

3.5. Appendix A

3.5.1 Arrhenius Plot of $CaBr_2:Tm^{2+}$

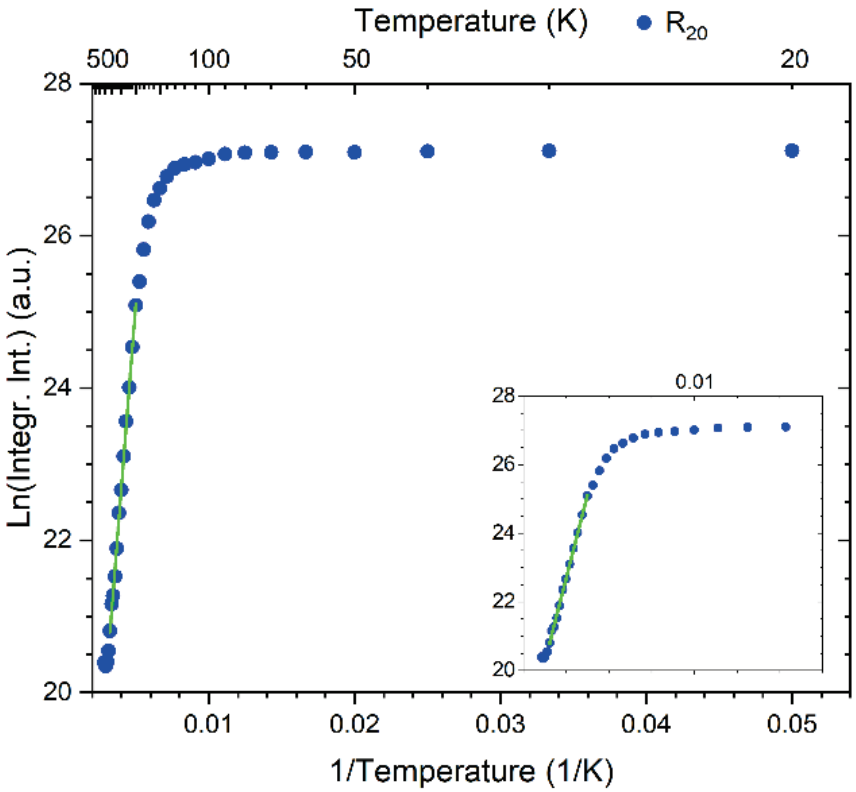

Figure 3.14: Arrhenius plot for emission R_{20} in $CaBr_2:Tm^{2+}$.

Arrhenius Equation: $k = A \cdot e^{\frac{-E_a}{kT}}$

Rewritten: $\ln(k) = \frac{-E_a}{k} \cdot \frac{1}{T} + \ln(A)$

Analogous to: $'y = a \cdot x + b'$

Table 3.5: Parameters obtained from the Arrhenius plot.

a (-)	Ea (cm^{-1})	b	A
2437	1694	12.93	$4.125 \cdot 10^5$

3.5.2 Arrhenius Plot of $CaCl_2:Tm^{2+}$

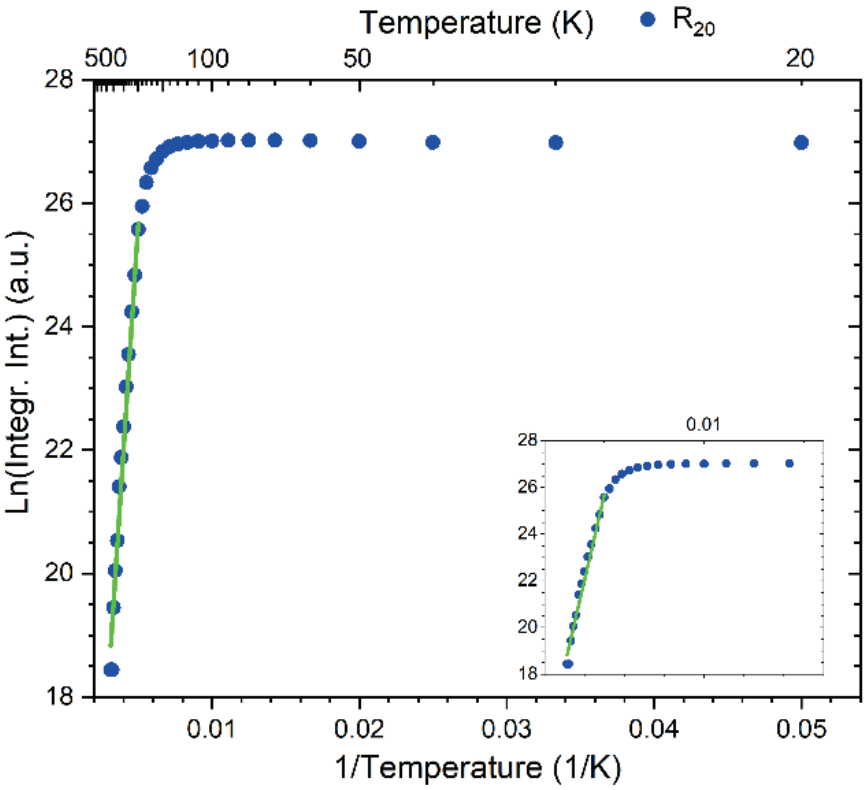

Figure 3.15: Arrhenius plot for emission R_{20} in $CaCl_2:Tm^{2+}$.

Table 3.6: Parameters obtained from the Arrhenius plot.

a (-)	Ea (cm^{-1})	b	A
3667	2549	6.366	$5.817 \cdot 10^2$

3.6. Appendix B

3.6.1 Non-Steady State Rate Equations

Rate Equations:

$$\frac{dN_2(t)}{dt} = \sigma P N_o - N_2(t)\{R_{20} + W_{21}(T)\}$$

$$\frac{dN_1(t)}{dt} = N_2(t)W_{21}(T) - N_1(t)R_{10}$$

Non-Steady State Solutions:

$$N_2(t) = e^{-(W_{21}(T)+R_{20})t}$$

$$N_1(t) = \frac{W_{21}(T)}{(W_{21}(T) + R_{20} - R_{10}) \cdot (e^{-R_{10}t} - e^{-(W_{21}(T)+R_{20})t})}$$

3.6.2 Steady State Rate Equations

Rate Equations:

$$\frac{dN_2(t)}{dt} = \sigma P N_o - N_2(t)\{R_{20} + W_{21}(T)\}$$

$$\frac{dN_1(t)}{dt} = N_2(t)W_{21}(T) - N_1(t)R_{10}$$

Steady State Solutions:

$$N_2 = \frac{\sigma P N_0}{R_{20} + W_{21}(T)}$$

$$N_1 = \frac{N_2 W_{21}(T)}{R_{10}}$$

Luminescence Intensity Relation:

$$I_{20} = c_{20} \cdot N_2 \cdot R_{20}$$

$$\rightarrow I_{20}(T) = \frac{c_{20} \sigma P N_0 R_{20}}{R_{20} + W_{21}(T)}$$

$$I_{10} = c_{10} \cdot N_1 \cdot R_{10}$$

$$\rightarrow I_{10}(T) = \frac{c_{10} N_2 W_{21}(T) R_{10}}{R_{10}}$$

Here c_{10} is defined as the QE of $4f^{13} \rightarrow 4f^{13}$ emission R_{10} at 300 K. This measured value combined with the ratio between the $4f^{13} \rightarrow 4f^{13}$ and $4f^{12}5d^1 \rightarrow 4f^{13}$ emission at 20 K, is used to estimate the QE of the latter emission at 20 K; leading to a c_{20} value. For all three materials, c_{10} and c_{20} are provided in table 3.7.

Table 3.7: List of c_{10} and c_{20} values.

Material (-)	Est. QE R_{10} 20 K (%)	20 K Em. Rat. (-)	c_{10} (%)	c_{20} (%)
$CaCl_2:Tm^{2+}$	1.3	1:21	24.7	26.0
$CaBr_2:Tm^{2+}$	0.3	1:86	27.4	25.8
$CaI_2:Tm^{2+}$	22.6	8:1	28.1	2.8

3.7. References

[1] M.G. Debije, P.P.C. Verbunt, Thirty Years of Luminescent Solar Concentrator Research: Solar Energy for the Built Environment, Adv. Energy Mater. (2011) 2.

[2] F. Meinardi, F. Bruni, S. Brovelli, Luminescent solar concentrators for building-integrated photovoltaics, Nat. Rev. Mater. (2017) 2 17072

[3] O.M. ten Kate, K.W. Krämer, E. Van der Kolk, Efficient luminescent solar concentrators based on self-absorption free, Tm^{2+} doped halides, Sol. Energy Mater Sol. Cells 115-120 (2015) 140.

[4] J. Grimm, H.U. Güdel, Five different types of spontaneous emission simultaneously observed in Tm^{2+} doped $CsCaBr_3$, Chemical Physics Letters 40–43 (2005) 404

[5] J. Grimm, J.F. Suyver, G. Carver, H. U. Güdel, Light-Emission and Excited-State Dynamics in Tm^{2+} Doped $CsCaI_3$, $CsCaBr_3$, and $CsCaI_3$, J. Phys. Chem. B 2093-2101 (2006) 110.

[6] E. Beurer, J. Grimm, P. Gerner, H.U. Güdel, Absorption, Light Emission, and Upconversion Properties of Tm^{2+}-doped $CsCaI_3$ and $RbCaI_3$, Inorg. Chem. 9901-9906 (2006) 45.

[7] J. Grimm, O.S. Wenger, K.W. Krämer, H.U. Güdel, 4f-4f and 4f-5d excited states and luminescence properties of Tm^{2+}-doped CaF_2, $CaCl_2$, $SrCl_2$, $BaCl_2$, J. Phys. Chem. B 101-105 (2006) 110.

[8] M.P. Plokker, E. van der Kolk, Temperature dependent relaxation dynamics of luminescent NaX:Tm^{2+} (X = Cl, Br, I), J. Lumin. (2019) 216.

[9] M. Zhuravleva, L. Stand, H. Wei, C. Hobbs, L.A. Boatner, J.O. Ramey, K. Shah, A. Burger, E. Rowe, P. Bhattacharya, E. Tupitsyn, C.L. Melcher, Hygroscopicity Evaluation of Halide Scintillators, Nuclear Science Symposium and Medical Imaging Conference (NSS/MIC), IEEE (2013) Seoul (South-Korea).

[10] M. Karbowiak, C. Rudowicz, Trends in Hamiltonian parameters determined by systematic analysis of f-d absorption spectra of divalent lanthanides in alkalihalides hosts: II. $CaCl_2$:Ln^{2+} (Ln = Sm, Eu, Tm, and Yb), J. Lumin. 66-75 (2018) 197.

[11] C. Raptis, M. Krobok, W.B. Holzapfel, Pressure dependence of Raman-active phonons of $CaBr_2$, High Pressure Research 27-30 (1992) 9.

[12] M. Baskurt, M. Yagmurcukardes, F. M. Peeters, H. Sahin, Stable single-layers of calcium halides (CaX_2, X = F, Cl, Br, I), J. Chem. Phys. 152 (2020) 164105.

[13] O.M. ten Kate, Z. Zhang, P. Dorenbos, H.T. Hintzen, E. van der Kolk, 4f and 5d energy levels of the divalent and trivalent lanthanide ions in $M_2Si_5N_8$ (M = Ca, Sr, Ba), J. Solid State Chem. 197 (2013) 209.

[14] E. Rogers, P. Dorenbos, J.T.M. de Haas, E. van der Kolk, Experimental study of the $4f^n \rightarrow 4f^n$ and $4f^n \rightarrow 4f^{n-1}$ $5d^1$ transitions of the lanthanide diiodides LnI_2 (Ln = Nd, Sm, Eu, Dy, Tm, Yb), J. Phys.: Condens. Matter (2012) 24.

[15] G.H. Dieke, H.M. Crosswhite, The Spectra of the Doubly and Triply Ionized Rare Earths, Appl. Opt. 675-686 (1963) 2.

[16] P. Dorenbos, Energy of the first $4f^7 \rightarrow 4f^6$5d transition of Eu^{2+} in inorganic compounds, J. Lumin. 239-260 (2003) 104.

[17] P.P. Larsen, Lumineszenz zweiwertiger Selten-Erd-Ionen in bromidischen Wirtsgittern, PhD thesis Universität zu Köln, (2004).

[18] W. Lehmann, Heterogeneous halide-silica phosphors, J. Electrochem. Soc. 122 (1975) 748.

[19] D.H. Gahane, N.S. Kokode, P.L. Muthal, S.M. Dhopte, S.V. Moharil, Luminescence of Eu^{2+} in some iodides, Opt. Mater. 18-21 (2009) 32.

[20] M. de Jong, A. Meijerink, L. Seijo, Z. Barandiarán, Energy Level Structure and Multiple $4f^{12}5d^1$ Emission Bands for Tm^{2+} in Halide Perovskites: Theory and Experiment, J. Phys. Chem. C 10095−10101 (2017) 121.

[21] C. van Aarle, P. Dorenbos, to be published article (2021)

[22] G. Blasse and B.C. Grabmeier, Luminescent Materials, Springer Verlag ISBN-13: 978-3-540-58019-5 (1994).

[23] C.W. Struck and W.H. Fonger, Understanding Luminescence Spectra and Efficiency Using W_p and Related Functions, Inorganic Chemistry Concepts 13, Springer Verlag ISBN 3-540-52766-4 (1991).

[24] M.P. Plokker, W. Hoogsteen, R.D. Abellon, K.W. Krämer, E. van der Kolk, Concentration and temperature dependent luminescence properties of the SrI_2-TmI_2 system, J. Lumin (2020) 225.

[25] R. Reisfeld, C.K. Jőrgensen, Lasers and Excited States of Rare-Earths, Inorganic Chemistry Concepts 1, Springer Verlag ISBN 3-540-08324-3 (1977).

[26] D. Yu, J. Ballato, R.E. Riman, Temperature-Dependence of Multiphonon Relaxation of Rare-Earth Ions in Solid-State Hosts, J. Phys. Chem. C J. 9958−9964 (2016) 120.

[27] S. Tanabe, S. Yoshii, K. Hirao, N. Soga, Upconversion properties, multiphonon relaxation, and local environment of rare-earth ions in fluorophosphate glasses, Phys. Rev. B 45 (1992) 9.

[29] W.M. Yen, S. Shionoya, H. Yamamoto, Phosphor Handbook 2nd edition, chapter 2, CRC Press Taylor & Francis Group ISBN 0-8493-3564-7 (2007).

[29] B. Di Bartolo, Advances in Nonradiative Processes in Solids, NATO Advanced Science Institutes Series, Series B. Physics V. 249, Springer Verlag ISBN 978-1-4419-3219-8 (1991).

[30] M. Suta, C. Wickleder, Spin Crossover of Yb^{2+} in $CsCaX_3$ and $CsSrX_3$ (X = Cl, Br, I) – A Guideline to Novel Halide – Based Scintillators, Adv. Funct. Mater. 27 (2017) 2.

[31] S. Koster, M. Reid, J.P. Wells, R. Reeves, Energy Levels and Dynamics of Tm^{2+} Doped into AMX_3 Salts, Msc Thesis S. Koster, University of Canterbury (2014)

[32] L.M. Uriarte, J. Dubessy, P. Boulet, V.G. Baonza, I. Bihannic, P. Robert, Reference Raman spectra of synthesized $CaCl_2 \cdot nH_2O$ solids (n = 0, 2, 4, 6), J. Raman Spectrosc. 46 (2015) 10.

[33] Y. Cui, R.Hawrami, E. Tupitysn, P. Bhattacharya, M. Groza, M. Bryant, V. Buliga, A. Burger, N.J. Cherepy, S.A. Payne, Raman spectroscopy study of BaI_2 :Eu and SrI_2 :Eu scintillator crystals, Solid State Commun. 151 (2011) 7.

[34] T. Tsuboi, H. Witzke, D.S. McClure, The $4f^{14} \rightarrow 4f^{13}5d$ transition of Yb^{2+} ion in NaCl crystals, J. Lumin. 305-308 (1981) 24-25 P1.

[35] M.S. Alekhin, D.A. Biner, K.W. Krämer, P. Dorenbos, Optical and scintillation properties of SrI_2:Yb^{2+}, Opt. Mater. 382-386 (2014) 37.

[36] M. Hendriks, E. van der Kolk, $4f \rightarrow 5d$ and anomalous emission in Yb^{2+} doped NaI, SrI_2 and LaI_3 powders prepared by rapid melting and quenching in vacuum, J. Lumin. 231-235 (2019) 207.

[37] Z. Pan, C.K. Duan, P.A. Tanner, Electronic spectra and crystal field analysis of Yb^{2+} in $SrCl_2$, Phys. Rev. B 77 (2008), 085114.

[38] E. Burstein, F. A. Johnson, R. Loudon, Selection Rules for Second-Order Infrared and Raman Processes in the Rocksalt Structure and Interpretation of the Raman Spectra of NaCl, KBr, and NaI, Phys. Rev. 139, (1965) A1239.

[39] D. Schreyer, V.Waschk, A.Châtelain, Raman spectroscopy in small crystals of $SrCl_2$, Surf. Sci. 336-344 1-3 (1981) 106.

4.

Photoluminescence and Excited States Dynamics of Tm^{2+}-doped $CsCa(Cl/Br)_3$ and $CsCa(Br/I)_3$ Perovskites

This chapter is based on the publication: M.P. Plokker, D.A. Biner, N. Dusoswa, P. Dorenbos, K.W. Krämer and E. van der Kolk, Photoluminescence and Excited States Dynamics of Tm^{2+}-doped $CsCa(Cl/Br)_3$ and $CsCa(Br/I)_3$ Perovskites, Journal of Physics: Materials 4 (2021).

Thanks to: J.T.M. de Haas, C. van Aarle and V. Khanin

Abstract

In this study, we systematically vary the Cl/Br and Br/I ratios in $CsCaX_3:Tm^{2+}$ (X = Cl, Br, I) and hereby gradually shift the positions of the Tm^{2+} $4f^{12}5d^1$-levels as relative to the two $4f^{13}$ levels. At low temperatures up to five distinct Tm^{2+} $4f^{12}5d^1 \rightarrow 4f^{13}$ emissions and the $4f^{13} \rightarrow 4f^{13}$ emission can be observed. As the temperature increases, most of the $4f^{12}5d^1 \rightarrow 4f^{13}$ emissions undergo quenching via multi-phonon relaxation and at room temperature only the lowest energy $4f^{12}5d^1 \rightarrow 4f^{13}$ and the $4f^{13} \rightarrow 4f^{13}$ emission remains. For all compositions a $4f^{13} \rightarrow 4f^{13}$ risetime phenomenon is then observed whose duration matches the $4f^{12}5d^1 \rightarrow 4f^{13}$ decay time. It shows the feeding of the $4f^{13}$ state after $4f^{12}5d^1$ excitation. Surprisingly, the feeding time becomes longer from Cl→Br→I, while the related $4f^{12}5d^1$-$4f^{13}$ energy gap becomes smaller. The temperature dependence of the $4f^{12}5d^1 \rightarrow 4f^{13}$ and $4f^{13} \rightarrow 4f^{13}$ emission intensity shows a anticorrelation as earlier observed in other systems and confirms that the feeding process is thermally stimulated. However, the thermally stimulated activation energies that control the feeding process, increase from Cl→Br→I despite our observation that the $4f^{12}5d^1$-$4f^{13}$ energy gap becomes smaller. An analysis reveals that the unexpected behaviour in risetime and activation energy, as a function of composition, cannot be explained by $4f^{12}5d^1 \rightarrow 4f^{13}$ feeding via interband crossing, but more likely via multi-phonon relaxation where the electron-phonon coupling strength decreases from Cl→Br→I. No strong relation was found between composition and the quantum efficiency of the $4f^{13} \rightarrow 4f^{13}$ emission, due to the presence of fluctuations that are likely caused by intrinsic differences in sample quality. Nevertheless, a $4f^{13} \rightarrow 4f^{13}$ quantum efficiency of up to 70% has been observed and the materials can therefore be used in luminescence solar concentrators.

4.1. Introduction

In recent years, organolead halide perovskites have received considerable attention in view of photosensitive and optoelectronic applications. [1-3] However, for studying the luminescence properties of Lanthanides (Ln), the bandgap of these host compounds is in most cases too small to allow for Ln^{2+} $4f^{12}5d^1 \rightarrow 4f^{13}$ emission [4] and suitable replacements are often found among $CsMX_3$ (M = Ba, Sr, Ca, Mg; X = Cl, Br, I) systems. Recent studies on divalent lanthanides include the works Suta et al. [5-8] on $CsMX_3:Yb^{2+}$ (M = Sr, Ca; X = Cl, Br, I) and $CsMBr_3:Eu^{2+}$ (M = Sr, Ca, Mg) and those of Lindsey and Loyd et al. [9,10,11] on $CsSrBr_3:Eu^{2+}$, $CsCaI_3:Eu^{2+}$ and solid solutions of $CsCa(I/Br)_3:Eu^{2+}$. These materials can be used as scintillators and low energy emitting LEDs. [5-11] For the divalent lanthanide Tm^{2+}, Grimm and Beurer et al. [12-17] were the first to study its luminescence properties and excited states dynamics in $CsCaX_3$ (X = Cl, Br, I) perovskites, in view of upconversion applications. At low temperature, up to six distinct Tm^{2+} emissions are present: five

$4f^{12}5d^1 \rightarrow 4f^{13}$ emissions and the $4f^{13} \rightarrow 4f^{13}$ emission. The quenching of the different $4f^{12}5d^1 \rightarrow 4f^{13}$ emissions at higher temperature was in each case attributed to Multi-Phonon Relaxation (MPR). The follow-up studies by de Jong et al. [18,19] revealed that the relative configurational displacement of the $4f^{12}5d^1(t_{2g})$ states is negligible, which supports the $4f^{12}(5d^1\text{-}5d^1)$ quenching via MPR. Our recent work on $CaX_2:Tm^{2+}$ (X = Cl, Br, I) [20] discloses that the quenching of the lowest energy $4f^{12}5d^1 \rightarrow 4f^{13}$ emission occurs via $4f^{12}5d^1\text{-}4f^{13}$ MPR at low temperatures and predominantly via Interband Crossing (IC) at the higher temperatures. Therefore, we have decided to re-examine the quenching of this emission in $CsCaX_3:Tm^{2+}$ (X = Cl, Br, I) compounds by systematically varying the Cl/Br and Br/I ratios. This enables us to alter the $4f^{12}5d^1$-level positions relative to the $4f^{13}$-levels, the Stokes shift and the phonon energies. The $4f^{12}5d^1$ tuning by chemical variation allows for a systematic study of the MPR and IC quenching processes as a function of the $4f^{12}5d^1\text{-}4f^{12}5d^1$ and $4f^{12}5d^1\text{-}4f^{13}$ energy gaps. Our temperature-dependent emission and excitation data is compared with the directly measured quantum efficiency of the $4f^{13} \rightarrow 4f^{13}$ emission. This parameter is ultimately governed by the Tm^{2+} excited states dynamics and determines the suitability of the materials for application in luminescence solar concentrators. [21]

In this article we start off with a structural and luminescence characterisation of the $CsCa(Cl/Br)_3:Tm^{2+}$ and $CsCa(Br/I)_3:Tm^{2+}$ samples, subsequently their $4f^{13} \rightarrow 4f^{13}$ quantum efficiency is determined and we finish with a description of the $4f^{12}(5d^1\text{-}5d^1)$ and $4f^{12}5d^1\text{-}4f^{13}$ quenching processes. We will show that the quenching of the lowest energy Tm^{2+} $4f^{12}5d^1 \rightarrow 4f^{13}$ emission, over temperature, is not straightforwardly explained by a reduced $4f^{12}5d^1\text{-}4f^{13}$ energy gap combined with phonon energies, but more likely governed by the electron-phonon coupling strength.

4.2. Experimental Methods

4.2.1 Sample Synthesis

Nominally 2% Tm^{2+}-doped $CsCa(Cl_{1-y}Br_y)_3$ (y = 0, 0.25, 0.5, 0.75, 1) and $CsCa(Br_xI_{1-x})_3$ (x = 0, 0.2, 0.4, 0.5, 0.6, 0.8, 1.0) samples were prepared by mixing stoichiometric amounts of CsBr, $CaBr_2$ and TmI_2 with CsCl and $CaCl_2$ or CsI and CaI_2 respectively. A small amount of Tm metal was added to prohibit any oxidation of Tm^{2+} towards Tm^{3+}. The powder mixtures were sealed in a tantalum ampoule by arc welding under 0.4 bar helium. The Ta ampoules were subsequently enclosed in a silica ampoule under vacuum and heated in a Carbolite RHF1600 chamber furnace (Carbolite Gero, Neuhausen, Germany) to 800^{o}C for 20 hours. After cooling back to room temperature, the obtained crystalline products were grinded to powder. All handling of starting materials and the final products was done under strictly inert and dry conditions in a glovebox (MBraun, Garching, Germany).

4.2.2 Sample Characterisation

The crystal structures of the samples at room temperature were investigated by powder x-ray diffraction using a STOE Stadi P diffractometer (Stoe & Cie GmbH, Darmstadt, Germany) with Bragg-Brentano geometry and $CuK_{\alpha1}$ radiation. The lattice parameters were determined from Rietveld refinements using the Fullprof software. [22]. Room temperature NIR absorption measurements were recorded with a Cary 6000i spectrophotometer (Varian Inc., Palo Alto, California) to confirm the absence of Tm^{3+} in the samples. The absorption spectra were measured in transmission from KBr pellets in gas-tight sample cells with silica windows. A part of the powder samples was mixed with KBr and pressed into a pellet under inert conditions. Luminescence quantum efficiency measurements were performed at room temperature using an Edinburgh FLS980 spectrometer (Edinburgh Instruments, Livingston, UK) containing an integrating sphere, 450 W Xenon arc lamp, and Hamamatsu C9940-02 NIR-PMT (Hamamatsu Photonics, Hamamatsu, Japan). Highly reflecting $BaSO_4$ and the un-doped host materials were used as reference samples. Room temperature time resolved measurements were carried out using a tuneable EKSPLA NT230 laser (EKSPLA, Vilnius, Lithuania) with a pulse duration of 7 ns. A DT5724F (0-2 ms) or DT5730 (0-40 ms) CAEN digitiser (CAEN, Viareggio, Italy) measured the signal from a H1033A-75 NIR-PMT or a Hamamatsu R7600U-20HV-800V PMT (Hamamatsu Photonics, Hamamatsu, Japan). Decay signals from a 1000 laser pulses were accumulated for each decay spectrum.

4.2.3 Temperature-Dependent Measurements

The temperature dependent excitation and emission spectra were obtained with help of a Xenon lamp coupled to a double monochromator with three sets of gratings (UV/VIS/NIR) and a R7600U-20HV-800V PMT, H1033A-75 NIR-PMT, or C9100-13 EM-CCD (all Hamamatsu Photonics, Hamamatsu, Japan) which were in turn attached to a single monochromator with three different gratings. A calibrated EPLAB NBS 1000 W quartz iodine lamp was used to acquire the wavelength dependent sensitivity of the detectors. The detection ranges were 400 to 1150 nm and 950 to 1600 nm for CCD and NIR-PMT, respectively. The spectral overlap allows to couple the output of both detectors and hence accurately determine the $4f^{12}5d^1 \rightarrow 4f^{13}$ and $4f^{13} \rightarrow 4f^{13}$ emission ratios over temperature. For samples that have no clear emission in the overlap region, a small amount of $Ca_2Si_5N_8:Yb^{3+}$ was added to the samples. After exciting the Yb^{3+} at 360 nm, the $^2F_{5/2} \rightarrow {}^2F_{7/2}$ emission at 985 nm was observed and used for scaling the emission spectra recorded with the two detectors. The samples were thermalized by an APD Cryogenic Helium cooler (APD Cryogenics, Allentown Pennsylvania, USA) and a Lakeshore temperature controller (Lakeshore Cryotronics, Westerville Ohio, USA).

Special sample holders were used for the hygroscopic materials during all measurements to prevent unwanted hydration or oxidation reactions. [23]

4.3. Results and Discussion

4.3.1 Sample Characterisation

Figure 4.1 shows the powder X-ray diffraction patterns of the $CsCa(Cl/Br)_3$ and $CsCa(Br/I)_3$:2% Tm^{2+} samples. The lattice parameters, molar volume, and space group of the samples are summarised in table 4.1. The evaluation of the diffraction patterns reveals that all $CsCa(Cl/Br)_3$ samples and the $CsCa(Br/I)_3$ samples up to the composition $CsCaBr_{1.5}I_{1.5}$ adopt the cubic perovskite structure ($CaTiO_3$ structure) with space group $Pm\bar{3}m$, see figure 4.2. This is in accordance to the work of Grimm et al. on $CsCaX_3$:Tm^{2+} (X = Cl, Br, I) [12,13] and structure reports on $CsCaCl_3$ [24] and $CsCaBr_3$ [25]. The Tm^{2+} ions have an octahedral coordination and randomly replace the Ca^{2+} ions on site (1a) with point symmetry O_h. Along the series Cl→Br→I, the diffraction peaks shift to slightly smaller 2-Theta values, see figure 4.1, and the lattice parameter increases. The molar volume increases linearly in good agreement with Vegard's rule. The values are reported in table 4.1 and displayed in figures 4.3 and 4.4.

For higher I content the crystal structures change in accordance with the well-known sequence of perovskite structures. $CsCaBr_{1.2}I_{1.8}$ and $CsCaBr_{0.6}I_{2.4}$ crystallise in the tetragonal $NaNbO_3$ structure with spacegroup $P4/mbm$, which was previously reported for e.g. $CsTmBr_3$ [26] and $CsDyBr_3$ [27]. The CaX_6 octahedra rotate around the *c*-axis to decrease the volume and accommodate the smaller M/X ratio, see figure 4.2b. Tm^{2+} ions on site (2a) have C_{4h} site symmetry. Finally, $CsCaI_3$ adopts the orthorhombic $GdFeO_3$ structure with space group $Pbnm$, where the octahedra are rotated and titled, see figure 4.2c. The point symmetry of the Tm^{2+} ions on site (4b) is reduced to C_i. The crystal structure of $CsDyI_3$ was

Table 4.1: Composition, space group, lattice parameters, and molar volume of the $CsCa(Cl/Br)_3$ and $CsCa(Br/I)_3$:2%Tm^{2+} samples.

Sample	Space group	a / Å	b / Å	c / Å	V / (cm^3/mol)
$CsCaCl_3$	$Pm\bar{3}m$ (no. 221)	5.40351(9)	-	-	95.025(3)
$CsCaCl_{2.25}Br_{0.75}$	$Pm\bar{3}m$	5.48002(14)	-	-	99.119(4)
$CsCaCl_{1.5}Br_{1.5}$	$Pm\bar{3}m$	5.55293(13)	-	-	103.129(4)
$CsCaCl_{0.75}Br_{2.25}$	$Pm\bar{3}m$	5.62403(15)	-	-	107.141(5)
$CsCaBr_3$	$Pm\bar{3}m$	5.69583(12)	-	-	111.297(4)
$CsCaBr_{2.4}I_{0.6}$	$Pm\bar{3}m$	5.7622(4)	-	-	115.232(15)
$CsCaBr_{1.8}I_{1.2}$	$Pm\bar{3}m$	5.8647(5)	-	-	121.492(16)
$CsCaBr_{1.5}I_{1.5}$	$Pm\bar{3}m$	5.9078(5)	-	-	124.19(2)
$CsCaBr_{1.2}I_{1.8}$	$P4/mbm$ (no. 127)	8.2608(8)	-	6.0899(5)	125.13(2)
$CsCaBr_{0.6}I_{2.4}$	$P4/mbm$	8.3991(7)	-	6.1822(5)	131.339(18)
$CsCaI_3$	$Pbnm$ (no. 62)	8.5540(5)	8.6237(5)	12.2885(7)	136.495(13)

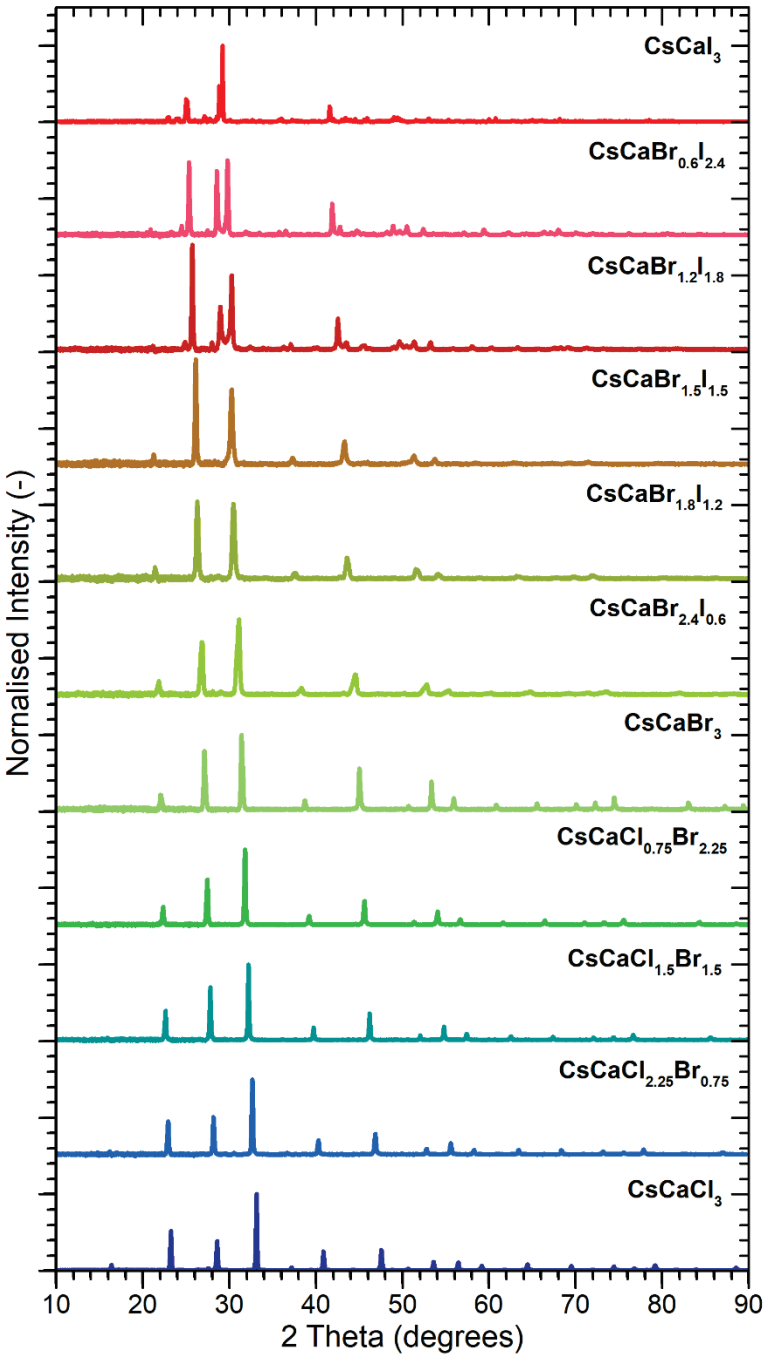

Figure 4.1: Powder X-ray diffraction patterns of the $CsCa(Cl/Br)_3:Tm^{2+}$ and $CsCa(Br/I)_3:Tm^{2+}$ samples at room temperature. The corresponding crystallographic data are summarised in table 4.1.

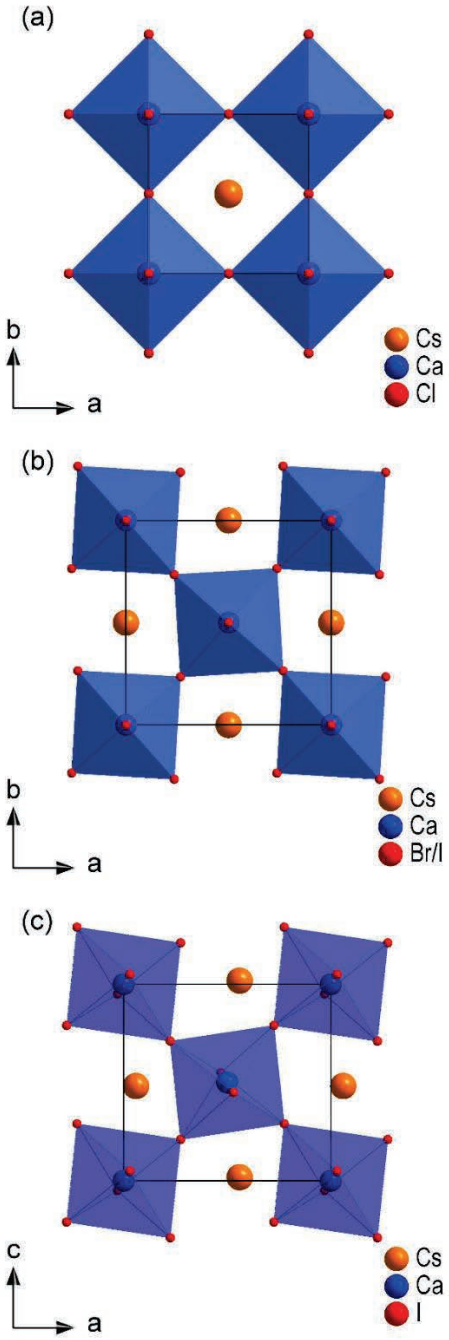

Figure 4.2: Crystal structures of (a) $CsCaCl_3$, (b) $CsCaBr_{1.2}I_{1.8}$, and (c) $CsCaI_3$ that respectively adopt the structures of $CaTiO_3$, $NaNbO_3$, and $GdFeO_3$ type perovskites.

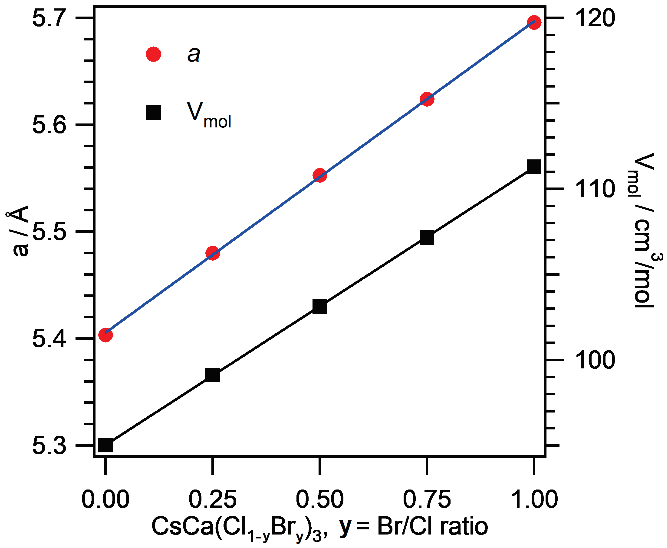

Figure 4.3: Plot of the lattice parameter *a* and the molar volume V_{mol}, obtained from Rietveld refinements, versus the Br/Cl ratio y of the $CsCa(Cl/Br)_3$:Tm^{2+} samples. All samples adopt the cubic CaTiO3 crystal structure with space group $Pm\bar{3}m$. The linear increase of *a* and V_{mol} corresponds to Vegard's rule and indicates complete miscibility.

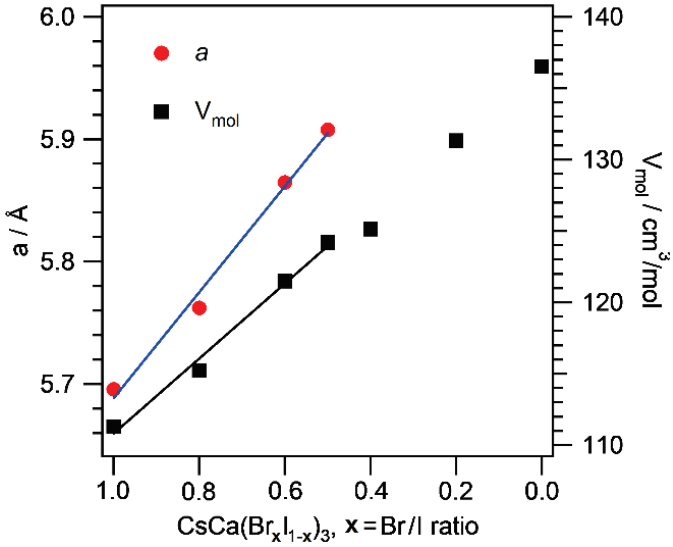

Figure 4.4: Plot of the lattice parameter *a* and the molar volume V_{mol} obtained from Rietveld refinements, versus the Br/I ratio x of the $CsCa(Br/I)_3$:Tm^{2+} samples. The samples crystallise in the cubic $CaTiO_3$ crystal structure for large x. For x = 0.4 and 0.2 the tetragonal $NaNbO_3$ crystal structure with space group $P4/mbm$ is observed. $CsCaI_3$ (x=0) crystallises in the orthorhombic $GdFeO_3$ structure with space group $Pbnm$. The lattice distortions for lower x values reduce the molar volume compared to the cubic parent structure.

previously determined [27] and lattice parameters of $CsCaI_3$ were reported by Schilling and Meyer [28], who discussed the stability ranges of the ternary AMX_3 phases for X = Br and I. The Tm^{2+} ions in the $CsCaX_3$ structures occupy the octahedral Ca^{2+}-sites with decreasing symmetry along the $CaTiO_3 \rightarrow NaNbO_3 \rightarrow GdFeO_3$ series, as discussed above. Additionally, the random halide mixture Cl/Br or Br/I slightly distorts the individual Tm^{2+} coordination, which can further split the 5d crystal field levels t_{2g} and e_g. In this work, we use the short hand notation $(^{2S+1}L_J,t_{2g})_S$ to assign the excited $4f^{12}5d^1$ levels, where $^{2S+1}L_J$ represents the state of $4f^{12}$ configuration, t_{2g} denotes the 5d-electron in a level originating from the triplet of the octahedral crystal field splitting, and the subscript S denotes the total electron spin of the $(4f^{12} + 5d^1)$ excited state.

The Near-Infrared (NIR) absorption spectra of the $CsCa(Cl/Br)_3:Tm^{2+}$ and $CsCa(Br/I)_3:Tm^{2+}$ samples are displayed in figure 4.5. The spectra reveal the presence of the characteristic Tm^{2+} $^2F_{7/2} \rightarrow {}^2F_{5/2}$ absorption near 1140 nm. The spectra do not show any signs of the distinct Tm^{3+} $^3H_6 \rightarrow {}^3H_5$ absorption, which is typically observed at around 1230 nm. [20,29-31] The samples thus only contain divalent Tm. The integrated values of the Tm^{2+} absorption peak show a deviation of ±7% from average, indicating that the Tm^{2+} doping percentages of the samples are quite close.

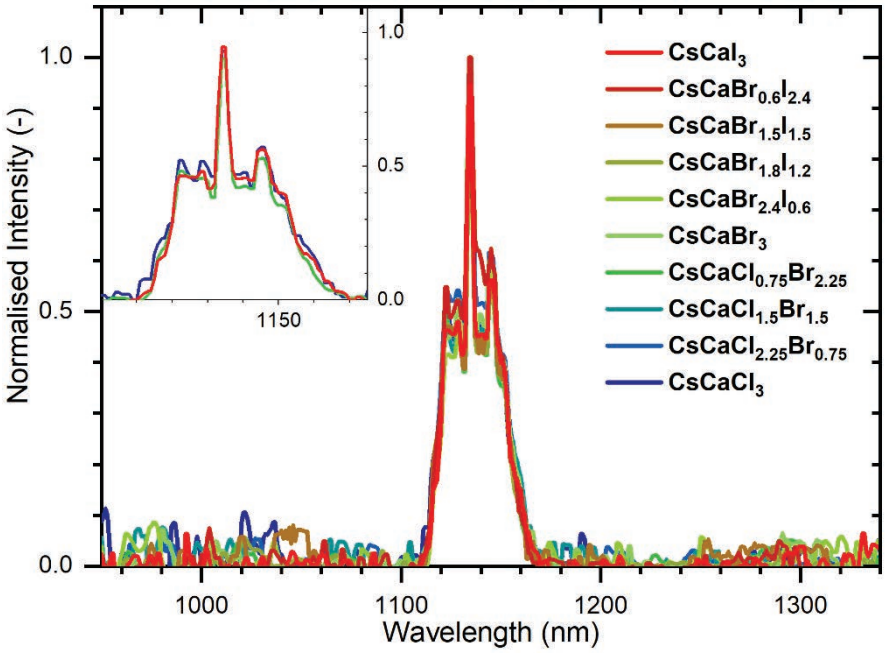

Figure 4.5: Room temperature NIR absorption spectra of the $CsCa(Cl/Br)_3:Tm^{2+}$ and $CsCa(Br/I)_3:Tm^{2+}$ samples. The Tm^{2+} $^2F_{7/2} \rightarrow {}^2F_{5/2}$ absorption is observed at 1140 nm. No Tm^{3+} $^3H_6 \rightarrow {}^3H_5$ absorption is seen at around 1230 nm. The inset shows a close-up of the $CsCaX_3:Tm^{2+}$ spectra for X = Cl, Br, I.

The Tm^{2+} $^2F_{5/2}$ and $^2F_{7/2}$ states arising from the $(4f)^{13}$ electron configuration are split by the crystal field into (2J+1)/2 Cramers doublets. Therefore, the $^2F_{7/2}\rightarrow{}^2F_{5/2}$ absorption peak comprises of multiple sharp absorption lines as can be observed in the inset of figure 4.5. As Tm^{2+} is octahedrally coordinated in each of the samples, the absorption pattern is largely the same. Minor differences are likely caused by differences in the distribution of Cl^-, Br^- and I^- ions around Tm^{2+} and shifts in the interatomic distances due to different crystal structures. For a more-detailed analysis of the Stark splitting in $CsCaX_3$:Tm^{2+} (X = Cl, Br, I), the reader is referred to the works of Grimm et al. [13,15]

4.3.2 Excitation and Emission Spectra

Figure 4.6 shows the excitation spectra as acquired on the Tm^{2+} $^2F_{5/2}\rightarrow{}^2F_{7/2}$ emission at 300 K. For the $CsCaX_3$:Tm^{2+} (X = Cl, Br, I) samples, the spectra are similar in shape to the 20 K UV/NIR/VIS absorption spectra reported before by Grimm et al.. [13,15,17] The provided classification of the lowest energetic 5d-levels is added to figure 4.6 and their positioning is shown for $CsCaCl_3$:Tm^{2+} by the vertical dashed lines. As can faintly be seen, the spin-forbidden $(^3H_6,t_{2g})_{S=3/2}$ levels are located at around 750-800 nm and positioned in the tail of the broad spin-allowed $(^3H_6,t_{2g})_{S=1/2}$ levels. The excitation spectra acquired on the $(^3H_6,t_{2g})_{S=3/2}\rightarrow{}^2F_{7/2}$ emission at 20 K are displayed in figure 4.7 and provide a much clearer sighting of the spin-forbidden $(^3H_6,t_{2g})_{S=3/2}$ levels. In addition, a second set of $(^3H_6,t_{2g})_{S=3/2}$ levels can be distinguished at around 620 nm. It is located in between the less broad $(^3H_6,t_{2g})_{S=1/2}$ levels. This was also the case in our recent work on CaX_2:Tm^{2+} (X= Cl, Br, I). [20] Near the end of section 4.3.4 we will discuss the differences between the $^2F_{5/2}\rightarrow{}^2F_{7/2}$ and $(^3H_6,t_{2g})_{S=3/2}\rightarrow{}^2F_{7/2}$ excitation spectra into more detail.

A mutual comparison between the $CsCaX_3$:Tm^{2+} (X = Cl, Br, I) spectra shows that the $4f^{12}5d^1$ levels undergo a redshift upon traversing from Cl→Br→I. In particular, the $(^3H_6,t_{2g})_{S=1/2}$ levels shift by around 240 cm^{-1} for Cl→Br and approximately 920 cm^{-1} in case of Br→I. It indicates a decrease of the centroid shift along the series. This is expected based on a decrease in the average bonding strength between anion and cation following the nephelauxetic sequence: Cl→Br→I. [32] In addition to that, figures 4.3 and 4.4 reveal an increase in the molar volume and lattice parameters for Cl→Br→I, leading to a decrease in the centroid shift and increase in the crystal field splitting along the series. [32,33]

Figure 4.2 already showed that, as the Cl/Br and Br/I ratios in the $CsCaX_3$:Tm^{2+} (X = Cl, Br, I) samples are adjusted, the anion coordination around Tm^{2+} remains octahedral and six-fold. The different anion species (Cl, Br, I) will be distributed randomly over the anion positions of the coordination polyhedra. This random distribution will result in many different anion surroundings for each individual Tm^{2+} ion with corresponding changes in size of the

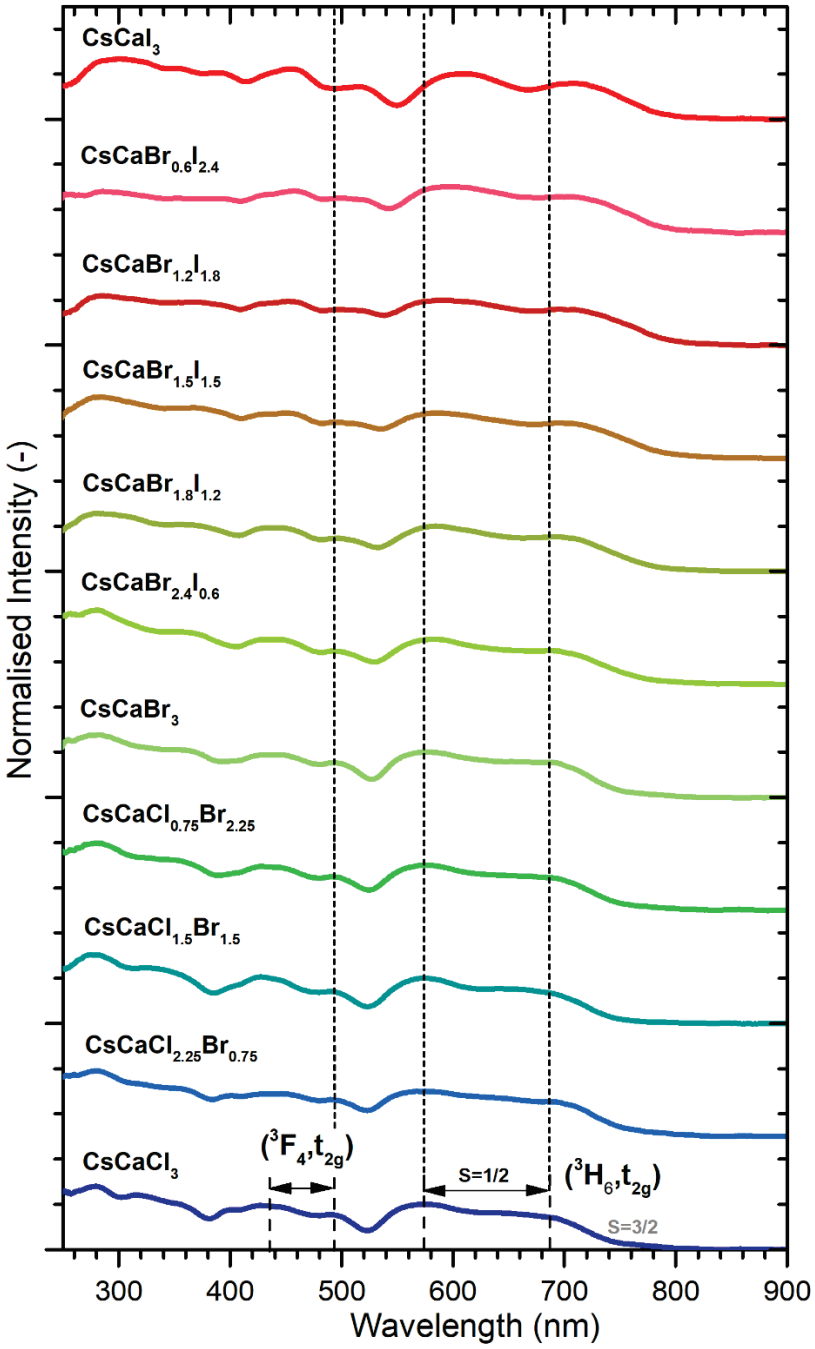

Figure 4.6: Excitation spectra of the $CsCa(Cl/Br)_3:Tm^{2+}$ and $CsCa(Br/I)_3:Tm^{2+}$ samples as acquired on $^2F_{5/2}\rightarrow{}^2F_{7/2}$ emission A at 300 K. The lowest energy $4f^{12}5d^1$-levels are indicated for $CsCaCl_3:Tm^{2+}$ and undergo a shift towards longer wavelengths upon traversing from Cl→Br→I.

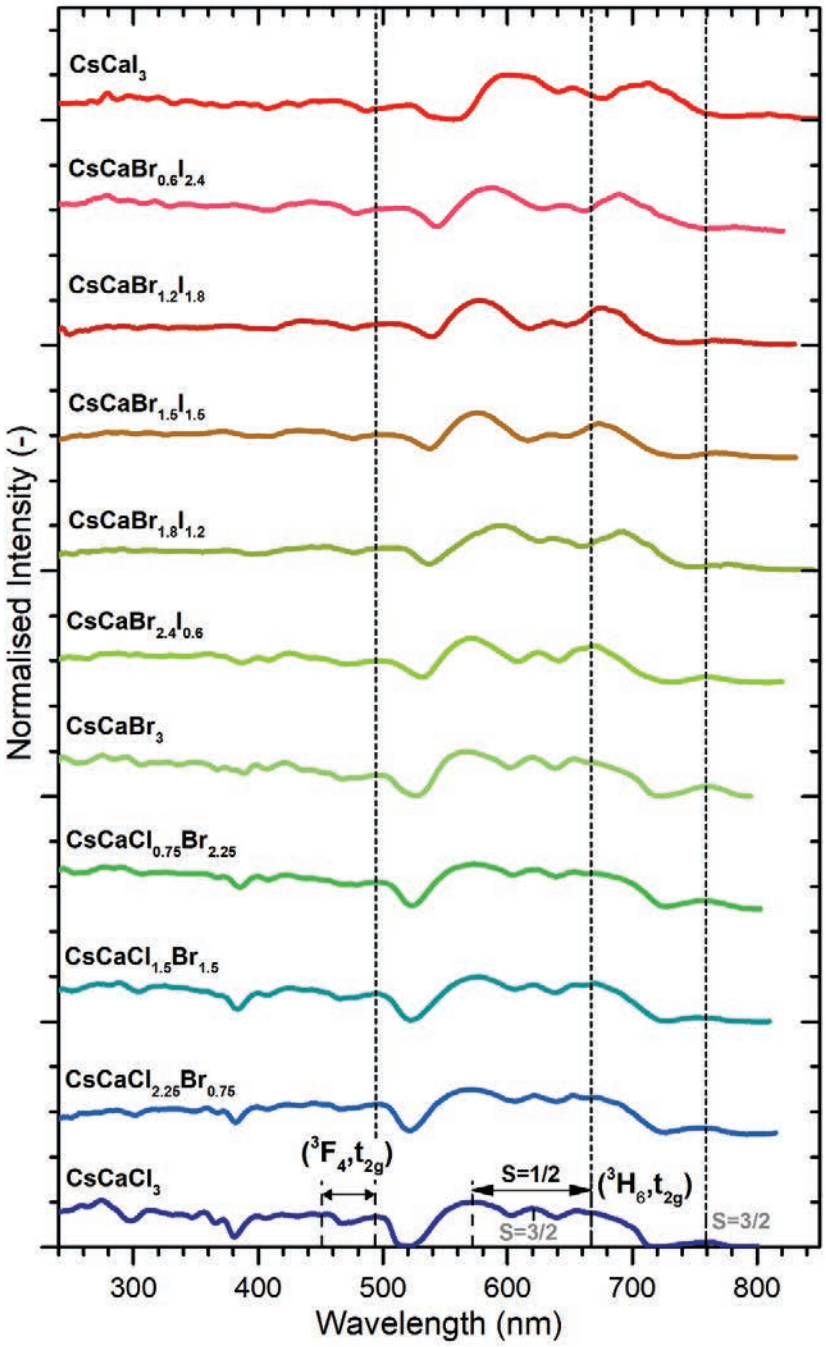

Figure 4.7: Excitation spectra of the $CsCa(Cl/Br)_3:Tm^{2+}$ and $CsCa(Br/I)_3:Tm^{2+}$ samples as acquired on the Tm^{2+} $(^3H_6,t_{2g})_{S=3/2} \rightarrow {}^2F_{7/2}$ emission B at 20 K. As compared to figure 4, the spin-forbidden $(^3H_6,t_{2g})_{S=3/2}$ levels can be distinguished more clearly.

coordination polyhedra. The mixed compounds will thus have slightly different values for the centroid shift and crystal field splitting.

Figure 4.8 displays the emission spectra of the samples after excitation into the $(^3F_4,t_{2g})_{S=1/2}$ levels. The full coloured curves were acquired at 20 K and reveal up to six distinct Tm^{2+} emissions: five $4f^{-12}5d^1 \rightarrow 4f^{13}$ emissions (B, C, D, E, F) and the $4f^{13} \rightarrow 4f^{13}$ emission (A). These emissions are labelled according to the classification introduced by Grimm and Beurer et al.. [12-14] A schematic overview of the transitions and their lettering is provided in figure 4.9. As the temperature increases, most of the $4f^{12}5d^1 \rightarrow 4f^{13}$ emissions (B, C, D, E, F) will quench and are no longer observed. This can be seen in the softly coloured emission spectra, that were acquired at 300 K and which are plotted alongside the 20 K spectra. $CsCaI_3:Tm^{2+}$ forms a special case where emissions A, B, C, and D are still, albeit weakly, present at 300 K. It will be discussed in more detail in section 4.3.4. For all studied compounds, however, emission B survives as the most intense $4f^{12}5d^1 \rightarrow 4f^{13}$ emission at 300 K, while the $4f^{13} \rightarrow 4f^{13}$ emission A has become the most dominant emission of all.

When traversing from Cl→Br→I, the dashed lines in figure 4.8 show that the emissions undergo a gradual shift towards longer wavelengths. The shifts in the related excitation levels is visualised by similar dashed lines in figure 4.7. Note that for all compounds, Tm^{2+} is octahedrally coordinated and the shift is related to nephelauxetic effects. Tables 4.2 and 4.3 in Appendix A provide an overview of the emission and excitation level positioning and characterises their shift as a function of composition. Based on these values, the energy gaps between the levels can be calculated. Such values are listed in table 4.4 in Appendix A and provide important information for the quenching of the emissions as discussed in section 4.3.4. Furthermore, the close-ups presented in figures 4.10-4.12 reveal that not all of the emissions are observed in every studied compound. For $CsCaCl_3:Tm^{2+}$ only emissions A, B and D are present at 20 K. The study by de Jong et al. [19] showed that the absence of emission C can be attributed to efficient multi-phonon relaxation since the gap between the $(^3H_6,t_{2g})_{S=1/2}$ and $(^3H_6,t_{2g})_{S=3/2}$ levels amounts to less than 5 times the maximum phonon energy. As the Br/Cl ratio is gradually increased, emission C abruptly emerges in $CsCaCl_{0.75}Br_{2.25}:Tm^{2+}$ and intensifies in $CsCaBr_3:Tm^{2+}$. In this latter compound, four emissions are observed at 20 K: A, B, C, and D. When the bromide anions are gradually substituted for iodide, the number of observed emissions still remains the same. Besides, emission B remains the most intense emission at 20 K. However, in $CsCaI_3:Tm^{2+}$, emissions E and F suddenly appear and emission D emerges as the most dominant emission at 20 K. Up to now emission F has only been reported in $CsCaI_3:Tm^{2+}$. [14,17] Its absence in $CsCaCl_3:Tm^{2+}$ and $CsCaBr_3:Tm^{2+}$ might be related to the close proximity of neighbouring levels in combination with relatively higher phonon energies as compared to $CsCaI_3:Tm^{2+}$. Emission

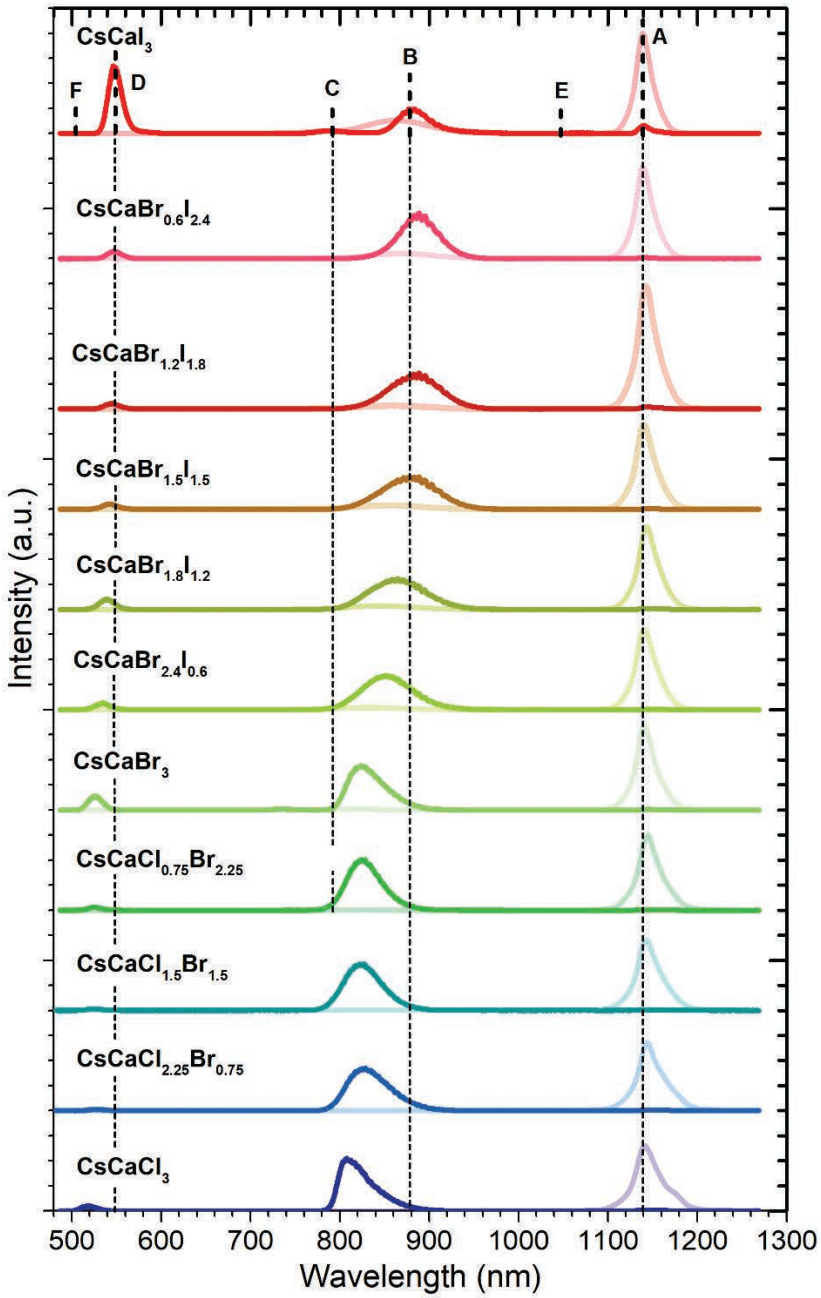

Figure 4.8: Emission spectra of the $CsCa(Cl/Br)_3:Tm^{2+}$ and $CsCa(Br/I)_3:Tm^{2+}$ samples as obtained after excitation into the $(^3F_4,t_{2g})_{S=1/2}$ levels. The full colored curves represent the spectra at 20 K, while the softly colored ones were made at 300 K. The spectra are corrected for the sensitivity of detection and scaled on the measured QE of $^2F_{5/2}\rightarrow{}^2F_{7/2}$ emission A at room temperature.

E was previously also observed in $CsCaCl_3:Tm^{2+}$ and $CsCaBr_3:Tm^{2+}$. [12,13] The reason for its absence in our low temperature spectra is not clear. Since the $(^3F_4,t_{2g})_{S=3/2}$ state has J=9/2 and the $^2F_{5/2}$ state J=5/2, it is forbidden by the ΔJ=1 or 0 selection rule and will therefore appear very weak in intensity. Furthermore, the much larger energy gap between the $(^3F_4,t_{2g})_{S=3/2}$ and $(^3H_6,t_{2g})_{s=1/2}$ levels in $CsCaI_3:Tm^{2+}$ combined with lower phonon energies will prolong an immediate quenching via multi-phonon relaxation, as might be the case for $CsCaCl_3:Tm^{2+}$ and $CsCaBr_3:Tm^{2+}$.

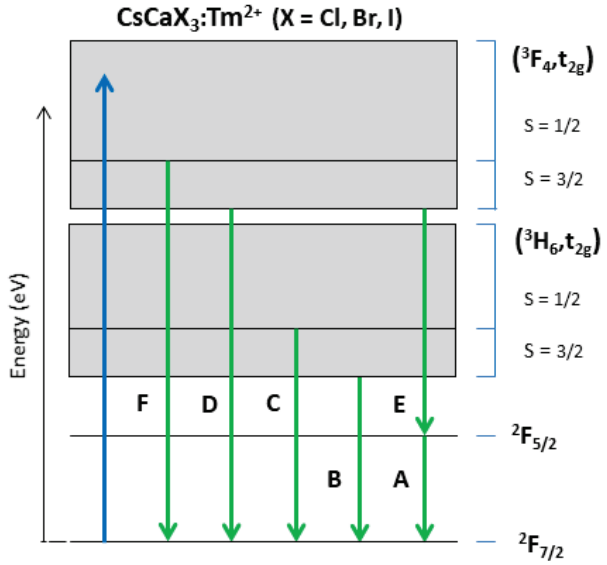

Figure 4.9: Schematic energy level diagram for the $CsCa(Cl/Br)_3:Tm^{2+}$ and $CsCa(Br/I)_3:Tm^{2+}$ samples at 20 K and after exciting into the $(^3F_4,t_{2g})_{S=1/2}$ levels. The six distinct Tm^{2+} emissions are labelled from A to F.

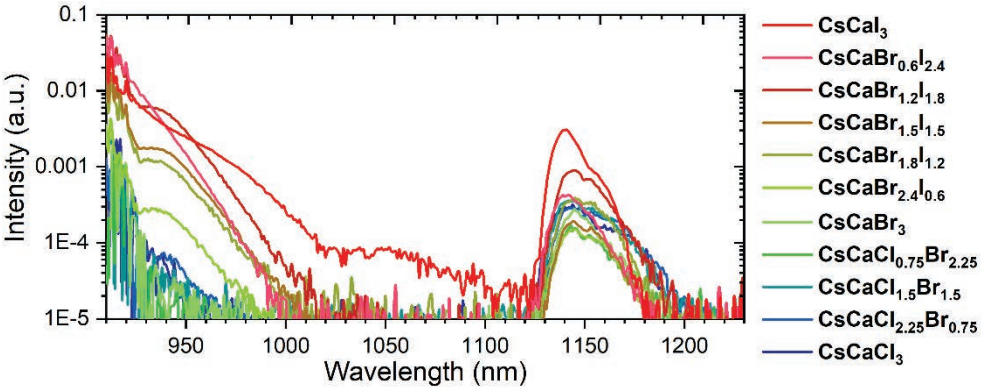

Figure 4.10: Close-up emission spectra of the $CsCa(Cl/Br)_3:Tm^{2+}$ and $CsCa(Br/I)_3:Tm^{2+}$ samples as centred on emissions A (1140 nm) and E (1050 nm). The spectra are plotted on a log scale as to provide a better view on the possible presence these emissions. At around 950 nm a mysterious small shoulder is observed for emission B (815-880 nm).

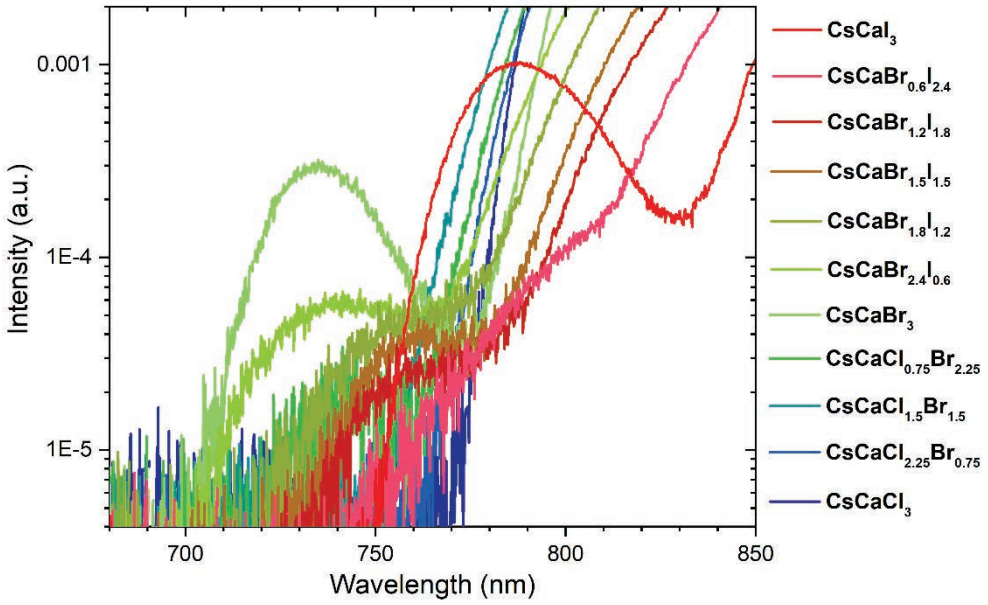

Figure 4.11: Close-up emission spectra of the $CsCa(Cl/Br)_3:Tm^{2+}$ and $CsCa(Br/I)_3:Tm^{2+}$ samples as centred on emission C (745-790 nm). In analogy to figure 4.10, the spectra are plotted on a log scale.

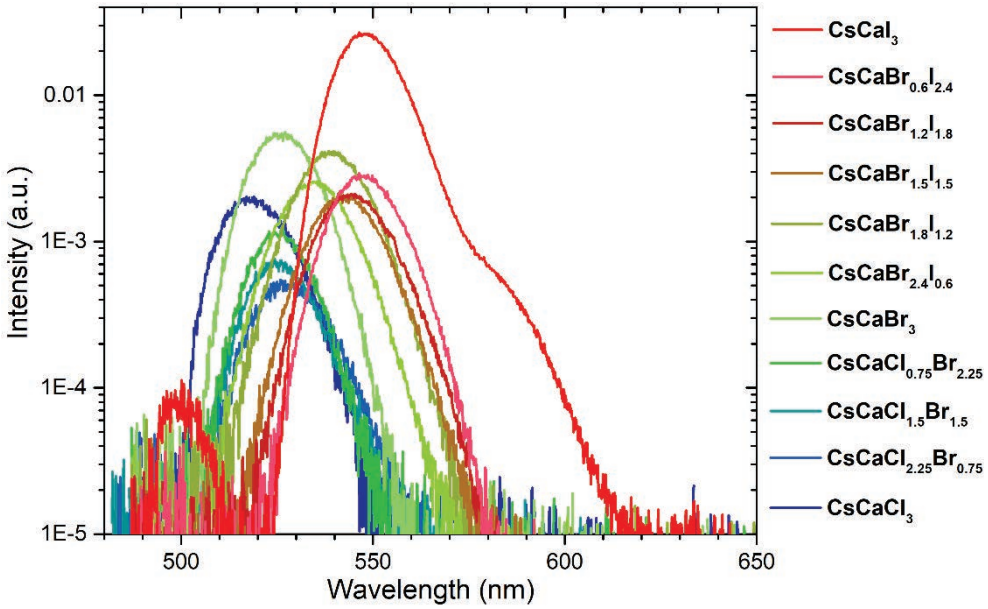

Figure 4.12: Close-up emission spectra of the $CsCa(Cl/Br)_3:Tm^{2+}$ and $CsCa(Br/I)_3:Tm^{2+}$ samples as centred on emissions D (520-550 nm) and F (500 nm). In analogy to figure 4.10, the spectra are plotted on a log scale. In case of $CsCaI_3:Tm^{2+}$ a small shoulder is observed for emission D at around 590 nm.

4.3.3 Luminescence Quantum Efficiency

For each of the $CsCa(Cl/Br)_3:Tm^{2+}$ and $CsCa(Br/I)_3:Tm^{2+}$ samples, the internal Quantum Efficiency (QE) of $^2F_{5/2}\rightarrow{}^2F_{7/2}$ emission A was determined after excitation into the lower energy $(^3H_6,t_{2g})_{S=1/2}$ levels. The obtained values are listed in table 4.5 in Appendix A and are plotted versus the Br/Cl and Br/I ratios in red in figure 4.13. For the $CsCa(Br/I)_3:Tm^{2+}$ samples, the room temperature presence of the $(^3H_6,t_{2g})_{S=3/2}\rightarrow{}^2F_{7/2}$ emission B allows it to determine its QE. These values are displayed in blue.

When adding up the QE contributions of emission A and B, the overall QE value ranges from 40-70%. However, it appears that the QE values of emission A in the mixed compounds undergo fluctuations with composition. These fluctuations were reproduced by a second independent measurement on another badge of the same sample, see the orange datapoints. The absorption, as displayed in black and grey, on the other hand stays almost constant over the entire sample series. This was also observed in the $4f^{13}\rightarrow4f^{13}$ absorption spectra back in figure 4.5. As the fluctuations do not have a correlation with composition and are not caused by measurement mistakes or sample degradation, we believe they are more likely related to intrinsic sample differences such as perhaps different defect densities. The large fluctuations prevent us to draw any conclusions on the QE of emission A for the $CsCa(Cl/Br)_3:Tm^{2+}$ sample series. Nevertheless, we are able to recognise a clear trend for the $CsCa(Br/I)_3:Tm^{2+}$ sample series. From $CsCaBr_{2.4}I_{0.6}:Tm^{2+}$ onwards, the QE of emission A decreases rapidly from around 70% to a mere value of around 15% at $CsCaI_3:Tm^{2+}$. In the same interval, the QE of emission B increases from around 7 to 45% and displays an anti-

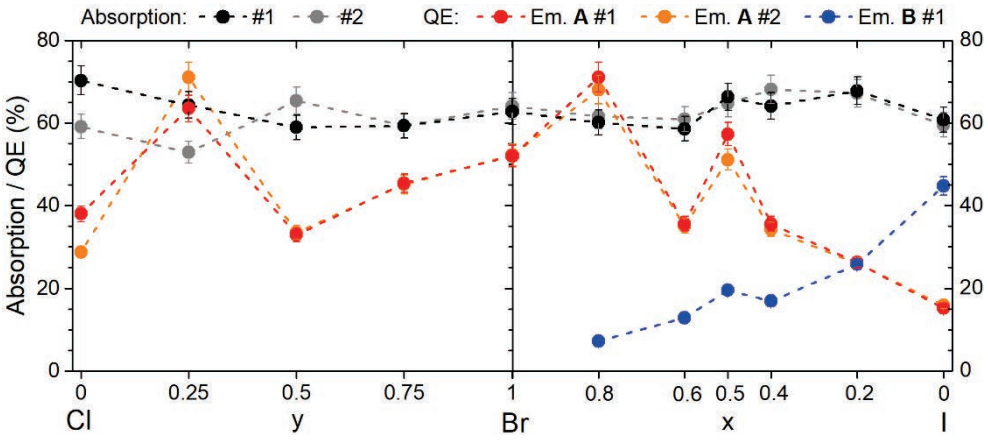

Figure 4.13: Quantum efficiency of the $^2F_{5/2}\rightarrow{}^2F_{7/2}$ emission A (red) and absorption (black) plotted versus the Br/Cl and Br/I ratio in the samples. For the $CsCa(Br/I)_3:Tm^{2+}$ samples, the QE of $(^3H_6,t_{2g})_{S=3/2}\rightarrow{}^2F_{7/2}$ emission B could also be determined (blue). Photoexcitation occurred at room temperature into the $(^3H_6,t_{2g})_{S=1/2}$ levels. The fluctuation among the QE datapoints was reproduced by a second independent measurement (orange). The absorption remained the same (grey).

correlated trend with respect to emission A. This feature was examined further by the room temperature decay curves presented in figure 4.14. Upon gradually traversing from Cl→Br→I, the decay curves related to emission B lengthen and the luminescence lifetime increases. The decay curves related to emission A, on the other hand, display a clear risetime due to a feeding phenomenon as measured and numerically modelled by us before [20,30,31]. Counter intuitively, it is observed that the risetime increases from Cl→Br→I, while the energy gap between the $(^3H_6,t_{2g})_{S=3/2}$ and $^2F_{5/2}$ levels decreases. This signifies a slower feeding rate. The inset shows that the lifetime of emission B and observed risetime for emission A are close in values for each of the compositions. It indicates that at room temperature there is a direct feeding from the $(^3H_6,t_{2g})_{S=3/2}$ to the $^2F_{5/2}$ levels, which was also concluded in our study on $CaX_2:Tm^{2+}$ (X = Cl, Br, I). [9] This explains the reversed trend in the anti-correlated behaviour of their QEs, as shown in figure 4.13. In the next section, we will study the quenching of the various Tm^{2+} emissions in $CsCaI_3:Tm^{2+}$ and zoom-in on the quenching mechanism of emission B and the feeding of the $^2F_{5/2}$ levels.

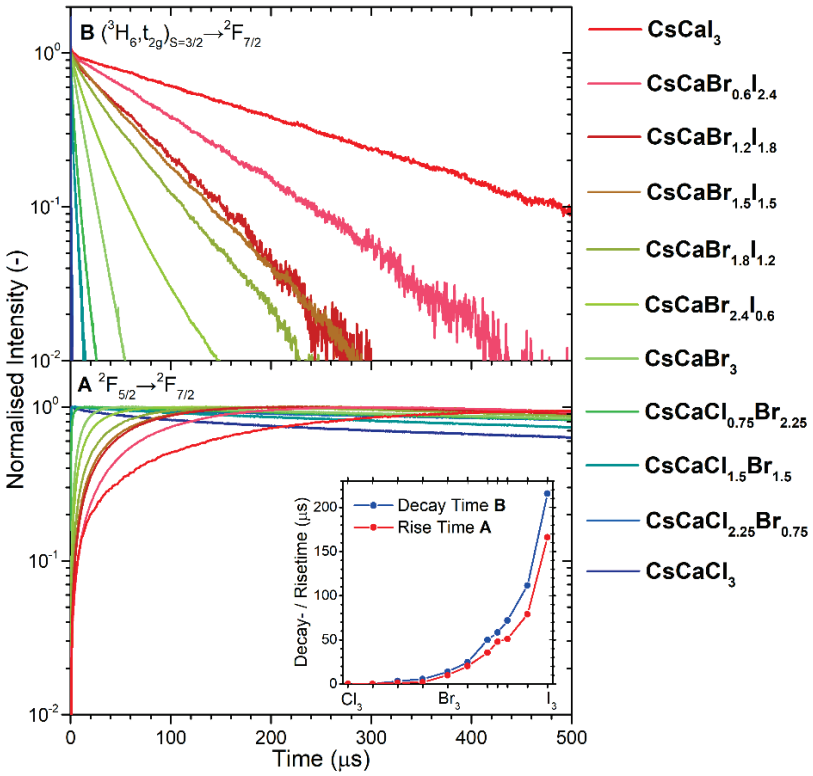

Figure 4.14: Room temperature decay curves of $(^3H_6,t_{2g})_{S=3/2}\rightarrow{}^2F_{7/2}$ emission B (top) and $^2F_{5/2}\rightarrow{}^2F_{7/2}$ emission A (bottom) after laser excitation into the $(^3H_6,t_{2g})_{S=1/2}$ levels. The curves of emission A display a clear risetime phenomena. The inset shows that its duration is close to the decay time of emission B.

4.3.4 Temperature-Dependent Luminescence

Since all of the observed emissions (A to F) are present in $CsCaI_3:Tm^{2+}$, we have decided to select this compound for a more detailed study on the luminescence quenching. This also allows it to disclose why, in this compound, emission D is much stronger than emission B.

Figure 4.15 shows a 3D-plot of the emission spectra versus temperature, as acquired after excitation into the $(^3F_4,t_{2g})_{S=1/2}$ levels. The spectra at 20 K and 300 K were previously presented in figure 4.8. The inset provides additional quantitative information on the luminescence behaviour. The excited-state absorption studies of de Jong et al. [7,8] revealed that for $CsCaCl_3:Tm^{2+}$ and $CsCaBr_3:Tm^{2+}$, the configurational coordinate displacement between the different $4f^{12}5d^1(t_{2g})$ states is negligible. Although such thorough information is missing for $CsCaI_3:Tm^{2+}$, we will assume that this displacement is also very small and that the $4f^{12}5d^1$-$4f^{12}5d^1$ quenching is therefore favoured by Multi-Phonon Relaxation (MPR).

As becomes apparent, $(^3F_4,t_{2g})_{S=1/2}\rightarrow{}^2F_{7/2}$ emission F already starts to quench at 20 K. The temperature-dependent emission spectra in figure 4.16 show that at 130 K it can no longer be perceived and has quenched completely.

Both $(^3F_4,t_{2g})_{S=3/2}\rightarrow{}^2F_{7/2}$ emission D and $(^3F_4,t_{2g})_{S=3/2}\rightarrow{}^2F_{5/2}$ emission E emerge from the lowest energy $(^3F_4,t_{2g})_{S=3/2}$ level and will therefore have a similar temperature dependence. The energy gap between the $(^3F_4,t_{2g})_{S=3/2}$ and $(^3H_6,t_{2g})_{s=1/2}$ levels is around 3025 cm^{-1} or 18 vibrational quanta. For $CsCaCl_3:Tm^{2+}$ and $CsCaBr_3:Tm^{2+}$, the gap between the $(^3F_4,t_{2g})_{S=3/2}$ and $(^3H_6,t_{2g})_{s=1/2}$ levels is of similar size to $CsCaI_3:Tm^{2+}$ and respectively amounts to around 3020 cm^{-1} and 2960 cm^{-1}. However, the required amount of vibrational quanta to bridge it is smaller and respectively resembles 10 and 14 quanta. This might explain why, at low temperature, emission D is more intense in $CsCaI_3:Tm^{2+}$ as compared to $CsCaCl_3:Tm^{2+}$ and $CsCaBr_3:Tm^{2+}$. Besides, in $CsCaI_3:Tm^{2+}$, the energy gap between the $(^3F_4,t_{2g})_{S=3/2}$ and $(^3H_6,t_{2g})_{s=1/2}$ levels is larger than the gap between the $(^3H_6,t_{2g})_{s=3/2}$ and $^2F_{5/2}$ levels, which is close to 2560 cm^{-1}. This is opposed to $CsCaCl_3:Tm^{2+}$ and $CsCaBr_3:Tm^{2+}$ where the former gap is smaller than the latter. It explains why emission D remains present up to 320 K and why at low temperature it is much more dominant as compared to emission B. A much similar, peculiar, situation was recently encountered by us in when comparing the temperature-dependent luminescence of $CaCl_2:Tm^{2+}$, $CaBr_2:Tm^{2+}$ and $CaI_2:Tm^{2+}$. [20]

As emission D quenches, it will feed the lower lying $(^3H_6,t_{2g})_{s=1/2}$ levels from which $(^3H_6,t_{2g})_{S=1/2}\rightarrow{}^2F_{7/2}$ emission C occurs. As the energy gap between the $(^3H_6,t_{2g})_{S=1/2}$ and $(^3H_6,t_{2g})_{S=3/2}$ levels amounts to 1360 cm^{-1} and resembles only 8 vibrational quanta, emission C will quench already at very low temperatures and will feed the $(^3H_6,t_{2g})_{S=3/2}$ levels. However, the feeding from the $(^3F_4,t_{2g})_{S=3/2}$ levels, as caused by the quenching of emission D, results in its presence even at room temperature. Evidence for this is provided in the

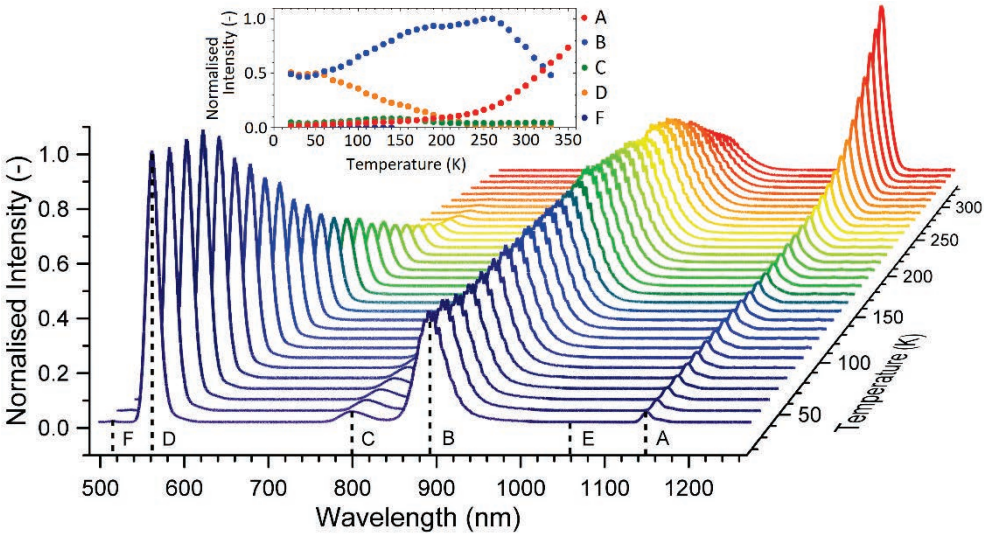

Figure 4.15: 3D-Plot showing the qualitative behaviour of the six Tm^{2+} emissions (A to F) in $CsCaI_3$:Tm^{2+} over temperature. The complementary inset presents the integrated luminescence signals over temperature and allows a qualitative description of the observed trends. The spectra are corrected for the sensitivity of detection and normalized on the $(^3F_4,t_{2g})_{S=3/2}\rightarrow{}^2F_{7/2}$ emission D at 20 K. Photoexcitation occurred into the $(^3F_4,t_{2g})_{S=1/2}$ levels at 455 nm.

temperature-dependent emission spectra in figure 4.17. In addition to that, the inset in figure 4.15 reveals a decreasing intensity trend for emission C up to 40 K and a sudden increase in intensity as emission D grows weaker.

From the $(^3H_6,t_{2g})_{S=3/2}$ levels emission B occurs. The inset in figure 4.15 displays a downward intensity trend for this emission at temperatures below 40 K. From 40 K onwards, however, it starts to increase firmly up to a temperature of 260 K. This abrupt increase in intensity indicates a sequential feeding route from $(^3F_4,t_{2g})_{S=3/2}\rightarrow$ $(^3H_6,t_{2g})_{S=1/2}\rightarrow$ $(^3H_6,t_{2g})_{S=3/2}$. Above 260 K the intensity of emission B decreases again, while that of emission A increases most strongly. The energy gap between the $(^3H_6,t_{2g})_{S=3/2}$ and $^2F_{5/2}$ levels resembles around 2560 cm^{-1}, or 15 vibrational quanta. However, since this quenching involves a $4f^{12}5d^1\rightarrow4f^{13}$ relaxation, the quenching might not necessarily occur via MPR. In the next subsection we will further investigate the quenching of emission B. To ease the analysis we will excite directly into the lower energy $(^3H_6,t_{2g})_{S=1/2}$ levels, which allows us to solely monitor the luminescence intensities of emissions A, B and C.

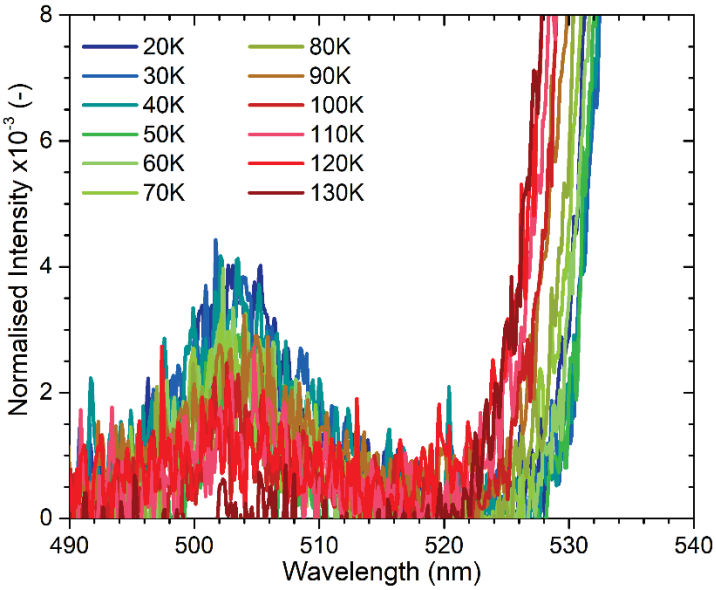

Figure 4.16: Close-up on the temperature-dependent emission spectra of $(^3F_4,t_{2g})_{S=1/2}\rightarrow{}^2F_{7/2}$ emission F in $CsCaI_3:Tm^{2+}$. Photoexcitation occurred into the $(^3F_4,t_{2g})_{S=1/2}$ levels at 455 nm. The sharp onset on the right of the spectrum is related to $(^3F_4,t_{2g})_{S=3/2}\rightarrow{}^2F_{7/2}$ emission D.

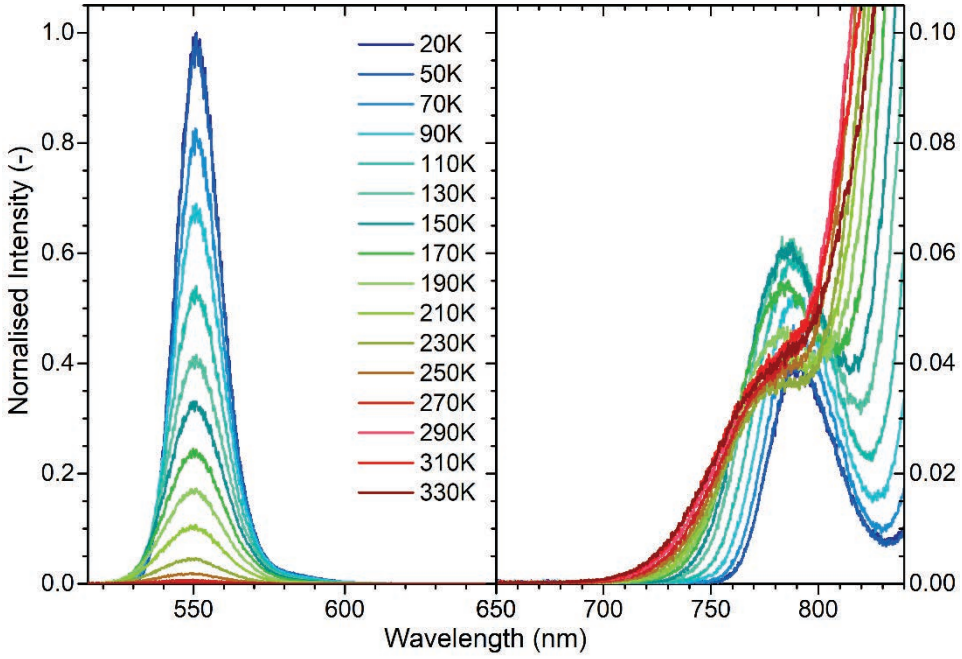

Figure 4.17: Temperature-dependent emission spectra of $(^3F_4,t_{2g})_{S=3/2}\rightarrow{}^2F_{7/2}$ emission D (left) and $(^3H_6,t_{2g})_{S=1/2}\rightarrow{}^2F_{7/2}$ emission C (right) in $CsCaI_3:Tm^{2+}$. Photoexcitation occurred into the $(^3F_4,t_{2g})_{S=1/2}$ levels at 455 nm.

Quenching Mechanisms of Emission B

The temperature-intensity plots in figure 4.18 and 4.19 once more emphasise the relation between the quenching of $(^3H_6,t_{2g})_{S=3/2}\rightarrow{}^2F_{7/2}$ emission B and the subsequent feeding and intensification of $^2F_{5/2}\rightarrow{}^2F_{7/2}$ emission A. In case of $CsCaBr_3:Tm^{2+}$ and $CsCaI_3:Tm^{2+}$, the relatively strong presence of $(^3H_6,t_{2g})_{S=3/2}\rightarrow{}^2F_{7/2}$ emission C allows for a clear separation with emission B and the integrated intensity curves are added to the plots. As discussed in the previous subsection, emission C rapidly undergoes quenching via MPR and feeds the $(^3H_6,t_{2g})_{S=3/2}$ levels, causing for a slight intensification of emission B.

For emission B, the temperature onset of the quenching undergoes a clear shift towards higher temperatures when traversing from Cl→Br→I. This, despite the fact that the energy gap between the $(^3H_6,t_{2g})_{S=3/2}$ and $^2F_{5/2}$ levels decreases along the series, from around 3610 to 2560 cm^{-1}, and a significant increase of the related Stokes shift, from around 824 to 1015 cm^{-1}, which presumes a larger configuration displacement between the two levels. Besides, the drop-off in the intensity curves of emission B in figures 4.18 and 4.19 becomes less steep from Cl→Br→I and the retrieved Arrhenius deactivation energies increase. Furthermore, the temperature at which the intensity of emission B has reached half of its original value, referred to as $T_{50\%}$, also shifts to higher values. An overview plot of the trends among these parameters, as a function of the Br/Cl and Br/I ratios in the samples, is provided in figure 4.20 with their values listed in table 4.6 in Appendix A.

Interband Crossing

The quenching of emission B involves a non-radiative $4f^{12}5d^1\rightarrow4f^{13}$ transition that can take place via Interband Crossing (IC). This quenching mechanism involves the crossing point between the parabolas representing the $(^3H_6,t_{2g})_{S=3/2}$ and $^2F_{5/2}$ states, which can be visualised in a Configurational Coordinate Diagram (CCD). In Appendix B, additional background information on this topic is provided. [34,35] The gathered data in table 4.6 in Appendix A yields the input parameters to draw the Configurational Coordinate Diagram (CCD) displayed in figure 4.21. These diagrams immediately reveal that the IC energy barrier ε, associated with the crossing point, is to large extent dependent upon the Stokes shift of the $(^3H_6,t_{2g})_{S=3/2}\rightarrow{}^2F_{7/2}$ emission and the energy gap between the $(^3H_6,t_{2g})_{S=3/2}$ and $^2F_{5/2}$ states. As the related Stokes shift increases from Cl→Br→I and the energy gap becomes smaller, the IC energy barrier will decrease from Cl→Br→I. The crossing point will therefore be situated at lowest energy for $CsCaI_3:Tm^{2+}$, followed by $CsCaBr_3:Tm^{2+}$ and lastly $CsCaCl_3:Tm^{2+}$. Emission B is then predicted to undergo quenching in the order of I→Br→Cl. However, this order does not match the trend of the retrieved Arrhenius deactivation energies and figures 4.18 and 4.19 portray an exact opposite quenching behaviour from Cl→Br→I.

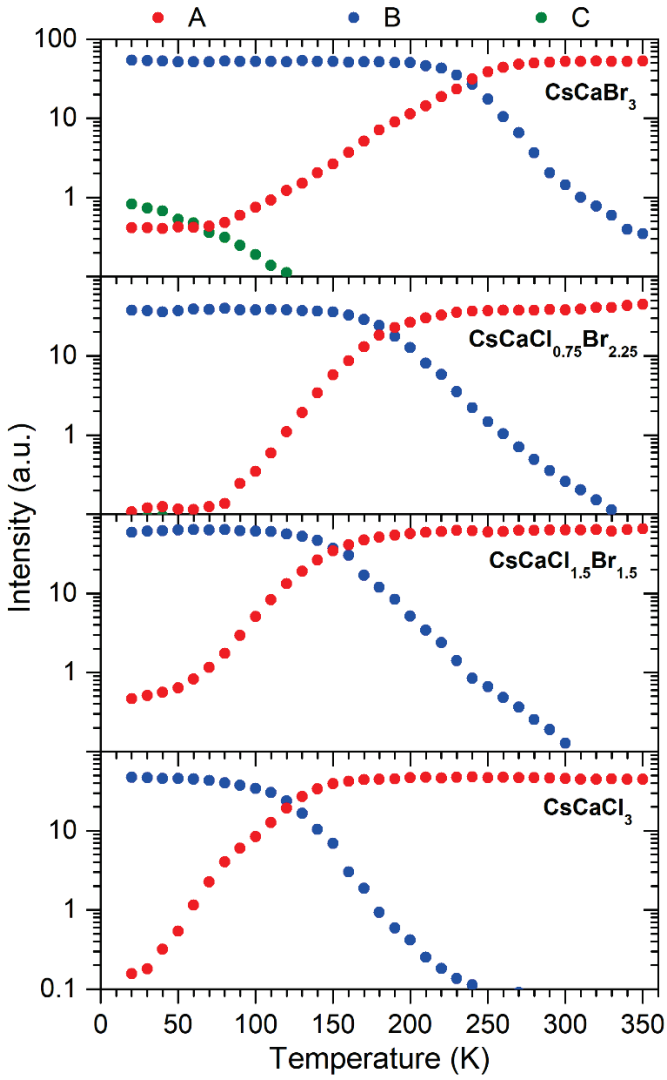

Figure 4.18: Temperature-intensity plots revealing the luminescence behaviour of $^2F_{5/2}\rightarrow{}^2F_{7/2}$ emission A and $(^3H_6,t_{2g})_{S=3/2}\rightarrow{}^2F_{7/2}$ emission B in the $CsCa(Cl/Br)_3:Tm^{2+}$ samples over temperature. The relatively strong presence of $(^3H_6,t_{2g})_{S=1/2}\rightarrow{}^2F_{7/2}$ emission C in $CsCaBr_3:Tm^{2+}$ allowed it to be monitored as well. The curves are corrected for the sensitivity of correction and scaled on the QE of $^2F_{5/2}\rightarrow{}^2F_{7/2}$ emission A at room temperature. Photoexcitation occurred into the $(^3H_6,t_{2g})_{S=1/2}$ levels.

Previously, Koster et al. [36] used a basic fitting routine to describe the quenching of emission B, in $CsCaCl_3:Tm^{2+}$ and $CsCaBr_3:Tm^{2+}$, via IC by fitting its luminescence lifetime over temperature. It was suggested that the related IC energy barrier in $CsCaCl_3:Tm^{2+}$ could be much smaller than that in $CsCaBr_3:Tm^{2+}$. The interpretation of our data, however, suggests that the barrier in $CsCaCl_3:Tm^{2+}$ is larger than in $CsCaBr_3:Tm^{2+}$.

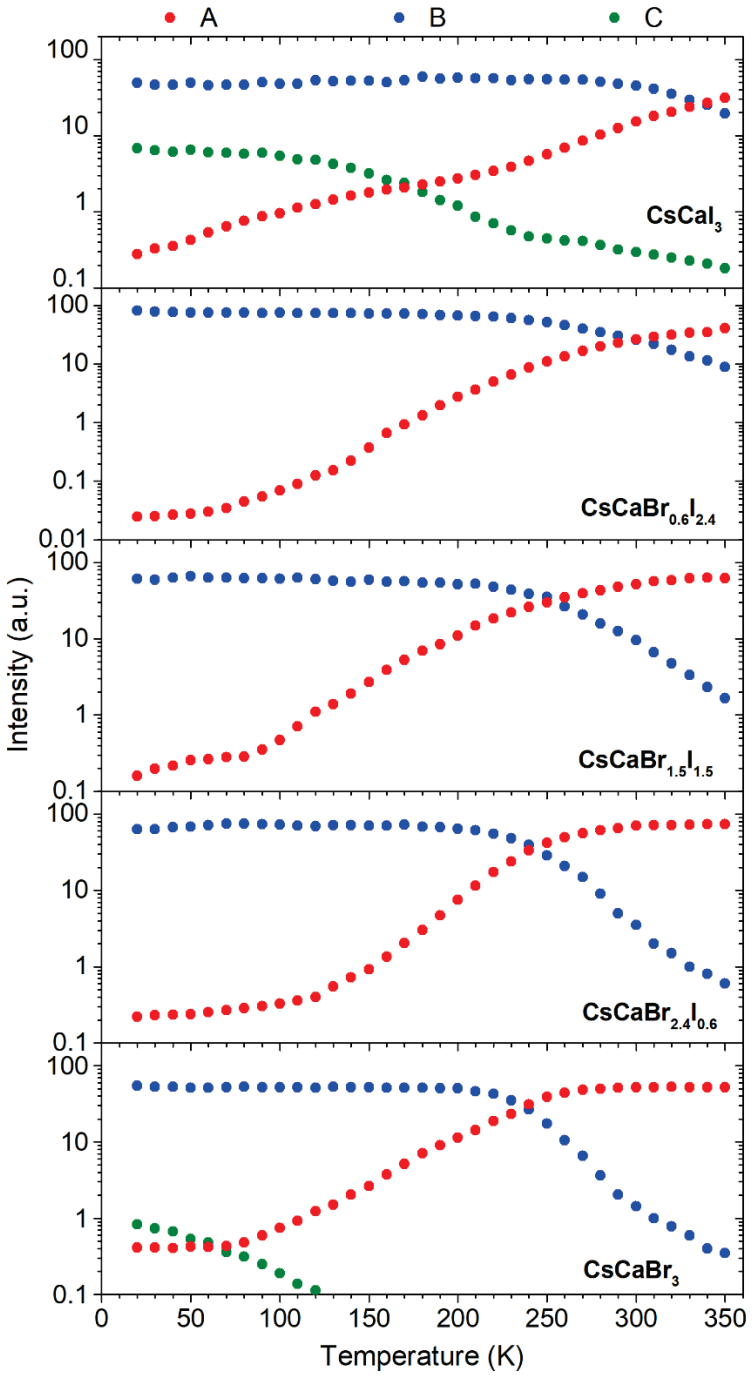

Figure 4.19: Temperature-intensity plots analogous to figure 4.18, but related to the $CsCa(Br/I)_3:Tm^{2+}$ samples.

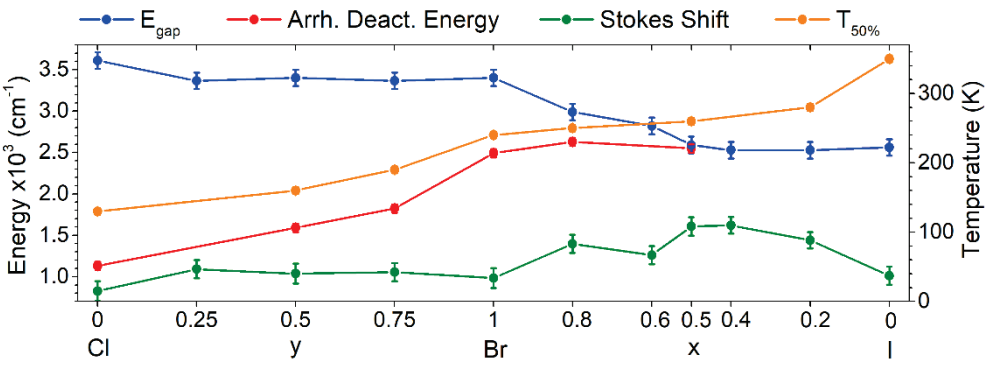

Figure 4.20: Diagram showing the behaviour of important $(^3H_6,t_{2g})_{S=3/2}$-$^2F_{5/2}$ quenching parameters as plotted versus the Br/Cl and Br/I ratios in the samples. Displayed are: the energy gap *Egap* between the $(^3H_6,t_{2g})_{S=3/2}$ and $^2F_{5/2}$ levels, the Stokes shift and the Arrhenius deactivation energy and $T_{50\%}$ of the $(^3H_6,t_{2g})_{S=3/2} \rightarrow {}^2F_{7/2}$ emission. Values are provided in table 4.6 in Appendix A.

The non-radiative transition rate related to the process of IC is governed by the relation: $W = s \cdot e^{-\varepsilon/kT}$. [20,37] In this relation: k is the Boltzmann constant, T represents temperature and s is a constant that represents the product of the transition probability between the $(^3H_6,t_{2g})_{S=3/2}$ and $^2F_{5/2}$ states and a frequency with which the excited state reaches the intersection point. This latter constant is weakly dependent upon temperature. [37] A mathematical interpretation of the non-radiative transition rate W in relation to the intensity curves of emission B in figures 4.18 and 4.19, shows that the onset of the quenching would be governed by s while the slope of the intensity curve is determined by ε and hence linked to the Arrhenius deactivation energy. Although the onset of the

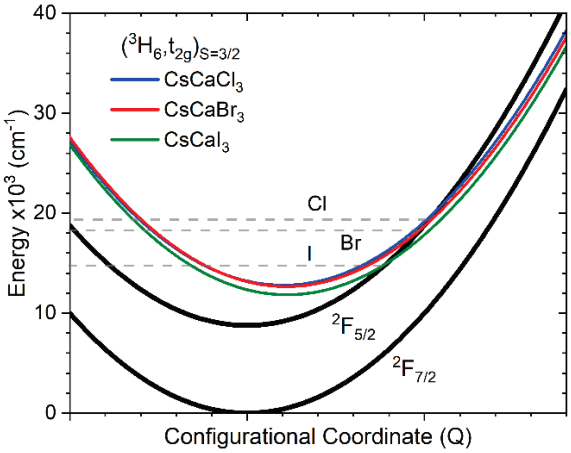

Figure 4.21: Configurational coordinate diagram revealing the Tm^{2+} $^2F_{5/2}$, $^2F_{5/2}$ and $(^3H_6,t_{2g})_{S=3/2}$ state parabolas. The latter ones are drawn for $CsCaX_3:Tm^{2+}$ (X = Cl, Br, I) using the information in Appendix B. Note: all state parabolas are drawn here with equal elastic force constant.

quenching of emission B could be explained by a different value for *s*, there is still a mismatch in trends between the IC energy barrier ε and the Arrhenius deactivation energy E_{deact}. This does not enable it to couple the quenching of emission B to the process of IC. Nevertheless it is still possible that this process is triggered at higher temperatures. This was also the case in our recent study [9], where we investigated the quenching of emission B in $CaBr_2$:Tm^{2+} via numerical modelling of the non-radiative relaxation rates of IC and MPR.

Multi-Phonon Relaxation

The quenching of $4f^{12}5d^1 \rightarrow 4f^{13}$ emission B can also occur via MPR. This mechanism was previously opted by Grimm and Beurer et al. [12-14] However, in these studies the energy gaps between the $(^3H_6,t_{2g})_{S=3/2}$ and $^2F_{5/2}$ levels was determined from absorption spectra and amounted to 2760, 2620 and 2700 cm^{-1} for $CsCaCl_3$:Tm^{2+}, $CsCaBr_3$:Tm^{2+} and $CsCaI_3$:Tm^{2+} respectively. The required amount of vibrational quanta to bridge these gaps were respectively calculated on 9, 13 and 16 quanta. This would mean that emission B undergoes quenching in the order of Cl→Br→I, which is exactly what is observed in figures 4.18 and 4.19. However, as the $(^3H_6,t_{2g})_{S=3/2}$ and $^2F_{5/2}$ levels are shifted in configurational coordinates, the energy gaps are more accurately determined from a subtraction of the $(^3H_6,t_{2g})_{S=3/2} \rightarrow {}^2F_{7/2}$ and $^2F_{5/2} \rightarrow {}^2F_{7/2}$ emission energies. If we perform such a calculation based on figure 4.8 and table 4.3, the energy gaps for $CsCaCl_3$:Tm^{2+}, $CsCaBr_3$:Tm^{2+} and $CsCaI_3$:Tm^{2+} respectively amount to around 3610, 3400 and 2560 cm^{-1}. Upon using the same phonon energies reported by Grimm et al. [6], the gaps respectively resemble 12, 16, and 15 vibrational quanta. In this sense, emission B would be expected to quench first in $CsCaCl_3$:Tm^{2+} and at almost equal temperature in $CsCaBr_3$:Tm^{2+} and $CsCaI_3$:Tm^{2+}. Figures 4.18 and 4.19 show that emission B indeed quenches first in $CsCaCl_3$:Tm^{2+} and then in $CsCaBr_3$:Tm^{2+}. However, it quenches at a much higher temperature for $CsCaI_3$:Tm^{2+}. Nevertheless, the calculated energy gap and required amount of phonons, as determined using our approach, are quite close to those found in the excited states absorption study by Karbowiak et al.. [38] As the quenching involves a $4f^{12}5d^1 \rightarrow 4f^{12}$ transition, and not a $4f^{x-1}5d^1 \rightarrow 4f^{x-1}5d^1$ or textbook $4f^x \rightarrow 4f^x$ transition, the electron-phonon coupling will be stronger. From Moos et al. [39] it follows that for $4f^x \rightarrow 4f^x$ transitions of Nd^{3+}, Dy^{3+} and Ho^{3+} in LaX_3 (X = F, Cl, Br), the coupling constant increases with the size of the crystal field splitting. This is confirmed also in a study by Riseberg et al. [40] on similar materials. It is thus very likely that the electron-phonon coupling is weaker in $CsCaI_3$:Tm^{2+} than in, for instance, $CsCaBr_3$:Tm^{2+} and hence more phonons would be required to bridge the gap between the $(^3H_6,t_{2g})_{S=3/2}$ and $^2F_{5/2}$ levels. This would result in a higher quenching temperature for emission B in $CsCaI_3$:Tm^{2+}, as compared to for instance $CsCaBr_3$:Tm^{2+}, and could hence perhaps explain the observed trends in figures 4.18 and 4.19.

Temperature-dependent Excitation Spectra

As the quenching mechanism related to emission B is perhaps explained by MPR and different electron-phonon coupling constants, we have decided to extend the investigation by studying the temperature-dependent excitation spectra of $^2F_{5/2}\rightarrow{}^2F_{7/2}$ emission A and $(^3H_6,t_{2g})_{S=3/2}\rightarrow{}^2F_{7/2}$ emission B in $CsCaI_3:Tm^{2+}$. Figure 4.22 shows these temperature-dependent excitation spectra as normalised on the $(^3H_6,t_{2g})_{S=1/2}$ band at longer wavelength. The excitation spectra acquired on emission B (lower panel) reveal that the intensity of the $(^3F_4,t_{2g})$ and higher energy levels undergo a relative increase over temperature, as compared to the $(^3H_6,t_{2g})$ levels. This can be explained by the fact that excitation into the $(^3F_4,t_{2g})$ levels at low temperature results predominantly in $(^3F_4,t_{2g})_{S=3/2}\rightarrow{}^2F_{7/2}$ emission D, and not in $(^3H_6,t_{2g})_{S=3/2}\rightarrow{}^2F_{7/2}$ emission B. As the temperature increases, emission D undergoes quenching and feeds the $(^3H_6,t_{2g})$ levels from which emissions B and C occur. However, this feeding will primarily result into emission B, because $(^3H_6,t_{2g})_{S=1/2}\rightarrow{}^2F_{7/2}$ emission C already starts to quench at 20 K. Besides, a direct excitation in the $(^3H_6,t_{2g})$ levels will, at all temperatures, result primarily in emission B. The excitation spectra thus confirm the sequential feeding route from $(^3F_4,t_{2g})_{S=3/2}\rightarrow$ $(^3H_6,t_{2g})_{S=1/2}\rightarrow$ $(^3H_6,t_{2g})_{S=3/2}$. A comparison between the spectra acquired on emission A (top panel) and B (lower panel), reveals that between 20 K and 200 K there is a significant difference in energy and shape of the excitation bands. As the temperature increases to above 250 K, the excitation bands that result in emission A start to broaden-up and shift in energy in such a way that at 300 K the

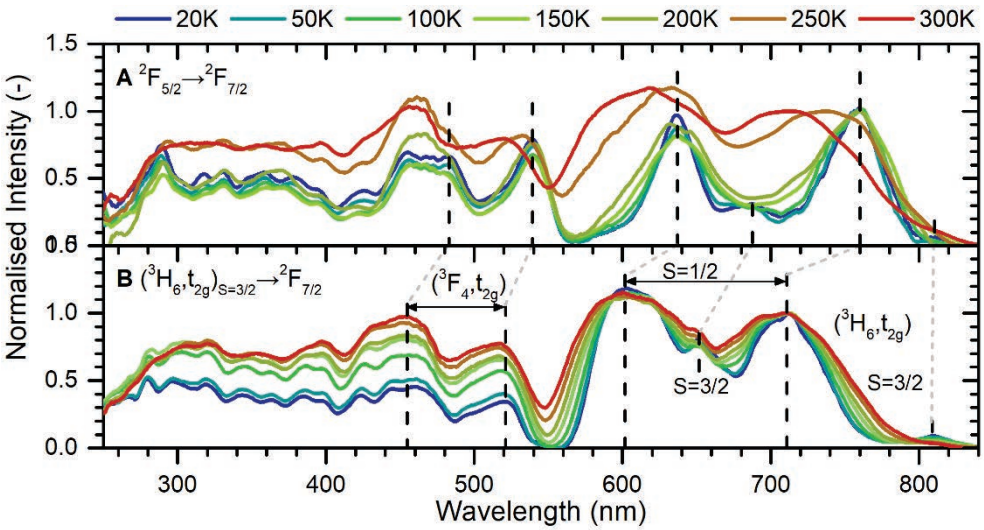

Figure 4.22: Excitation spectra as acquired on $^2F_{5/2}\rightarrow{}^2F_{7/2}$ emission A and $(^3H_6,t_{2g})_{S=3/2}\rightarrow{}^2F_{7/2}$ emission B in $CsCaI_3:Tm^{2+}$ at various temperatures. The lowest energy $4f^{12}5d^1$-levels are indicated in the figure. Normalisation occurred on the $(^3H_6,t_{2g})_{S=1/2}$ band at longer wavelength (710-780 nm).

spectra monitoring emission A and B are almost identical.

One explanation for this peculiar observation could be the presence of two luminescent Tm^{2+} sites in the material: a 'dominant' site and a 'minority' site. The Tm^{2+} ions that occupy the 'minority' site are responsible for the weak presence of $4f^{13}\rightarrow4f^{13}$ emission A at low temperature. As these Tm^{2+} ions have a different anion coordination geometry and undergo a large crystal field splitting, a different excitation spectrum is witnessed in figure 4.22. When the temperature increases to 250 K, $4f^{12}5d^{1}\rightarrow4f^{13}$ emission B from the 'dominant' site starts to quench and, consequently, the intensity of $4f^{13}\rightarrow4f^{13}$ emission A from the 'dominant' site increases. It becomes typically a 100x stronger in intensity as compared to emission A from the 'minority' site, which is only visible at low temperature when emission A from the 'dominant' site has no intensity. For temperatures above 250 K, the excitation spectra of emission A now resembles that of the 'dominant' site. The Tm^{2+} ions that occupy this site undergo a smaller crystal field splitting as compared to the 'minority' site. Nevertheless, the Rietveld refinement revealed the presence of a single phase for $CsCaI_3$:Tm^{2+} and also our emission spectra give no hints for the presence of two sites that for example would display multiple emission bands at different energies.

Alternatively, the change in shape of the $4f^{13}\rightarrow4f^{13}$ excitation spectra could perhaps be explained via different thermally-activated non-radiative relaxation routes, as illustrated by the schematics in figure 4.23. Already at low temperature, the excitation spectra as acquired on $^2F_{5/2}\rightarrow{}^2F_{7/2}$ emission A reveal the presence of the $(^3H_6,t_{2g})_{S=3/2}$ levels. It indicates a low

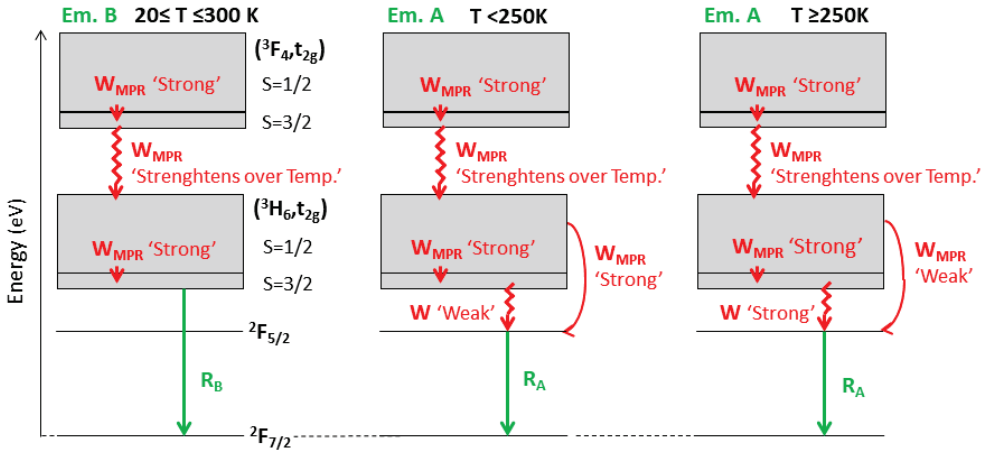

Figure 4.23: Possible explanation for the different excitation spectra as observed in figure 15. The left diagram explains the excitation spectra observed for $(^3H_6,t_{2g})_{S=3/2}\rightarrow{}^2F_{7/2}$ emission B at 20≤ T ≤300 K. The central diagram explains the excitation spectra of $^2F_{5/2}\rightarrow{}^2F_{7/2}$ emission A at T <250 K using a strong W_{MPR} feeding from the $(^3H_6,t_{2g})_{S=1/2}$ levels to the $^2F_{5/2}$ level, whereas the right diagram explains this situation at T ≥250 K.

temperature relaxation route from the $(^3H_6,t_{2g})_{S=3/2}$ levels to the $^2F_{5/2}$ level. However, the temperature-dependent emission spectra in figure 4.15 reveal that $(^3H_6,t_{2g})_{S=3/2}\rightarrow{}^2F_{7/2}$ emission B is very intense at these temperatures. It could therefore be that the $^2F_{5/2}$ level is fed via a different non-radiative relaxation route. In our previous work on $CaX_2:Tm^{2+}$ (X = Cl, Br, I) we came to a similar interpretation. [20] There the low-temperature risetime phenomena in the decay curves of emission A showed a clear discrepancy in timing with the luminescence lifetime of emission B. As the temperature increased, the duration of the risetime increased as well and started to converge to the lifetime measured for emission B. It was proposed that at low temperature, a feeding via MPR occurs from the $(^3H_6,t_{2g})_{S=1/2}$ levels to the $^2F_{5/2}$ level. In case of such a $(^3H_6,t_{2g})_{S=1/2}\rightarrow{}^2F_{5/2}$ relaxation route, it is likely that certain $4f^{12}5d^1$ levels within the $(^3H_6,t_{2g})_{S=1/2}$ bands have a relatively stronger or weaker feeding contribution to the $^2F_{5/2}$ level as compared to the $(^3H_6,t_{2g})_{S=1/2}\rightarrow(^3H_6,t_{2g})_{S=3/2}\rightarrow{}^2F_{5/2}$ relaxation route. If we assume the $(^3H_6,t_{2g})_{S=1/2}\rightarrow{}^2F_{5/2}$ route to be dominant at low temperature, the excitation spectra as acquired on $^2F_{5/2}\rightarrow{}^2F_{7/2}$ emission A could have a different shape. With the profound quenching of $(^3H_6,t_{2g})_{S=3/2}\rightarrow{}^2F_{7/2}$ emission B at 250 K, the $(^3H_6,t_{2g})_{S=3/2}\rightarrow{}^2F_{5/2}$ relaxation route is likely to become the dominant $^2F_{5/2}$ feeding route. The excitation spectra as acquired on emissions A and B would then have a similar shape.

4.4 Summary and Conclusions

In this study we systematically vary the Cl/Br and Br/I ratios in $CsCaX_3:Tm^{2+}$ (X = Cl, Br, I) compounds. A structural analysis reveals that the samples exhibit the cubic $CaTiO_3$ perovskite structure, with space group $Pm\bar{3}m$, from $CsCaCl_3$ up to $CsCaBr_{1.5}I_{1.5}$. As the Br/I ratio is increased further, the lattice of the $CsCaBr_{1.2}I_{1.8}$ and $CsCaBr_{0.6}I_{2.4}$ samples adopts the tetragonal $NaNbO_3$ structure with space group $P4/mbm$. The CaX_6 octahedra are now rotated around the crystallographic c-axis. For $CsCaI_3$ the crystal structure finally changes into the orthorhombic $GdFeO_3$ structure with space group $Pbnm$, where the octahedra are both rotated around the c-axis and titled. In all cases, the Tm^{2+} ions occupy the Ca^{2+}-site and exhibit a six-fold octahedral coordination geometry.

Excitation spectra acquired on the Tm^{2+} $^2F_{5/2}\rightarrow{}^2F_{7/2}$ and $(^3H_6,t_{2g})_{S=3/2}\rightarrow{}^2F_{7/2}$ emissions in the samples, reveal that the $4f^{12}5d^1$ $(^3F_4,t_{2g})$ and $(^3H_6,t_{2g})$ levels gradually shift towards longer wavelengths for Cl→Br→I. As a result, the energy gap between the $4f^{12}5d^1$ $(^3H_6,t_{2g})_{S=3/2}$ and the $4f^{13}$ $^2F_{5/2}$ levels becomes smaller. The low temperature emission spectra reveal up to six distinct Tm^{2+} emissions. These emissions also undergo a shift towards longer wavelengths for Cl→Br→I. Moreover, the Stokes shifts between the absorption and emission increases. As the temperature rises, the various $4f^{12}5d^1\rightarrow4f^{13}$ emissions undergo quenching. As the configurational displacement between the $4f^{12}5d^1$ levels is negligible, most of the $4f^{12}5d^1\rightarrow4f^{13}$ emissions will quench via multi-phonon relaxation. In case of the lowest

energy $4f^{12}5d^1 \rightarrow 4f^{13}$ emission, the quenching can occur via multi-phonon relaxation and/or interband crossing. Temperature-intensity plots reveal that the temperature onset of the quenching of this $(^3H_6,t_{2g})_{S=3/2} \rightarrow {}^2F_{7/2}$ emission gradually shifts towards higher temperatures when traversing from Cl→Br→I. In addition, the Arrhenius deactivation energy increases from Cl→Br→I. This is contrary to our expectation as the energy gap between the $(^3H_6,t_{2g})_{S=3/2}$ and $^2F_{5/2}$ levels decreases along the series. An analysis reveals that the process of interband crossing is unable to explain the quenching of the $(^3H_6,t_{2g})_{S=3/2} \rightarrow {}^2F_{7/2}$ emission, as the energy gap and Stokes shift predict it to quenching in the order I→Br→Cl. In case of multi-phonon relaxation, the required amount of phonons to bridge the energy gap in $CsCaCl_3:Tm^{2+}$ is smaller than in $CsCaBr_3:Tm^{2+}$, and about equal for $CsCaBr_3:Tm^{2+}$ and $CsCaI_3:Tm^{2+}$. A decrease of the electron-phonon coupling strength in the direction Cl→Br→I could explain the observed quenching trend in the samples. This would entail an additional, required, amount of phonons to activate the quenching in $CsCaI_3:Tm^{2+}$. However, no such information is available from literature. It would request a detailed investigation of how the vibrational modes of the host couple to the electronic states of Tm^{2+}.

An additional investigation into the temperature-dependent excitation spectra of the $^2F_{5/2} \rightarrow {}^2F_{7/2}$ and $(^3H_6,t_{2g})_{S=3/2} \rightarrow {}^2F_{7/2}$ emissions reveals a peculiar difference in the shape of the spectra. This difference is observed at temperatures where the $^2F_{5/2} \rightarrow {}^2F_{7/2}$ emission intensity is weak and almost independent of temperature. However, the $^2F_{5/2} \rightarrow {}^2F_{7/2}$ and $(^3H_6,t_{2g})_{S=3/2} \rightarrow {}^2F_{7/2}$ emission intensities display a clear anti-correlated trend in both time and temperature for all of the studied compounds. This anti-correlation is also observed in the measured quantum efficiencies. When traversing from Br→I, the quantum efficiency of the $^2F_{5/2} \rightarrow {}^2F_{7/2}$ emission decreases from around 70% to 15%, while the quantum efficiency of the $(^3H_6,t_{2g})_{S=3/2} \rightarrow {}^2F_{7/2}$ emission increases to around 45%. However, large random fluctuations, of several tens of percent, are observed among the measured quantum efficiencies. This makes us believe that the quantum efficiency is largely governed by defects, such as vacancies, that are present in the materials. Without them, the quantum efficiency can approach 100%, as no non-radiative relaxation routes to the ground state have been identified.

4.5 Appendix A

4.5.1 Emission and Absorption Energies

In tables 4.2 and 4.3 the energies of the observed Tm^{2+} emissions are listed alongside the absorption energy of the level from these are emitted. Such energies are determined from the emission spectra in figure 4.8 and the excitation spectra in figures 4.6 and 4.7.

Table 4.4 lists the energy gaps between the related levels, as calculated from the emission energies. In situations where there is no emission observed, the energy gaps are calculated from the absorption energies to obtain an indication of its size. This is for instance performed for the $(^3H_6,t_{2g})_{S=1/2}$ - $(^3H_6,t_{2g})_{S=3/2}$ energy gap.

Table 4.2: The energies of emissions D, E and F, and the absorption energy of the $(^3F_4,t_{2g})_{S=3/2}$ level for all of the $CsCa(Cl/Br)_3:Tm^{2+}$ and $CsCa(Br/I)_3:Tm^{2+}$ samples.

Sample	Emission x10³ (cm⁻¹)			Absorption x10³ (cm⁻¹)
	F $(^3F_4,t_{2g})_{S=1/2}\rightarrow{}^2F_{7/2}$	**D** $(^3F_4,t_{2g})_{S=3/2}\rightarrow{}^2F_{7/2}$	**E** $(^3F_4,t_{2g})_{S=3/2}\rightarrow{}^2F_{5/2}$	$(^3F_4,t_{2g})_{S=3/2}$
$CsCaCl_3$	-	19.27 ±0.19	-	20.41 ±0.21
$CsCaCl_{2.25}Br_{0.75}$	-	18.94 ±0.18	-	20.41 ±0.21
$CsCaCl_{1.5}Br_{1.5}$	-	19.05 ±0.18	-	20.41 ±0.21
$CsCaCl_{0.75}Br_{2.25}$	-	19.05 ±0.18	-	20.41 ±0.21
$CsCaBr_3$	-	19.01 ±0.18	-	20.20 ±0.21
$CsCaBr_{2.4}I_{0.6}$	-	18.69 ±0.18	-	20.20 ±0.21
$CsCaBr_{1.8}I_{1.2}$	-	18.52 ±0.17	-	20.00 ±0.20
$CsCaBr_{1.5}I_{1.5}$	-	18.42 ±0.17	-	20.00 ±0.20
$CsCaBr_{1.2}I_{1.8}$	-	18.35 ±0.17	-	19.80 ±0.20
$CsCaBr_{0.6}I_{2.4}$	-	18.25 ±0.17	-	19.61 ±0.19
$CsCaI_3$	20.08 ±0.20	18.25 ±0.17	9.52 ±0.05	19.42 ±0.19

Table 4.3: The energies of emissions B and C, as well as the absorption energies of the $(^3H_6,t_{2g})_{S=1/2}$ and $(^3H_6,t_{2g})_{S=3/2}$ levels listed for all of the $CsCa(Cl/Br)_3:Tm^{2+}$ and $CsCa(Br/I)_3:Tm^{2+}$ samples.

Sample	Emission x10³ (cm⁻¹)		Absorption x10³ (cm⁻¹)		
	C $(^3H_6,t_{2g})_{S=1/2}\rightarrow{}^2F_{7/2}$	**B** $(^3H_6,t_{2g})_{S=3/2}\rightarrow{}^2F_{7/2}$	$(^3H_6,t_{2g})_{S=1/2}$ [a]	$(^3H_6,t_{2g})_{S=1/2}$ [b]	$(^3H_6,t_{2g})_{S=3/2}$
$CsCaCl_3$	-	12.38 ±0.08	17.39 ±0.15	14.93 ±0.11	13.21 ±0.09
$CsCaCl_{2.25}Br_{0.75}$	-	12.14 ±0.07	17.39 ±0.15	14.60 ±0.11	13.23 ±0.09
$CsCaCl_{1.5}Br_{1.5}$	-	12.17 ±0.08	17.39 ±0.15	14.71 ±0.11	13.21 ±0.09
$CsCaCl_{0.75}Br_{2.25}$	13.61 ±0.09	12.14 ±0.07	17.39 ±0.15	14.71 ±0.11	13.19 ±0.09
$CsCaBr_3$	13.61 ±0.09	12.17 ±0.08	17.24 ±0.15	14.60 ±0.11	13.16 ±0.09
$CsCaBr_{2.4}I_{0.6}$	13.46 ±0.09	11.76 ±0.07	17.24 ±0.15	14.60 ±0.11	13.16 ±0.09
$CsCaBr_{1.8}I_{1.2}$	13.19 ±0.09	11.59 ±0.07	17.09 ±0.15	14.49 ±0.11	12.85 ±0.08
$CsCaBr_{1.5}I_{1.5}$	13.11 ±0.09	11.36 ±0.07	16.95 ±0.15	14.29 ±0.10	12.97 ±0.09
$CsCaBr_{1.2}I_{1.8}$	13.07 ±0.09	11.30 ±0.06	16.95 ±0.15	14.19 ±0.10	12.92 ±0.08
$CsCaBr_{0.6}I_{2.4}$	-	11.30 ±0.06	16.67 ±0.14	14.29 ±0.10	12.74 ±0.08
$CsCaI_3$	12.69 ±0.09	11.33 ±0.07	16.39 ±0.14	14.09 ±0.10	12.35 ±0.08

[a] $(^3H_6,t_{2g})_{S=1/2}$ band located at higher energy in figures 4.6 and 4.7

[b] $(^3H_6,t_{2g})_{S=1/2}$ band located at lower energy in figures 4.6 and 4.7

Table 4.4: The relative energy gaps between the various levels as calculated from the emission energies and in some cases from the absorption energies. Such values are reported for all of the $CsCa(Cl/Br)_3:Tm^{2+}$ and $CsCa(Br/I)_3:Tm^{2+}$ samples. Note that in the calculation of the $(^3H_6,t_{2g})_{S=3/2}$ - $^2F_{5/2}$ energy gap, an emission energy of 8770 cm^{-1} was used for emission A.

Sample	Energy Gap x10^3 (cm^{-1})		
	$(^3F_4,t_{2g})_{S=3/2}$ - $(^3H_6,t_{2g})_{S=1/2}$ [a]	$(^3H_6,t_{2g})_{S=1/2}$ - $(^3H_6,t_{2g})_{S=3/2}$ [b]	$(^3H_6,t_{2g})_{S=3/2}$ - $^2F_{5/2}$
$CsCaCl_3$	3.02 ±0.28	1.72 ±0.14 [b]	3.61 ±0.10 [c]
$CsCaCl_{2.25}Br_{0.75}$	3.02 ±0.28	1.37 ±0.14 [b]	3.37 ±0.10 [c]
$CsCaCl_{1.5}Br_{1.5}$	3.02 ±0.28	1.50 ±0.14 [b]	3.40 ±0.10 [c]
$CsCaCl_{0.75}Br_{2.25}$	3.02 ±0.28	1.47 ±0.13 [c]	3.37 ±0.10 [c]
$CsCaBr_3$	2.96 ±0.28	1.43 ±0.13 [c]	3.40 ±0.10 [c]
$CsCaBr_{2.4}I_{0.6}$	2.96 ±0.28	1.70 ±0.13 [c]	2.99 ±0.10 [c]
$CsCaBr_{1.8}I_{1.2}$	2.91 ±0.26	1.60 ±0.12 [c]	2.82 ±0.10 [c]
$CsCaBr_{1.5}I_{1.5}$	3.05 ±0.26	1.74 ±0.13 [c]	2.59 ±0.10 [c]
$CsCaBr_{1.2}I_{1.8}$	2.85 ±0.26	1.77 ±0.12 [c]	2.53 ±0.10 [c]
$CsCaBr_{0.6}I_{2.4}$	2.94 ±0.25	1.55 ±0.13 [b]	2.53 ±0.10 [c]
$CsCaI_3$	3.02 ±0.25	1.36 ±0.13 [c]	2.56 ±0.10 [c]

[a] Based on the $(^3H_6,t_{2g})_{S=1/2}$ band at higher energy in figures 4.6 and 4.7

[b] Based on the absorption energies

[c] Based on the emission energies

4.5.2 Quantum Efficiency and Absorption Values

Table 4.5 provides the list of retrieved internal quantum efficiencies and obtained absorption values that were used in the construction of figure 4.13.

Table 4.5: List of the internal quantum efficiencies of emissions A and B and the related absorption after excitation into the $(^3H_6,t_{2g})_{S=1/2}$.band at lower energy (see figure 4.6 and 4.7).

Sample	Attempt #1			Attempt #2	
	Abs. (%) [a]	QE (%) Em. A [b]	QE (%) Em. B [c]	Abs. (%) [a]	QE (%) Em. A [b]
$CsCaCl_3$	70.3 ±4	38.0 ±2	-	59.1 ±3	28.8 ±1
$CsCaCl_{2.25}Br_{0.75}$	64.4 ±3	63.5 ±3	-	52.9 ±3	71.1 ±4
$CsCaCl_{1.5}Br_{1.5}$	58.9 ±3	32.9 ±2	-	65.4 ±3	33.5 ±2
$CsCaCl_{0.75}Br_{2.25}$	59.3 ±3	45.4 ±2	-	59.4 ±3	45.1 ±2
$CsCaBr_3$	62.8 ±3	52.0 ±3	-	64.1 ±3	52.3 ±3
$CsCaBr_{2.4}I_{0.6}$	60.1 ±3	71.1 ±4	7.2 ±0.4	64.1 ±3	52.3 ±3
$CsCaBr_{1.8}I_{1.2}$	58.6 ±3	35.6 ±2	12.9 ±1	61.6 ±3	68.0 ±3
$CsCaBr_{1.5}I_{1.5}$	66.3 ±3	57.3 ±3	19.5 ±1	60.9 ±3	35.1 ±2
$CsCaBr_{1.2}I_{1.8}$	64.1 ±3	35.6 ±2	16.9 ±1	64.7 ±3	51.1 ±3
$CsCaBr_{0.6}I_{2.4}$	67.8 ±3	26.2 ±1	25.8 ±1	68.1 ±3	34.3 ±2
$CsCaI_3$	60.8 ±3	15.2 ±1	44.7 ±2	67.2 ±3	26.0 ±1

[a] $^2F_{7/2}\rightarrow(^3H_6,t_{2g})_{S=1/2}$ transition

[b] $^2F_{5/2}\rightarrow{}^2F_{7/2}$ transition

[c] $(^3H_6,t_{2g})_{S=3/2}\rightarrow{}^2F_{7/2}$ transition

4.5.3 List of Important Quenching Parameters

Table 4.6 provides the values used in the construction of figure 4.20.

Table 4.6: List of main quenching parameters such as: the energy gap *Egap* between the $(^3H_6,t_{2g})_{S=3/2}$ and $^2F_{5/2}$ levels and the estimated amount of phonons required to bridge it N_{ph}, the absorption energy of the $(^3H_6,t_{2g})_{S=3/2}$ level and the $(^3H_6,t_{2g})_{S=3/2} \rightarrow {}^2F_{7/2}$ emission energy from which the Stokes shift is calculated, the Arrhenius deactivation energy and $T_{50\%}$ of emission B.

Sample	E_{gap} x10^3 (cm^{-1}) [a]	N_{ph} (-)	E_{Abs} x10^3 (cm^{-1})	E_{Em} x10^3 (cm^{-1})	$E_{Stokes\ Shift}$ x10^3 (cm^{-1}) [b]	$E_{Arrh.\ Deact}$ x10^3 (cm^{-1}) [b]	$T_{50\%}$ (K) [b]
$CsCaCl_3$	3.61 ±0.10	12	13.21 ±0.09	12.38 ±0.08	0.83 ±0.12	1.13 ±0.05	130 ±5
$CsCaCl_{2.25}Br_{0.75}$	3.37 ±0.10	- [c]	13.23 ±0.09	12.14 ±0.07	1.09 ±0.11	- [c]	- [c]
$CsCaCl_{1.5}Br_{1.5}$	3.40 ±0.10	- [c]	13.21 ±0.09	12.17 ±0.08	1.04 ±0.12	1.59 ±0.05	160 ±5
$CsCaCl_{0.75}Br_{2.25}$	3.37 ±0.10	- [c]	13.19 ±0.09	12.14 ±0.07	1.06 ±0.11	1.82 ±0.05	190 ±5
$CsCaBr_3$	3.40 ±0.10	16	13.16 ±0.09	12.17 ±0.08	0.98 ±0.12	2.49 ±0.05	240 ±5
$CsCaBr_{2.4}I_{0.6}$	2.99 ±0.10	- [c]	13.16 ±0.09	11.76 ±0.07	1.40 ±0.11	2.63 ±0.05	250 ±5
$CsCaBr_{1.8}I_{1.2}$	2.82 ±0.10	- [c]	12.85 ±0.08	11.59 ±0.07	1.26 ±0.11	- [c]	- [c]
$CsCaBr_{1.5}I_{1.5}$	2.59 ±0.10	- [c]	12.97 ±0.09	11.36 ±0.07	1.61 ±0.11	2.55 ±0.05	260 ±5
$CsCaBr_{1.2}I_{1.8}$	2.53 ±0.10	- [c]	12.92 ±0.08	11.30 ±0.06	1.62 ±0.10	- [c]	- [c]
$CsCaBr_{0.6}I_{2.4}$	2.53 ±0.10	- [c]	12.74 ±0.08	11.30 ±0.06	1.44 ±0.10	- [d]	280 ±5
$CsCaI_3$	2.56 ±0.10	15	12.35 ±0.08	11.33 ±0.07	1.01 ±0.11	- [d]	350 ±5

[a] Based on the calculated $(^3H_6,t_{2g})_{S=3/2}$ - $^2F_{5/2}$ energy gap in table 4.5.

[b] Retrieved from $(^3H_6,t_{2g})_{S=3/2} \rightarrow {}^2F_{7/2}$ emission B.

[c] Not available.

[d] Could not be determined from figure 4.19.

4.6 Appendix B

4.6.1 Configurational Coordinate Diagram [34,35]

In its simplest form, an isolated luminescence center can be modelled in accordance to the Configurational Coordinate Diagram (CCD) shown in figure 4.24. With the harmonic and adiabatic approximations, the electronic states can be represented by parabolic potential energy curves and plotted one dimensionally as a function of the configurational coordinate Q. In figure 4.24, the parabola E_g represents the ground state of the luminescence center with its minimum located at $Q = Q_g$ and $E = E_{0g}$. In addition, the parabolas E_{4f} and E_{5d} correspond to excited states with respective minima at $Q = Q_{4f}$ and $E = E_{04f}$, and at $Q = Q_{5d}$ and $E = E_{05d}$. Note that for simplicity reasons: $Q_g = Q_{4f} = 0$ and $E_{0g} = 0$. The parabolas are relatively shifted from the ground state E_g by a configurational displacement $\Delta Q_{g-4f} = |Q_{4f} - Q_g| = 0$ and $\Delta Q_{g-5d} = |Q_{5d} - Q_g| = |Q_{5d}|$ and have a relative and respective displacement in energy of $\Delta E = |E_{04f} - E_{0g}| = |E_{04f}|$ and $\Delta E = |E_{05d} -$

$E_{0g}| = |E_{05d}|$. The three parabolas can then mathematically be described by relations (1a), (2a) and (3a).

$$E_g = k_g \frac{Q^2}{2} \quad (1a)$$

$$E_{4f} = E_{04f} + k_{4f} \frac{Q^2}{2} \quad (2a)$$

$$E_{5d} = E_{05d} + k_{5d} \frac{(Q-Q_{5d})^2}{2} \quad (3a)$$

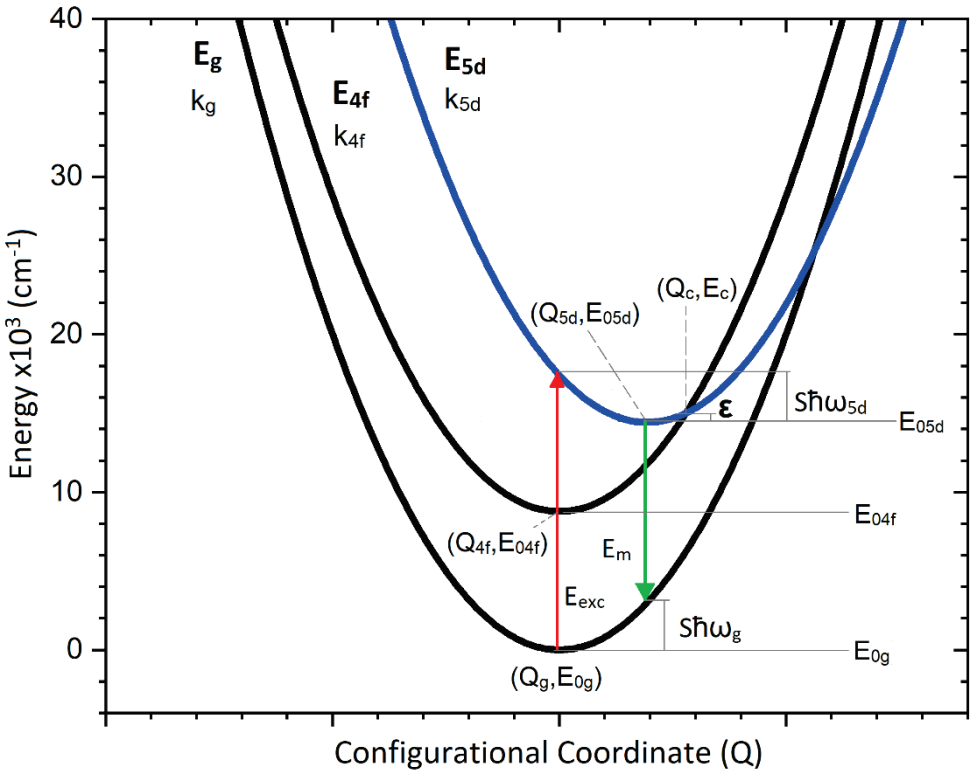

Figure 4.24: Configurational coordinate diagram of an isolated luminescence center with three electronic states: ground state E_g and excited states E_{4f} and E_{5d}. These states are respectively represented by the potential energy parabolas with minima at (Q_g,E_{g0}), (Q_{4f},E_{4f0}) and (Q_{5d},E_{5d0}). In addition, the respective states have characteristic elastic force constants k_g, k_{4f} and k_{5d}, and an electron lattice coupling energy $S\hbar\omega_g$, $S\hbar\omega_{4f}$ and $S\hbar\omega_{5d}$. Assuming equal elastic force constants: $k_g = k_{4f} = k_{5d} = k$ and $S\hbar\omega_g = S\hbar\omega_{4f} = S\hbar\omega_{5d} = S\hbar\omega$. Both k and $S\hbar\omega$ can in approximation be determined from the Stokes shift: $E_{exc} - E_{em}$. The excited states E_{5d} and E_{4f} share a crossing point for which the energy barrier ε plays a key role in the quenching process of interband crossing.

In these relations k_g, k_{4f} and k_{5d} are elastic force constants related to the chemical bond. In the assumption of equal force constants: $k_g = k_{4f} = k_{5d} = k$, relations (1a), (2a) and (3a) can respectively be rewritten into relations (1b), (2b) and (3b).

$$E_g = k\frac{Q^2}{2} \quad (1b)$$

$$E_{4f} = E_{04f} + k\frac{Q^2}{2} \quad (2b)$$

$$E_{5d} = E_{05d} + k\frac{(Q-Q_{5d})^2}{2} \quad (3b)$$

For each electronic state, an electron-lattice coupling energy can be defined: $S\hbar\omega_g$, $S\hbar\omega_{4f}$ and $S\hbar\omega_{5d}$. In general, the elastic force constant *k* and the electron-lattice coupling energy are related in the following manner: $k \cdot \Delta Q^2 = 2S\hbar\omega$. In the earlier made assumption of equal force constants: $S\hbar\omega_g = S\hbar\omega_{4f} = S\hbar\omega_{5d} = S\hbar\omega$.

The Franck-Condon rule states that electronic transitions that correspond to maximum absorption and emission take place without a change in configurational coordinate *Q*. In case of an excitation from E_g into E_{5d}, the electron lattice coupling energy $S\hbar\omega$ can then be defined via relation (4).

$$S\hbar\omega = \frac{(E_{exc}-E_{em})}{2} \quad (4)$$

Where E_{exc} is the energy of $E_g \rightarrow E_{5d}$ excitation and E_{em} is the energy of $E_{5d} \rightarrow E_g$ emission. The energy difference: $E_{exc} - E_{em}$ represents the Stokes shift. Note that the energy difference $\Delta E = E_{05d} - E_{0g} = E_{05d}$ can now be written as: $\Delta E = E_{exc} - S\hbar\omega = E_{em} + S\hbar\omega$ and $\Delta E = \frac{E_{exc}+E_{em}}{2}$. In addition, the elastic force constant becomes: $k = \frac{2S\hbar\omega}{{Q_{5d}}^2}$. Relations (2b) and (3b) can then respectively be transformed into relations (2c) and (3c).

$$E_{4f} = E_{04f} + S\hbar\omega\left(\frac{Q}{Q_{5d}}\right)^2 \quad (2c)$$

$$E_{5d} = E_{05d} + S\hbar\omega\left(\frac{Q}{Q_{5d}} - 1\right)^2 \quad (3c)$$

As the configurational displacements are very difficult to determine accurate by and from experiments, the elastic force constant *k* (which determines the curvature of the parabolas) is here chosen as $k = 2$. In such cases where the excitation is still from ground state E_g

towards excited state E_{5d}: $S\hbar\omega = {Q_{5d}}^2 = \left(\frac{E_{exc}-E_{em}}{2}\right)$. relations (2c) and (3c) then respectively change into relations (2d) and (3d).

$$E_{4f} = E_{04f} + Q^2 \quad (2d)$$

$$E_{5d} = \left(\frac{E_{exc}+E_{em}}{2}\right) + \left(Q - \sqrt{\frac{E_{exc}-E_{em}}{2}}\right)^2 \quad (3d)$$

These two parabolas cross each other at:

$$\frac{Q_c}{Q_{5d}} = \frac{1}{2}\left(\frac{E_{05d}-E_{04f}+S\hbar\omega}{S\hbar\omega}\right) \rightarrow Q_c = \frac{1}{2\sqrt{S\hbar\omega}}\left(E_{05d} - E_{04f} + S\hbar\omega\right)$$

$$E_c = E_{04f} + \frac{(E_{05d} - E_{04f} + S\hbar\omega)^2}{4S\hbar\omega}$$

The energy barrier ε related to the crossing point can then be estimated via: $\varepsilon = E_c - E_{05d}$.

4.7 References

[1] A. Mathur, H. Fan, V. Maheshwari, Organolead halide perovskites beyond solar cells: self-powered devices and the associated progress and challenges, Mater. Adv. (2021), Advance Article.

[2] H.-S. Kim, S.H. Im, N.-G. Park, Organolead Halide Perovskite: New Horizons in Solar Cell Research, J. Phys. Chem. C 5615–5625 118 (2014) 11.

[3] L. Su, Z.X. Zhao, H.Y. Li, J. Yuan, Z.L. Wang, G.Z. Cao, G. Zhu, High-Performance Organolead Halide Perovskite-Based Self-Powered Triboelectric Photodetector, ACS Nano 11310–11316 9 (2015) 11.

[4] R.H.P. Awater and P. Dorenbos, The vacuum referred electron binding energies in the $^1S_0$ and $^3P_1$ states of Pb^{2+} and Tl^+ in inorganic compounds, J. Lumin. 783-793 (2017) 192.

[5] M. Suta, W. Urland, C. Daul, C. Wickleder, Photoluminescence properties of Yb^{2+} ions doped in the perovskites $CsCaX_3$ and $CsSrX_3$ (X = Cl, Br, and I)- a comparative study, Phys. Chem. Chem. Phys. 13196 (2016) 18.

[6] M. Suta, P.Larsen, F.Lavoie-Cardinal, C.Wickleder, Photoluminescence of $CsMBr_3:Eu^{2+}$ (M = Mg, Ca, Sr)- A novel strategy for the development of low-energy emitting phosphors, J. Lumin. 35-44 (2014) 149.

[7] M. Suta, C. Wickleder, Spin Crossover of Yb^{2+} in $CsCaX_3$ and $CsSrX_3$ (X = Cl, Br, I)- A Guideline to Novel Halide-Based Scintillators, Adv. Funct. Mater. 1602783 (2017) 27.

[8] M. Suta, T. Senden, J. Olchowka, M. Adlung, A. Meijerink, C. Wickleder, Decay times of the spin-forbidden and spin-enabled transitions of Yb^{2+} doped in $CsCaX_3$ and $CsSrX_3$ (X = Cl, Br, I), Phys. Chem. Chem. Phys. 7188 (2017) 19.

[9] A. Lindsey, W. McAlexander, L. Stand, Y. Wu, M. Zhuravleva, C.L. Melcher, Crystal growth and spectroscopic performance of large crystalline boules of CsCaI3:Eu scintillator, J. Cryst. Growth 42-47 (2015) 427.

[10] M. Loyd, A. Lindsey, M. Patel, M. Koschan, C.L. Melcher, M. Zhuravleva, Crystal structure and thermal expansion of CsCaI3:Eu and CsSrBr3:Eu scintillators, J. Cryst. Growth 35-30 (2018) 481

[11] M. Loyd, A. Lindsey, L. Stand, M. Zhuravleva, C.L. Melcher, M. Koschan, Tuning the structure of CsCaI3:Eu via substitution of bromine for iodine, Opt. Mater. 47-52 (2017) 68.

[12] J. Grimm, H.U. Güdel, Five different types of spontaneous emission simultaneously observed in Tm^{2+} doped $CsCaBr_3$, Chem. Phys. Lett. 40–43 (2005) 404.

[13] J. Grimm, J.F. Suyver, G. Carver, H. U. Güdel, Light-Emission and Excited-State Dynamics in Tm^{2+} Doped $CsCaI_3$, $CsCaBr_3$, and $CsCaI_3$, J. Phys. Chem. B 2093-2101 (2006) 110.

[14] E. Beurer, J. Grimm, P. Gerner, H.U. Güdel, Absorption, Light Emission, and Upconversion Properties of Tm^{2+}-doped $CsCaI_3$ and $RbCaI_3$, Inorg. Chem. 9901-9906 (2006) 45.

[15] J. Grimm, E. Beurer, H.U. Güdel, Crystal absorption spectra in the region of 4f-4f and 4f-5d excitations in Tm^{2+}-doped $CsCaCl_3$, $CsCaBr_3$, and $CsCaI_3$, Inorg. Chem. 10905-10908 (2006) 45.

[16] E. Beurer, J. Grimm, P. Gerner, H.U. Güdel, New type of near-infrared to visible photon upconversion in Tm^{2+}-doped $CsCaI_3$, JACS 3110-3111 (2006) 128.

[17] J. Grimm, E. Beurer, P. Gerner, H.U. Güdel, Upconversion between 4f–5d excited states in Tm^{2+}-doped $CsCaCl_3$, $CsCaBr_3$, and $CsCaI_3$, Chem. Eur. J. 1152-1157 (2007) 13.

[18] M. de Jong, D. Biner, K.W. Krämer, Z. Barandiarán, L. Seijo, A. Meijerink, New Insights in $4f^{12}5d^1$ Excited States of Tm^{2+} through Excited State Excitation Spectroscopy, J. Phys. Chem. Lett. 2730−2734 (2016) 7.

[19] M. de Jong, A. Meijerink, L. Seijo, Z. Barandiarán, Energy Level Structure and Multiple $4f^{12}5d^1$ Emission Bands for Tm^{2+} in Halide Perovskites: Theory and Experiment, J. Phys. Chem. C 10095−10101 (2017) 121.

[20] M.P. Plokker, I.C. van der Knijff, A.V. de Wit, B. Voet, T. Woudstra, V. Khanin, P. Dorenbos, E. van der Kolk, Experimental and numerical analysis of Tm^{2+} excited-states dynamics and luminescence in CaX_2 (X = Cl, Br, I), J. Phys.: Condens. Matter 255701 (2021) 33.

[21] O.M. ten Kate, K.W. Krämer, E. Van der Kolk, Efficient luminescent solar concentrators based on self-absorption free, Tm^{2+} doped halides, Sol. Energy Mater Sol. Cells 115-120 (2015) 140.

[22] J. Rodriguez-Carvajal, program FullProf.2k, version 5.2, July-2011, Institute Laue Langevin.

[23] E. Rogers, P. Dorenbos, J.T.M. de Haas, E. van der Kolk, Experimental study of the $4f^n \rightarrow 4f^n$ and $4f^n \rightarrow 4f^{n-1}5d^1$ transitions of the lanthanide diiodides LnI_2 (Ln = Nd, Sm, Eu, Dy, Tm, Yb), J. Phys.: Condens. Matter (2012) 24.

[24] National Bureau of Standards, NBS Monograph 25, 5 (1967) 21.

[25] H.J. Seifert, D. Habenauer, Z. Anorch. Allg. Chem. 491 (1982) 301.

[26] G. Schilling, C. Kunert, Th. Schleid, G. Meyer, Metallothermische Reduktion der Tribromide und -iodide von Thulium und Ytterbium mit Alkalimetallen, Z. Anorgn. Allg. Chem. 618 (1992) 7.

[27] C. Hohnstedt, G. Meyer, Metallothermische Reduktion des Tribromids und -iodids von Dysprosium mit Alkalimetallen, Z. Anorch. Allg. Chem. 619 (1993) 1374.

[28] G. Schilling, G. Meyer, Ternäre Bromide und Iodide zweiwertiger Lanthanide und ihre Erdalkali-Analoga vom Typ AMX_3 und AM_2X_5, Z. Anorch. Allg. Chem. 622 (1996) 759.

[29] G.H. Dieke, H.M. Crosswhite, The Spectra of the Doubly and Triply Ionized Rare Earths, Appl. Opt. 675-686 (1963) 2.

[30] M.P. Plokker, E. van der Kolk, Temperature dependent relaxation dynamics of luminescent NaX:Tm^{2+} (X=Cl, Br, I), J. Lumin. (2019) 216.

[31] M.P. Plokker, W. Hoogsteen, R.D. Abellon, K.W. Krämer, E. van der Kolk, Concentration and temperature dependent luminescence properties of the SrI2-TmI2 system, J. Lumin (2020) 225.

[32] P. Dorenbos, Ce3+ 5d-centroid shift and vacuum referred 4f-electron binding energies of all lanthanide impurities in 150 different compounds, J. Lumin. 135 (2013) 93.

[33] P. Dorenbos, Crystal field splitting of lanthanide $4f^n$–15^d-levels in inorganic compounds, J. Alloys Compounds 341 (2002) 156.

[34] C.W. Struck and W.H. Fonger, Understanding Luminescence Spectra and Efficiency Using Wp and Related Functions, Inorganic Chemistry Concepts 13, Springer Verlag ISBN 3-540-52766-4 (1991).

[35] M. Grinberg, T. Lesniewski, Non-radiative processes and luminescence quenching in Mn^{4+} doped phosphors, J. Lumin (2019) 214.

[36] S. Koster, M. Reid, J.P. Wells, R. Reeves, Energy Levels and Dynamics of Tm2+ Doped into AMX3 Salts, Msc Thesis S. Koster, University of Canterbury (2014)

[37] W.M. Yen, S. Shionoya, H. Yamamoto, Phosphor Handbook 2nd edition, chapter 2, CRC Press Taylor & Francis Group ISBN 0-8493-3564-7 (2007).

[38] M. Karbowiak, R. Lisiecki, P. Solarz, J. Komar, W. Ryba-Romanowski, Spectroscopic peculiarities of $CsCaI_3:Tm^{2+}$ single crystals examined through one-photon and excited state excitation spectroscopy, J. Alloys Compounds 1165-1171 (2018) 740.

[39] H.W. Moos, spectroscopic relaxation processes of rare earth ions in crystals, J. Lumin 106-121 (1970) 1,2.

[40] L.A. Riseberg, H.W. Moos, multiphonon orbit-lattice relaxation of excited states of rare-earth ions in crystals, Phys. Rev. 2 (1968) 174.

5.

Concentration and Temperature Dependent Luminescence Properties of the SrI_2-TmI_2 System

This chapter is based on the publication: M.P. Plokker, W. Hoogsteen, R.D. Abellon, K.W. Krämer and E. van der Kolk, Concentration and Temperature Dependent Luminescence Properties of the SrI_2-TmI_2 System, Journal of Luminescence 225 (2020)

Thanks to: BE. Terpstra, D.A. Biner, J.T.M. de Haas, F. van Dam

Abstract

The concentration dependent luminescence of the SrI_2-TmI_2 system was investigated. For Tm^{2+} concentrations up to 5 mol %, the quantum efficiency (QE) of the $^2F_{5/2}\rightarrow{}^2F_{7/2}$ emission exhibits a constant value above 50%. The QE drops for higher Tm^{2+} concentrations, partly due to concentration quenching, as evidenced by a decreasing luminescence lifetime of the $^2F_{5/2}\rightarrow{}^2F_{7/2}$ emission, and partly due to the formation of a second crystal phase with $CdCl_2$ structure, in which the $^2F_{5/2}\rightarrow{}^2F_{7/2}$ emission is quenched. The temperature and time dependent relaxation dynamics were studied to identify the origin of the limited QE for Tm^{2+}-doping levels below 5 mol %. An anti-correlation between the $4f^{12}5d^1\rightarrow4f^{13}$ $(^3H_6,t_{2g})_{S=3/2}\rightarrow{}^2F_{7/2}$ and $4f^{13}\rightarrow4f^{13}$ $^2F_{5/2}\rightarrow{}^2F_{7/2}$ emission intensities was found and rationalised by non-radiative, thermally stimulated, $4f^{12}5d^1\rightarrow4f^{13}$ interband crossing to the emitting $^2F_{5/2}$ level of Tm^{2+}. Both, the risetime of the $4f^{13}\rightarrow4f^{13}$ and the decay time of the $4f^{12}5d^1\rightarrow4f^{13}$ emission become shorter with increasing temperature. We suggest a similar non-radiative relaxation from the $4f^{12}5d^1$-level towards the $^2F_{7/2}$ ground state to limit the QE below unity. This route becomes more efficient when the $4f^{12}5d^1$ $(^3H_6,t_{2g})_{S=3/2}$ state moves closer to the $4f^{13}$ $^2F_{5/2}$ and $^2F_{7/2}$ states, which is the case for the $CdCl_2$ phase with a QE close to zero.

5.1. Introduction

Tm^{2+}-doped halides are promising materials for Luminescent Solar Concentrators (LSCs). [1] LSCs absorb, re-emit and concentrate sunlight to solar cells mounted on the edges of a transparent plate, like a window. Luminescent materials adopted in a LSC should ideally exhibit broad absorption bands across the visible and ultraviolet spectral regions to absorb large parts of the solar spectrum. The emitting centre should have a high quantum efficiency and no spectral overlaps with absorption bands to prevent self-absorption losses. [2,3]

Organic dyes, such as: Coumarin CRS040 and Lumogen F-Red305, demonstrate high internal quantum efficiencies (~98%) [4], but also have a limited absorption range and suffer from significant self-absorption losses. [1,2] Quantum Dots (QDs), especially core-shell QDs, have lower quantum efficiencies, but enable it to spectrally tune the absorption and emission and hereby circumvent self-absorption losses. [2] Nevertheless, most LSC QDs, like: PbS, PbS/CdS, CdSe/CdS, still suffer from these effects. [3] For rare-earth based LSC materials, such as: Nd^{3+}/Yb^{3+}-, and Cr^{3+}-doped glasses, the absorption bands and emission are spectrally separated and hence self-absorption is absent. However, absorption ranges and quantum efficiencies are low. Besides, the emission and the silicon solar cell band gap share a non-perfect spectral match. [2]

In comparison, Tm^{2+}-doped halides have several advantages over the aforementioned materials. They absorb up to 63% of the solar spectrum (AM 1.5) and no self-absorption

occurs due to the energy difference between the $4f^{13} \rightarrow 4f^{12}5d^1$ absorption and the $4f^{13} \rightarrow 4f^{13}$ emission. [1] The Tm^{2+} $^2F_{5/2} \rightarrow {}^2F_{7/2}$ emission has negligible multi-phonon relaxation losses in low phonon energy halide lattices. The emission energy fits well with the bandgap of Copper Indium Gallium Selenide (CIGS) solar cells. An optimised Tm^{2+}-doped halide coating can appear colourless due to its broad absorption over the entire visible region. [1] Tm^{2+} luminescence in halide host materials was investigated with respect to temperature dependence and relaxation dynamics [5-9]. A detailed study of the concentration dependent emission intensity and internal quantum efficiency is missing so far. These properties are essential for material optimisation in view of a LSC application.

In this chapter, we investigate SrI_2 samples nominally doped with 1 to 40 mol % Tm^{2+}. The crystalline phases are characterised by powder X-ray diffraction and Rietveld refinement. The Tm^{2+} concentrations were determined by Inductively Coupled Plasma Optically Enhanced Spectroscopy (ICP-OES) and Kubelka-Munk (K-M) absorption spectroscopy. The Tm^{2+} luminescence and QE were investigated at room temperature. Last but not least, the temperature-dependent relaxation dynamics was studied. Results show that we are able to reach a QE of over 50% and an AM 1.5 absorption fraction of 44%. [1,10] Although this study focusses on powders, the hygroscopicity of SrI_2 as single crystal is reported to be less intense than that of the scintillator materials $LaBr_3$ and $CeBr_3$. [11] This all makes the material SrI_2:Tm^{2+} a good candidate for Rare-Earth-based LSC applications.

5.2. Experimental Section

5.2.1 Powder Synthesis

A series of eight SrI_2:Tm^{2+} powder samples was synthesised by mixing SrI_2 (Alfa Aesar, 99.99%) with 1, 3, 5, 7, 9, 15, 25, and 40 mol % TmI_2 (Sigma Aldrich, 99.9%). The mixture was grinded to obtain a homogeneous powder, transferred into a silica ampoule, and attached to a vacuum/inert gas system. After evacuating and purging three times with dry nitrogen gas, the ampoule was evacuated to 10^{-4} mbar. Then the powder was molten completely for 1-1.5 minutes using four Tecla burners. The melting points of SrI_2 and TmI_2 are 515 °C and 756 °C, respectively. The melting temperature and duration should be minimised to reduce reactions with the silica ampoule and the formation of Tm^{3+} side products. After cooling to room temperature, the sample was removed from the ampoule and grinded. All handling of the hygroscopic and oxidation sensitive starting materials and products was done under strictly inert and dry conditions in a glovebox (MBraun, Garching, Germany) or sealed sample containers.

5.2.2 Analytical Characterisation

Powder X-ray diffraction patterns were obtained on a Philips X'pert-Pro diffractometer (Philips, Eindhoven, The Netherlands) in Bragg-Brentano geometry using CuK_α radiation. The patterns were measured at room temperature from 8° to 80° 2-Theta with a resolution of 0.008°. The diffraction patterns were evaluated by the Rietveld method using the FullProf software. [12]

The actual Tm concentration of the samples was determined by ICP-OES measurements on a Perkin Elmer Optima 4300DV spectrometer (Perkin Elmer, Waltham Massachusetts, USA). An intensity-concentration calibration line was established from diluted standard solutions of Tm and Sr. Diffuse reflectance spectra were measured on a Bruker Vertex V80 spectrometer (Bruker, Karlsruhe, Germany) to determine the K-M absorption and to estimate the Tm^{2+}/Tm^{3+} ratio of the samples. The latter is based on the ratio of the integrated absorption bands of the Tm^{2+} $^2F_{7/2}\rightarrow{}^2F_{5/2}$ and the Tm^{3+} $^3H_6\rightarrow{}^3H_5$ transitions, as combined with their relative absorption strengths in NaI which amount to 1 and 3.4, respectively. The relative absorption strengths were established from purely Tm^{2+}- and Tm^{3+}-doped NaI samples; their integrated absorption band values were corrected for their ICP-OES Tm concentrations.

5.2.3 Spectroscopic Measurements

Room temperature emission spectra were acquired using an Edinburgh FLS980 spectrometer (Edinburgh Instruments, Livingston, UK) with an integrating sphere, a 450 W Xenon arc lamp, and a Hamamatsu C9940-02 near infrared (NIR) photomultiplier tube (PMT) (Hamamatsu Photonics, Hamamatsu, Japan). From the same setup, absorption spectra were calculated by measuring the amount of reflected light. Highly reflecting $BaSO_4$ and the host material SrI_2 were used as reference samples. From the measured amount of emitted photons and the determined number of absorbed photons, QE values were calculated for all samples.

Temperature dependent emission and excitation spectra were acquired using a Xenon lamp coupled to a double monochromator with three gratings and a Hamamatsu C9100-13 EM-CCD or H1033A-75 NIR-PMT (Hamamatsu Photonics, Hamamatsu, Japan) that was attached to a single monochromator with three gratings to record the luminescence signals emerging from the samples. The sensitivity ranges of these detectors are 400:1150 nm and 950:1600 nm, respectively. Time resolved measurements were performed with a tuneable EKSPLA NT230 laser (EKSPLA, Vilnius, Lithuania) with a 7 ns pulse duration and 10 mJ pulse power. A DT5724F (0-2 ms) or DT5730 (0-40 ms) CAEN digitiser (CAEN, Viareggio, Italy) measured the signal from a H1033A-75 NIR-PMT or a Hamamatsu R7600U-20HV-800V PMT (Hamamatsu Photonics, Hamamatsu, Japan). Signals from 1000 laser pulses were

cumulated for each decay spectrum. The samples were heated and cooled by aid of an APD Cryogenic Helium cooler (APD Cryogenics, Allentown Pennsylvania, USA) and Lakeshore temperature controller (Lakeshore Cryotronics, Westerville Ohio, USA).

During all measurements, sealed containments protected the samples against moisture and oxidation reactions. Similar sample holders were described by Rogers et al.. [13]

5.3. Results and Discussion

5.3.1 Sample Characterisation

The lattice parameters and phase composition of the samples were determined by X-ray diffraction. In general SrI_2 is known to crystallise in the orthorhombic space group Pbca. [14] The Rietveld refinements on the samples reveal a single-phase SrI_2 structure [14] for SrI_2:Tm samples with Tm contents below 8 mol %, see figure 5.1 along with tables 5.1 and 5.2 for lattice parameters and atomic positions, respectively. The crystal structure has one cation site (8c) with sevenfold coordination and C_1 point symmetry, as illustrated in figure 5.3a. Within the series of SrI_2:Tm^{2+} samples, the Tm ions replace Sr^{2+} on regular lattice sites. Since Tm^{2+} is slightly smaller than Sr^{2+}, their ionic radii being 1.09 Å and 1.21 Å [15] for coordination number (CN) 7, respectively, the lattice parameters decrease with Tm doping, see table 5.1. From 1 to 5% Tm doping the changes are rather small and the molar volume shrinks from 74.97 to 74.94 cm^3/mol.

Table 5.1: Lattice information of the SrI_2:Tm samples (Pbca no. 61 Z=8 SrI_2 phase) acquired by Rietveld refinement.

Sample:	SrI_2:	a (Å)	b (Å)	c (Å)	R_{wp} (%)	V_{mol} (cm^3/mol)
S04	1% Tm	15.2685(3)	8.24824(15)	7.90670(16)	5.4	74.968(2)
S06	3% Tm	15.2694(3)	8.24867(15)	7.90650(16)	5.4	74.974(2)
S3	5% Tm	15.2704(3)	8.24622(17)	7.90428(18)	5.1	74.936(3)
S5	7% Tm	15.2585(4)	8.2377(2)	7.9012(2)	5.7	74.771(4)
S7	9% Tm	15.2551(4)	8.2408(2)	7.9010(2)	5.8	74.780(4)
S12	15% Tm	15.2458(6)	8.2366(4)	7.8959(4)	5.6	74.648(5)
S21	25% Tm	15.2388(7)	8.2282(4)	7.8892(4)	4.6	74.472(6)
S36	40% Tm	15.2528(17)	8.2345(9)	7.883(1)	5.0	74.544(15)

Rietveld fit with 20 parameters: zero point, scale factor, lattice parameters (a, b, c), half width parameters (u, v, w, y), temperature factor (B_{ov}), atomic positions (x, y, z of Sr/Tm, I1, I2), and pref. orientation along [210]. The Tm content was fixed according to the formula.

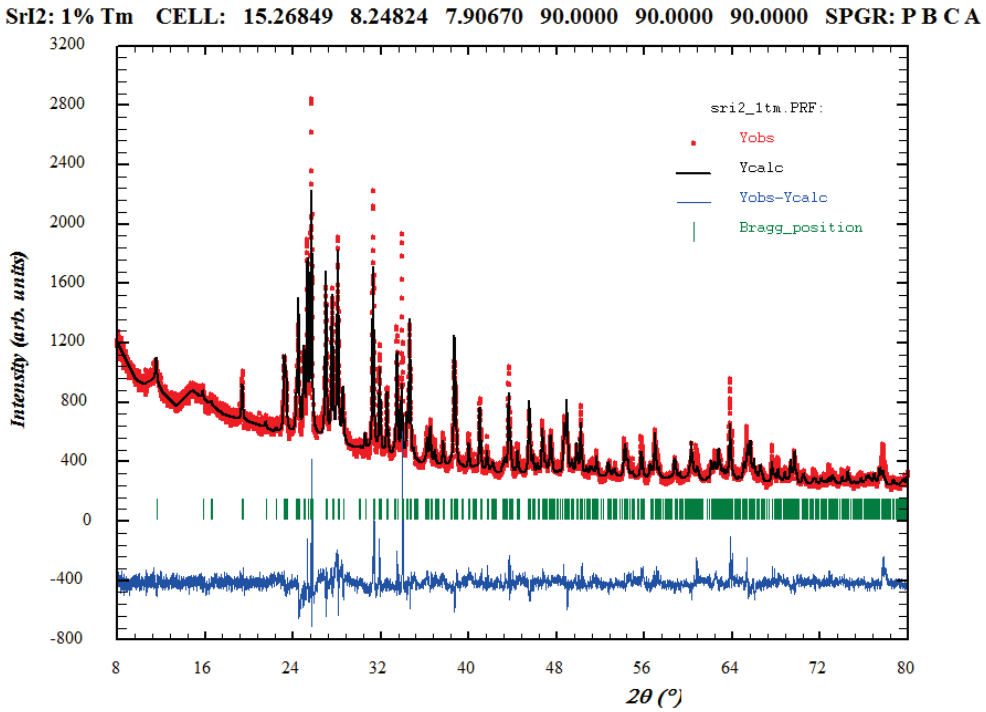

Figure 5.1: Rietveld fit of sample S04, SrI_2: 1% Tm.

Table 5.2: Atomic positions of SrI_2: Tm samples from Rietveld refinements.

Atom	Site	x / a	y / b	z / c
Sr/Tm	(8c)	0.1051(2)	0.4460(5)	0.2723(7)
I1	(8c)	0.2038(2)	0.1098(4)	0.1709(4)
I2	(8c)	-0.0367(2)	0.2659(5)	0.0063(7)

S04, SrI_2: 1% Tm, SrI_2 phase, space group Pbca (no. 61), Z=8 [14]

For higher doping of 15, 25, and 40% Tm a second crystalline phase with $CdCl_2$ structure [16] appears aside the SrI_2 phase, see the diffraction pattern in figures 5.1 and 5.2. The fraction of the $CdCl_2$ phase increases from 13 to 36 and 62 mol %, respectively. The $CdCl_2$ phase crystallizes in the rhombohedral space group R-3m, see tables 5.3 and 5.4 for lattice parameters and atomic positions. The crystal structure of $CdCl_2$ has one cation site (3a) with sixfold coordination and D_{3d} point symmetry, see figure 5.3b.

The appearance of a $CdCl_2$ phase can be rationalized from the sequence of crystal structures adopted by the rare-earth dihalides along the lanthanide contraction [17]. Here, the SrI_2 structure (CN 7) is followed by the $CdCl_2$ (CN 6) and CdI_2 (CN 6) structures for decreasing cation size. DyI_2 crystallizes in the $CdCl_2$ structure, TmI_2 and YbI_2 in the CdI_2 structure [18].

The SrI_2 samples with higher Tm contents form a $CdCl_2$ phase since their average cation size ranges between Sr^{2+} and Tm^{2+}. For even higher doping than 40% Tm the formation of a CdI_2 phase is expected, as for pure TmI_2. The presence of two crystalline phases in these samples indicates a non-equilibrium situation. Only one phase is thermodynamically stable and a phase transition might be kinetically hindered. The molar volume of the $CdCl_2$ phase is about 7% larger than for the corresponding SrI_2 phase, see table 5.1. The crystal packing is less dense in the $CdCl_2$ phase due to the reduction in coordination number from seven to six and the layer-type structure with van-der-Waals bonds between the iodide ions. The coordination number and molar volume indicate that the $CdCl_2$ phase might actually be a metastable high temperature phase.

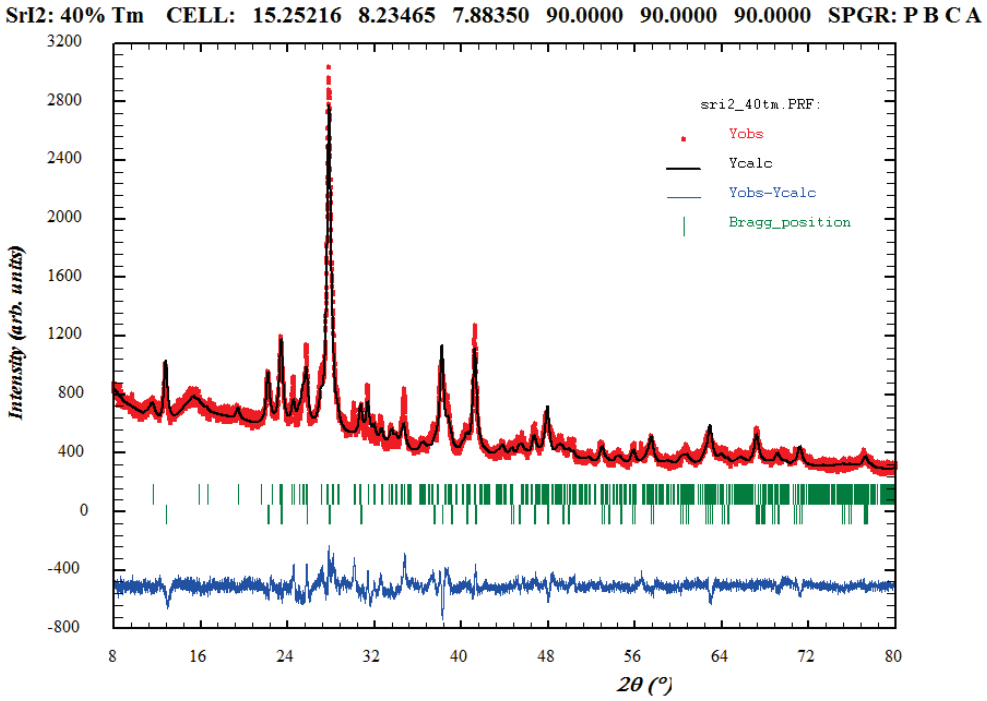

Figure 5.2: Rietveld fit of sample S36, SrI_2: 40% Tm. The sample contains two phases with SrI_2 (37.6(4) mol%) and $CdCl_2$ (62.4(5) mol%) structures.

Table 5.3: Atomic positions of SrI_2: Tm samples from Rietveld refinements.

Atom	Site	x / a	y / b	z / c
Sr/Tm	(3a)	0	0	0
I	(6c)	0	0	0.24721(13)

S36, SrI_2: 40% Tm, $CdCl_2$ phase, space group R-3m (no. 166), Z = 3 [16]

Table 5.4: Lattice information of the SrI_2:Tm samples (R-3m no. 166 Z=3 $CdCl_2$ phase) from the Rietveld refinement.

Sample:	SrI_2:	a (Å)	b (Å)	c (Å)	V_{mol} (cm^3/mol)	Fract. / mol%
S12	15% Tm	4.7238(3)	20.673(2)	4.6	80.207(10)	12.6(3)
S21	25% Tm	4.71664(16)	20.7044(9)	4.6	80.085(5)	36.4(4)
S36	40% Tm	4.70588(19)	20.729(1)	5.0	79.813(6)	62.4(5)

Rietveld fit with 15 parameters: zero point, scale factor (2 phases), lattice parameters (a, b, c (SrI_2); a, c ($CdCl_2$)), half width parameters (u, v, w, y), temperature factor (B_{ov}), atomic position (z of I), and pref. orientation along [001] ($CdCl_2$).

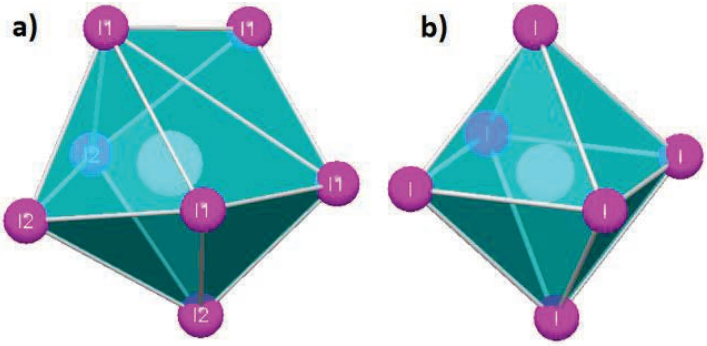

Figure 5.3: a) Seven-fold coordination of Tm^{2+} by I^- in the SrI_2 phase and b) six-fold coordination in the $CdCl_2$ phase.

The Tm^{2+} concentration in all samples was determined by ICP-OES and K-M absorption measurements. The analytical Tm^{2+} concentrations are reasonably close to the nominal values according to the SrI_2/TmI_2 molar ratio of the starting materials, see table 5.5.
The K-M absorption spectra are shown in figure 6.4. From these spectra the Tm^{2+}/Tm^{3+} ratio of the samples was determined. The spectra are normalised to the broad Tm^{2+} $4f^{13}\rightarrow4f^{12}5d^1$ absorption band at 650 nm and vertically shifted by 0.2 relative to each other. The $4f^{13}\rightarrow4f^{13}$ absorption bands of Tm^{2+} $^2F_{7/2}\rightarrow{}^2F_{5/2}$ at 1140 nm and Tm^{3+} $^3H_6\rightarrow{}^3H_5$ at 1230 nm, were integrated, normalised to their respective absorption in NaI, and multiplied by the Tm concentration from the ICP-OES to obtain the analytical and actual Tm^{2+} doping concentration. Table 5.5 summarises the results of the analytical characterisations, where the composition of the samples with respect to the SrI_2 and $CdCl_2$ phases is reported alongside the ICP-OES Tm concentration (column 3) and the Tm^{2+}/Tm^{3+} ratio (column 4). The samples are named after their analytical Tm^{2+} concentration (column 5).

Table 5.5: Analytical characterisations of the SrI_2:Tm^{2+} samples.

Sample	Mol % TmI_2 [a]	Mol % Tm ICP-OES	Tm^{2+} / Tm^{3+} ratio [b]	Mol % Tm^{2+} [c]	SrI_2 / $CdCl_2$ phases
S04	1	0.5	0.7 / 0.3	0.4	100 / 0
S06	3	0.7	0.9 / 0.1	0.6	100 / 0
S3	5	2.8	0.9 / 0.1	2.6	100 / 0
S5	7	5.5	0.9 / 0.1	4.9	100 /0
S7	9	8.4	0.9 / 0.1	7.2	100 / 0
S12	15	14.2	0.8 / 0.2	12.0	87.4 / 12.6
S21	25	22.5	0.9 / 0.1	21.0	63.6 / 36.4
S36	40	43.2	0.8 / 0.2	36.0	37.6 / 62.4

[a] nominal doping [b] from K-M absorption spectra [c] calculated from ICP-OES and K-M absorption spectra

The coordination of the Tm^{2+} ions strongly affects the crystal field splitting of the $4f^{12}5d^1$-state. The higher symmetry and shorter Tm-I distances in the sixfold coordination of the $CdCl_2$ phase give rise to a stronger crystal field splitting, which shifts its lowest $4f^{12}5d^1$-level beyond that of the SrI_2 phase. This additional low energy $4f^{12}5d^1$ band becomes visible at 740 nm in the absorption spectra of figure 5.4. It is weak for sample S7 and increases with the fraction of the $CdCl_2$ phase towards sample S36.

Figure 5.5 shows a picture of the SrI_2:Tm^{2+} samples with calculated Tm^{2+}-doping concentrations indicated in their name. As is observed, the colouring of the samples changes from white (0 mol % Tm^{2+}) to light green (1-5) and finally dark green (x-y mol %

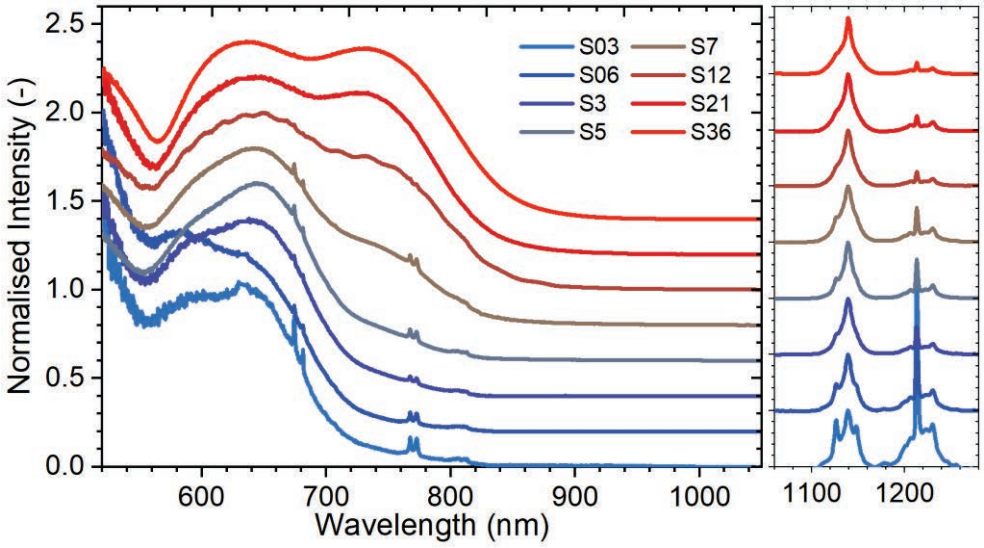

Figure 5.4: Kubelka-Munk absorption spectra of SrI_2:Tm samples. Sample names refer to table 5.5. The spectra are normalised to the broad Tm^{2+} $4f^{13}\rightarrow4f^{12}5d^1$ absorption band at 650 nm and vertically shifted (by 0.2) relative to each other. (right) $4f^{13}\rightarrow4f^{13}$ absorption peaks of Tm^{2+} $^2F_{7/2}\rightarrow{}^2F_{5/2}$ at 1140 nm and Tm^{3+} $^3H_6\rightarrow{}^3H_5$ at 1230 nm.

Tm^{2+}). This colour gradient can be explained based on figure 5.4 and 5.5, where the spectra display a clear absorption minima at around 550 nm. Imminent light of such wavelengths on the samples is thus very weakly absorbed and instead strongly reflected as compared to other visible light. This gives rise to a yellowish emerald green sample colour. In case of the undoped sample S0, all incoming visible light is likely to be reflected in an uniform manner, as no Tm^{2+} is present, yielding a white colour. Since the light absorption strength of phosphors is strongly dependent upon the dopant concentration, the reflected light emerging from the samples with higher Tm^{2+}-concentrations will contain a larger proportion of green as compared to other visible colours, explaining the colour intensification and relatively darker appearance.

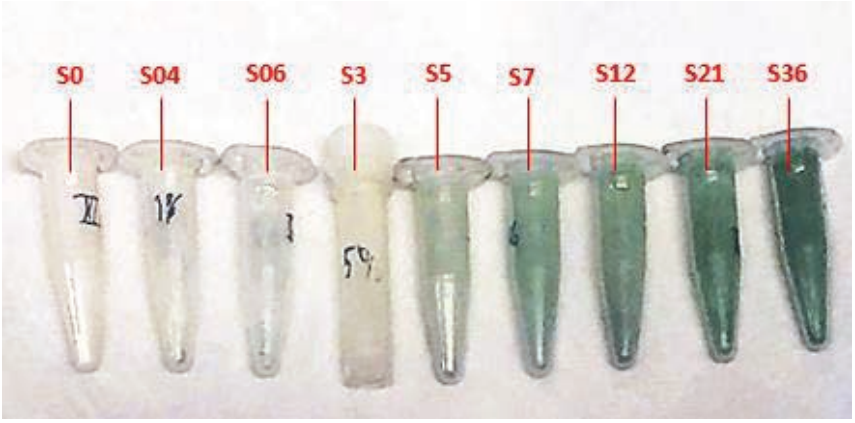

Figure 5.5: Picture of the SrI_2:Tm^{2+} samples in glovesbox. The samples are arranged from low to high Tm^{2+} concentration samples and display a clear green colour gradient The sample names refer to the calculated Tm^{2+} concentrations as listed in table 5.5.

5.3.2 Concentration-Dependent Luminescence

With their Tm^{2+}-doping concentrations estimated and their structural properties examined, the room temperature luminescence characteristics of the samples are explored. Figure 5.6 shows the excitation spectra of the different samples monitoring the Tm^{2+} $^2F_{5/2}\rightarrow{}^2F_{7/2}$ emission. For convenience, the K-M absorption spectra are plotted in this figure, too. As is immediately observed, the $4f^{13}\rightarrow4f^{12}5d^1$ absorption band related to the $CdCl_2$ phase is absent in the excitation spectra. This illustrates that the Tm^{2+} ions that occupy the Sr-sites in this phase have very little to no contribution to the $^2F_{5/2}\rightarrow{}^2F_{7/2}$ emission at room temperature.

Furthermore, the overall shape of the excitation spectra seems to change for increasing Tm^{2+}-doping concentrations. Most notably, the excitation bands located between 220-400

nm undergo a drop in intensity as the doping concentration increases from 3 to 5 mol %. In addition to that, the excitation bands located between 550-750 nm also seem to undergo a change of shape as the Tm^{2+} concentration increases from 12 to 36 mol %; which is the interval where the $CdCl_2$ phase intensifies. A possible explanation for this could be that as the Tm^{2+} concentration is increased, the average distance between the Tm^{2+} ions decreases; resulting in an alteration in the local surroundings of these ions. As a consequence, the affined excitation bands are shifted leading to a change in local spectra intensity.

After a selective photoexcitation at 655 nm, the absorption and emission properties of the samples were examined. Figure 5.7a shows that the reflectance of the samples decreases steadily as the Tm^{2+} concentration is increased from 0.4 to 3 mol %; indicating an increased absorption contribution of the SrI_2:Tm^{2+} luminescence centres. As the Tm^{2+}-doping concentration reaches a value of 12 mol % the reflectance, and hence also the absorption, of the samples slowly saturates. In addition, figure 5.7b shows that as the Tm^{2+}-doping concentration is increased from 0.4 to 3 mol %, the luminescence intensity of the Tm^{2+} $^2F_{5/2}\rightarrow{}^2F_{7/2}$ emission also increases. However, upon reaching a doping concentration of 5 mol %, it decreases again as shown in panel c.

In order to better determine the absorption contribution of the SrI_2:Tm^{2+} luminescence centres to the overall absorption of the samples, the reflectance of pure SrI_2 powder (Alfa Aeser, 99.99%) was compared to purely reflecting $BaSO_4$ (Sigma Aldrich, 99.99%) at the selected wavelength of photoexcitation. The SrI_2 host absorption contribution to the samples was hereby estimated to be 10-13%. The host corrected relative values for the absorption and integrated emission were used to determine the internal quantum efficiency of the samples. For each specific sample, these quantities are plotted versus their estimated Tm^{2+} concentration in figure 5.8, whereas table 5.6 provides a summary overview. As is perceived, the red integrated emission curve qualitatively follows from the product of the green quantum efficiency curve and the blue relative absorption curve.
As the Tm^{2+}-doping concentration increases from 0.6 up to 5 mol %, the relative absorption rapidly increases to a value of 59%. Meanwhile, the QE remains virtually constant at the a value of 52%. The luminescence intensity is therefore controlled by the absorption. For Tm^{2+} concentrations higher than about 5 mol %, the QE starts to decrease while the increase in absorption becomes less brisk. As a result, the luminescence intensity reaches an optimum at a Tm^{2+} concentration of 3 mol % after which it starts to follow the QE.

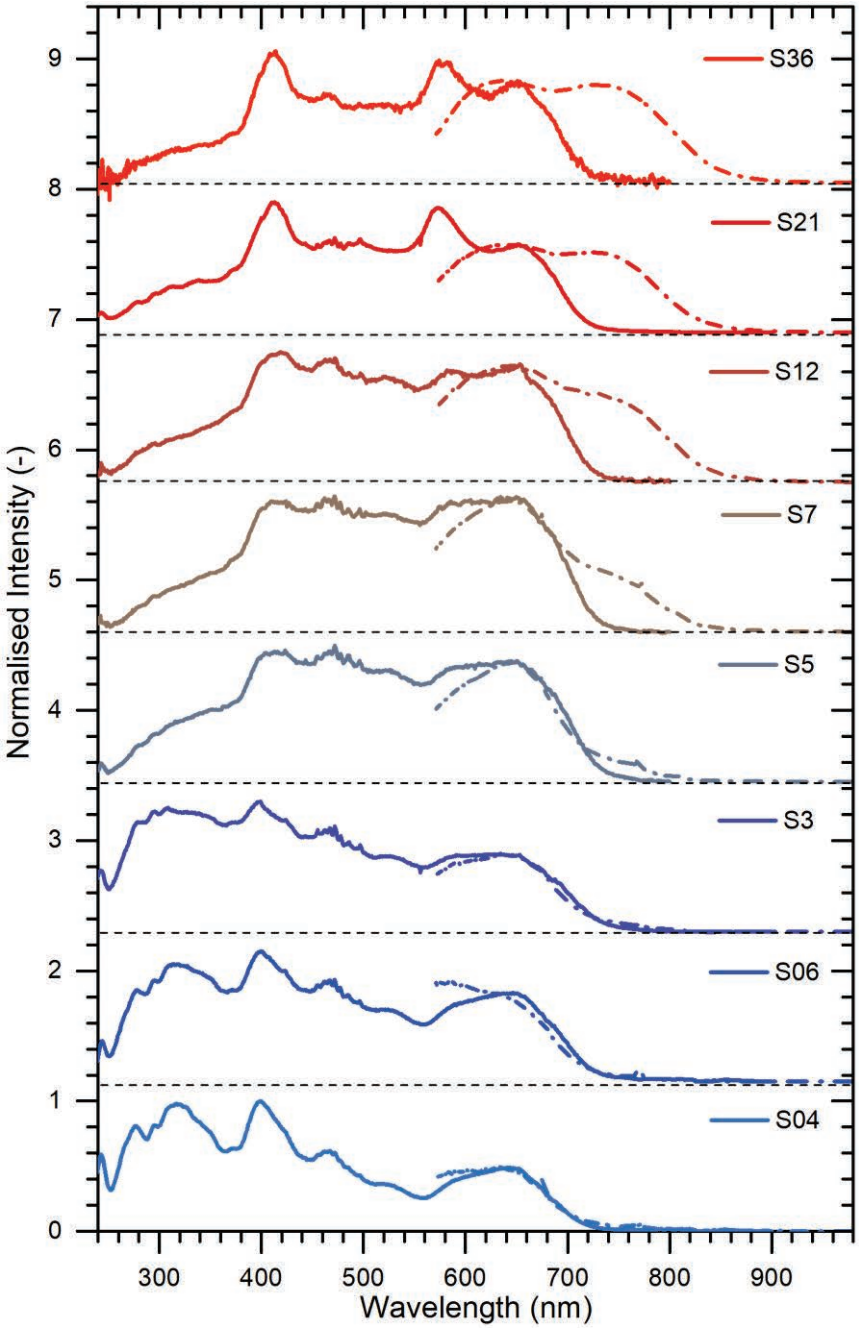

Figure 5.6: Excitation (full line) and K-M absorption (dotted line) spectra of the $SrI_2:Tm^{2+}$ samples at room temperature. The excitation spectra were recorded for the Tm^{2+} $^2F_{5/2}\rightarrow{}^2F_{7/2}$ transition at 1140 nm and are normalized to the band at 410 nm. The sample names refer to table 5.5.

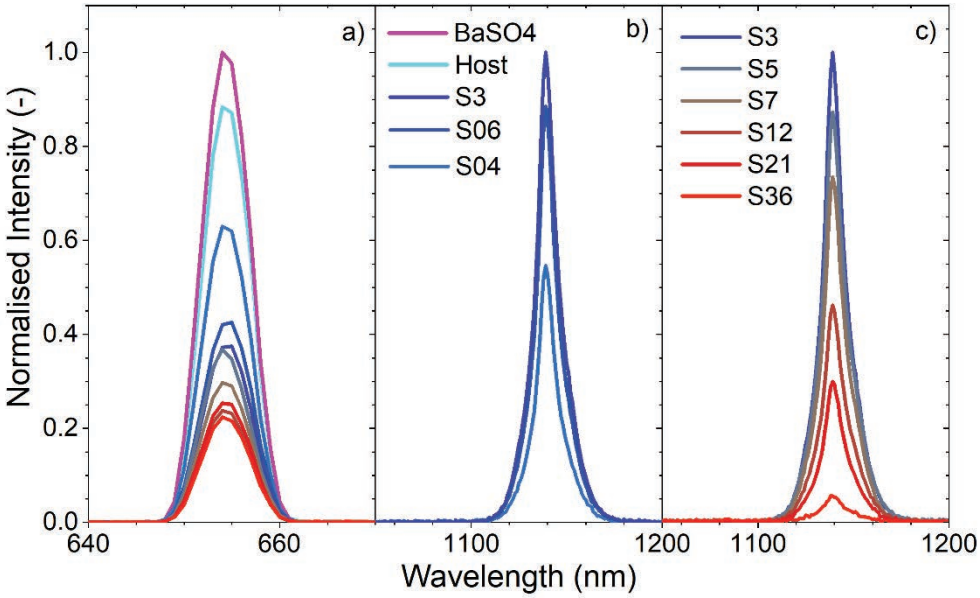

Figure 5.7: (a) Reflectance spectra of the samples and SrI_2 (host) relative to $BaSO_4$. (b,c) Tm^{2+} $^2F_{5/2}\rightarrow{}^2F_{7/2}$ emission spectra. The sample names refer to table 5.5.

The luminescence lifetime of the Tm^{2+} $^2F_{5/2}\rightarrow{}^2F_{7/2}$ emission, indicated by the orange curve, was also investigated for all eight samples. The corresponding decay curves are plotted in figure 5.9 and reveal that the slope of the decay curves stays constant up to a concentration of 5 mol %. This implies that the luminescence lifetime, also presented in table 5.6, remains constant. For higher Tm^{2+}-doping concentrations, the tail part of the decay curves can be approximated by a single exponential with luminescence lifetimes steadily decreasing.

Table 5.6: Overview of the integrated emission intensity Φ_λ, quantum efficiency QE, and the luminescence lifetime τ of the Tm^{2+} $^2F_{5/2}\rightarrow{}^2F_{7/2}$ emission and the relative absorption A_{rel} of the eight different SrI_2:Tm^{2+} samples.

Sample [-]	Φ_λ [%]	A_{rel} [%]	QE [%]	T [ms]
S04	52 ±3	29 ±1	55 ±3	1.1 ±1·10^{-2}
S06	86 ±4	51 ±3	51 ±2	1.1 ±1·10^{-2}
S3	100 ±5	58 ±3	53 ±3	1.1 ±1·10^{-2}
S5	93 ±5	59 ±3	49 ±3	1.1 ±1·10^{-2}
S7	79 ±4	66 ±3	35 ±2	1.0 ±1·10^{-2}
S12	49 ±2	73 ±4	21 ±1	0.9 ±1·10^{-2}
S21	31 ±2	71 ±4	13 ±1	0.6 ±1·10^{-2}
S36	6 ±0.3	75 ±4	3 ±0.2	0.5 ±1·10^{-2}

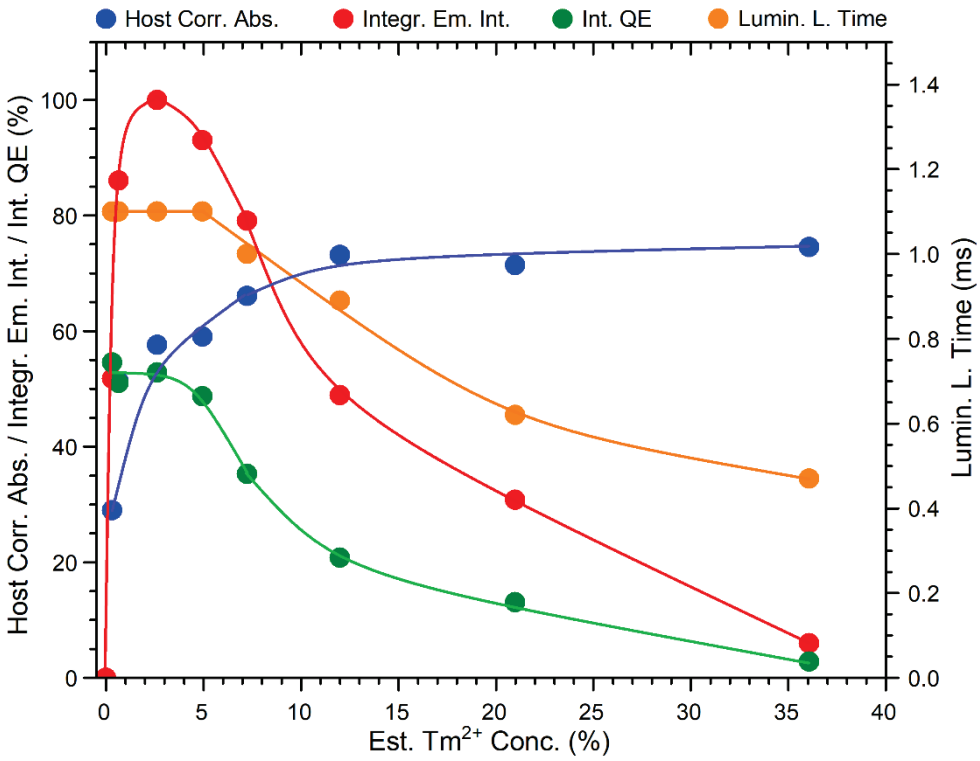

Figure 5.8: The absorption relative to the pure host, normalised integrated $^2F_{5/2}\rightarrow{}^2F_{7/2}$ emission intensity, internal quantum efficiency, and the $^2F_{5/2}\rightarrow{}^2F_{7/2}$ emission lifetimes of the samples as plotted versus their estimated Tm^{2+} concentrations.

Since the luminescence lifetime is proportional to the quantum efficiency, one would expect an equal decline over concentration. The QE declines by a factor of almost 20, from 55% at the lowest Tm^{2+} concentration to 3% at a Tm^{2+} concentration of 36 mol %. The decay time however only drops by a factor of 2. This apparent discrepancy can be explained by the presence of the $CdCl_2$ phase at higher Tm^{2+} concentrations. As table 6.5 reveals, sample S12 already contains a large fraction of the $CdCl_2$ phase. The Tm^{2+}-doping ions that occupy the Sr-sites in this phase have a significant impact on the absorption, yet there is only a very small contribution to the $^2F_{5/2}\rightarrow{}^2F_{7/2}$ emission intensity. The non-equivalent decrease can hence be explained by the fact that the QE measurements are based on the contributions of both structural phases; whereas the luminescence lifetime measurements only involve the contributions of the Tm^{2+} ions that are present in the regular SrI_2 phase.

Upon reaching a Tm^{2+}-doping concentration of 36 mol %, the highest in the sample series, the internal quantum efficiency has decreased to a mere 3%, while the integrated emission

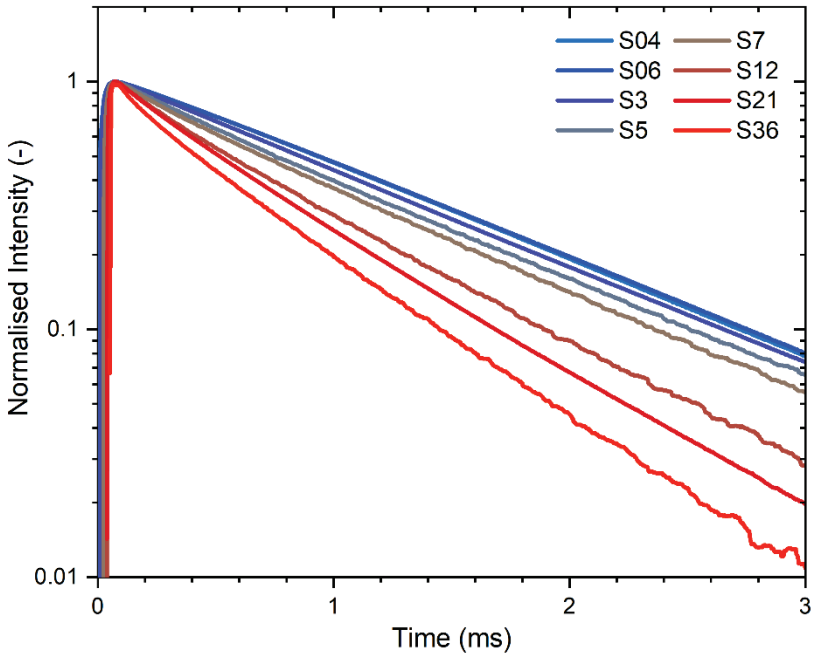

Figure 5.9: Normalised decay curves of the Tm^{2+} $^2F_{5/2} \rightarrow {}^2F_{7/2}$ emission under 410 nm pulsed laser excitation at room temperature. The intensity is plotted on a log-scale. The sample names refer to table 6.5.

intensity has reduced to 6%. In addition, the luminescence lifetime reaches a value of 0.47 ms. The host corrected absorption has become constant with concentration and attains at 75%.

Since all measurements were performed at the same temperature, thermal quenching mechanisms cannot be responsible for the decrease in the luminescence lifetime and emission intensity. Since the Tm^{2+}-doping concentration is the only parameter varied, the quenching can be attributed to concentration quenching, where the Tm^{2+} concentration of about 5 mol % forms the critical concentration.

5.3.3 Temperature-Dependent Luminescence

As became apparent in the previous section, the QE of the samples is limited to 53% and does not reach a full 100%. This observation has incited us to investigate the temperature dependent relaxation dynamics of three selected samples. Sample S3 contains only the regular SrI_2 phase and its Tm^{2+}-doping concentration lies below the critical value where concentration quenching is encountered. Sample S7 also contains the regular SrI_2 phase, but lies slightly above the critical concentration. Sample S21 contains a substantial amount of the $CdCl_2$ phase aside the SrI_2 phase and its Tm^{2+} content ranges far above the critical concentration.

Classification of Excitation Bands and Emissions

Figure 5.10 shows the emission spectra of the three samples as photoexcited at 410 nm and for the temperatures of 20 K and 300 K. Up to four distinct Tm^{2+} emissions are observed. The emissions are labelled A to C in analogy to the work of Grimm et al. and our previous article [5-9]. For all samples, $4f^{12}5d^1 \rightarrow 4f^{13}$ emission B appears to be very intense at low temperature; while $4f^{13} \rightarrow 4f^{13}$ emission A is most dominant at room temperature. Furthermore, $4f^{12}5d^1 \rightarrow 4f^{13}$ emission C only appears in samples S3 and S21; while for the latter sample an additional 5d-4f emission is observed which is labelled as B*. Since all emissions are present in sample S21, excitation spectra were recorded for each emission peak and are displayed in figure 5.11. The excitation spectrum of emission B* deviates distinctively from the others. The observed bands and emissions are shown in an energy level diagram in figure 5.12.

For SrI_2:Yb^{2+} the lowest energy $4f^{14} \rightarrow 4f^{13}5d^1$ spin-forbidden excitation band is located at 418 nm. [19] Using the constant, material independent energy difference of 1.2 eV between the $4f^{12}5d^1$-state energies of Yb^{2+} and Tm^{2+}, as discussed by Dorenbos et al. [20], the lowest energy spin-forbidden excitation band of Tm^{2+} in SrI_2 should be located at around 728 nm. The excitation spectrum of emission B in figure 5.11 shows indeed such a band located at around 724 nm. The lowest energy spin-allowed $4f^{13} \rightarrow 4f^{12}5d^1$ excitation band for SrI_2:Yb^{2+} is observed at 390nm. For SrI_2:Tm^{2+} its location is therefore predicted at around 651 nm. [19] Figure 5.11 shows a band at 654 nm in the excitation spectra of emissions A, B, and C. The excitation spectrum of emission B*, does not match any of those bands. It shows a band at around 740 nm which resembles the K-M absorption spectra shown in figure 5.4. It can therefore be concluded that emission B* emerges from the Tm^{2+} ions in the $CdCl_2$ phase.

Now that the lowest energy $4f^{13} \rightarrow 4f^{12}5d^1$ excitation bands have been identified, Stokes shift values can be used to classify the emissions. The Stokes shift of the Yb^{2+} $4f^{13}[^2F_{5/2}]5d^1 \rightarrow 4f^{14}$ spin-allowed emission in SrI_2 amounts to 0.21 eV. [19] When adding this value to the Tm^{2+} $4f^{12}5d^1 \rightarrow 4f^{13}$ emissions in SrI_2, a good agreement is achieved with the excitation bands in figure 5.11. Emission B in sample S21 is observed at 823 nm. Subtracting the Stokes shift energy, an excitation band should be expected near 720 nm. The excitation spectrum shows the presence of a weak band at 724 nm. Therefore, emission B can be classified as the transition from the $(^3H_6)_{S=3/2}$ spin-forbidden $4f^{12}5d^1$-level towards the $^2F_{7/2}$ $4f^{13}$ ground state, see figure 5.12. Similarly emission C corresponds to an excitation band located at 665nm, which represents the spin-allowed $(^3H_6)_{S=1/2}$ 5d level. Consequently, emission C is related to the $(^3H_6)_{S=1/2} \rightarrow {}^2F_{7/2}$ transition. The decay time of emission B at 20 K is provided in table 5.7; it is in the order of a few hundred microseconds. In contrast, emission C decays in a few

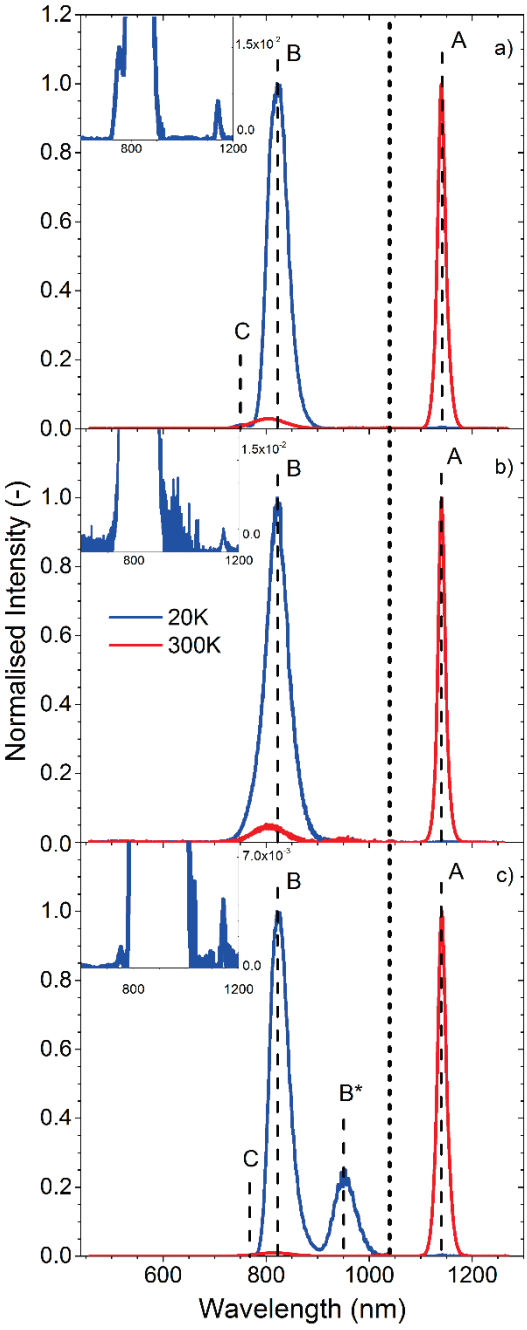

Figure 5.10: Emission spectra of samples S3 a), S7 b), and S21 c) under 410 nm excitation at 20 K and 300 K. The dashed line at 1040 nm separates the CCD and NIR-PMT detector ranges with different sensitivities. The CCD spectra are normalised on emission B at 20 K, the NIR-PMT spectra on emission A at 300 K. The sample names refer to table 5.5 and emission labels to figure 5.12.

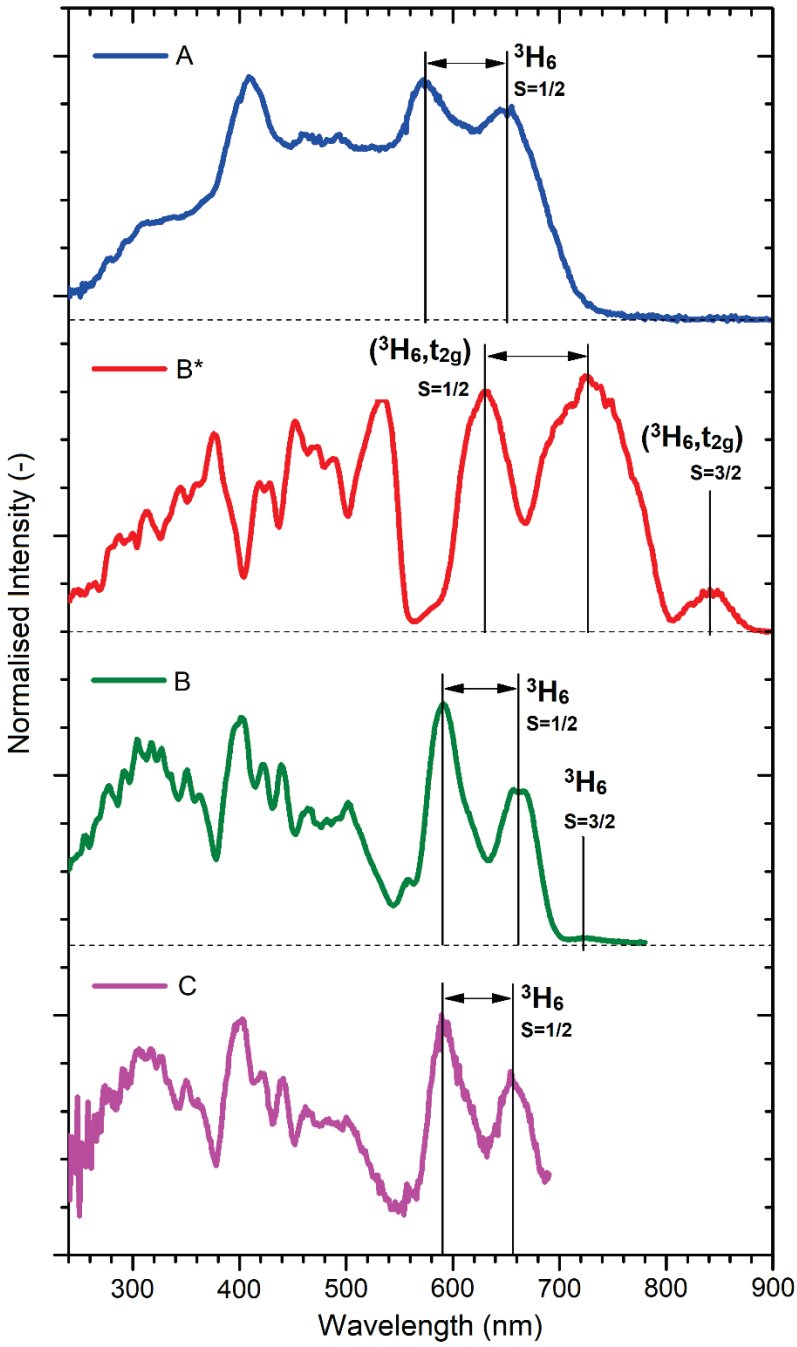

Figure 5.11: Excitation spectra of the four distinct Tm^{2+} emissions in sample S36. The spectra are normalised on the band between 560-630 nm and recorded at 20 K (B, B*, C) or 300 K (A). Excitation band labels refer to figure 5.12.

hundred nanoseconds which is three orders of magnitude faster. This difference in decay times is caused by the spin-forbidden and spin-allowed nature of the respective transition. Emission A is located at 1140 nm and represents the Tm^{2+} $^2F_{5/2}\rightarrow{}^2F_{7/2}$ $4f^{13}\rightarrow4f^{13}$ emission. Its relatively slow decay time of 618 µs reflects the parity forbidden nature of this emission.
Upon adding the Stokes shift energy value to emission B*, an excitation band should be present at 820 nm. Such a band can only be observed in the excitation spectrum of emission B* itself. It is located close to 841 nm and assigned to the $(^3H_6,t_{2g})_{S=3/2}$ spin-forbidden $4f^{12}5d^1$-level of the Tm^{2+} ions in the $CdCl_2$ phase. Hence, the emission is associated with the $(^3H_6,t_{2g})_{S=3/2}\rightarrow{}^2F_{7/2}$ transition.

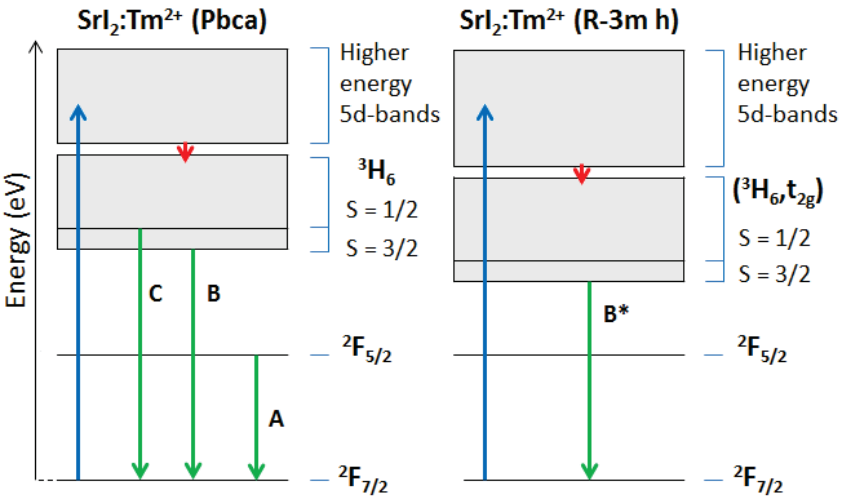

Figure 5.12: Energy level diagram of SrI_2:Tm^{2+} in the SrI_2 (Pbca) and $CdCl_2$ (R-3m h) phases. After excitation at 410 nm (blue arrow) four distinct emissions (green arrows) are observed at 20 K. The emission labels refer to table 5.7.

Table 5.7: Overview on the four distinct Tm^{2+} emissions observed in samples S3, S7, and S21.

Sample	Emission	Transition	Wavelength (20 K) [nm]	Energy (20 K) [eV]	Decay Time(s)
S3	C	$(^3H_6)_{S=1/2}\rightarrow{}^2F_{7/2}$	755	1.64	310 ns, 765 ns (20 K)
	B	$(^3H_6)_{S=3/2}\rightarrow{}^2F_{7/2}$	822	1.51	260 µs (20 K)
	A	$^2F_{5/2}\rightarrow{}^2F_{7/2}$	1141	1.09	1.10 ms (300 K)
S7	B	$(^3H_6)_{S=3/2}\rightarrow{}^2F_{7/2}$	821	1.51	265 µs (20 K)
	A	$^2F_{5/2}\rightarrow{}^2F_{7/2}$	1141	1.09	1.03 ms (300 K)
S21	C	$(^3H_6)_{S=1/2}\rightarrow{}^2F_{7/2}$	752	1.65	210 ns, 635 ns (20 K)
	B	$(^3H_6)_{S=3/2}\rightarrow{}^2F_{7/2}$	823	1.51	260 µs (20 K)
	B*	$(^3H_6)_{S=3/2}\rightarrow{}^2F_{7/2}$	954	1.30	80 µs, 220 µs (20 K)
	A	$^2F_{5/2}\rightarrow{}^2F_{7/2}$	1142	1.09	618 µs (300 K)

Temperature Dependence of Emission Intensities

At a temperature of 20 K all four observed emissions are present. The temperature plots in figure 5.13 show that, for all three samples, emission B is most intense at 20 K. As the temperature increases to 100 K, its luminescence intensity stays relatively constant, see also figure 5.14. Above 100 K the intensity decreases rapidly and the emission starts to quench. An Arrhenius analysis shows that the thermal deactivation energies related to the quenching process amount to 203, 104, and 225 meV for samples S3, S7, and S21 respectively. As emission B starts to quench, the luminescence intensity of emission A displays an anti-correlated trend and increases rapidly. It indicates that the quenching of $4f^{12}5d^1 \rightarrow 4f^{13}$ emission B leads to a likely feeding of $4f^{13} \rightarrow 4f^{13}$ emission A over temperature. The energy gap between the $(^3H_6)_{S=3/2}$ and $^2F_{5/2}$ levels is around 417 meV or 3415 cm^{-1} and resembles around 32 vibrational quanta. [21] It is similar in size to $CaBr_2:Tm^{2+}$, see table 3.3, but in case of $SrI_2:Tm^{2+}$ many more phonons are required to bridge it. Furthermore, the Stokes shift of $SrI_2:Tm^{2+}$ amounts to 1632 cm^{-1} and is around 30% larger as compared to $CaBr_2:Tm^{2+}$. This indicates that in $SrI_2:Tm^{2+}$, the configurational crossing point between the $(^3H_6)_{S=3/2}$ and $^2F_{5/2}$ states is likely to be positioned at a lower energy and hence the quenching process of interband crossing would be activated at a much lower temperature. It is therefore likely that the quenching of emission B, primarily, occurs via interband crossing with perhaps additional quenching via multi-phonon relaxation at higher temperature.
Noteworthily, the point of equal intensity between emissions A and B seems to undergo a shift in both temperature and intensity, when comparing sample S3 with samples S7 and S21. The shift is likely to be related to concentration quenching effects that are known to occur in the latter two samples.

The observations in the luminescence intensity of emission B over temperature are supported by trends in its luminescence lifetime. At 20 K, its lifetime amounts to 265 µs for sample S7. For temperatures up to 100 K, the decay curves remain parallel to each other and hence the luminescence lifetime remains constant, as illustrated in figure 5.15c. Above 100 K the decay curves contract, which indicates that the emission undergoes quenching. The luminescence lifetime reaches a value of 11 µs at 300 K. Similar trends were observed in the luminescence lifetime spectra of samples S3 and S21, where the lifetime is around 260 µs at 20 K and 9 µs and 23 µs at 300 K respectively.

Emission A is already weakly present at the lowest studied temperature of 20 K, where its decay curve, in figure 5.15a, displays a small risetime phenomena. It has a duration of 22 µs and is one order of magnitude shorter than the lifetime of $4f^{12}5d^1 \rightarrow 4f^{13}$ emission B. As the temperature is increased to 100 K, the risetime duration changes from 22 µs to 30 µs;

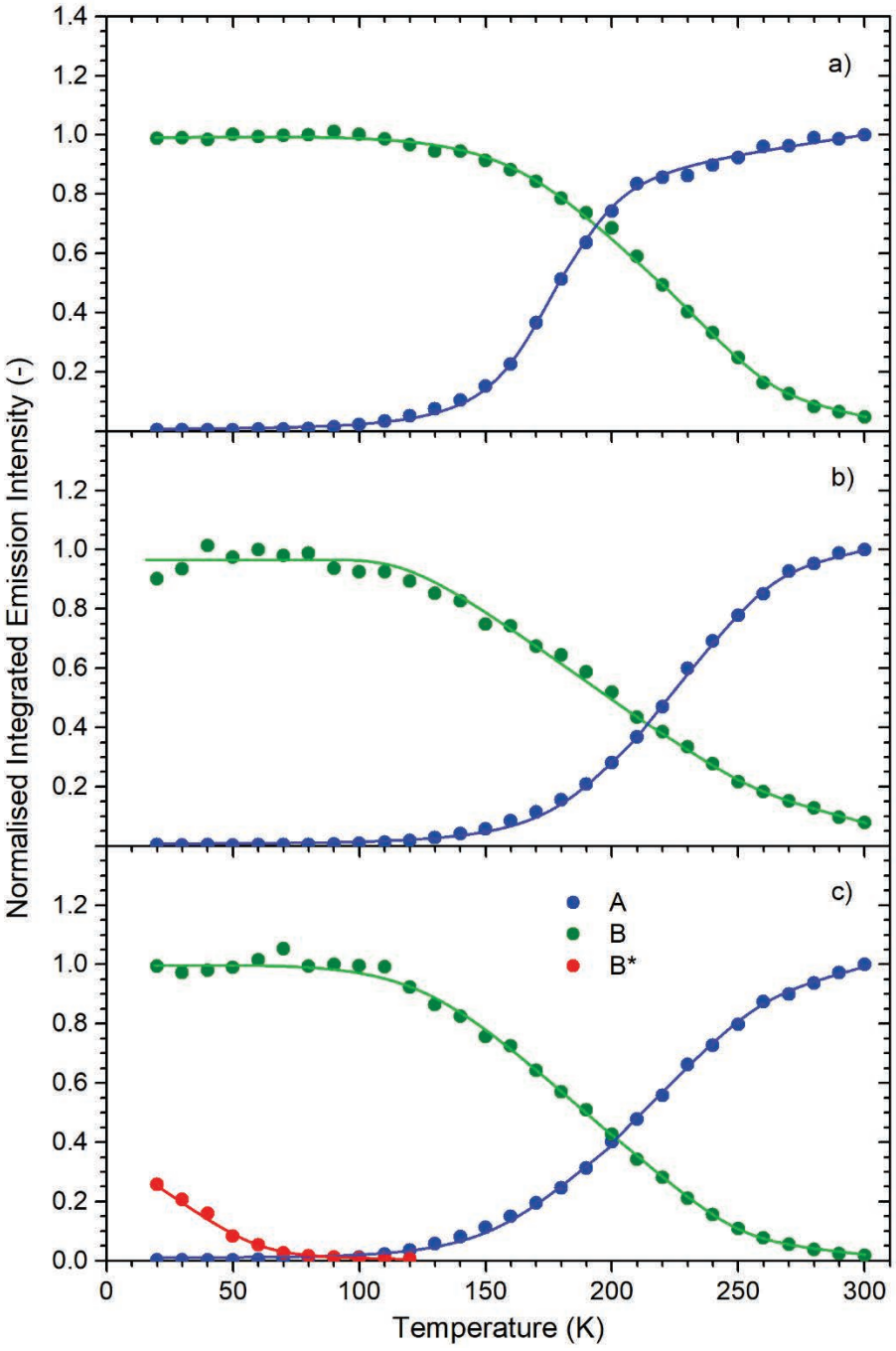

Figure 5.13: Temperature dependence of the normalised integrated Tm^{2+} emission intensity of emissions A, B, and B* for samples S3 a), S7 b), and S21 c). Samples were excited at 410 nm. Sample names refer to table 5.5 and emission labels to table 5.7. The solid lines serve as a guide to the eye.

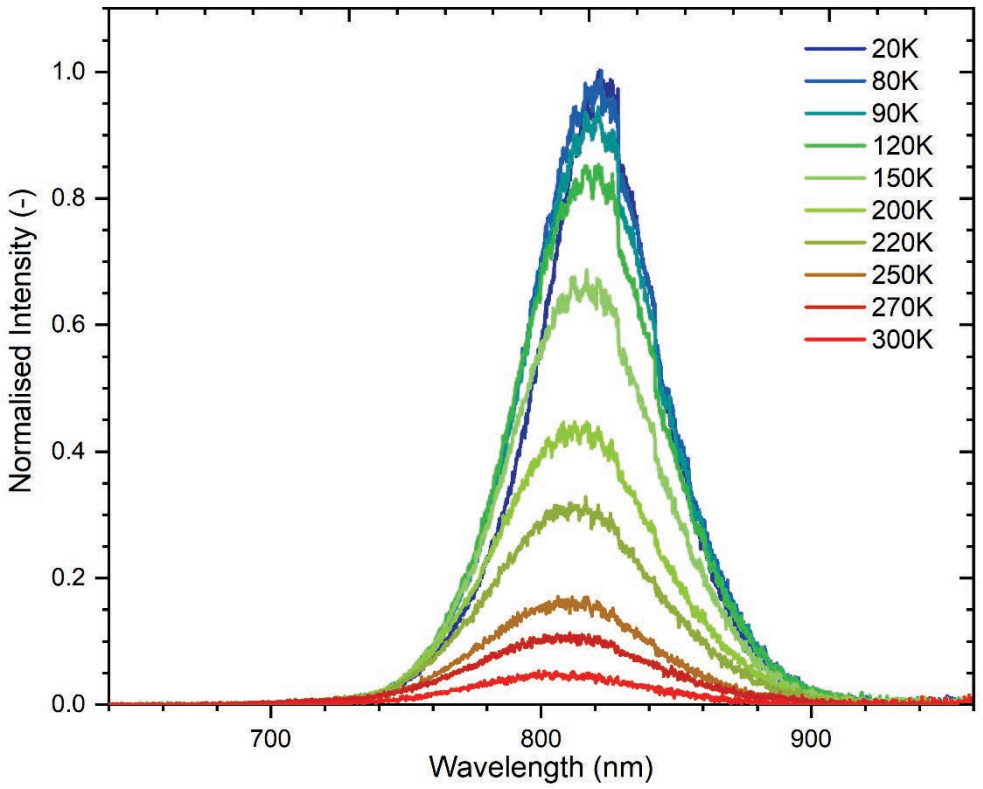

Figure 5.14: Temperature dependence of the Tm^{2+} $({}^3H_6,t_{2g})_{S=3/2} \rightarrow {}^2F_{7/2}$ emission B of sample S7 under 410 nm excitation at 20 K. The spectra are normalised to 20 K.

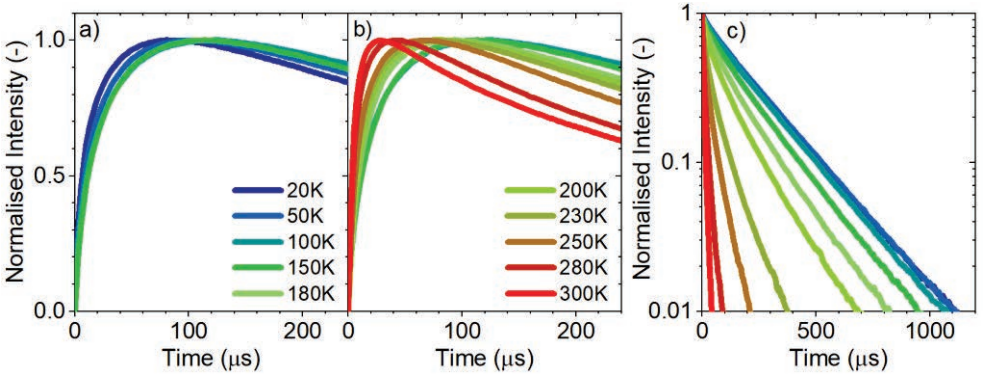

Figure 5.15: The time resolved spectra showing the risetime phenomena as present in the decay curves of ${}^2F_{5/2} \rightarrow {}^2F_{5/2}$ emission A (ab) and the decay curves of $({}^3H_6,t_{2g})_{S=3/2} \rightarrow {}^2F_{7/2}$ emission B (c) in sample S7 at different temperatures. The time-resolved spectra were acquired using pulsed laser excitation at 410 nm

suggesting that the luminescence feeding process slows down. Much similar observations were previously reported in section 3.3.5 for $CaX_2:Tm^{2+}$ (X = Cl, Br, I), where the low temperature discrepancy between the lifetime of $4f^{12}5d^1 \rightarrow 4f^{13}$ emission B and risetime of $4f^{13} \rightarrow 4f^{13}$ emission A was attributed to a $4f^{12}5d^1 \rightarrow 4f^{13}$ multi-phonon relaxation route from the $(^3H_6)_{S=1/2}$ levels to the $^2F_{5/2}$ level with strong electron-phonon coupling. At higher temperatures 100-300 K, the risetime duration shortens from 30 µs to 13 µs; indicating a faster feeding. This occurs in the temperature range in which emission B quenches. The lifetime of emission B and risetime of emission A then become of the same order of magnitude and start to converge. This can be explained by a thermal activation of the $(^3H_6)_{S=1/2} \rightarrow (^3H_6)_{S=3/2}$ and $(^3H_6)_{S=3/2} \rightarrow {}^2F_{5/2}$ relaxation routes, beside the already active $(^3H_6)_{S=1/2} \rightarrow {}^2F_{5/2}$ route.

As an alternative view, the Vacuum Referred Binding Energy (VRBE) diagram of SrI_2, displayed in figure 5.16 with permission from Alekhin et al. [22], reveals that the Tm^{2+} $(^3H_6)_{S=1/2}$ $4f^{12}5d^1$-band used for photoexcitation is likely to be located close to the conduction band. The weak presence of emission A at low temperatures and the related risetime feature and behaviour could then also be explained by a feeding mechanism via conduction band states. A similar mechanism was opted and described earlier on in section

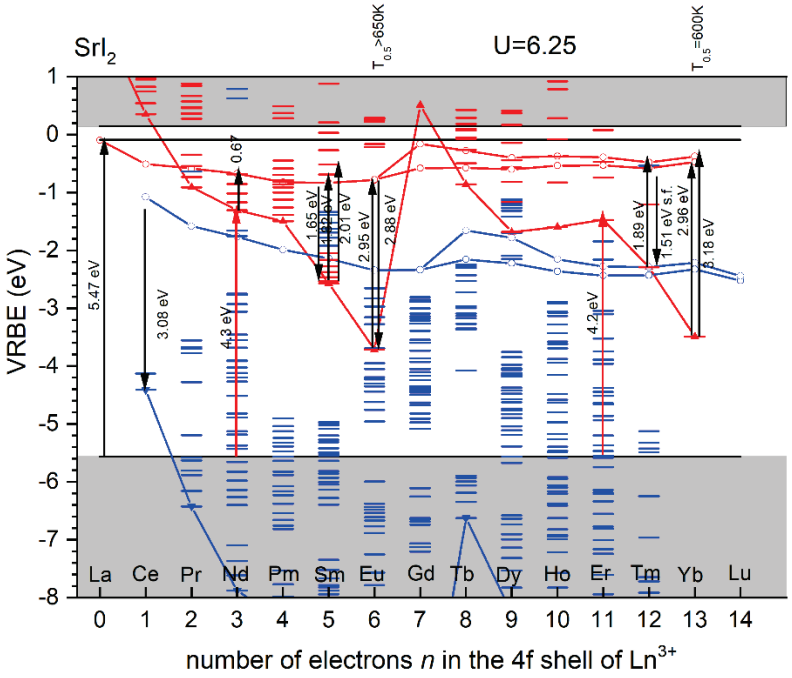

Figure 5.16: The VRBE diagram of SrI_2 based on acquired data by Alekhin et al [19,22,23] on $SrI_2:Er^{3+}$ and $SrI_2:Ln^{2+}$ (Ln = Yb, Sm, Eu), displayed with permission from authors, and extended with data on $SrI_2:Ln^{3+}$ (Ln = Ce [24], Nd [25]) and our own data on $SrI_2:Tm^{2+}$.

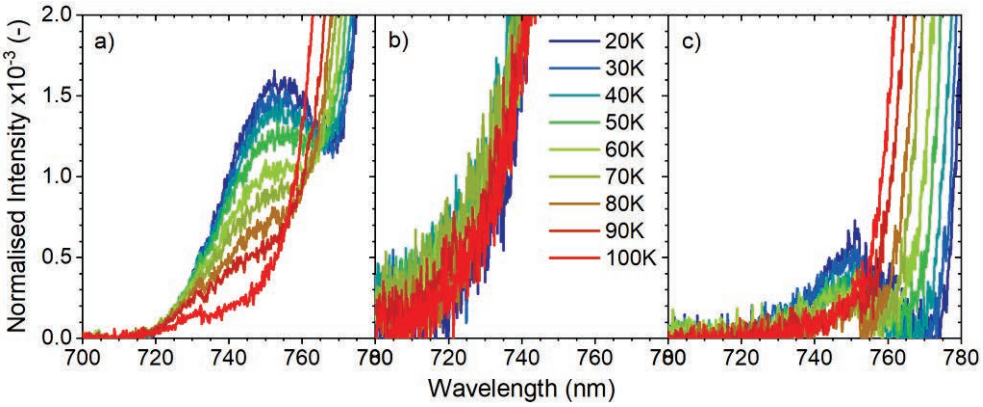

Figure 5.17: The temperature dependent emission spectra of the $(^3H_6)_{S=1/2}\rightarrow{}^2F_{7/2}$ emission C of samples (a) S3, (b) S7, and (c) S21. The spectra were excited at 410 nm and are normalized on $(^3H_6)_{S=3/2}\rightarrow{}^2F_{7/2}$ emission B at 20 K.

2.4 for $NaBr:Tm^{2+}$. Such a feeding process is known to be largely independent of temperature and might also explain why the QE is not 100%.

Emission C is only observed in samples S3 and S21. The temperature dependent emission spectra in figure 5.17 reveal that, for both samples, it is most intense at 20 K. As the temperature increases, the intensity of emission C decreases and it starts to undergo quenching; having quenched completely at 100 K. As the energy gap between the $(^3H_6)_{S=1/2}$ and $(^3H_6)_{S=3/2}$ levels is close to 140 meV or 1570 cm^{-1}, representing 15 vibrational quanta [21], the quenching can most likely be associated with multi-phonon relaxation.

Emission B* emerges from the Tm^{2+} ions in the $CdCl_2$ phase and originates from the $(^3H_6,t_{2g})_{S=3/2}$ level. It is only present in sample S21 and figures 5.13 and 5.18 show that its luminescence intensity already starts to decrease rapidly at 20 K. At 100-120 K, the emission is quenched completely. The energy difference between the $(^3H_6,t_{2g})_{S=3/2}$ and $^2F_{5/2}$ levels is around 384 meV, or 3100 cm^{-1}, and represents around 30 vibrational quanta. Since the amount of quanta to bridge this gap is almost similar to that of emission B, and with emission B* quenching at a much lower temperature, it is very likely that interband crossing is the dominant quenching process for both emissions.

Room temperature excitation into the $(^3H_6,t_{2g})_{S=3/2}$ level at 840 nm reveals a very weak $^2F_{5/2}\rightarrow{}^2F_{7/2}$ emission that is not there at 20 K, see figure 5.19. At this excitation wavelength the Tm^{2+} ions in the regular SrI_2 phase are not excited and the observed $^2F_{5/2}\rightarrow{}^2F_{7/2}$ emission can only emerge from the Tm^{2+} ions in the $CdCl_2$ phase. However, the perceived $^2F_{5/2}\rightarrow{}^2F_{7/2}$ emission at 300 K is much weaker than emission B* at 20 K. This could indicate the presence of a quenching route towards the ground state, possibly via $(^3H_6,t_{2g})_{S=3/2}\rightarrow{}^2F_{7/2}$ interband crossing.

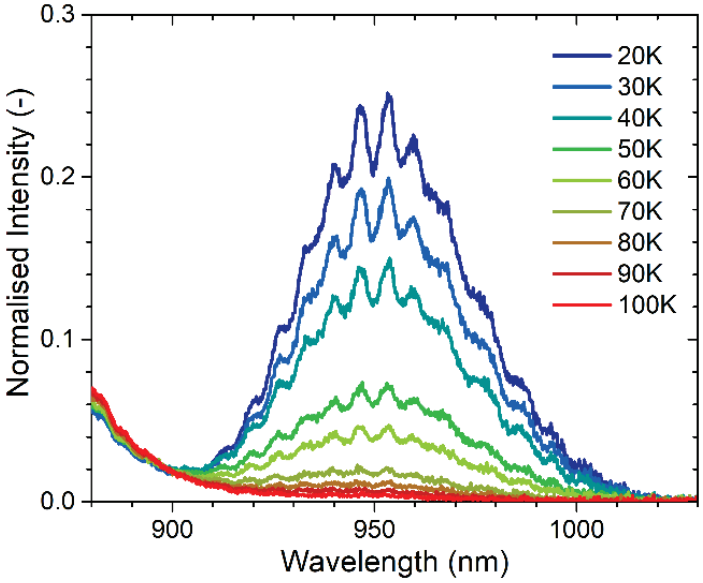

Figure 5.18: The temperature dependent emission spectra of the Tm^{2+} $(^3H_6)_{S=3/2} \rightarrow {}^2F_{7/2}$ emission (B*) corresponding to the Tm^{2+} ions occupying the $CdCl_2$ phase as present in sample S21. The spectra are normalised on $(^3H_6)_{S=3/2} \rightarrow {}^2F_{7/2}$ emission B at 20 K and photoexcitation occurred at 410 nm.

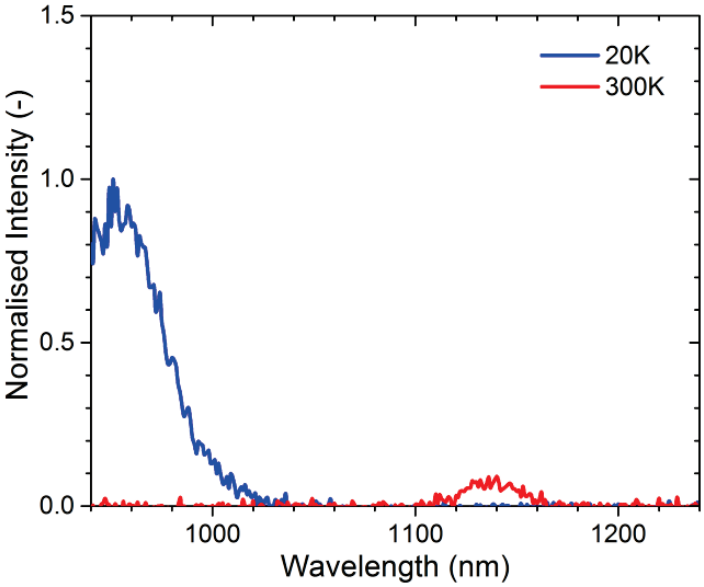

Figure 5.19: Emission spectra at 20 and 300 K showing the Tm^{2+} $(^3H_6)_{S=3/2} \rightarrow {}^2F_{7/2}$ and $^2F_{5/2} \rightarrow {}^2F_{7/2}$ emissions after photoexcitation at 840nm into the $(^3H_6)_{S=3/2}$ level of the Tm^{2+} ions occupying the $CdCl_2$ phase. The spectra are corrected for the sensitivity of the NIR-PMT detector.

5.4. Conclusions

For the SrI_2-TmI_2 system, the QE of the $^2F_{5/2}\rightarrow{}^2F_{7/2}$ emission attains a value of over 50%. As the Tm^{2+}-doping concentration reaches the critical value of 5 mol %, the QE starts to decrease due to concentration quenching effects and the appearance of a second structural phase that has a profound contribution to the absorption yet a negligible effect on the $^2F_{5/2}\rightarrow{}^2F_{7/2}$ emission. Since the QE partly determines the overall efficiency of the LSC application, a Tm^{2+}-doping concentration below the critical value is therefore desired. In an attempt to explain why the QE value is bounded to 50%, the temperature dependent relaxation dynamics were investigated. In resemblance to other Tm^{2+}-doped halide studies, the $(^3H_6)_{S=3/2}\rightarrow{}^2F_{7/2}$ emission quenches over temperature and feeds the $^2F_{5/2}\rightarrow{}^2F_{7/2}$ emission. This quenching most likely occurs via $(^3H_6,t_{2g})_{S=3/2}\rightarrow{}^2F_{5/2}$ interband crossing with possibly a small additional contribution from $(^3H_6,t_{2g})_{S=3/2}\rightarrow{}^2F_{5/2}$ multi-phonon relaxation. In addition, the presence of the $^2F_{5/2}\rightarrow{}^2F_{7/2}$ emission at low temperatures can likely be explained via $(^3H_6,t_{2g})_{S=1/2}\rightarrow{}^2F_{5/2}$ multiphonon relaxation with strong electron-phonon coupling, as was also concluded for CaX_2:Tm^{2+} (X = Cl, Br, I). Nevertheless, there is no clear indication why the QE is limited to 50%. It is suggested that there might be a non-radiative route from the $(^3H_6,t_{2g})_{S=3/2}$ state towards the $^2F_{7/2}$ ground state possibly via $(^3H_6,t_{2g})_{S=3/2}\rightarrow{}^2F_{7/2}$ interband crossing. It is therefore recommended to investigate this possibility further by analysis of the sensitivity corrected relative $(^3H_6,t_{2g})_{S=1/2}\rightarrow{}^2F_{7/2}$, $(^3H_6,t_{2g})_{S=3/2}\rightarrow{}^2F_{7/2}$ and $^2F_{5/2}\rightarrow{}^2F_{7/2}$ emission intensities, instead of the normalised values as presented in figures 5.11 and 5.13, and in combination with theoretical modelling via rate-equations using a sophisticated three-level model.

5.5 References

[1] O.M. ten Kate, K.W. Krämer, E. Van der Kolk, Efficient luminescent solar concentrators based on self-absorption free, Tm^{2+} doped halides, Sol. Energy Mater Sol. Cells 115-120 (2015) 140.

[2] M.G. Debije, P.P.C. Verbunt, Thirty Years of Luminescent Solar Concentrator Research: Solar Energy for the Built Environment, Adv. Energy Mater. (2011) 2.

[3] F. Meinardi, F. Bruni, S. Brovelli, Luminescent solar concentrators for building-integrated photovoltaics, Nat. Rev. Mater. (2017) 2 17072

[4] W.G.J.H.M. van Sark, K.W.J. Barnham, LH. Slooff, A.J. Chatten, A. Büchtemann, A. Meyer, S.J. McCormack, R. Koole, D.J. Farrell, R. Bose, E.E. Bende, A.R. Burgers, T. Budel, J. Quilitz, M. Kennedy, T. Meyer, C. De Mello Donegá, A. Meijerink, D. Vanmaekelbergh, Luminescent Solar Concentrators - A review of recent results, Opt. Express (2008) 16 26 21773

[5] J. Grimm, H.U. Güdel, Five different types of spontaneous emission simultaneously observed in Tm^{2+} doped $CsCaBr_3$, Chemical Physics Letters 40–43 (2005) 404

[6] J. Grimm, O.S. Wenger, K.W. Krämer, H.U. Güdel, 4f-4f and 4f-5d excited states and luminescence properties of Tm^{2+}-doped CaF_2, $CaCl_2$, $SrCl_2$, $BaCl_2$, J. Phys. Chem. B 101-105 (2006) 110.

[7] J. Grimm, J.F. Suyver, G. Carver, H. U. Güdel, Light-Emission and Excited-State Dynamics in Tm^{2+} Doped $CsCaI_3$, $CsCaBr_3$, and $CsCaI_3$, J. Phys. Chem. B 2093-2101 (2006) 110.

[8] E. Beurer, J. Grimm, P. Gerner, H.U. Güdel, Absorption, Light Emission, and Upconversion Properties of Tm^{2+}-doped $CsCaI_3$ and $RbCaI_3$, Inorg. Chem. 9901-9906 (2006) 45.

[9] M.P. Plokker, E. van der Kolk, Temperature dependent relaxation dynamics of luminescent NaX:Tm^{2+} (X=Cl, Br, I), J. Lumin. (2019) 216.

[10] T. Dienel, C. Bauer, I. Dolamic, D. Brühwiler, Spectral-based analysis of thin film luminescent solar concentrators, Solar Energy 1366-1369 (2010) 84(4).

[11] M. Zhuravleva, L. Stand, H. Wei, Hygroscopicity Evaluation of Halide Scintillators, Conference Paper, Nuclear Science Symposium and Medical Imaging Conference (NSS/MIC) IEEE, Seoul, South Korea (2013).

[12] J. Rodriguez-Carvajal, program FullProf.2k, version 5.2, July-2011, Institute Laue Langevin.

[13] E. Rogers, P. Dorenbos, J.T.M. de Haas, E. van der Kolk, Experimental study of the $4f^n \rightarrow 4f^n$ and $4f^n \rightarrow 4f^{n-1}5d^1$ transitions of the lanthanide diiodides LnI_2 (Ln = Nd, Sm, Eu, Dy, Tm, Yb), J. Phys.: Condens. Matter (2012) 24.

[14] S.A. Hodorowicz, H.A. Eick, An X-ray diffraction study of the SrBrxI2−x system, J. Solid State Chem. 313-320 (1983) 46.

[15] R.D. Shannon, Revised Effective Ionic Radii and Systematic Studies of Interatomic Distances in Halides and Chalcogenides, Acta Crystallogr. A32 (1976) 751.

[16] D.E. Partin and M.J. O'Keefe, The structures and crystal chemistry of magnesium chloride and cadmium chloride, Solid State Chem. 176-183 (1991) 95.

[17] G. Meyer, Reduced halides of the rare-earth elements, Chem. Rev. 93-107 (1989) 88.

[18] G. Jantsch and W. Klemm, Über das Auftreten niederer Wertigkeiten bei den Halogeniden der seltenen Erden, Z. Anorg. Allg. Chem. 216 (1933) 80.

[19] M.S. Alekhin, D.A. Biner, K.W. Kraemer, P. Dorenbos, Optical and scintillation properties of SrI_2:Yb^{2+}, Opt. Mater. 382-386 (2014) 37.

[20] P. Dorenbos, Energy of the first 4f7→4f65d transition of Eu2+ in inorganic compounds, J. Lumin. 239-260 (2003) 104.

[21] Y. Cui, R.Hawrami, E. Tupitysn, P. Bhattacharya, M. Groza, M. Bryant, V. Buliga, A. Burger, N.J. Cherepy, S.A. Payne, Raman spectroscopy study of BaI_2 :Eu and SrI_2 :Eu scintillator crystals, Solid State Commun. 151 (2011) 7.

[22] M.S. Alekhin, R.H.P. Awater, D.A. Biner, K.W. Kraemer, J.T.M. de Haas, P. Dorenbos, Luminescence and spectroscopic properties of Sm^{2+} and Er^{3+} doped SrI_2, J. Lumin. 347-351 (2015) 167.

[23] M.S. Alekhin; J.T.M. de Haas; K.W. Kraemer, P. Dorenbos, Scintillation Properties of and Self Absorption in $SrI_2:Eu^{2+}$, IEEE Trans Nucl Sci 58 (2011) 5.

[24] E.V. van Loef, C.M. Wilson, N.J. Cherepy, G. Hull, S.A. Payne, W.S. Choong, W.W. Moses, K.S. Shah, Crystal Growth and Scintillation Properties of Strontium Iodide Scintillators, IEEE Trans Nucl Sci 869-872 56 (2009)

[25] I.N. Ogorodnikova, V.A. Pustovarova, A.A. Goloshumovab, L.I. Isaenkob, A.P. Yelisseyevb, V.M. Pashkovb, A luminescence spectroscopy study of $SrI_2:Nd^{3+}$ single crystals, J. Lumin. 101-107 (2013) 143.

6.

Research Summary

Tm^{2+}-doped halides exhibit excellent properties for use in Luminescence Solar Concentrator (LSC) applications. Such LSCs consist of a glass waveguide with small Copper-Indium-Selenide (CIS) solar cells attached to its edges. The waveguide contains a luminescent coating based on a Tm^{2+}-doped halide, whose $4f^{12}5d^1$ absorption bands are able to absorb a large fraction of the AM 1.5 solar spectrum. As the absorption occurs over the entire visible light range (380-750 nm) and with a largely uniform absorption strength, the coating can appear colourless and semi-transparent. Via the Tm^{2+} excited states dynamics, the absorbed sunlight will be converted into the $^2F_{5/2} \rightarrow {}^2F_{7/2}$ emission that has a wavelength of 1140 nm. Since this emission falls outside the range of the $4f^{12}5d^1$ absorption bands, no self-absorption losses can occur. These generally pose a significant limitation to the overall LSC efficiency. Subsequently, the converted light is re-emitted by the coating and propagates via total internal reflection through the waveguide that directs it towards the CIS solar cells. These solar cells then photovoltaically convert it into electricity. LSC coatings based on Tm^{2+}-doped halides can be applied as a sustainable window technology and, as part of Building-Integrated Photovoltaics (BIPV), can reduce the energy consumption of buildings making them self-sustaining and less dependent on fossil fuels. [1]

Although the optical and luminescence properties of primarily $CaF_2:Tm^{2+}$, $CsCaX_3:Tm^{2+}$ (X = Cl, Br, I) and $MCl_2:Tm^{2+}$ (M = Ba, Ca, Sr) have been investigated, a substantial amount of other Tm^{2+}-doped halides remain unexplored. Above all, key topics such as the internal Quantum Efficiency (QE) and Tm^{2+} concentration quenching in such materials remains completely unaddressed. The former property has a direct influence on the overall LSC efficiency and is governed by the Tm^{2+} excited states dynamics of the material. In the past, the Tm^{2+} excited states dynamics has been studied in depth for Tm^{2+}-doped $CsCaX_3$ (X = Cl, Br, I) trihalide perovskites. [2-5] However, in these works no other options beside quenching via multi-phonon relaxation has been considered and no correlation was made to QEs nor were such values ever reported. It is therefore the goal of this dissertation to investigate the Tm^{2+} excited states dynamics in various halides as a function of composition, temperature and time, and in connection to the $^2F_{5/2} \rightarrow {}^2F_{7/2}$ QE. Both a qualitative and quantitative analysis is provided on the different $4f^{12}5d^1 \rightarrow 4f^{12}5d^1$ and $4f^{12}5d^1 \rightarrow 4f^{13}$ non-radiative quenching processes.

In **chapter 2**, the Tm^{2+} excited state dynamics was investigated in NaX (X = Cl, Br, I) compounds. The 20 K emission spectra revealed the presence of up to five distinct Tm^{2+} emissions: four $4f^{12}5d^1 \rightarrow 4f^{13}$ emissions and the $4f^{13} \rightarrow 4f^{13}$ emission. An accompanying level scheme is provided in figure 6.1. As the temperature increases to 120 K, most of the $4f^{12}5d^1 \rightarrow 4f^{13}$ emissions undergo quenching via multi-phonon relaxation and only the lowest energy $4f^{12}5d^1 \rightarrow 4f^{13}$, $(^3H_6,t_{2g})_{S=3/2} \rightarrow {}^2F_{7/2}$, emission and the $4f^{13} \rightarrow 4f^{13}$, $^2F_{5/2} \rightarrow {}^2F_{7/2}$, emission remain. For NaBr:Tm^{2+}, the intensity of the $(^3H_6,t_{2g})_{S=3/2} \rightarrow {}^2F_{7/2}$ emission starts to decrease rapidly for temperatures above 170 K. At these temperatures, the $^2F_{5/2} \rightarrow {}^2F_{7/2}$ emission intensity is anti-correlated to that of the $(^3H_6,t_{2g})_{S=3/2} \rightarrow {}^2F_{7/2}$ emission and hence it increases significantly. This indicates a $(^3H_6,t_{2g})_{S=3/2} \rightarrow {}^2F_{5/2}$ non-radiative feeding, as confirmed by the presence of a risetime phenomenon in the $^2F_{5/2} \rightarrow {}^2F_{7/2}$ decay curves. The risetime is of similar size to decay time of the $(^3H_6,t_{2g})_{S=3/2} \rightarrow {}^2F_{7/2}$ emission. As the temperature increases, the feeding speeds up and at room temperature only the $^2F_{5/2} \rightarrow {}^2F_{7/2}$ emission is present. The room temperature QE of the $^2F_{5/2} \rightarrow {}^2F_{7/2}$ emission in NaBr:Tm^{2+} was measured to be 32±2%. The non-unity QE is explained by the presence of multiple Tm^{2+}-sites and defects as caused by the required

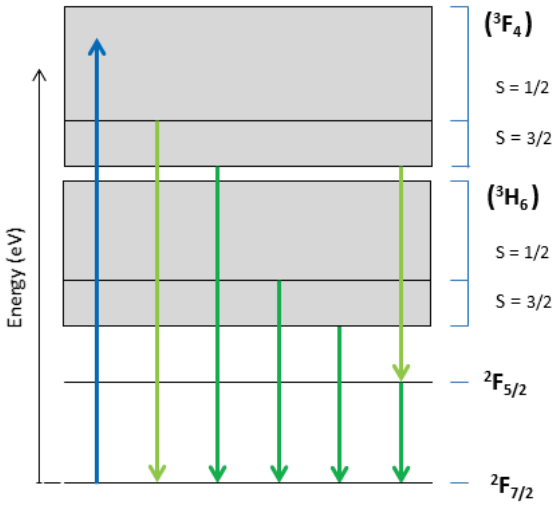

Figure 6.1: Energy level diagram of a typical Tm^{2+}-doped halide with the two lowest energy $4f^{12}5d^1$-levels: ($^3F_4$) and ($^3H_6$). Both levels are split into spin-allowed (S=1/2) and spin-forbidden (S=3/2) states. The latter are positioned at relatively lower energies. Also drawn are the ($^2F_{5/2}$) $4f^{13}$ excited state and ($^2F_{7/2}$) $4f^{13}$ ground state. The various Tm^{2+} emission are indicated by green arrows. The light green arrows represent 'rarely' observed Tm^{2+} emissions, such as the $(^3F_4)_{S=1/2} \rightarrow {}^2F_{7/2}$ emission, which has up to now only been perceived in $CsCaI_3$:Tm^{2+} [2,3, chapter 5], and the $(^3F_4)_{S=3/2} \rightarrow {}^2F_{5/2}$ emission that can be found in $CsCaX_3$:Tm^{2+} (X = Cl, Br, I) [2, 4, chapter 5] and NaY:Tm^{2+} (Y = Cl, Br) [chapter 2]. The $(^3H_6)_{S=1/2} \rightarrow {}^2F_{7/2}$ emission is almost always absent in Chloride compounds and up to now has only been reported in $BaCl_2$:Tm^{2+}. [5]

charge compensation when Tm^{2+} enters the mono-halides on the Na^{+}-site. In addition, the selected ($^3F_4$,t_{2g}) excitation level is located at higher energies and might therefore be positioned close to the conduction band, allowing for non-radiative relaxation via impurity bound exciton states towards the ($^2F_{5/2}$) $4f^{13}$ excited state and ($^2F_{7/2}$) $4f^{13}$ ground state.

Chapter 3 focussed on the Tm^{2+} excited states dynamics in CaX_2 (X = Cl, Br, I), where there is no requirement for charge compensation. In analogy to NaI:Tm^{2+}, the 20 K emission spectra exhibit four different Tm^{2+} emissions. In case of CaI_2:Tm^{2+}, the ($^3F_4$,t_{2g})→$^2F_{7/2}$ emission from the higher energy $4f^{12}5d^1$-state appears much more intense at 20 K than the ($^3H_6$,t_{2g})$_{S=3/2}$→$^2F_{7/2}$ emission. A similar situation was previously reported for $CsCaI_3$:Tm^{2+}. [4] It can be explained by a relatively larger energy gap between the ($^3F_4$,t_{2g})-($^3H_6$,t_{2g})$_{S=1/2}$ states, as compared to the ($^3H_6$,t_{2g})$_{S=3/2}$-($^2F_{5/2}$) states, and hence the ($^3F_4$,t_{2g})→$^2F_{7/2}$ emission quenches, via multi-phonon relaxation, at a much higher temperature. In case of $CaCl_2$:Tm^{2+} and $CaBr_2$:Tm^{2+}, most of the $4f^{12}5d^1$→$4f^{13}$ emissions quench, via multi-phonon relaxation, below 100 K and only the ($^3H_6$,t_{2g})$_{S=3/2}$→$^2F_{7/2}$ emission and the $^2F_{5/2}$→$^2F_{7/2}$ emission remain. A rate equation model was developed to describe the subsequent ($^3H_6$,t_{2g})$_{S=3/2}$→$^2F_{5/2}$ non-radiative feeding. The model was successfully fitted onto the temperature- and time-dependent luminescence intensity data of $CaBr_2$:Tm^{2+} and $CaCl_2$:Tm^{2+}. This analysis revealed that the non-radiative relaxation occurs via two different processes. At low temperatures multi-phonon relaxation towards the ($^2F_{5/2}$) $4f^{13}$ excited level dominates. As this process is less temperature dependent at the lowest temperatures, it explains the presence of the $^2F_{5/2}$→$^2F_{7/2}$ emission at 20 K. As the temperature increases, to typically 130 K, the additional process of interband crossing becomes thermally activated. As a result only the $^2F_{5/2}$→$^2F_{7/2}$ emission is observed at room temperature. Although the quantitative fitting approach described the overall temperature- and time-dependent behaviour of the ($^3H_6$,t_{2g})$_{S=3/2}$→$^2F_{7/2}$ well, two main discrepancies were observed. At low temperature, the $^2F_{5/2}$→$^2F_{7/2}$ risetime is significantly shorter than predicted by our model. Luminescence decay measurements at 20 K reveal that the decay time of the ($^3H_6$,t_{2g})$_{S=3/2}$→$^2F_{7/2}$ emission is 15 times longer than the $^2F_{5/2}$→$^2F_{7/2}$ risetime. As the temperature increases to 150 K, the $^2F_{5/2}$→$^2F_{7/2}$ risetime start to converge on the ($^3H_6$,t_{2g})$_{S=3/2}$→$^2F_{7/2}$ decay time reaching an almost identical value at room temperature. This phenomenon can likely be explained by the presence of a low temperature ($^3H_6$,t_{2g})$_{S=1/2}$→$^2F_{5/2}$ feeding route via multi-phonon relaxation that has a strong electron-phonon coupling and which is absent in our model. In addition, the model predicted a $^2F_{5/2}$→$^2F_{7/2}$ QE of 100%, while measured values at room temperature range between 20-30%. This was also observed for the NaX:Tm^{2+} monohalides.

In **chapter 4**, the Cl/Br and Br/I ratios in $CsCaX_3$:Tm^{2+} (X = Cl, Br, I) solid solutions were systematically varied, leading to a series of 11 different materials. By tuning the

composition, the positions of the Tm^{2+} $4f^{12}5d^1$-levels are consistently shifted as relative to the ($^2F_{5/2}$) and ($^2F_{7/2}$) $4f^{13}$-levels. At low temperatures, up to five distinct Tm^{2+} $4f^{12}5d^1 \rightarrow 4f^{13}$ emissions can be observed, along with the $^2F_{5/2} \rightarrow {}^2F_{7/2}$ emission. As the temperature increases, most the $4f^{12}5d^1 \rightarrow 4f^{13}$ emissions quench via multi-phonon relaxation and by far only the $(^3H_6,t_{2g})_{S=3/2} \rightarrow {}^2F_{7/2}$ and the $^2F_{5/2} \rightarrow {}^2F_{7/2}$ emission remain present at room temperature. For all compositions, a $^2F_{5/2} \rightarrow {}^2F_{7/2}$ risetime phenomenon is observed whose duration matches the $(^3H_6,t_{2g})_{S=3/2} \rightarrow {}^2F_{7/2}$ decay time. This reveals a direct feeding from the $(^3H_6,t_{2g})_{S=3/2}$ level towards the $^2F_{5/2}$ level. The feeding becomes less efficient from Cl→Br→I, as evidenced by a shorter risetime. This is unexpected because the related $(^3H_6,t_{2g})_{S=3/2}$-$^2F_{5/2}$ energy gap becomes smaller from Cl→Br→I. The temperature dependence of the $(^3H_6,t_{2g})_{S=3/2} \rightarrow {}^2F_{7/2}$ and $^2F_{5/2} \rightarrow {}^2F_{7/2}$ emission intensities displayed an anti-correlation and confirmed that the feeding process is thermally stimulated. The thermally stimulated activation energies that control the temperature dependence increase from Cl→Br→I, despite the observation that the $(^3H_6,t_{2g})_{S=3/2}$-$^2F_{5/2}$ energy gap becomes smaller. Our analysis revealed that the unexpected behaviour in risetime and activation energy, as a function of composition, cannot be explained by $(^3H_6,t_{2g})_{S=3/2} \rightarrow {}^2F_{5/2}$ feeding via interband crossing, but can be explained via multi-phonon relaxation when we assume that the electron-phonon coupling strength decreases from Cl→Br→I. No strong relation was found between the varying Cl/Br and Br/I ratios in composition and the $^2F_{5/2} \rightarrow {}^2F_{7/2}$ QE, as the measured values at room temperature fluctuated between 40-70% and were without a clear trend. The fluctuations must therefore be related to intrinsic sample differences introduced during synthesis or handling.

In **chapter 5**, the influence of the Tm^{2+}-doping percentage on the QE of the $^2F_{5/2} \rightarrow {}^2F_{7/2}$ emission was investigated in SrI_2. As the Tm^{2+}-doping concentration increases from 0.4 to 5 mol %, the $^2F_{5/2} \rightarrow {}^2F_{7/2}$ QE and decay time remain at a constant value of, respectively, 55 ±3% and 1.1 ±1·10^{-2} ms. In this concentration range, the absorption and integrated luminescence intensity both increase linearly and then start to saturate. At 5 mol % Tm^{2+}-doping, the absorption reaches a value of 59 ±3%. As the Tm^{2+}-doping concentration is increased from 5 mol % to 36 mol %, concentration quenching effects occur that cause for a decrease in the $^2F_{5/2} \rightarrow {}^2F_{7/2}$ QE and luminescence decay time, while the absorption saturates further. However, the QE decreases by a factor of almost 20, from 55 ±3% to 3 ±0.2%, while the decay time only decreases by a factor 2. This discrepancy is explained by the presence of a second crystal phase, with $CdCl_2$ structure, that starts to form at a Tm^{2+}-doping percentage of 12 mol %. It is discovered from a Rietveld refinement on the X-ray diffraction data and is

evidenced by the strong presence of a broad band that emerges in the absorption spectra. Since this band is not observed in the excitation spectra as acquired on the $^2F_{5/2}\rightarrow{}^2F_{7/2}$ emission, the Tm^{2+}-doping ions that occupy the Sr-sites in the $CdCl_2$ structure have a negligible contribution to the $^2F_{5/2}\rightarrow{}^2F_{7/2}$ emission intensity. The Tm^{2+} ions in the $CdCl_2$ phase thus have a much lower $^2F_{5/2}\rightarrow{}^2F_{7/2}$ QE than in the regular SrI_2 phase. The Tm^{2+} excited states dynamics was also investigated in these samples. At a temperature of 100 K, a $^2F_{5/2}\rightarrow{}^2F_{7/2}$ risetime phenomenon is encountered that is of similar order to the decay time of the $(^3H_6,t_{2g})_{S=3/2}\rightarrow{}^2F_{7/2}$ emission, indicating the presence of a $(^3H_6,t_{2g})_{S=3/2}\rightarrow{}^2F_{5/2}$ feeding process. At lower temperatures, the risetime is also present but much shorter than the $(^3H_6,t_{2g})_{S=3/2}\rightarrow{}^2F_{7/2}$ decay time. A much similar situation was encountered for $CaCl_2$:Tm^{2+} and $CaBr_2$:Tm^{2+}, as discussed in **chapter 3**. The $(^3H_6,t_{2g})_{S=3/2}\rightarrow{}^2F_{7/2}$ and $^2F_{5/2}\rightarrow{}^2F_{7/2}$ emission intensities follow an anti-correlated trend over temperature, where the former emission starts to quench at 100 K. Furthermore, the Tm^{2+} ions in the $CdCl_2$ crystal phase give rise to an additional emission that already quenches at 20 K. Since the $(^3H_6,t_{2g})_{S=3/2}$-$^2F_{5/2}$ energy gap is only slightly smaller in the $CdCl_2$ phase, as compared to the regular SrI_2 phase, the quenching cannot primarily stem from multi-phonon relaxation and will most likely occur via $(^3H_6,t_{2g})_{S=3/2}\rightarrow{}^2F_{5/2}$ interband crossing. The lower than unity QE of the Tm^{2+} ions in the regular SrI_2 phase, and the low QE of the Tm^{2+} ions in the $CdCl_2$ phase, might then be explained by a room temperature interband crossing between the $(^3H_6,t_{2g})_{S=3/2}$ state and the $^2F_{7/2}$ ground state.

6.1 References

[1] O.M. ten Kate, K.W. Krämer, E. Van der Kolk, Efficient luminescent solar concentrators based on self-absorption free, Tm^{2+} doped halides, Sol. Energy Mater Sol. Cells 115-120 (2015) 140.

[2] E. Beurer, J. Grimm, P. Gerner, H.U. Güdel, Absorption, Light Emission, and Upconversion Properties of Tm^{2+}-doped $CsCaI_3$ and $RbCaI_3$, Inorg. Chem. 9901-9906 (2006) 45.

[3] J. Grimm, E. Beurer, P. Gerner, H.U. Güdel, Upconversion between 4f–5d excited states in Tm^{2+}-doped $CsCaCl_3$, $CsCaBr_3$, and $CsCaI_3$, Chem. Eur. J. 1152-1157 (2007) 13.

[4] J. Grimm, J.F. Suyver, G. Carver, H. U. Güdel, Light-Emission and Excited-State Dynamics in Tm^{2+} Doped $CsCaI_3$, $CsCaBr_3$, and $CsCaI_3$, J. Phys. Chem. B 2093-2101 (2006) 110.

[5] J. Grimm, O.S. Wenger, K.W. Krämer, H.U. Güdel, 4f-4f and 4f-5d excited states and luminescence properties of Tm^{2+}-doped CaF_2, $CaCl_2$, $SrCl_2$, $BaCl_2$, J. Phys. Chem. B 101-105 (2006) 110.

7.

Samenvatting

Tm^{2+}-gedoopte haliden bezitten uitstekende eigenschappen voor Luminescente Zonnecollectoren (*Engels: Luminescence Solar Concentrators {LSCs}*) toepassingen. Dergelijke LSC's bestaan uit een glazen golfgeleider met aan de randen koper-indium-selenide *(Engels: Copper-Indium-Selenide {CIS})* zonnecellen. De golfgeleider bevat een luminescente coating gebaseerd op een Tm^{2+}-gedoopte halide, waarvan de $4f^{12}5d^{1}$-absorptiebanden in staat zijn om een groot deel van het AM 1.5-zonnespectrum te absorberen. Omdat de absorptie plaatsvindt over het gehele zichtbare licht (380-750 nm) en met een grotendeels uniforme absorptiesterkte, toont de coating kleurloos en semi-transparant. Het geabsorbeerde zonlicht wordt vervolgens via de Tm^{2+} relaxatie dynamica omgezet in de Tm^{2+} $^2F_{5/2}\rightarrow{}^2F_{7/2}$ emissie met een golflengte van 1140 nm. Aangezien deze emissie buiten het bereik van de $4f^{12}5d^{1}$-absorptiebanden valt, kunnen er geen zelfabsorptieverliezen optreden. Deze vormen over het algemeen een belangrijke beperking voor de totale LSC-efficiëntie. Het omgezette licht wordt vervolgens door de coating uitgezonden en propageert via totale interne reflectie door de golfgeleider, welke het naar de CIS-zonnecellen geleidt. Deze zonnecellen zetten het licht vervolgens, via een fotovoltaïsche reactie, om in elektriciteit. LSC-coatings gebaseerd op Tm^{2+}-gedoopte haliden kunnen aldus worden toegepast als duurzame raamtechnologie en zijn daarmee, als onderdeel van Building-Integrated Photovoltaics (BIPV), in staat om, het energieverbruik van gebouwen verminderen, waardoor deze zelfvoorzienend worden en minder afhankelijk zijn van fossiele brandstoffen. [1]

Hoewel de optische en luminescentie-eigenschappen van voornamelijk CaF_2:Tm^{2+}, $CsCaX_3$:Tm^{2+} (X = Cl, Br, I) en MCl_2:Tm^{2+} (M = Ba, Ca, Sr) reeds zijn onderzocht, blijft er een aanzienlijke hoeveelheid aan Tm^{2+}-gedoopte haliden onbestudeerd. Daarnaast zijn belangrijke thema's zoals de interne Kwantum Efficienctie *(Engels: Quantum Efficiency {QE})* en de Tm^{2+} concentratie-uitdoving in dergelijke materialen nog nooit eerder onderzocht. Zo is de QE van de $^2F_{5/2}\rightarrow{}^2F_{7/2}$ emissie van directe invloed op de algehele LSC-efficiëntie. Deze parameter wordt bepaald door de Tm^{2+} relaxatie dynamica van aangeslagen toestanden in het materiaal. In het verleden is deze dynamica enkel grondig bestudeerd voor Tm^{2+} gedoopte $CsCaX_3$ (X = Cl, Br, I) trihaliden perovskieten. [2-5] In deze studies zijn echter geen andere opties overwogen dan uitdoving via multi-fononen relaxatie en er werd geen correlatie gemaakt met QEs, nochtans werden dergelijke waarden ooit gerapporteerd.

Het is daarom het hoofddoel van dit proefschrift om de Tm^{2+} relaxatie dynamica van aangeslagen toestanden in verschillende haliden te onderzoeken. Dit als functie van hun samenstelling, temperatuur- en tijdsafhankelijkheid, en in relatie met de $^2F_{5/2} \rightarrow {}^2F_{7/2}$ QE. Hierbij wordt er zowel een kwalitatieve als kwantitatieve analyse gegeven van de verschillende $4f^{12}5d^1 \rightarrow 4f^{12}5d^1$ en $4f^{12}5d^1 \rightarrow 4f^{13}$ stralingloze verval processen.

In **hoofdstuk 2** werd de Tm^{2+} relaxatie dynamica van aangeslagen toestanden onderzocht in NaX (X = Cl, Br, I) verbindingen. De 20 K emissiespectra onthulden de aanwezigheid van maximaal vijf verschillende Tm^{2+} emissies: vier $4f^{12}5d^1 \rightarrow 4f^{13}$ emissies en de $4f^{13} \rightarrow 4f^{13}$ emissie. Een bijbehorend niveauschema is weergegeven in figuur 7.1. Naarmate de temperatuur stijgt tot 120 K, ondergaan de meeste $4f^{12}5d^1 \rightarrow 4f^{13}$ emissies een uitdoving via multi-fononen relaxatie en blijven alleen de laagste energetische $4f^{12}5d^1 \rightarrow 4f^{13}$, $(^3H_6,t_{2g})_{S=3/2} \rightarrow {}^2F_{7/2}$, emissie en de $4f^{13} \rightarrow 4f^{13}$, $^2F_{5/2} \rightarrow {}^2F_{7/2}$, emissie over. Voor NaBr:Tm^{2+} begint de intensiteit van de $(^3H_6,t_{2g})_{S=3/2} \rightarrow {}^2F_{7/2}$ emissie snel af te nemen bij temperaturen boven 170 K. De $^2F_{5/2} \rightarrow {}^2F_{7/2}$ emissie intensiteit vertoont dan een directe anticorrelatie met de intensiteit van de $(^3H_6,t_{2g})_{S=3/2} \rightarrow {}^2F_{7/2}$ emissie en neemt dus significant toe. Dit duidt op een

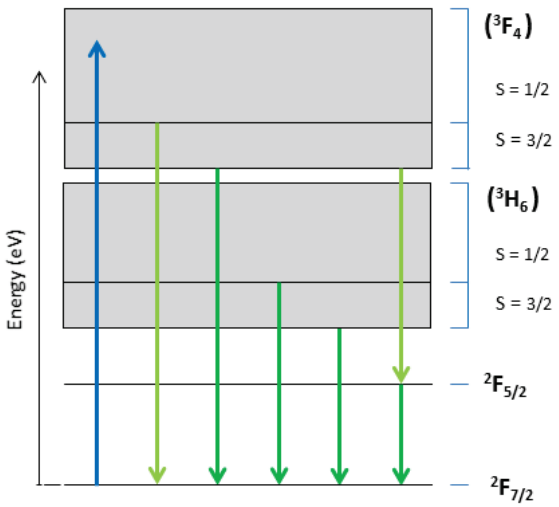

Figuur 7.1: Energieniveaudiagram van een typische Tm^{2+}-gedoopte halide. Weergegeven zijn de twee laagste $4f^{12}5d^1$-energieniveaus: ($^3F_4$) en ($^3H_6$). Beide niveaus zijn onderverdeeld in spin-toegestane (S=1/2) en spin-verboden (S=3/2) toestanden. Deze laatste zijn gepositioneerd op relatief lagere energie. Eveneens weergegeven zijn de ($^2F_{5/2}$) $4f^{13}$ aangeslagen toestand en ($^2F_{7/2}$) $4f^{13}$ grondtoestand. De verschillende Tm^{2+} emissies zijn aangegeven met groene pijlen, waarbij de lichtgroene pijlen slechts zelden waargenomen Tm^{2+} emissies vertegenwoordigen. Dit betreft de $(^3F_4)_{S=1/2} \rightarrow {}^2F_{7/2}$ emissie, die tot nu toe alleen werd waargenomen in $CsCaI_3$:Tm^{2+} [2,3, hoofdstuk 5], en de $(^3F_4)_{S=3/2} \rightarrow {}^2F_{5/2}$ emissie die gevonden kan worden in $CsCaX_3$:Tm^{2+} (X = Cl, Br, I) [2, 4, hoofdstuk 5] en NaY:Tm^{2+} (Y = Cl, Br) [Hoofdstuk 2]. De $(^3H_6)_{S=1/2} \rightarrow {}^2F_{7/2}$ emissie is vrijwel altijd afwezig in chlorideverbindingen en is tot nu toe alleen gerapporteerd in $BaCl_2$:Tm^{2+}. [5]

$(^3H_6,t_{2g})_{S=3/2}\rightarrow{}^2F_{5/2}$ stralingsloze voeding, zoals bevestigd door de aanwezigheid van een stijgtijdverschijnsel in de $^2F_{5/2}\rightarrow{}^2F_{7/2}$ vervalcurven. De stijgtijd is van vergelijkbare grootte als de vervaltijd van de $(^3H_6,t_{2g})_{S=3/2}\rightarrow{}^2F_{7/2}$ emissie. Naarmate de temperatuur stijgt, versnelt het stralingsloze voeden en bij kamertemperatuur blijft alleen de $^2F_{5/2}\rightarrow{}^2F_{7/2}$ emissie over. De kamertemperatuur QE van de $^2F_{5/2}\rightarrow{}^2F_{7/2}$ emissie in NaBr:Tm^{2+} werd gemeten als 32±2%. Dat de QE geen 100% is, wordt verklaard door de aanwezigheid van meerdere Tm^{2+}-sites en defecten zoals veroorzaakt door de vereiste ladingscompensatie wanneer Tm^{2+} de monohaliden op de Na^+-site bezet. Bovendien bevindt het geselecteerde $(^3F_4,t_{2g})$-excitatieniveau zich op hogere energie en mogelijk dicht bij de geleidingsband, waardoor waardoor stralingsloos verval mogelijk is via Tm^{2+}-gebonden excitontoestanden naar de $(^2F_{5/2})$ $4f^{13}$-aangeslagen toestand en de $(^2F_{7/2})$ $4f^{13}$ grondtoestand.

Hoofdstuk 3 richtte zich op de Tm^{2+} relaxatie dynamica van aangeslagen toestanden in CaX_2 (X = Cl, Br, I), waarbij er geen ladingscompensatie vereist is. De 20 K emissiespectra tonen vier verschillende Tm^{2+} emissies, zoals analoog aan NaI:Tm^{2+}. Voor CaI_2:Tm^{2+} is de $(^3F_4,t_{2g})\rightarrow{}^2F_{7/2}$ emissie, vanuit de op hogere energie gelegen $4f^{12}5d^1$-toestand, veel intenser op 20 K dan de $(^3H_6,t_{2g})_{S=3/2}\rightarrow{}^2F_{7/2}$ emissie. Een vergelijkbare situatie werd eerder gemeld voor $CsCaI_3$:Tm^{2+}. [4] Dit kan worden verklaard door een relatief grotere energiekloof tussen de $(^3F_4,t_{2g})$-$(^3H_6,t_{2g})_{S=1/2}$ toestanden, zoals vergeleken met de $(^3H_6,t_{2g})_{S=3/2}$-$(^2F_{5/2})$ energiekloof, waardoor de $(^3F_4,t_{2g})\rightarrow{}^2F_{7/2}$ emissie op een veel hogere temperatuur uitdooft via multi-fononen relaxatie. In het geval van $CaCl_2$:Tm^{2+} en $CaBr_2$:Tm^{2+} doven de meeste $4f^{12}5d^1\rightarrow4f^{13}$ emissies, via multi-fononen relaxatie, op een temperatuur van 100 K en blijven alleen de $(^3H_6,t_{2g})_{S=3/2}\rightarrow{}^2F_{7/2}$ en de $^2F_{5/2}\rightarrow{}^2F_{7/2}$ emissies over. Om de hierop volgende $(^3H_6,t_{2g})_{S=3/2}\rightarrow{}^2F_{5/2}$ stralingsloze voeding te beschrijven, werd er een reactie-snelheidsmodel ontwikkeld. Dit model werd met succes gefit op de temperatuur- en tijdsafhankelijke luminescente-intensiteitsdata van $CaBr_2$:Tm^{2+} en $CaCl_2$:Tm^{2+}. Deze analyse onthulde dat de stralingsloze relaxatie plaatsvindt via twee verschillende processen. Bij lage temperaturen domineert multi-fononen relaxatie naar de $(^2F_{5/2})$ $4f^{13}$ aangeslagen toestand. Aangezien dit proces bij de laagste temperaturen minder temperatuurafhankelijk is, verklaart dit de aanwezigheid van de $^2F_{5/2}\rightarrow{}^2F_{7/2}$ emissie op 20 K. Naarmate de temperatuur stijgt, tot typisch 130 K, wordt het tweede proces van interband-kruising thermisch geactiveerd. Bijgevolg wordt alleen de $^2F_{5/2}\rightarrow{}^2F_{7/2}$ emissie waargenomen op kamertemperatuur. Hoewel de kwantitatieve fit benadering de algehele temperatuur- en tijdsafhankelijkheid van de $(^3H_6,t_{2g})_{S=3/2}\rightarrow{}^2F_{7/2}$ goed beschreef, werden twee belangrijke discrepanties waargenomen. Bij lage temperaturen is de $^2F_{5/2}\rightarrow{}^2F_{7/2}$ stijgtijd aanzienlijk korter dan voorspeld door ons model. Luminescentie vervalmetingen op 20 K laten zien dat de vervaltijd van de $(^3H_6,t_{2g})_{S=3/2}\rightarrow{}^2F_{7/2}$ emissie 15 keer langer is dan de $^2F_{5/2}\rightarrow{}^2F_{7/2}$ stijgtijd. Naarmate de temperatuur stijgt tot 150 K, begint de $^2F_{5/2}\rightarrow{}^2F_{7/2}$ stijgtijd te convergeren naar de

$(^3H_6,t_{2g})_{S=3/2}\rightarrow{}^2F_{7/2}$ vervaltijd en bereikt deze een bijna identieke waarde op kamertemperatuur. Dit fenomeen kan waarschijnlijk worden verklaard door de aanwezigheid van een $(^3H_6,t_{2g})_{S=3/2}\rightarrow{}^2F_{5/2}$ voedingsroute via multi-fononen relaxatie op lage temperatuur, welke een sterke elektron-fonon koppeling heeft en die afwezig is in ons model. Bovendien voorspelde het model een $^2F_{5/2}\rightarrow{}^2F_{7/2}$ QE van 100%, terwijl de gemeten waarden bij kamertemperatuur tussen 20-30% lagen. Dit werd ook waargenomen voor de NaX:Tm^{2+} monohaliden.

In **hoofdstuk 4** werden de Cl/Br en Br/I verhoudingen in $CsCaX_3$:Tm^{2+} (X = Cl, Br, I), vaste oplossingen, systematisch gevarieerd. Dit resulteerde in een reeks van 11 verschillende materialen. Door de compositie te tunen, worden de posities van de Tm^{2+} $4f^{12}5d^1$-niveaus consequent verschoven ten opzichte van de ($^2F_{5/2}$) en ($^2F_{7/2}$) $4f^{13}$-niveaus. Bij lage temperaturen kunnen tot vijf verschillende Tm^{2+} $4f^{12}5d^1\rightarrow4f^{13}$ emissies worden waargenomen, tezamen met de $^2F_{5/2}\rightarrow{}^2F_{7/2}$ emissie. Naarmate de temperatuur stijgt, doven de meeste $4f^{12}5d^1\rightarrow4f^{13}$ emissies uit via multi-fononen relaxatie en verreweg alleen de $(^3H_6,t_{2g})_{S=3/2}\rightarrow{}^2F_{7/2}$ en de $^2F_{5/2}\rightarrow{}^2F_{7/2}$ emissie blijven op kamer temperatuur aanwezig. Voor alle composities wordt een $^2F_{5/2}\rightarrow{}^2F_{7/2}$ stijgtijdverschijnsel waargenomen waarvan de duur overeenkomt met de $(^3H_6,t_{2g})_{S=3/2}\rightarrow{}^2F_{7/2}$ vervaltijd. Dit onthult een directe voeding van het $(^3H_6,t_{2g})_{S=3/2}$ niveau naar het $^2F_{5/2}$ niveau. De voeding wordt minder efficiënt van Cl→Br→I, wat blijkt uit een kortere stijgtijd. Dit is onverwacht gezien de gerelateerde $(^3H_6,t_{2g})_{S=3/2}$-$^2F_{5/2}$ energiekloof kleiner wordt van Cl→Br→I. De temperatuurafhankelijkheid van de $(^3H_6,t_{2g})_{S=3/2}\rightarrow{}^2F_{7/2}$ en $^2F_{5/2}\rightarrow{}^2F_{7/2}$ emissie-intensiteiten vertoonde een anticorrelatie en bevestigde de thermische stimulatie van het voedingsproces. De thermisch gestimuleerde activeringsenergieën die de temperatuurafhankelijkheid regelen, nemen toe van Cl→Br→I, ondanks de waarneming dat de $(^3H_6,t_{2g})_{S=3/2}$-$^2F_{5/2}$ energiekloof kleiner wordt. Uit onze analyse bleek dat het onverwachte gedrag in stijgtijd en activeringsenergie, als functie van de samenstelling, niet kan worden verklaard door $(^3H_6,t_{2g})_{S=3/2}\rightarrow{}^2F_{5/2}$ voeding via interband-kruising, maar eerder via multi-fononen relaxatie wanneer aangenomen wordt dat de elektron-fonon koppelingssterkte afneemt van Cl→Br→I. Er werd geen sterke relatie gevonden tussen de variërende Cl/Br- en Br/I-verhoudingen in de samenstellingen en de $^2F_{5/2}\rightarrow{}^2F_{7/2}$ QE, aangezien de gemeten waarden bij kamertemperatuur schommelden tussen 40-70% en geen duidelijke trend vertoonden. De fluctuaties moeten daarom gerelateerd zijn aan intrinsieke sample verschillen die worden geïntroduceerd tijdens synthese of aanverwante handelingen.

In **hoofdstuk 5** werd de invloed van het Tm^{2+}-dopingpercentage op de QE van de $^2F_{5/2}\rightarrow{}^2F_{7/2}$ emissie onderzocht in SrI_2. Naarmate de Tm^{2+}-dopingconcentratie toeneemt van 0,4 tot 5 mol%, blijven de $^2F_{5/2}\rightarrow{}^2F_{7/2}$ QE en de vervaltijd op een constante waarde van respectievelijk

55 ±3% en 1,1 ±1·10-2 ms. In deze concentratie-range nemen de absorptie en de geïntegreerde luminescentie-intensiteit beide lineair toe en beginnen dan te verzadigen. Bij 5 mol% Tm^{2+}-doping bereikt de absorptie een waarde van 59 ±3%. Naarmate de Tm^{2+}-dopingconcentratie wordt verhoogd van 5 mol% naar 36 mol%, treden concentratie-uitdovingseffecten op die leiden tot een afname van de $^2F_{5/2}\rightarrow{}^2F_{7/2}$ QE en luminescentievervaltijd, terwijl de absorptie verder verzadigt. De QE neemt echter met een factor van bijna 20 af, van 55 ± 3% naar 3 ± 0,2%, terwijl de vervaltijd slechts met een factor 2 afneemt. Deze discrepantie wordt verklaard door de aanwezigheid van een tweede kristalfase, met $CdCl_2$-structuur, die zich begint te vormen bij een Tm^{2+}-dopingpercentage van 12 mol%. De $CdCl_2$ structuur volgt uit een Rietveld-verfijning op de röntgendiffractiegegevens en blijkt ook uit de sterke aanwezigheid van een brede band die op komt in de absorptiespectra. Aangezien deze band niet wordt waargenomen in de excitatiespectra zoals verkregen op de $^2F_{5/2}\rightarrow{}^2F_{7/2}$ emissie, hebben de Tm^{2+}-dopingionen die de Sr-plaatsen in de CdCl2-structuur bezetten een verwaarloosbare bijdrage aan de $^2F_{5/2}\rightarrow{}^2F_{7/2}$ emissie-intensiteit. De Tm^{2+}-ionen in de $CdCl_2$-fase hebben dus een veel lagere $^2F_{5/2}\rightarrow{}^2F_{7/2}$ QE dan in de reguliere SrI_2-fase. De Tm^{2+} relaxatie dynamica van aangeslagen toestanden werd ook in deze materialen onderzocht. Bij een temperatuur van 100 K treedt een $^2F_{5/2}\rightarrow{}^2F_{7/2}$ stijgtijdverschijnsel op dat vergelijkbaar is met de vervaltijd van de $(^3H_6,t_{2g})_{S=3/2}\rightarrow{}^2F_{7/2}$ emissie. Dit wijst op de aanwezigheid van een $(^3H_6,t_{2g})_{S=3/2}\rightarrow{}^2F_{5/2}$ voedingsproces. Bij lagere temperaturen is de stijgtijd ook aanwezig, maar veel korter dan de $(^3H_6,t_{2g})_{S=3/2}\rightarrow{}^2F_{7/2}$ vervaltijd. Een vergelijkbare situatie deed zich voor bij $CaCl_2$:Tm^{2+} en $CaBr_2$:Tm^{2+}, zoals besproken in **hoofdstuk 3**. De $(^3H_6,t_{2g})_{S=3/2}\rightarrow{}^2F_{7/2}$ en $^2F_{5/2}\rightarrow{}^2F_{7/2}$ emissie-intensiteiten volgen een anti-gecorreleerde trend over temperatuur, waarbij de eerstgenoemde emissie begint af te nemen bij 100 K. Verder geven de Tm^{2+} ionen in de $CdCl_2$ kristalfase aanleiding tot een extra emissie die al begint uit te doven bij 20 K. Aangezien de $(^3H_6,t_{2g})_{S=3/2}$-$^2F_{5/2}$ energiekloof slechts iets kleiner is in de $CdCl_2$ fase, zoals vergeleken die in de reguliere SrI_2-fase, kan de uitdoving niet primair het gevolg zijn van multi-fononen relaxatie en zal deze hoogstwaarschijnlijk plaatsvinden via $(^3H_6,t_{2g})_{S=3/2}\rightarrow{}^2F_{5/2}$ interband-kruising. De lagere QE van de Tm^{2+}-ionen in de reguliere SrI_2-fase, en de lage QE van de Tm^{2+}-ionen in de $CdCl_2$-fase, zou dan kunnen worden verklaard door een interband-kruising bij kamertemperatuur tussen de $(^3H_6,t_{2g})_{S=3/2}$ toestand en de $^2F_{7/2}$ grondtoestand.

7.1 Bronnen

[1] O.M. ten Kate, K.W. Krämer, E. Van der Kolk, Efficient luminescent solar concentrators based on self-absorption free, Tm^{2+} doped halides, Sol. Energy Mater Sol. Cells 115-120 (2015) 140.

[2] E. Beurer, J. Grimm, P. Gerner, H.U. Güdel, Absorption, Light Emission, and Upconversion Properties of Tm^{2+}-doped $CsCaI_3$ and $RbCaI_3$, Inorg. Chem. 9901-9906 (2006) 45.

[3] J. Grimm, E. Beurer, P. Gerner, H.U. Güdel, Upconversion between 4f–5d excited states in Tm^{2+}-doped $CsCaCl_3$, $CsCaBr_3$, and $CsCaI_3$, Chem. Eur. J. 1152-1157 (2007) 13.

[4] J. Grimm, J.F. Suyver, G. Carver, H. U. Güdel, Light-Emission and Excited-State Dynamics in Tm^{2+} Doped $CsCaI_3$, $CsCaBr_3$, and $CsCaI_3$, J. Phys. Chem. B 2093-2101 (2006) 110.

[5] J. Grimm, O.S. Wenger, K.W. Krämer, H.U. Güdel, 4f-4f and 4f-5d excited states and luminescence properties of Tm^{2+}-doped CaF_2, $CaCl_2$, $SrCl_2$, $BaCl_2$, J. Phys. Chem. B 101-105 (2006) 110.

Dankwoord

Dit proefschrift zou nooit tot stand zijn gekomen zonder de steun en toewijding van velen. In de eerste plaats wil ik mijn dagelijkse begeleider Dr. Erik van der Kolk hartelijk bedanken voor alle supervisie en technische ondersteuning die ik de afgelopen 4¼ jaar heb mogen ontvangen. Jouw deur stond altijd voor mij open, ook ten tijde van de COVID-19 pandemie. Tezamen hebben we eindeloze uren naar papieren grafieken gestaard. Tot mijn grote genoegen delen we de hartstocht voor sport, waaronder met name die voor het hardlopen. Daarnaast wil ik Prof.dr. Pieter Dorenbos zeer hartelijk bedanken voor het delen van zijn scherpe visie en waardevolle inzichten. Zonder jouw krachtige blik zouden mijn artikelen een stuk minder fraai geweest zijn. Het was daarnaast een privilege om met jou als grootheid rond de tafel te zitten. Wat bijzonder dat onze onderzoeksinteressen plotseling convergeerden naar het fenomeen van de 'Plokker' emissie. Het leidde in de onderzoeksgroep deels tot een herboren tijdperk voor haliden gast-roosters. Ik ben tevens veel dank verschuldigd aan Prof.dr. Karl Krämer. Het was een grote eer om als gast-onderzoeker bij u in Bern te mogen verblijven. Het was daarnaast ook een heel avontuur! Ik kijk dan ook met volle zekerheid terug op de ongetwijfeld mooiste periode van het project. Uw onuitputtelijke kennis over de halide materialen, hun structuur en synthese is overweldigend en heeft ons vele malen geholpen in het complementeren van de partituur: getuige de artikelen. Ware het niet uw aanstekelijke enthousiasme of uitzonderlijk optimisme, dan zal ik de beklimming naar 2000 meter hoogte nooit vergeten! Eveneens veel dank aan de altijd belangstellende Dr. Bert Hintzen. Als chemicus binnen de vakgroep beschikt u over een zeldzaam kennisgebied voor wat betreft synthese en structurele eigenschappen der lichtgevende materialen. Mijn studenten en ik zijn u veel dank verschuldigd zijn voor de vele Kazànistische tips en trucs. Voorts hebben we beide ook een grootse interesse in de laatste technologische ontwikkelingen op het gebied van duurzame energie. Dit geeft de gesprekken een extra levendige impuls. Ook veel dank aan Dr.ir. Melvin ten Kate, voor de bereidwilligheid tot het altijd beantwoorden van dringende vragen betreffende een voor jou inmiddels afgesloten onderzoeksthema. In hedendaagse termen laat zich dit vertalen in een unicum.

Vanzelfsprekend ben ik de technici eveneens enorm veel dank verschuldigd. In de eerste plaats betreft dit ing. Johan de Haas. Heel erg bedankt voor alle technische hulp bij het opstarten van metingen en voor het almaar verbeteren van de PLE en decay opstelling. Het is hoogst wonderbaarlijk om te zien hoe jij met jouw kennis en kunde de soms ook wel over-geromantiseerde wensen en dromen van gebruikers in vervulling laat gaan. Daarnaast ben ik ook veel dank verschuldigd aan ing. Baukje Terptra van de ARI-vakgroep. Met uw hulp zijn we uiteindelijk in staat geweest om op een nauwkeurige manier de Tm^{2+} concentraties in

onze samples te bepalen: een knipogend vaarwel naar het zweverige procedé van vooraf afgewogen hoeveelheden. Ir. Ruben Abellon en ing. Nick Dusoswa van de OMEC-vakgroep op ChemE wil ik bedanken voor de vele QE metingen. Het was niet alleen leerzaam, maar stiekem ook Hollands gezellig! Drs. Cees Goubitz, Ing. Michel Steenvoorden en Ing. Robert Dankelman wil ik bedanken voor de technische ondersteuning met de XRD. Of het nu spectra of diffractogrammen waren, de apparatuur functioneerde altijd perfect! Dr. Bert Zwart, bedankt voor de vele quartz ampoules! Cruciale elementen in de fabricage van onze Tm^{2+}-gedoopte halides, welke ook veelvoudig aftrek vonden onder de studenten. Ing. Jan Huizenga, bedankt voor de boeiende gesprekken over recent gespotte vogels en verrekijkers. Van de Nieuw-Zeelandse spur-winged plover tot lepelaar, we hebben ze uitvoerig tegen het daglicht gehouden. Selbstverständlich auch viel Dank an der Daniel Biner. Een man met een enorme geestdrift die elke morgen tal van kristallografische kunstwerken uit de befaamde Bernse ovens tovert. Het Corona-Epoche maakte het ons niet gemakkelijk, maar ik heb veel van je geleerd! An die nette Frau Beatrice Frey, vielen Dank für alles und damit gemeint natürlich auch die Schweizer Gemütlichkeit. Trudy Beentjes, onmisbare schakel in het grote geheel, bedankt voor jouw onuitputtelijke administratieve ondersteuning en de geanimeerde gesprekken!

Vanzelfsprekend ben ik ook mijn studenten: Dwayne Rutjes (.BSc), Mels Kerklaan (.BSc), Floor van Dam (.BSc), Inge van der Knijff (.BSc), Anne de Wit (.BSc), Bas van der Pol (.BSc), ir. Wietse Hoogsteen, Sophie Vlaar (.BSc), Aaron Bakx (.BSc), Boyd Voet (.BSc), ir. Thom Woudstra en Stan Bergkamp (.BSc) veel dank verschuldigd. Jullie hebben uiterst fanatiek gevochten en met grote vastberadenheid, zoals echte Romeinen. Samen hebben we de fantasievolle gedachtespinsels verwezenlijkt tot authentieke resultaten. Er zijn momenten geweest waarop ik jullie de Mont Blanc heb laten beklimmen op een klosje garen, maar jullie waren nooit alleen op dit avontuur! Ik wens jullie al het beste en voorspoed in de toekomstige carrière. Wellicht kruisen onze paden zich ooit nogmaals.

Mijn collega´s wil ik bedanken voor de prettige sfeer en de tal van wetenschappelijke en alledaagse gesprekken: Francesco, Hongde, Roy, Jarno, Tianshuai, Beien, Casper, Jasper, Minh, Alexandros, Robin, Vasilli, Yuan-Chen, Monika, Weronika, Maxim, Eveline, Hanan, Evgenii, Rogier, Fahimeh, Najbul en vele anderen. We hebben er een mooie tijd van gemaakt! Vasilli bedankt voor al jouw hulp. Ik ga graag nog een keer met je basketballen. Jasper en Casper het was tussen het werken door erg gezellig op de kamer! Hilarisch om te zien dat jullie mijn aanwezigheid in de laatste maand zo erg begonnen te missen, dat er een pop uit kartonnen dozen werd vervaardigd. Leuk dat jullie verder gaan met de haliden! Ik ben daarmee blij dat ik jullie de gebouwde synthese opstelling en ontworpen hygroscopische samplehouders cadeau kan doen en dat daarmee het geheel niet uit gaat

als een flikkerende nachtkaars. Maxim, het was supergaaf om elk half jaar met jou de RID/RST Pubquiz te organiseren. Wat hebben we hard gelachen om potentiële strikvragen en game changers. We zouden bijna een bv. kunnen starten. Daarnaast ook een zeer veel dank aan Dr. Roy Awater. Door een kortstondige samenloop van toevalligheden was daar naast het werk ineens een hechte vriendschap. Grappig hoe het leven soms kan lopen! Ik wil jou en óók Elise heel hartelijk bedanken voor het delen van de vele mooie momenten naast het travail. Enorm veel dank ook dat je als paranimf zo dadelijk de voorste linies bemant. Maikel Awater, veel dank voor het ontwerp van de kaft. Het resultaat is wederom een traktatie voor het oog.

Dr. Lourens van Dijk en Dr. Wilma Eerenstein ben ik veel dank verschuldigd voor de waardevolle tips, inzichten en observaties die uiteindelijk hebben geleid tot mijn zoektocht naar een promotiepositie. Dr. Stephan Eijt wil ik hier eveneens voor bedanken. Onze onderzoekswegen hebben zich inmiddels op onmiskenbare wijze gescheiden, maar ik heb me nooit een betere leermeester met zoveel toewijding en zorgzaamheid kunnen wensen of indenken! Dhr. Holwerda ben ik op de grootst mogelijke manier dank verschuldigd voor de uitzonderlijke mogelijkheid en exceptionele kans die ik van hem heb mogen ontvangen op het moment dat alles aan me voorbij leek te gaan. Dhr. Robert Grootendorst wil ik bedanken voor de interessante tussentijdse uitstapjes naar oorlogsmusea en verdedigingswerken van indrukwekkend technisch vernuft. Mijn buren: Em. prof.dr. Ignatz de Schepper, dhr. Luc Hendriks, mevr. Margriet de Schepper en wijlen Ds. Bram van Minnen wil ik heel hartelijk bedanken voor alle morele steun tijdens mijn eerste Delftse studiejaren en de verworven vriendschap. Ignatz, u bent in alle opzichten een markante verschijning en een uitstekend raadsheer. Tim van der Maas, je hebt werkelijk alles in de waagschaal geworpen om jouw levensdoel te bereiken: als klinisch fysicus mensen medisch te hulp schieten. Fantastisch! Jammer dat je met Evianne zo ver weg bent gaan wonen. Het is altijd super gezellig en vaak is de tijd te kort. Veel dank ook dat je zitting neemt als paranimf. De stellingen zoals uitgesproken met jouw prachtige Zeeuwse dialect zullen me vast veel geluk brengen. Martin Glimmerveen en Ci-Wah Kan, bedankt voor het organiseren van de vele leuke bordspel avonden! Voor mij een nimmer te vergeten moment dat jullie me op doorreis kwamen opzoeken in Bern. Helaas hebben we de Einhorn Marsch niet kunnen lopen, maar aan gezelligheid was er geen gebrek. Martijn de Jonge, bijzonder dat we tijdens onze stages bij Exasun bv. bevriend zijn geraakt en nog steeds regelmatig contact hebben. Bedankt voor de gezelligheid en de boeiende gesprekken. Majoor Guy Riela, hoewel je tijdens dit schrijven op uitzending bent in Mali, wil ik jou en Marloes erg bedanken voor de leuke en gezellige tijd in Hellevoetsluis. Wat uniek dat we al zolang bevriend zijn. Michiel Kleij, jou wil ik hier eveneens voor bedanken. Hoewel je vaak druk in de weer bent met werk of het sleutelen aan jouw auto's, is het altijd erg gezellig om weer eens bij te praten. Vénusia

Bertin, quelle chance d'avoir vécu près de vous à Berne. Ce que la distance et l'avenir nous réservent est incertain. Mais chaque moment partagé est spécial et donne de l'énergie positive. Et chaque appel me motive pour la semaine de travail à venir.

Mijn broers Matthijs en Michiel wil ik bedanken voor de vele avonturen, hun wijze raad, en de onvoorwaardelijke gastvrijheid als er even een bittere pil moest worden doorgeslikt en de behoefte naar een tijdelijk kuuroord groot was. Aileen, je bent een prachtige Duitse gesprekspartner en ware een zus voor me. Je had het lef me last-minute te vergezellen met het Sportabzeichen en hebt daarmee wederom bewezen dat de Duitse vrouw nog altijd een deuk in een pak boter slaat. Pilar, ook jou beschouw ik als mijn hervonden zus. Jouw eeuwige positivisme is me tijdens het onderzoek zeker ten goede gekomen. We dronken samen tal van kostbare wijnen, Jimmy's juweeltjes uit de vorige eeuw, en bespraken de stand van het leven. Mijn ouders wil ik bedanken voor de financiële en morele steun tijdens de vele jaren van studie en onderzoek. Hugo, zonder jouw enorme toewijding en inzet was ik nooit technische natuurkunde gaan studeren. Ik heb hier nimmer spijt van gehad. Al van jongs af aan heb je me geleerd om goed te presteren, verantwoordelijkheid te nemen en om recht door zee te zijn. Pretpakketen waren een verboden beginsel. Wis- en natuurkunde vormden daarentegen een essentiële basis. Met kennis van Archimedes en consorten is het leven inderdaad veel waardevoller. Hoewel de zeilvakanties met soms eindeloze dagen op zee niet altijd een even inspirerend decor vormden, heb ik veel van je opgestoken omtrent: GPS navigatie, het NATO alfabet en de noodzakelijke scheepsknopen. Qua karakter ben ik heel veel op je gaan lijken. Wilma, zonder jouw doorzettingsvermogen was ik nooit geboren. Vanaf dat moment waren we dan ook onafscheidelijk. Je leerde me eerlijkheid, oprechtheid, mezelf te zijn en om nooit bij de pakken neer te gaan zitten. Jouw liefde, passie en zorgzaamheid voor het welzijn van mensen deel ik!

List of Publications

1. **M.P. Plokker**, N. Dusoswa, D.A. Biner, P. Dorenbos, K.W. Krämer and E. van der Kolk, *Photoluminescence and Excited States Dynamics of Tm^{2+}-doped $CsCa(Cl/Br)_3$ and $CsCa(Br/I)_3$ Perovskites*, Journal of Physics: Materials 4 (2021) p. 045004 1-19.

2. **M.P. Plokker**, I.C. van der Knijff, A.V. de Wit, B. Voet, T. Woudstra, V. Khanin, P. Dorenbos and E. van der Kolk*, Experimental and Numerical Analysis of Tm^{2+}Excited States Dynamics and Luminescence in CaX_2 (X = Cl, Br, I),* Journal of Physics: Condensed Matter 33 (2021) p. 255701 1-12.

3. **M.P. Plokker**, W. Hoogsteen, R.D. Abellon, K.W. Krämer and E. van der Kolk, *Concentration and Temperature Dependent Luminescence Properties of the SrI_2-TmI_2 System,* Journal of Luminescence 225 (2020) p. 117327 1-8.

   Oral Presentation: Bern University, Department of Chemistry, Biochemistry and Pharmaceutical Sciences, Section of Solid State Chemistry, Bern, Switzerland, 25th September 2020.

4. **M.P. Plokker**, E. van der Kolk, *Temperature Dependent Relaxation Dynamics of Luminescent NaX:Tm^{2+} (X = Cl, Br, I),* Journal of Luminescence 216 (2019) p. 116694 1-9.

   Oral Presentation: 20th International Conference on Dynamical Processes in Excited States of Solids (DPC19), Christchurch, New-Zealand, 26-30th August 2019.

   Poster Presentation: RST Science Day, Delft, The Netherlands, 2nd April 2019.

   Poster Presentation: Physics@Veldhoven, Veldhoven, The Netherlands, 23-24th January 2018.

Other Publications:

1. **M.P. Plokker**, S.W.H. Eijt, F. Naziris, H. Schut, F. Nafezarefi, H. Schreuders, S. Cornelius, B. Dam, *Electronic structure and vacancy formation in photochromic yttrium oxy-hydride thin films studied by positron annihilation*, Solar Energy Materials and Solar Cells 177 (2017) p. 97-105.

   Poster Presentation: 12th International Meeting on Electrochromism (IME12), Delft, The Netherlands, 28th August – 1st September 2016.

2. J. Melskens, A. Schnegg, A. Baldansuren, K. Lips, **M.P. Plokker**, S.W.H. Eijt, H. Schut, M. Fischer, M. Zeman, A.H.M. Smets, *Structural and electrical properties of metastable defects in hydrogenated amorphous silicon*, Physical Review B 91 (2015) p. 245207 1-6.

Thesis Supervision

Bachelor Students

- D. Rutjes, Quantum Efficiency Measured by an Integrating Sphere, June (2018).

- M. Kerklaan, Sample Synthesis and Luminescence Properties of NaI:$Tm^{2+/3+}$: Exploring Possibilities for Quantum Cutting, July (2018).

- F. van Dam, Preparation, Synthesis and Analysis of CaI_2:XTm^{2+} (X = 1, 2, 3, 4, 5, 6, 7, 8 mol %) for Studying Concentration Quenching, August (2018).

- I.C. van der Knijff, Temperature-Dependent Relaxation Dynamics of $CaCl_2$:Tm^{2+} and CaI_2:Tm^{2+}, October (2018).

- A.V. de Wit, Temperature-Resolved Luminescence and Relaxation Dynamics of $CaBr_2$:Tm^{2+}, January (2019).

- B. van der Pol, Numerical Modelling of Excited State Relaxation Dynamics for Various Tm^{2+}-Doped Halides, June (2019).

- S. Vlaar, Temperature Dependent Relaxation Dynamics of $BaCl_2$:Tm^{2+}, July (2019).

- A.H.J. Bakx, The Search for Quantum-Cutting in Mixed Valent Thulium Doped Barium Dihalides to Increase Solar Cell Efficiency, July (2019).

- B. Voet, Computational Analysis of Luminescence Processes in Divalent Thulium Doped Halides, September (2019).

- S.W. Bergkamp, Exploring Energy Transfer in BaCl2:$Tm^{2+/3}$: Examining the Possibility of Quantum Cutting through Down-Conversion in Mixed Di-/Trivalent Thulium Doped Barium Chloride, August (2021).

Master Students

- W. Hoogsteen, Quantifying the Concentration Dependent Luminescent Properties of SrI_2:Tm^{2+}, November (2019).

- T. Woudstra, Luminescence of Tm^{2+}-doped Calcium dihalides: An in-depth study on the temperature dependent decay dynamics of CaX_2:Tm^{2+} (X = Cl, Br, I), February (2021).

About the Author

Maarten Pieter Plokker was born on the 3rd of May 1989 in Hellevoetsluis, the Netherlands. He attended the Bahûrim secondary school in Brielle where he acquired his his Vmbo-TL diploma in 2005. Thereafter, he transferred to the Jacob van Liesveldt in Hellevoetsluis where he graduated for his HAVO pre-college degree in 2007 and subsequently advanced on for his VWO pre-university degree. In 2009 he moved to Delft to study Applied Physics.

At the TU Delft he obtained his Bachelor degree in Applied Physics in 2013 on the topic of 'Hydrogenated amorphous silicon thin film solar cell absorber layers'. Parts of his results were published in the journal of Solar Energy Materials & Solar Cells. In 2016 he acquired his Masters degree in Applied Physics. His graduation project centred on the theme of 'Photochromic yttriumoxihydides for smart window applications'. Together with his supervisor, Dr. Stephan Eijt, he wrote an article on their discoveries which was admitted in the journal of Solar Energy Materials & Solar Cells. In addition, he poster presented his findings on the 12th International Meeting on Electrochromism. Conclusively he followed an internship at Linesolar BV where he constructed a sensor panel for testing the performance of a novel concentrator photovoltaic module.

After his graduation from university he worked for several months as a research engineer at Exasun BV, where he constructed a PV testfield and automated parts of the solar module production process. He then found a new challenge at the Reactor Institute Delft, where he started a PhD project under supervision of Dr. Erik van der Kolk and Prof.dr. Pieter Dorenbos. The results of this enterprise are published in this dissertation.

Parallel to his studies, Plokker worked for 9 years as a receptionist and host in a home of the elderly. In his spare time, he has a profound interest in history and military technology. Another great passion resides with sports: field athletics, road athletics, long-distance hiking and swimming. He obtained the German sportsbadge in silver, the Nijmegen Vierdaagsekruis with crown and among many other things participated in a two-hours non-stop swimming event and completed a 100 km walk through the fields of Flanders in 24 hours.

TU Delft